Sources and Transport Characteristics of Mineral Dust in Dronning Maud Land, Antarctica

Dissertation zur Erlangung des Grades

Dr. rer. nat.

vorgelegt dem
Fachbereich Geowissenschaften
der Universität Bremen

von
Anna Wegner

Sources and Transport Characteristics of Mineral Dust in Dronning Maud Land, Antarctica

Contents

Contents

Abstract

Mineral dust in polar ice cores provides unique information about climate induced changes both in dust sources and on the atmospheric transport of dust particles from the source to the polar ice sheets.

The presented work investigates changes in sources and transport of dust in the EPICA-DML (EPICA-DML: European Project for Ice Coring in Antarctica - Dronning Maud Land) ice core during Glacial and during the transition to the Holocene.

Changes in dust concentration and size were determined on seasonal timescale during cold and warm climate stages in two time slices at 25600 yr BP (Glacial) and 13200 yr BP (Antarctic Cold Reversal (ACR)). The contribution of transport and source to the observed changes in dust concentration were estimated using a one dimensional transport model. Dust sources were investigated by comparing Rare Earth Element (REE) fingerprints from 33 new samples from potential source areas (PSA) with those in the ice core in a quasi-continuous profile (398 out of 613 m) spanning a period from 26600 yr BP to 7500 yr BP.

For the first time, data on dust concentration and size in seasonal resolution were obtained, showing differences in seasonal variation in the Glacial and in ACR. It could be shown that during the Glacial dust concentrations exceed concentrations during ACR by a factor of 28, though the size does not differ significantly (Glacial: $\mu = 1.88 \pm 0.15 \ \mu m$, ACR: $\mu = 1.96 \pm 0.13 \ \mu m$). On seasonal scale during the Glacial, size changes of 0.2 - 0.3 μm and during the ACR of 0.2 - 0.35 μm occur in phase with mean dust concentration changes of a factor of 7.6 in the Glacial and a factor of 3.5 in the ACR. During the Glacial a clear maximum in concentration and size occurs during austral winter.

The difference in dust concentration between Glacial and ACR cannot be explained by transport. On seasonal scale, during the Glacial 30 - 63% of the observed dust concentration changes can be explained by transport, during the ACR even 70 - 100%. This implies that the source did not change significantly during the ACR, during the Glacial by a factor of 1.5 - 2.6, and between Glacial and ACR actually by a factor of ≈ 28.

Data show that REE can be used to determine sources of mineral dust in Antarctic ice cores. For the time period 26600 - 15200 yr BP, South America was identified as source for dust in the EPICA-DML ice core. Between 15200 and 7500 yr BP, the source could not be identified unambiguously by using REE fingerprints. However, the South American influence seems to weaken and the influence of other source areas seems to increase in warm periods.

Zusammenfassung

Mineralischer Staub in polaren Eiskernen bietet einzigartige Informationen über klimabedingte Änderungen sowohl in den Staubquellen als auch während des atmosphärischen Transports der Staubpartikel von der Quelle zu den polaren Eisschilden.

In der vorliegenden Arbeit werden Veränderungen in den Quellen und im Transport des Staubes im EPICA-DML (EPICA-DML: European Project for Ice Coring in Antarctica - Dronning Maud Land) Eiskern während des Glazials und während des Übergangs zum Holozän untersucht: Staubkonzentrations- und Staubgrößenänderung wurden in saisonaler Auflösung während Kalt- und Warmzeiten in zwei Zeitfenstern um 25600 Jahre vor heute (Glazial) und um 13200 Jahre vor heute (Antarctic Cold Reversal (ACR)) ermittelt. Die Beiträge von Transport und Quelle zu den beobachteten Staubkonzentrationsänderungen wurden mit Hilfe eines eindimesionalen Transportmodells abgeschätzt. Die Staubquellen wurden über den Vergleich der Verhältnisse der Seltenen Erden in 33 neuen Proben aus den potentiellen Quellgebieten mit denen im Eiskern über einen Zeitraum von 7.500 - 26.600 Jahre vor heute in einem quasi-kontinuierlichen Profil (398 von 613 m) untersucht.

Zum ersten Mal wurden Daten von Staubkonzentrationen und -größen in saisonaler Auflösung gewonnen, die Unterschiede in der saisonale Variation im Glazial und im ACR aufweisen. Es konnte gezeigt werden, dass die Staubkonzentrationen während des Glazials die des ACRs um das 28fache übersteigen. Die Größe unterscheidet sich jedoch nicht signifikant (Glazial: $\mu = 1.88 \pm 0.15 \ \mu m$, ACR: $\mu = 1.96 \pm 0.13 \ \mu m$). Auf saisonaler Zeitskala treten im Glazial Größenänderungen von 0.2 - 0.3 μm und im ACR von 0.2 - 0.35 μm auf, die mit mittleren Änderungen der Konzentration um einen Faktor von 7.6 im Glazial und von 3.5 im ACR einhergehen. Im Glazial tritt ein Maximum in Größe und Konzentration im Winter auf.

Der Unterschied in der Staubkonzentration zwischen Glazial und ACR kann nicht durch den Transport erklärt werden. Auf saisonaler Skala kann im Glazial 30 - 63 % der Staubkonzentrationsänderungen durch Transportvariationen erklärt werden, im ACR sogar 70 - 100 %. Die bedeutet, das sich auf saisonaler Zeitskala im ACR die Quelle fast nicht geändert hat, im ACR um einen Faktor von 1.5 - 2.6, und zwischen Glazial und ACR sogar um einen Faktor von $\approx$28.

Das gewonnene Datenmaterial zeigt, dass sich Seltenen Erden dazu eignen Quellen von Staub in antarktischen Eiskernen zu bestimmen. Für den Zeitraum von 26600 - 15200 Jahren vor heute konnte Südamerika als Quelle für Staub im EPICA-DML Eiskern identifiziert werden. Von 15200 - 7500 Jahren vor heute konnte keine eindeutige Quelle identifiziert werden. Allerdings scheint der Einfluss von Südamerika abzunehmen und der Einfluss anderer Quellen scheint zu steigen.

1 Introduction

The importance of the understanding of climate is demonstrated by awarding the No-
bel Price for peace 2007 to the Intergovernmental Panel on Climate Change (IPCC)
and Al Gore "for their efforts to build up and disseminate greater knowledge about
man-made climate change, and to lay the foundations for the measures that are
needed to counteract such change". Indeed, the climate system of our planet is
very complex and still far from being understood. The investigation of naturally
occurring climate change is the key to the understanding of anthropogenic influence
on climate change. Mineral dust and other aerosols as well as trace gases present
in the atmosphere have a great effect on our climate even without any human ac-
tivity, where the net effect of aerosol on the radiative budget of the Earth is still
insufficiently constrained ([IPCC, 2007]). Figure 1.1 illustrates different species in-
fluencing the world's climate. CO_2 and the other greenhouse gases have the largest
amplifying effect. The contribution of aerosols, which also include mineral dust, to
radiative forcing can be divided into direct and indirect effects. A direct effect occurs
through light scattering on particles in the atmosphere (e.g. [Tegen et al., 1997],
[Harrison et al., 2001], [Sokolik et al., 2001]). Reflection of incoming solar radiation
with shorter wave length causes a cooling, whereas scattering of outgoing infrared
radiation with longer wave length causes a warming of the atmosphere. Depending
on a variety of factors, like particle size and the nature of the underlying earths
surface, one or the other effect dominates ([Arimoto, 2001]). A recent study demon-
strated far reaching, also economical, consequences of this effect ([Lau and Kim,
2007]): A large dust storm event in the Sahara during the early hurricane season
(July - September) in 2006 produced a high dust load in the atmosphere over the
Atlantic. The accompanying cooling of the sea surface temperature, could be the
reason for the absence of strong hurricanes reaching the North American continent
later during that year. Beside the direct effect of dust on the radiation balance, an
indirect consequence is possible by particles acting as cloud condensation nuclei and
influencing the cloud cover ([Duce, 1995], [Mahowald and Kiehl, 2003]). Both direct
an indirect effect have still a high degree of uncertainty indicated by the large error
bars in Figure 1.1. Dust can provide reaction surfaces not only for water vapour,
but also for other reactive gases and therewith moderate chemical processes in the
atmosphere ([Dentener et al., 1996]).
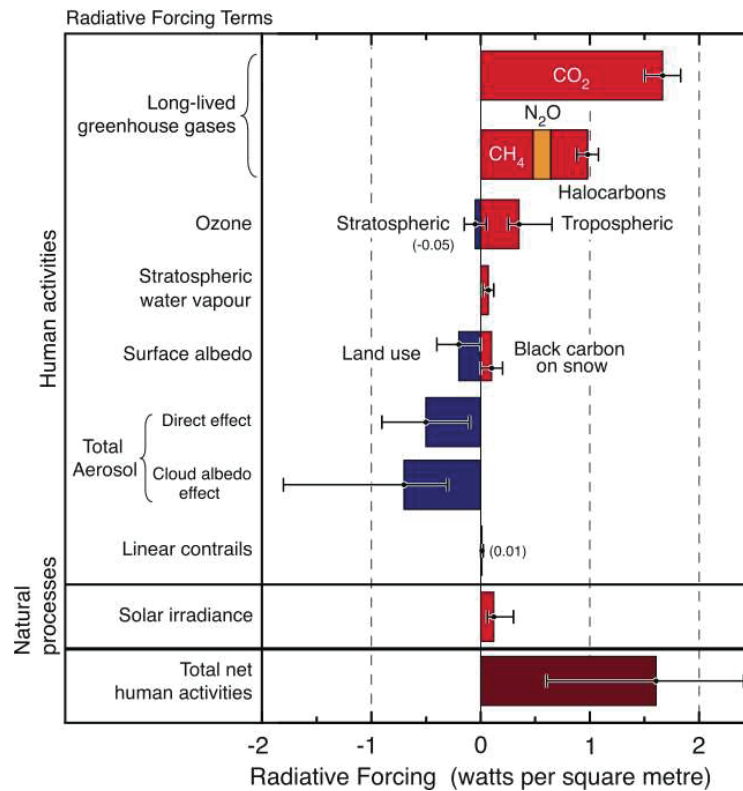
Figure 1.1: Components contributing to radiative forcing, 1750 - 2005, (figure taken from [IPCC, 2007]).

Beside its physical properties, the chemical qualities of dust have a large impact on the global climate. The mean concentration of iron in the upper continental crust, the parent material for dust, is 30.9 mg $\cdot$ g^{-1} ([Wedepohl, 1995]). The major portion of the earth surface consists of water and represents a large sink for aeolian dust. Hence dust is an important source of iron to the world´s oceans. Enhanced iron supply to the ocean increases the algae growth accompanied by an increased potential for CO_2-uptake of the ocean ([Watson et al., 2000]). This connection is especially important for the iron limited regions in the Southern Ocean. Here atmospheric dust supply is low, originating from small dust sources in Argentina, Australia, and South Africa ([Prospero et al., 2002]). Changes in these small desert regions may have a disproportionately large global impact ([Jickells et al., 2005]). Climate archives show an up to two orders of magnitude higher dust concentration during glacial times than during Interglacials (e.g. [EPICA Community Members, 2004]). The lower atmospheric dust load during warmer climate causes a lower dust input into the oceans and therewith a decrease of their biological productivity. The CO_2 concentration in the atmosphere raises and therewith the temperature accompanied with low dust concentrations. On the other hand, high dust concentrations in the atmosphere and high dust input into the oceans during Glacials produce a

lower atmospheric CO_2 concentration and lower temperature, associated with higher atmospheric dust load. Therewith, CO_2 and dust compose a self-energizing system ([Ridgwell and Watson, 2002], [Ridgwell, 2002]), which can explain CO_2 changes of 20 - 30 ppmv ([Koehler et al., 2005]). Not only oceans, but also terrestrial systems are suspected to be fertilized by eolian input of iron. One example is the saharan dust transported over the Atlantic ocean, which could be a major supplier of nutrients for the Amazon rainforest ([Swap et al., 1992], [Arimoto, 2001]). All these examples show the importance of mineral dust for our climate.

Dust is not only important as a species influencing our climate, it is also used as a proxy indicator for aridity and changes in the past global wind systems ([Rea, 1994], [Kohfeld and Harrison, 2001], [Yung et al., 1996]). The climate from the past has to be studied, to understand the naturally occurring climate change. Ice cores (e.g. [EPICA-community members, 2006], [EPICA Community Members, 2004]), marine sediments (e.g. [Lisiecki and Raymo, 2005]) or tree rings ([Martinelli, 2004]) are valuable archives storing information about paleo climate. Especially in ice cores, a wealth of information is enclosed simultaneously covering a period of up to almost one million years: Isotopic composition of oxygen and hydrogen yields information about paleo temperature (e.g. [EPICA Community Members, 2006]). Air kept in bubbles in the ice represents the gas composition of the paleo atmosphere (e.g. [Spahni et al., 2005], [Siegenthaler et al., 2005]). Changes in the solar activity and the geomagnetic field intensity can be reconstructed using ^{10}Be measured in ice cores (e.g. [Beer et al., 1988], [Beer et al., 2006]). Dust and ions from ice cores give the past aerosol composition. A peculiar quality of dust as a paleo climate proxy is, that different information can be obtained on the same particle: size, chemical composition and total concentration in the archive. Particles with a diameter of a few micro meter or less can be transported by winds over long distances (e.g. [Grousset et al., 2003]). In general, the dust size decreases during transport from the source to the sink due to gravitational settling. Hence, dust size profiles obtained at a certain site are unique data to reconstruct past wind intensities ([Rea, 1994]). By comparing the chemical or isotopical composition of dust in the archive with the one in the potential source areas (PSAs), the sources of the dust in the archive can be identified ([Grousset and Biscaye, 2005]). Finally, dust concentrations reflect changes in the dust source and during transport.

The dust input on ice sheets in remote polar regions is solely aeolian origin. Thus, ice cores drilled in this area are a unique possibility to study past dust transport characteristics. Within the European Project for Ice Coring in Antarctica (EPICA) two deep drillings were conducted in Antarctica (Figure 1.2). One of them in Dron-
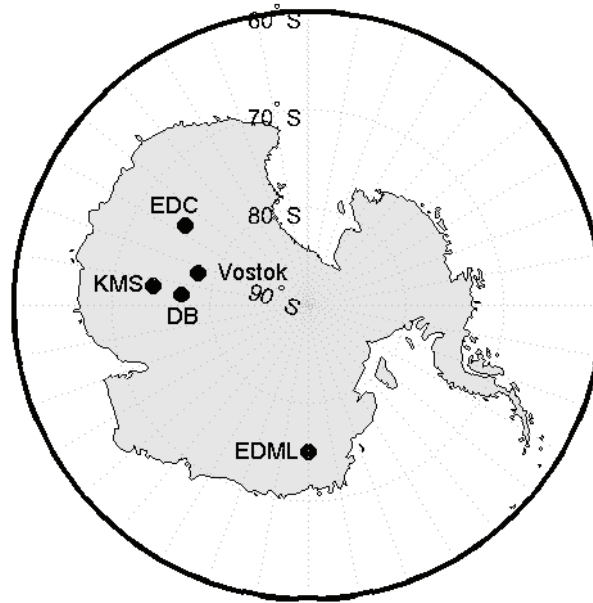
Figure 1.2: Map of Antarctica with selected drilling locations of ice cores, where dust concentration and size profiles were measured: EDML: EPICA-DML (this work), EDC: EPICA-Dome C, DB: Dome B, KMS: Komsomolskaya ([Delmonte et al., 2005]).

ning Maud Land (DML) facing the Atlantic Ocean and the other one at Dome C in a region of Antarctica facing the Indian ocean. The latter has a lower accumulation rate of 25 kg m^{-2} year^{-1} offering a long record of more than 800000 years ([EPICA Community Members, 2004]). The former has a rather high accumulation rate (64 kg m^{-2} year^{-1}, [Ruth et al., 2007b]) offering a higher resolution up to marine isotope stage (MIS) 4 ([Fischer et al., 2007a]). The two EPICA ice cores have a common age scale established by a tight synchronization of volcanic horizons ([Ruth et al., 2007b], [Severi et al., 2007]).

Measurements of dust in ice cores from Antarctica show dust concentration changes on Glacial - Interglacial timescales of about two orders of magnitude (e.g. [EPICA Community Members, 2004], [Fischer et al., 2007a], [Delmonte et al., 2004b]). These measurements represent always mean values of several years. Up to now the observed amplitude of Glacial - Interglacial dust concentration changes cannot be reproduced by global circulation models ([Mahowald et al., 2006]). Model results for Greenland ice cores indicate, that taking into account seasonal changes in dust emission and deposition is necessary to explain the observed dust concentration changes ([Werner et al., 2002]). For Antarctica no dust measurements in glacial ice in seasonal resolution are published up to now. However, the high accumulation EPICA-DML ice core enables dust measurements showing seasonal variations in dust concentration and size.

Isotopic measurements on Strontium and Neodymium defined the Patagonian desserts as the source for dust in the Indian sector of Antarctica during the Glacials with some possible contributions from another source during Interglacials ([Delmonte et al., 2002a]) most likely of Australian origin ([Revel-Rolland et al., 2006]). Due to its geographic location closer to South America than the other ice cores drilled in East Antarctica and its position downwind of the cyclonically curved atmospheric pathway from Patagonia ([Reijmer et al., 2002]), a strong influence of the Australian source seems unlikely in DML ([Fischer et al., 2007a]). But this assumption was not confirmed by measurements up to now. Isotopic measurements on Strontium and Neodymium need large volume of ice (300 g to 2-3 kg in Glacial and Interglacial samples, respectively, [Delmonte, 2003]). Since drilling ice cores in Antarctica requires a huge effort in time, money and logistics, ice is very precious and sample volume very limited. Analysis on ice cores have to performed on as small samples volume as possible. Rare Earth Elements (REE) fingerprints were used to identify dust provenances e.g. in Australia ([Marx et al., 2005b]) and may serve as a tool to identify sources of Antarctic ice core dust using a sample volume significantly smaller than for isotopic measurements on Sr and Nd.

In this work changes in dust concentration, size and composition of the REE are investigated in the EPICA-DML ice core. The underlying questions are:

1. How did the dust concentration and size change on subannual timescales during cold and warm stages?

2. How much of the (seasonal) dust concentration changes can be explained by the source and how much by transport?

3. Do REE have the potential to be used to identify the sources of dust in Antarctic ice cores?

4. Wherefrom originates dust reaching the EPICA-DML drill site in the last Glacial and how did the sources change during the transition to the Holocene?

Topic 1 and 2 will be discussed in Chapter 5, topic 3 and 4 in Chapter 6. Chapter 2 and 3 provide background information about dust and REE. Chapter 4 describes the measurements of dust concentration and size. Additionally four papers are attached, which evolved during this work. Paper I describes the connection between southern and northern hemisphere inferred by the EPICA-DML ice core. Paper II focuses on sea-salt and dust concentration in the two EPICA ice cores and explains how much of the Glacial-Interglacial changes in the dust concentration can be explained by the source and by transport. The personal contribution to both papers was

laboratory work on the continuous flow analysis to obtain, ionic species, dust and other parameters and discussion of the results. Paper III will be submitted to Analytica Chimica Acta. Different inductively coupled plasma mass spectrometer (ICP-MS) systems for the analysis of REE are compared. A new method using the ICP-Time of flight-MS is presented. The personal contribution were measurements on the ICP-Sector Field-MS and the discussion of the results. Paper IV is submitted to Environmental Science & Technology. It compares different proxy parameter, that are used to describe dust. The personal contribution was the discussion of the results and the calibration for the laser sensor system.

2 Physical and Chemical Characteristics of Dust

2.1 Dust as an Aerosol

Solid and liquid suspended particles in the atmosphere are denoted as aerosol ([Feichter, 2003]). From the earth surface discharged aerosol, so called primary aerosol, includes sea salt and dust. The sink of aerosol in the atmosphere is removal by wet and dry deposition. Sea salt refers to aerosol emitted from the oceans surface, whereas dust consists of wind deflated mineral material from continental areas, material ejected during volcanic eruptions, industrial emission, fire and cosmic material. The first one of these represents the main portion of the dust aerosol in the small size class with a diameter $d < 2 \ \mu m$ ([Pye, 1987]). In the following the term dust denotes windblown mineral material from continental areas. It is characterized by its chemical properties like its elemental composition and its physical properties like its size or shape. Common size classes for dust are clay ($d < 2.5 \ \mu m$), silt (2.5 $\mu m < d < 60 \ \mu m$) and sand (60 $\mu m < d < 2 \ mm$). Due to stronger gravitational settling with increasing size only clay plays an important role in long range transport. Further aspects of the size of long traveled dust will be specified in Section 2.3.

The influence of dust on the climate is well known, even if the strength of the influence has a large uncertainty [IPCC, 2007]. Impact on the radiative balance occur directly by scattering and absorbtion of radiation by dust particles and indirectly through cloud formation, when particles act as condensation nuclei. In addition, enhanced biological activity in the Southern Ocean through iron fertilization by dust input can influence the atmospheric budget of the greenhouse gas CO_2 ([Ridgwell and Watson, 2002]).

Another important factor of dust, beside its influence on climate, is its potential to be interpreted as a climate proxy (e.g. [EPICA community members, 2004]). High aridity and storminess increase the dust input into the atmosphere and lower precipitation, accompanying higher aridity, reduce the wash-out from the atmosphere, thus enable higher atmospheric dust load and more effective transport especially in remote areas, like Antarctica and Greenland.

Therefore it is of great value to measure dust in different palaeo climate archives like marine sediments (e.g. [Rea, 1994]), peat bogs (e.g. [Martinez Cortizas et al.,

2005]) and ice cores (e.g. [Wolff et al., 2006]). Different dust characteristics are used to extract information from the archive. In ice core science, Ca^{2+} (rather nssCa = Ca^{2+} corrected for Ca^{2+} originating from sea salt) is widely used as a tracer for mineral dust, since it can be easily measured by standard ion chromatography (IC) (e.g. [Fischer et al., 2007a], [Röthlisberger et al., 2002], [Ruth et al., 2002]). Ca^{2+} has a mean abundance of 4.6 % in the continental crust ([Albarede, 2003]), but, like for all other chemical species used as a proxy for dust, the mineralogical and chemical composition is variable and influences also the Ca^{2+}-content in the dust. Moreover, by using IC only the water soluble fraction of the dust is quantified. Other elements, like Fe and Al can serve as tracer for mineral dust as well, but more challenging methods like Inductively Coupled Plasma Mass Spectrometry (ICP-MS) have to be performed to measure these elements. Furthermore, the problem of varying abundance and solubility, is size dependent for all elements ([Claquin et al., 1999], [Fung et al., 2000], [Mahowald et al., 2002]). Another approach to quantify dust, which avoids these problems, is to measure the particle concentration by laser blocking sensor or electric sensing zone techniques to quantify the non water soluble fraction of the dust (e.g. [Delmonte et al., 2002a], [Ruth et al., 2003]). Thus, not only the concentration, but also the size of the unsoluble dust can be measured. A detailed comparison of different proxies for dust measured in ice cores is performed by [Ruth et al., 2007a]. In the following, if not specified otherwise, dust is denoted as the non water soluble particle concentration measured by electric sensing zone technique or laser blocking sensor.

2.2 Dust in Ice Cores

Successively deposited snow layers on polar ice caps are a valuable archive for past climate up to 800 000 years ([EPICA community members, 2004], [EPICA community members, 2006], [NGRIP-Members, 2004]). Owing to its 98 % coverage with ice and its long distance to the surrounding continents, Antarctica represents one of the cleanest areas in the world and dust concentrations in ice cores are extremely low (7-9 $\frac{ng}{mL}$ in Holocene ice, [Delmonte et al., 2004b]). This demands very high analytical efforts not to contaminate samples during the analysis in the lab. Additionally, obtaining ice cores from this remote locations requires a high logistic effort, which increases with both the length and the size of the obtained core. Therefore the sample volume available for the analysis is very limited.

Figure 2.1 shows the dust and deuterium record of the Dome C ice core record. Dust concentrations vary by 2 orders of magnitude in anti phase with the temperature proxy δD between glacial and interglacial times, with lower values during
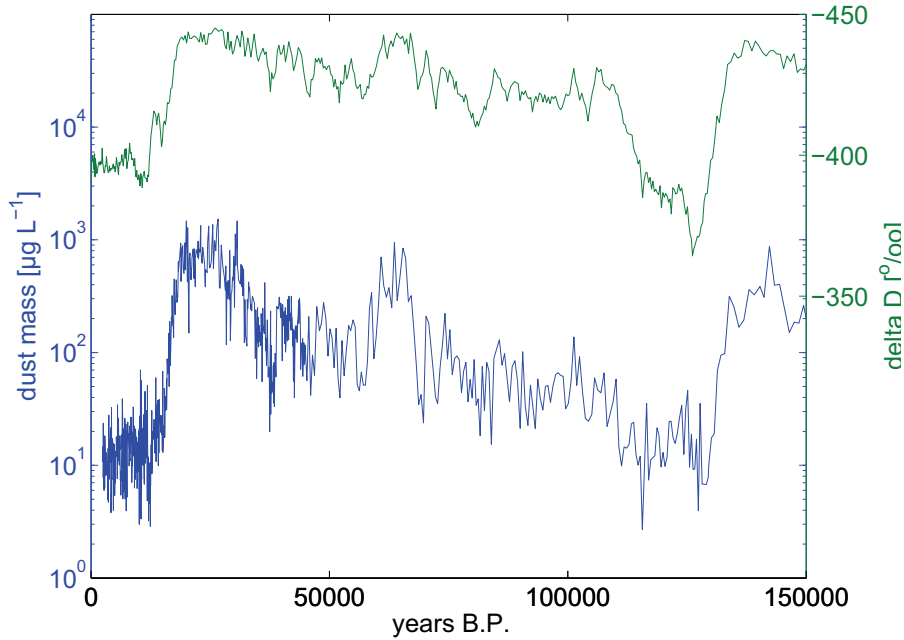
Figure 2.1: Deuterium (top, green) and dust (bottom, blue) record of the Dome C ice core ([EPICA community members, 2004]). The strong relationship between dust and temperature is obvious.

warmer climate (indicated by higher δD values). Even small excursions to warmer climate during the last Glacial found in the δD record (Antarctic isotope maxima), have its counterpart in the dust record evidencing a strong relationship between dust concentration and temperature. To explain, how much of these changes is caused by source influences and how much the transport affects these changes is part of this work.

2.3 Description of the Dust Size

The dust size can be described by several parameters: Widely used in ice core science is the logarithmic normal distribution (log-normal distribution, Figure 2.2, [Royer et al., 1983], [de Angelis et al., 1984], [Steffensen, 1997], [Ruth et al., 2003]).

$$V(logd) = \frac{a_0}{\sqrt{2\pi}log\sigma_V}e^{-\frac{1}{2}\frac{(logd-log\mu_V)^2}{log^2\sigma_V}}$$

The log-normal distribution is defined by the modal value μ_V, the amplitude $A = \frac{a_0}{\sqrt{2\pi}log\sigma_V}$ and the standard deviation $log\sigma_V$. The volume or mass size distribution has to be distinguished from the number distribution. Volume and mass size distribution only differ by a factor of ≈ 2.5 g·cm^{-2}, whereas the number distribution is shifted to lower sizes. In the following the modal value of the volume or mass size distribution will be used and denoted with mode or μ. An example obtained in the EPICA-DML ice core is given in Figure 2.2. Typical values for the mode in Antarctic ice cores
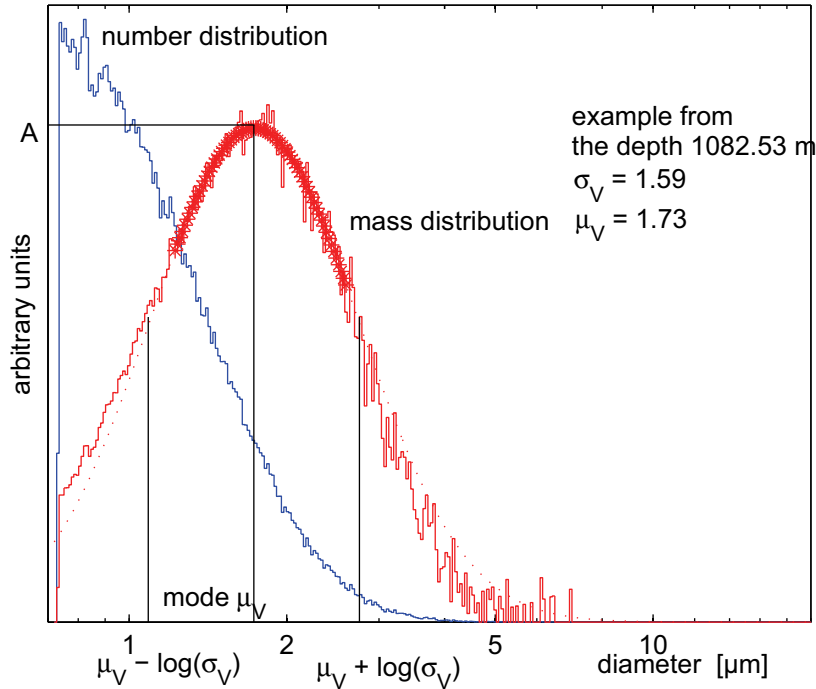
Figure 2.2: Example for a size distribution measured in the EPICA-DML ice core at a depth of 1082.53 m. The mass or volume distribution is shown in red, the number distribution in blue. The dotted line follows the logarithmic normal distribution, which is fitted to the mass distribution using the part of the distribution marked with the thick red line.

lie around 1.9 - 2 μm (e.g. [Delmonte et al., 2002a]) and 1.5 to 2 μm in Greenland ([Ruth et al., 2003], [Steffensen, 1997]). $\log\sigma_V$ gives the width of the distribution by its deflection points which are located at $\log\mu_V + \log\sigma_V$ and $\log\mu_V - \log\sigma_V$. Since this distribution has several mathematical advantages, it is very convenient to use, however does not fully reflect the features of measured size distributions in ice cores. Therefore, [Delmonte et al., 2002b] introduced the 4-parameter Weibull distribution, which takes into account the slight asymmetry of the particle spectra. For discussing dust size changes over longer time scales the fine and coarse particle percentage (FPP and CPP) are used as well ([Delmonte et al., 2004b], [Delmonte et al., 2005]). With FPP (CPP) a mass fraction of particles with diameter smaller (larger) than the modal value is denoted. Other alternatives to describe the size distribution are the mean mass diameter (MMD) ([Alfaro and Gomes, 2001]) or mean number diameter (MND).

Dust size measured in remote areas such as Antarctic or Greenland ice cores gives an indication for the efficiency of the dust transport. This and the two other factors influencing the dust concentration and size at the sink - processes and conditions at the source and during deposition - will be presented in the following sections.
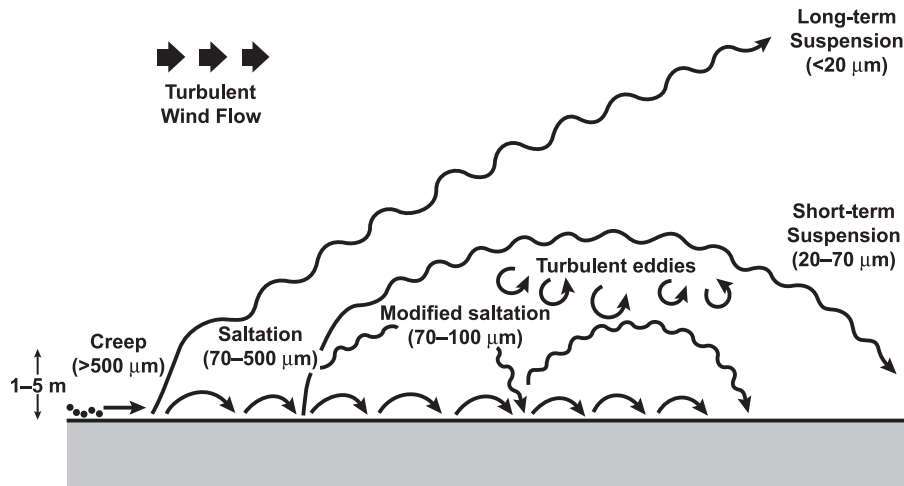
Figure 2.3: Modes of particle transport by wind. Indicated particle-size ranges in different transport modes are those typically found during moderate windstorms ([Pye, 1987]).

2.4 Sources of Dust

The main factors determining dust mobilization are wind speed, soil moisture and the presence of non erodible elements, like vegetation cover and rocks ([Mahowald et al., 2005]). Figure 2.3 illustrates the process of dust entrainment into the atmosphere: Through surface winds, larger particles ($> 500 \ \mu m$) are eroded, blown over the surface (*surface creep*) and blast smaller particles ($< 70 \ \mu m$), that may be lifted up from the surface (*saltation*). Cohesive forces keep particles bound to the soil. These forces are larger for smaller particles, therefore they cannot be lifted up directly by the wind ([Grini et al., 2002], [Alfaro and Gomes, 2001]). Note, the saltation process are the driving process for the uplift.

After entrainment, larger particles gravitate very soon. Only sufficiently small particles ($< 20 \ \mu m$) can be lifted up into the free troposphere and transported over long distances ([Pye, 1987]). Dust concentrations in the atmosphere vary with altitude and show, beside the self-evident maximum at the surface, another smaller concentration maximum in the boundary layer ([Tie et al., 2005]). Dependencies of the dust erosion from the wind speed v were found to be between the v^2 and v^4 ([Alfaro and Gomes, 2001], [Gilette, 1978], [Gillette, 1988], [Duce, 1995]). The frequency of occurrence of storm events has a large impact of the mobilization, as most of the dust load in the atmosphere is raised in single events. The seasonal cycle of vegetation has a strong control on the timing on the dust emissions ([Werner et al., 2002]). Currently global models predict dust emissions of 1-2 $Pg \cdot year^{-1}$ for particles with a radius of less than 10 μm (e.g. [Mahowald et al., 2005], [Jickells et al., 2005]).
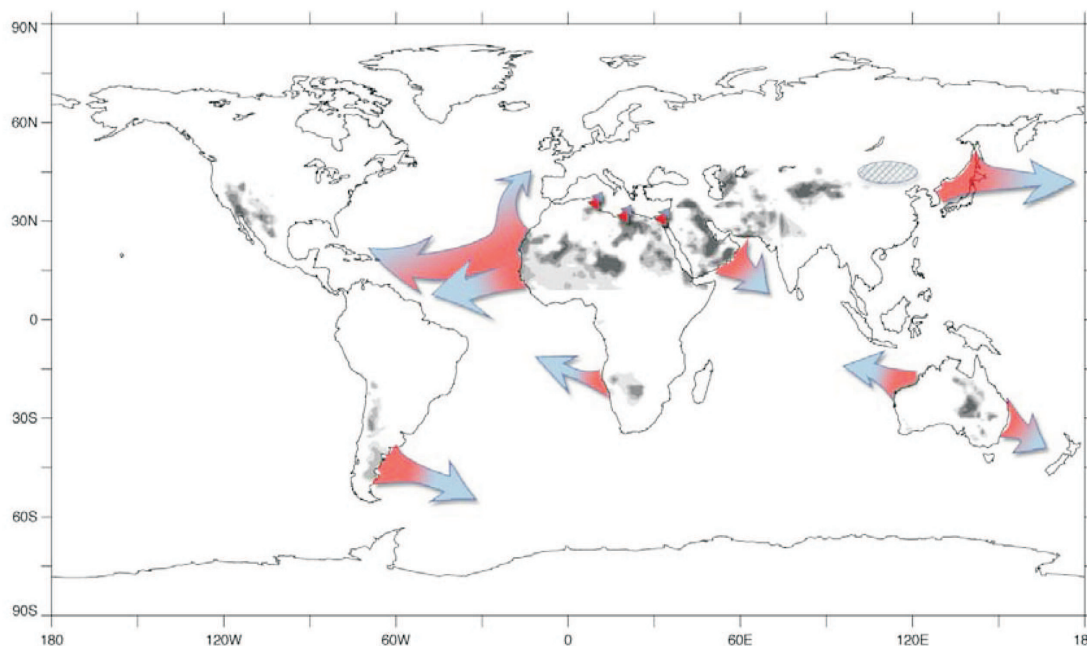
Figure 2.4: Estimate of the largest global dust sources and their downwind trajectories ([Mahowald et al., 2005], [Prospero et al., 2002]). The width of the arrows indicate the source strength. The dominant source for dust in Antarctic ice cores is South America.

Silt- and clay-size particles are formed by chemical and physical weathering. Physical weathering summarizes processes, that disintegrate parent material in a mechanical way including among others glacial grinding, frost weathering, fluvial comminution and aeolian abrasion. It tends to develop in colder and arid regions. Chemical weathering means processes leading to chemical alteration or complete dissolution of minerals from the parent material and rather occurs in warmer and wetter regions. These processes are not mutually exclusive but may occur contemporaneously.

Major dust sources can be identified by satellite observations (Figure 2.5, [Prospero et al., 2002]). They often can be associated with geomorphical features like topographical lows in arid or semiarid regions ([Prospero et al., 2002]), and are often located over basin regions drained from highlands, which serve as a source of supply of small particles ([Mahowald et al., 2005]). Figure 2.4 gives an overview of the world´s main dust sources and their downwind trajectories. Clearly identifiable are the large sources on the northern hemisphere located in northern Africa and Asia, and on the southern hemisphere in South America, southern Africa and Australia. Even though dust sources in southern Africa, Australia and southern South America are smaller by their strength and their extent than the sources in northern Africa, their vicinity to the Southern Ocean and their potential for iron fertilization in the areas of high nutrient and low chlorophyll concentration (HNLC) makes them particularly important ([Mahowald et al., 2002]). Figure 2.5 allows a

(a) Africa   (b) South America   (c) Australia
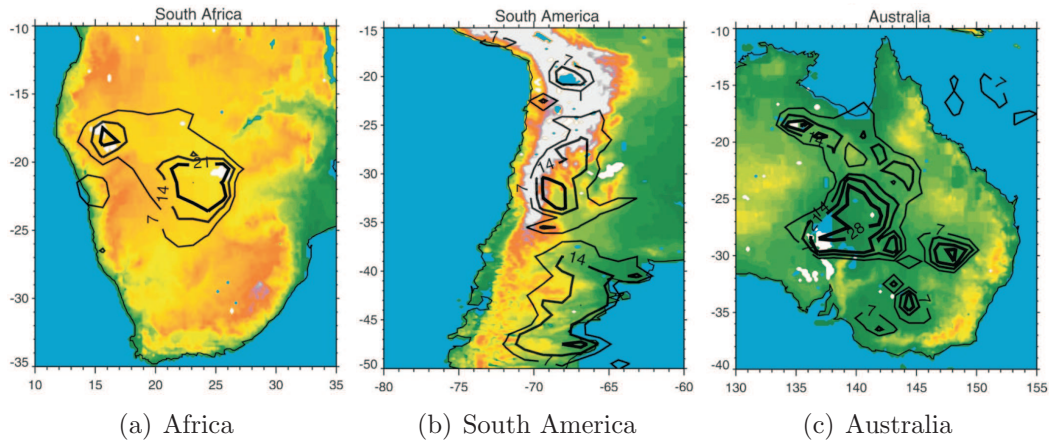
Figure 2.5: Dust sources on the Southern Hemisphere. The numbers, an index describing the source strength, increase with increasing source strength (taken from [Prospero et al., 2002]).

closer look to the dust sources of the southern hemisphere identified with satellite imagery. In South America three persistent sources were identified: Patagonia (39° - 52° S), central-western Argentina (26° - 33° S) and the Puna-Altiplano plateau (19° - 26° S). In Australia the main dust source is located in the Great Artesian Basin, the drainage area of Lake Eyre. Three sources located in southern Africa were identified: northwest of the Okavango Delta in the lowest part of the Kalahari desert, the Etosha Pan and the weakest one in the Namib desert.

Up to now isotopic measurements are used to identify sources of dust in ice cores. On the basis of comparing the clay mineralogy and the Sr, Nd and Pb isotopic fingerprint of dust samples from PSAs with dust in the GISP2 ice core, the east Asian deserts were identified as sources for the dust in Greenland ice cores ([Biscaye et al., 1997]). Patagonia and the Argentinean Pampas were identified as the main source for dust in East Antarctic ice cores during the Glacial with minor contributions from Australian sources during Interglacials ([Basile et al., 1997], [Delmonte et al., 2002a], [Revel-Rolland et al., 2006]). The dust sources for DML were not determined up to now. Since DML is directly downwind of Patagonia it has likely the same source as Dome C, but it was up to now never verified. The main characteristics of the Patagonian region are summarized by [Gaiero et al., 2003] and [Gaiero et al., 2004].

There are some disadvantages using isotopic measurements as a tool for provenance analysis of Antarctic dust: The amount of samples from the PSAs is limited and they do not separate completely. Using Sr and Nd isotopic fingerprints, Africa is separated well, but all other PSAs show an overlap ([Delmonte, 2003]). The sample volume used for the analysis varied between 300 g and 2-3 kg for Glacial and Interglacial dust concentrations, respectively ([Delmonte, 2003]). Since retrieving

---

[0]GISP2: Greenland ice sheet project
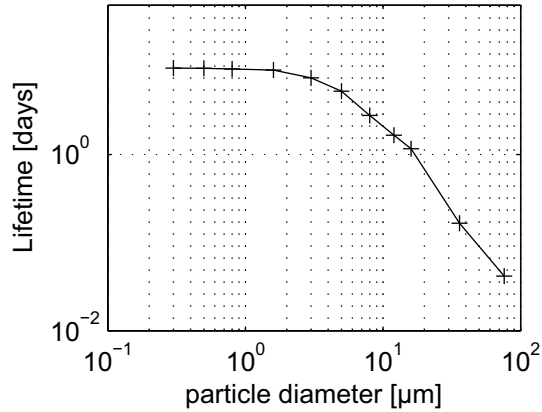
Figure 2.6: Atmospheric lifetime of different dust size classes ([Tegen and Fung, 1994], [Tegen and Lacis, 1996])

Antarctic ice cores is extremely expensive and needs extremely high logistic effort, which increases with sample volume, it is in great demand to use as little sample volume as possible for the analysis. Measurements of REE using ICP-SF-MS may offer another possibility to identify sources using smaller sample volume than for isotopic measurements.

2.5 Transport of dust

Besides the source, other main factors influencing the dust concentration in ice cores are processes occurring en route and deposition processes. The dust concentration in an air parcel en route $c_{air}(t)$ can be described at any time in a first order approximation by

$$c_{air}(t) = c_{air}(0)e^{-\frac{t}{\tau}} \tag{2.1}$$

with a dust concentration close to the source $c_{air}(0)$, the transport time t and the average atmospheric residence time τ. Typical values for τ were determined in a range from several days to weeks, dependent on size, ranging for example from 13 days for clay ($d \approx 0.7\mu m$) to 1 hour for sand ($d \approx 38\mu m$) (Figure 2.6, [Tegen and Fung, 1994]).

Removal of dust from the atmosphere is governed by wet and dry deposition processes. Wet deposition can be distinguished in in-cloud or below-cloud processes. The former occurs when particles act as condensation nuclei during cloud formation. Smaller particles may be incorporated in already existing droplets through precipitation scavenging, when rain droplets or snow flakes remove particles from the atmosphere by capturing them while falling. Wet deposition is always associated with precipitation and is virtually independent of the particle size. Dry deposition

is governed by sedimentation caused by gravitation and is particularly important for larger particles. For low precipitation areas like the East Antarctic plateau, dry deposition is the dominant deposition process ([Legrand and Mayewski, 1997]).

For dust in ice cores in Greenland the transport changes en route are described by a simple quantitative model by [Ruth et al., 2003] (improved by [Fischer et al., 2007b]). It hypothesizes, that the dust concentration in the atmosphere $c_{air}(t)$ is changed with time from the initial dust concentration in the atmosphere $c_{air}(0)$ by wet deposition v_{wet} and dry deposition v_{dry} proportional to $c_{air}(t)$. v_{dry} is governed by Stoke's settling and therewith proportional to d^2. v_{wet} is dependent on the scavenging efficiency ε, and the precipitation rate during the transport A and is independent from the particle diameter. For an individual size, the differential equation describing c_{air} emerges as follows:

$$H\frac{dc_{air}(d,t)}{dt} = -c_{air}[v_{dry} + v_{wet}] = -c_{air}[kd^2 + \varepsilon A(t)] \tag{2.2}$$

with H the hight of the scavenging column, k a constant. This assumption holds even for each individual size class by neglecting interaction between different size classes. Assuming a log-normal distribution of the particles volume (for details see chapter 2.3)

$$V(t, logd) = \frac{a_0}{\sqrt{2\pi}log\sigma_0}e^{-\frac{1}{2}\frac{(logd - log\mu_0)^2}{log^2\sigma_0}}$$

and a loss in the concentration described in Equation 2.2, this leads to a relation for the shift of the mode during transport, which can be described by

$$log\frac{\mu_{air}}{\mu_0} = -2ln10k\mu_{air}^2\frac{t}{H} \cdot log^2\sigma_0. \tag{2.3}$$

With Equation 2.3 for two different stages I and II (e.g. summer and winter) a relation between the ratio in transport time and the mode of the log-normal distribution emerges as

$$log\frac{\mu_{air}^I}{\mu_{air}^{II}} = log\frac{\mu_{air}^I}{\mu_0}(1 - \frac{\mu_{air}^{II}{}^2}{\mu_{air}^I{}^2}\frac{t^{II}}{t^I}). \tag{2.4}$$

Using Equation 2.1 for two different stages I and II

$$\frac{C_{air}^I(t^I)}{C_{air}^{II}(t^{II})} = \frac{C_{air}^I(0)e^{-\frac{t^I}{\tau^I}}}{C_{air}^{II}(0)e^{-\frac{t^{II}}{\tau^{II}}}}$$

the concentration change can be described with

$$\frac{C_{air}^I(t^I)}{C_{air}^{II}(t^{II})} = \frac{C_{air}^I(0)}{C_{air}^{II}(0)} \cdot e^{\frac{t^{II}}{\tau^{II}}(1 - \frac{t^I}{t^{II}}\frac{\tau^{II}}{\tau^I})}. \tag{2.5}$$

With this relation dust concentration changes in ice cores can be quantified in a contribution inferred by the source $\frac{C_{air}^{I}(0)}{C_{air}^{II}(0)}$ and by the transport $exp(\frac{t^{II}}{\tau^{II}}(1 - \frac{t^{I}}{t^{II}}\frac{\tau^{II}}{\tau^{I}}))$. The detailed derivation of this relation is given in Appendix F.

This simple model allows to separate changes in the dust concentration in ice cores quantitatively in changes attributed to the source or during transport. [Ruth et al., 2003] applied this model to dust size measurements in Greenland ice cores.

Size distribution measurements constraining the dust transport to Antarctica were performed on four ice cores on the East Antarctic plateau (Dome C, Vostok, Dome B and Komsomolskaia (KMS)) ([Delmonte et al., 2004b]). In the Dome C and the KMS core a decrease in the mode from 16000 yr BP corresponding to the late transition to 12000 years corresponding to the early Holocene is observed. In Dome B in the same time interval the mode increases. The FPP shows an opposite behavior in the different locations during the Glacial-Interglacial transition, as well. While it increases in KMS and Dome C, it decreases in Dome B from 20000 yr BP to 10000 yr BP ([Delmonte et al., 2004b]). The authors explain this phenomenon by transport in different elevations for coarser and finer dust. They suggest that relatively coarse dust is transported with air masses penetrating the polar atmosphere from the middle-lower troposphere and fine dust lifted up in the upper troposphere air masses and penetrate through subsidence in the polar troposphere. The opposite changes of the dust size at different locations is explained by progressive southward displacement of the polar vortex during the last climatic transition ([Delmonte et al., 2004b]) changing the relative contribution of those two dust pathways at the individual sites. This hypothesis explains well the dust size changes at the four above mentioned sites. Measurements from the EDML site show no significant change in the mode and the MMD between the last Glacial and the Holocene ([Ruth et al., 2006], [Fischer et al., 2007b]) and cannot be explained by this hypothesis. This opposite behavior of the dust size at the different sites indicate, that dust transport to Antarctica is complex and exclude a generalized transport pattern to all sites.

3 Rare Earth Elements

One aspect of this work is to study the potential of the REE to distinguish the geographic sources of the dust in Antarctic ice. The following chapter provides background information to illustrate this concept.

REE include elements with the atomic number 57 to 71 (Figure 3.1). These elements are Lanthanum (La), Cerium (Ce), Praseodymium (Pr), Neodymium (Nd), Promethium (Pm), Samarium (Sm), Europium (Eu), Gadolinium (Gd), Terbium (Tb), Dysprosium (Dy), Holmium (Ho), Erbium (Er), Thulium (Tm), Ytterbium (Yb) and Lutetium (Lu). The 14 elements following La in the periodic table are also called "Lanthanides". The electron configuration is [Xe] $6s^2 4f^n$, with n = 1 to 14, with the exception of La with an electron configuration [Xe] $5d^1 6s^2$, Gd ([Xe] $4f^7 5d^1 6s^2$) and Lu ([Xe] $4f^{14} 5d^1 6s^2$). With increasing atomic number the inner f-shell is filled up with electrons, whereas the outer electron configuration remains the same. Although the REE have in general very similar chemical properties they show small but significant differences. With increasing nuclear charge, and the thereby accompanied increasing attractive inner atomic forces, the atomic radius decreases. This is known as the "lathanides-contraction". By their increasing atomic weight the REE are often grouped into light REE (LREE, La-Nd), medium REE (MREE, Pm-Dy) and heavy REE (HREE, Ho-Lu).

Generally, REE form the +3 oxidation state, with the exception of Eu and Ce, which, depending on the redox environment, tend to form the +2 and +4 oxidation states, respectively. These two features, the lanthanide contraction and the different ionic states, cause the main differences in the REE patterns in rocks during their formation (see below).

The REE concentrations in rocks plotted versus the REE's atomic number show a very characteristic saw tooth pattern (Figure 3.2). This is caused by the processes during the nucleo genesis, since nuclei with even atomic numbers are energetic more favourable, and therefore more abundant than nuclei with odd atomic numbers. In addition, the abundance of REE generally decrease with their atomic weight. This systematic effect can be eliminated by normalization of the REE pattern. That means the measured REE values are divided by reference REE values (see Equation 3.1).

Figure 3.1: Periodic table of elements. REE are marked with red boxes.

$$REE_{norm} = \frac{REE}{REE_{reference}} \tag{3.1}$$

Commonly used reference values are the concentration in Chondrites (CI), the upper continental crust (UCC) and the post-Archean Australian shale (PAAS), but any other normalization could be used. In this study mainly the UCC ([Wedepohl, 1995]) is applied for normalization. As Pm lacks a stable isotope the REE pattern is interrupted at this position. The Pm isotope with the longest halflife of 17.7 years is ^{145}Pm.

REE are trace elements (TE) and are incorporated into minerals during mineral formation. The concentration of TE and therefore REE can change during the transition between two states of the mineral. The degree of REE incorporation into a mineral can be described with the distribution coefficient D.

$$D = \frac{c_A}{c_B} \tag{3.2}$$

with c_A the element concentration in phase A, for example liquid phase, and c_B the element concentration in phase B, for example solid phase. D depends on several parameters like temperature, pressure, structure of the mineral, ionic state, and ionic radius (e.g. [Adam and Green, 1993]). Generally, TE occupy places in the lattice by replacing major elements. The occupation of defects in the lattice can be quantitatively neglected ([Buseck and Veblen, 1978]). If two different ions in the same ionic state compete for one lattice place, the ionic radius is the determining factor ([Ringwood, 1955],[Philpotts, 1978] and references therein). Because of that the LREE and the HREE will have different distribution coefficients due to their
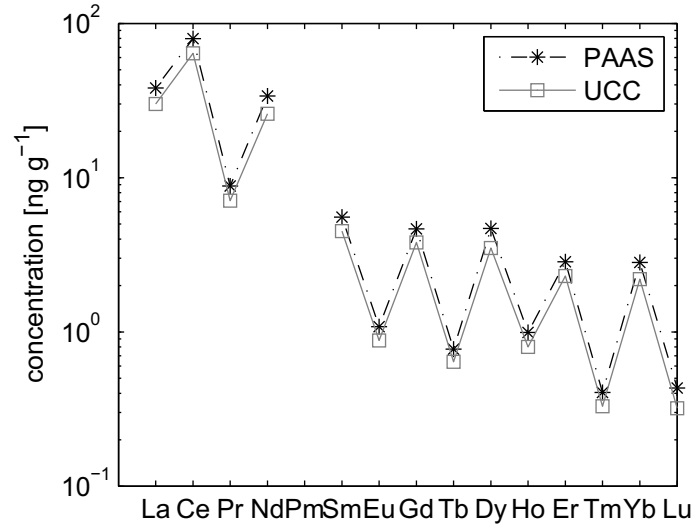
Figure 3.2: REE concentration in the upper continental crust (UCC) and the post-Archean Australian shale (PAAS) ([Taylor and McLennan, 1985], [McLennan, 1989]). The pattern is interrupted at the position of Pm because of the lack of a stable isotope of this element.

different radii. The distribution coefficients of Eu and Ce show an anomaly due to their different oxidation state. Figure 3.3 gives examples for distribution coefficients of specific minerals relative to their bulk abundance in a basaltic melt. Clearly visible is the Eu-anomaly and the differences in the HREE-LREE ratios in different minerals. Elements with a distribution coefficient between fractionated solid state and residual melt $D < 1$ are called *compatible*, those with $D > 1$ *incompatible* ([Albarede, 2003]).

According to their distribution coefficients, the REE are built into the minerals during rock formation and produce a characteristic fingerprint for the specific rock. Figure 3.4 gives a simplified overview of the REE differentiation during rock formation. The primitive earth mantle has the chondritic REE pattern. During the extraction of the earths crust, the more compatible LREE are enriched in the crust, while the mantle becomes progressively depleted in LREE. Through inner crustal differentiation Eu gets enriched in the lower crust and depleted in the upper crust, respectively. From the mantle material, mid-ocean ridge basalts (MORB) may form and cause a further LREE depletion in the residual mantle. In subduction zones, crustal material returns into the earth mantle and may form new crust. Partial melting of upper mantle rocks is a major process of incompatible element accumulation in the crust ([Wedepohl, 1995]).

Due to the very similar chemical behaviour of the REE the imprinted characteristic fingerprint survives also during weathering. Through physical and chemical weathering from the rocks small particles are generated that may travel as dust
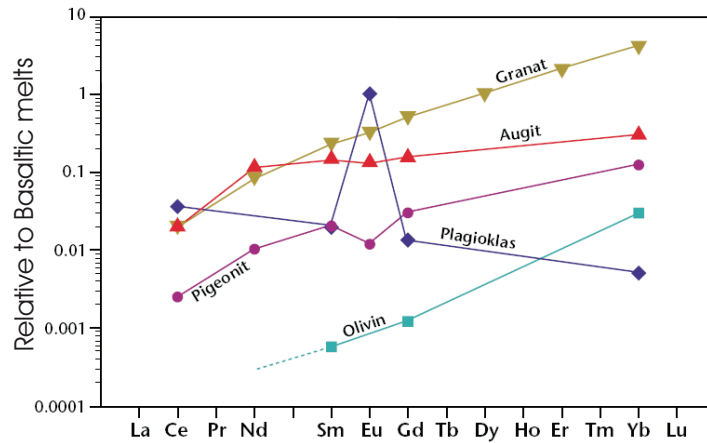
Figure 3.3: Examples for distribution coefficients of different minerals relative to their bulk abundance in a basaltic melt ([McKay, 1989]).

aerosols over long distances (see Section 2.5). Because the REE pattern is already imprinted during the initial rock formation, it might serve as a means to identify the sources of this mineral dust.

In the literature there is no clear evidence how the differences in the minerals are represented in different continents. [Taylor and McLennan, 1985] reports the largest changes of REE composition in rocks during the archean proterozoic boundary. On the other hand [Gibbs et al., 1986] attribute this difference to the different rocks available from the archean and from the proterozoic era. There are several studies showing differences in REE fingerprints, e.g. in Australia, New Zealand ([McGowan et al., 2005], [Marx et al., 2005a]), South America ([Gaiero et al., 2004]) and in the Pacific Ocean ([Greaves et al., 1999]), but there is no systematic study published, how REE pattern differ between the continents. The first question to be answered is, if the dust sources of the continents in the Southern Hemisphere show enough differences in their REE fingerprints to separate them from each other. For this study 33 samples from PSAs of Antarctic dust were analyzed on their REE concentrations and compared to each other. In a next step it was investigated, whether these fingerprints can be found in Antarctic ice core samples.
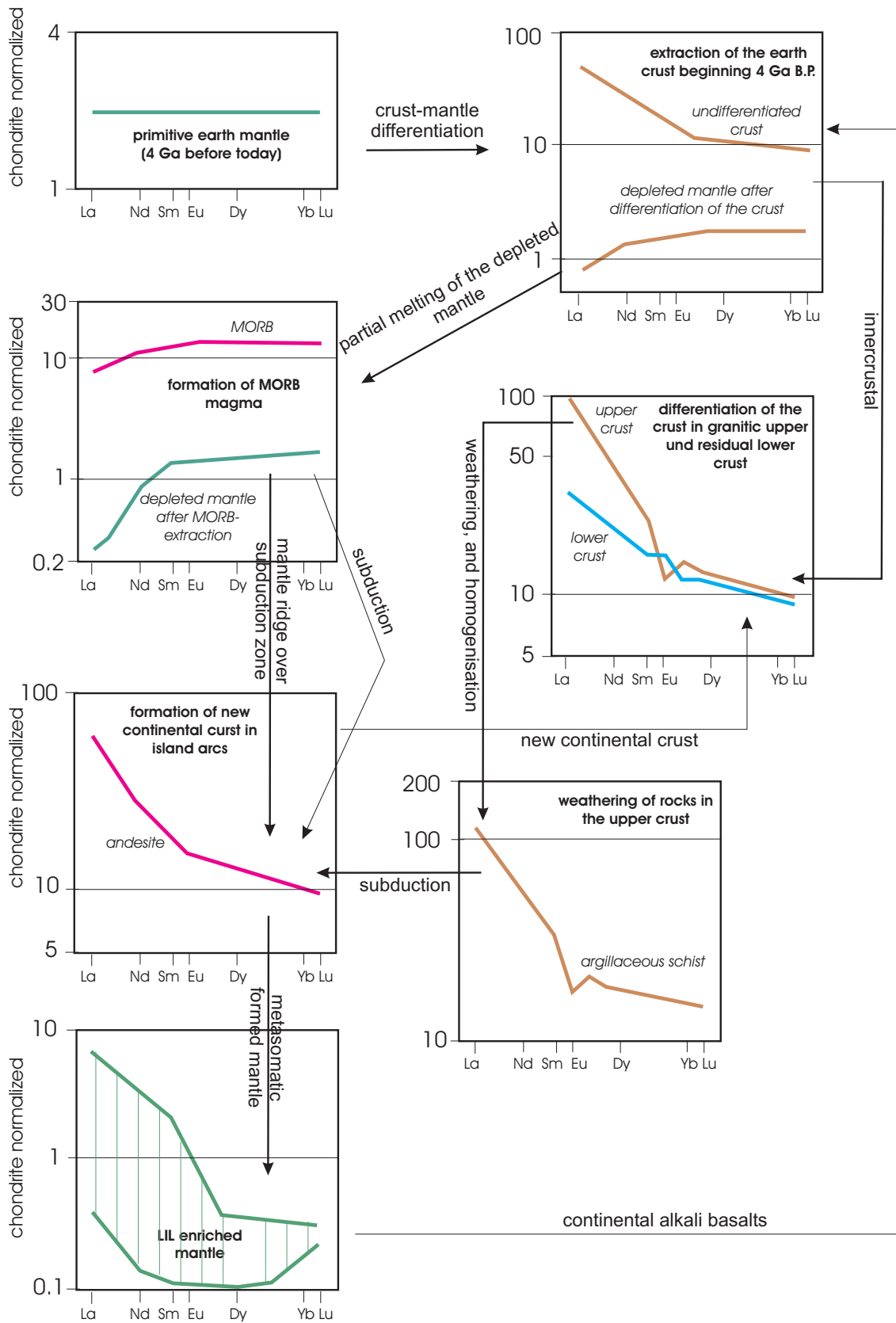
Figure 3.4: Simplified schematic overview of the REE cycle.

4 Dust Measurements in Ice Cores

For the filling and decontamination of the samples a melt head in combination with a continuous flow system was used ([Ruth et al., 2002], [Röthlisberger et al., 2000]). Figure 4.1 illustrates the system in a schematic setup. An ice bar with a cross section of 32×32 mm^2 cut out of the inner part of the ice core (Figure 4.2) is continuously melted on a heated melt head. The melt head is subdivided in two sections. The melt water from the outer part is used for measurements not endangered to contamination, e.g. interplanetary dust ([Winckler and Fischer, 2006]) or is discarded, whereas the melt water from the inner section is used for measurements with a high risk of contamination. A detailed description of the continuous flow system is given by [Ruth et al., 2002] and [Röthlisberger et al., 2000]. Depending on purpose different measurements can be conducted on the clean melt water from the inner part of the melt head. In this work two different methods are used to measure the concentration and size distribution of dust in ice core samples. The first technique is based on an optical detection of the particles using a laser sensor (LS), the second technique is based on the impedance of the particles in an electrolyte, the so called Coulter principle, using the Coulter Counter (CC). In the following the two methods are described briefly.

4.1 Laser Sensor

The principle of measurement with the LS relies on an optical method (see Figure 4.3). After melting the ice or snow sample (possibly coming from the melt head), the water is pumped through a small cuvette, transilluminated by a laser. A particle passing the laser beam causes a shading, that is detected by a photodiode located opposite to the laser. The shading is induced by a superposition of scattering and shadowing processes. Thus the cross section of the particle is detected and is converted into volume assuming spherical shape. The presence of non-spherical particles produces errors ([Hayakawa et al., 1995b], [Hayakawa et al., 1995c], [Hayakawa et al., 1995a]). This is particularly important for elongated and irregular shaped particles ([Naito et al., 1998]). The calibration provided by the manufacturer was performed with spherical latex particles. The particles in ice cores do not have to be spherical. Therefore, the results achieved by a calibration using spherical particles may be
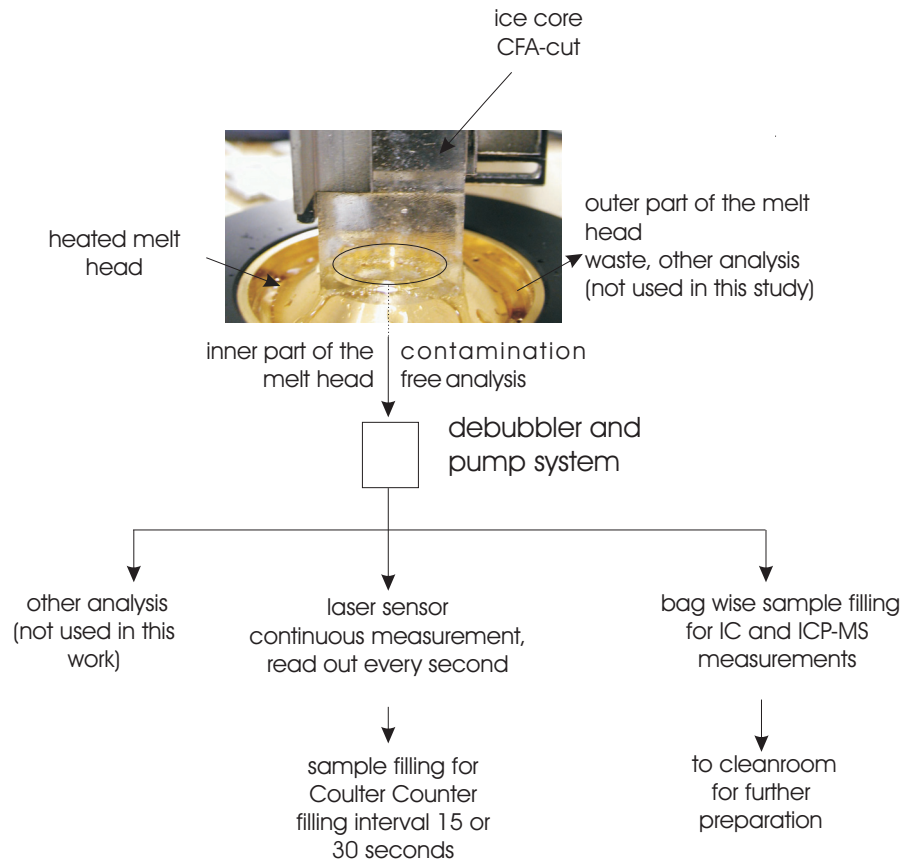
Figure 4.1: Schematic setup of the CFA-system: The water line coming from the melt head is split up in different analysis. For the LS calibration the entire melt water from the inner part of the melt head, first passes the LS, , where the size distribution is acquired with a frequency of 1 s^{-1}, and is afterwards filled in distinct samples for CC analysis. For the REE analysis, samples are filled into PS vials (photograph of the melt head by Urs Ruth).
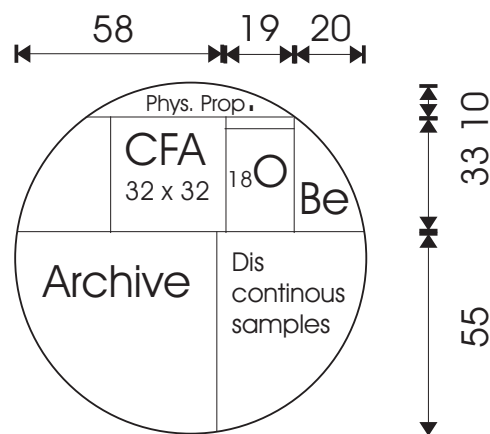
Figure 4.2: Cutting scheme for the EDML ice core. The ice used for the CFA analysis is taken from the inner part, labeled with "CFA". The number are given in mm. Additionally CFA pieces were cut out of the part denoted by "discontinuous samples" (see text).
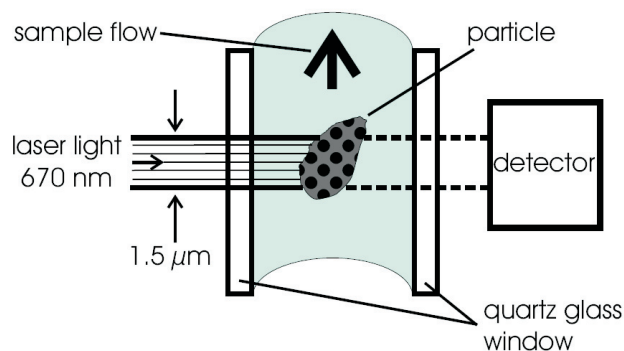
Figure 4.3: Schematic overview of the LS's operating mode (figure taken from [Ruth et al., 2002]). The particle passing the laser beam causes a shading, that is detected by a photodiode located opposite to the laser.

subjected to errors when measuring ice samples. This concerns particle size, though not number. However, when measuring samples with a high dust concentration, particles passing the laser beam simultaneously cannot be resolved as two distinct particles, but will be identified as one larger particle. This coincidence process affects in any case the number of measured particles. The influence of the mass will be evaluated in this study. In order to improve the size calibration an intercalibration between the CC and the LS was carried out by measuring identical snow and ice samples with the CC and the LS. A detailed description of the calibration procedure is given in Section 4.4 and by [Koopmann, 2006]. One major benefit of the LS is the possibility to run it in a continuous mode within a CFA-system ([Ruth et al., 2002], [Röthlisberger et al., 2000]). With the setup used in this work the size distribution can be read out every second, thus enabling very high resolution dust profiles in ice cores with up to one measured value per 0.2 mm. However, the dispersion of the sample in the tubes limits the overall resolution to 1 cm (personal communication P. Kaufmann). By taking the water line from the inner section of the melt head no additional sample preparation and decontamination is needed and the sample can be used for other measurements after passing the sensor. The whole system is easily transportable enabling measurements in the field. The LS used in this work was built by Markus Klotz GmbH, Bad Liebenzell, Germany, equipped with a diode running at a wavelength of 670 nm. The measurement range lies between 0.8 and 10 μm and can be subdivided in 32 size bins. The data readout was performed with a control device so called "Abakus", also built by Markus Klotz GmbH, Bad Liebenzell, Germany.
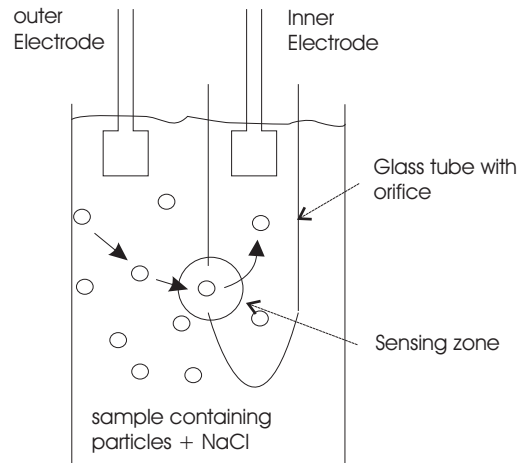
Figure 4.4: Schematic overview of the Coulter Principle: The sample containing the particles to be analyzed is pumped through the hole marked with "sensing zone". The voltage pulse induced by the passing particles through the hole is proportional to the particles volume. The sample volume between the "sensing zone" and the lower end of the glass tube is dead volume.

4.2 Coulter Principle

The Coulter principle was invented by Wallace Henry Coulter in 1959 ([Coulter, 1959]). It is based on the effect that particles pulled through an orifice, concurrent with an electrical current, produce a change in impedance proportional to the volume of the particle passing the orifice (Figure 4.4). For the measurements a glass tube with a small aperture is brought into the sample. To provide an electrical current an electrolyte (in this work a 20 % NaCl solution made of NaCl (reinst, Merck) and ultra pure water (Resistivity: 18.2 MW·cm, Milli-Q-System, Millipore)) has to be added. A voltage is applied between the outer and the inner part of the glass tube. While pumping the electrolytic sample through the aperture, particles passing the orifice displace the electrolyte by their own volume. This displacement causes a voltage pulse, whose height is proportional to the particle volume. Thus, the Coulter Principle quantifies directly the volume, which is converted into size in terms of a radius assuming spherical particles. The size calibration is performed with a single point, but is checked with several other size standards (Partikelzählstandard, BS-Partikel Wiesbaden, Germany) (Figure 4.5(a)).

The influence of changes in the conductivity of the electrolyte was tested and found to be not crucial (Figure 4.5(b)). In the range from 0.5 to 2 % NaCl solution the result shows a very slight decreasing trend, but does only change within the error bars, which give the half width of the calibration peaks. The measurements of ice core samples were performed in a 1 % NaCl solution. This method needs at least 5 mL of sample, which is given by the dead volume below the orifice, that cannot
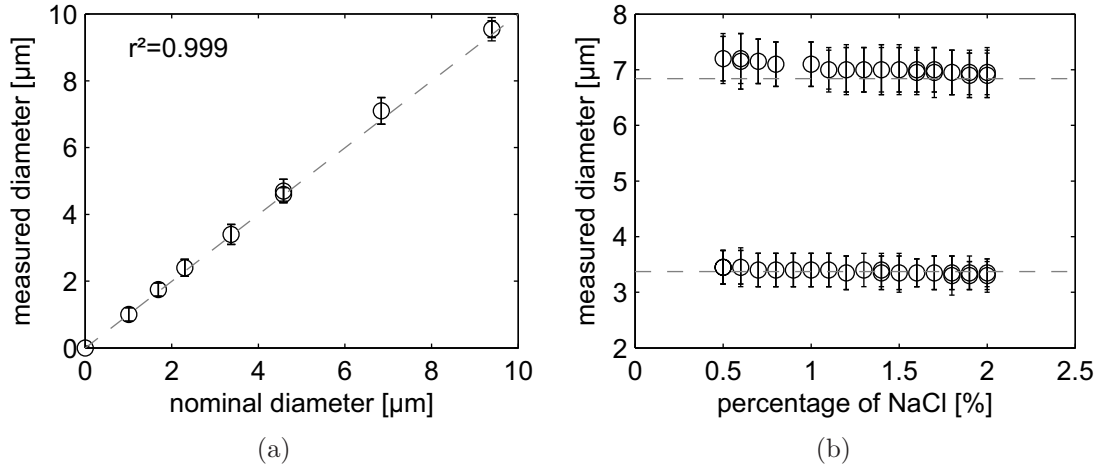
Figure 4.5: Size calibration of the Coulter Counter measurements. The error bars give the half width of the obtained peaks. (a) Calibration line, the dashed line gives the x=y relation. (b) Dependency on the NaCl-concentration, the dashed lines give the nominal diameter of the used calibration standard.

be used for the measurement. The sample cannot be used for other measurements afterwards due to the added electrolyte. The duration of the measurement depends on the dimension of the orifice and the required counting statistics, which in turn is dependent on the particle concentration in the sample. For Antarctic ice core samples it ranges from approximately 3 to 10 minutes depending on the concentration in the sample. In this work the Multisizer III built by Beckman Coulter, Inc. was used. Up to 300 size channels can be chosen in a range from 2 to 60 % of the aperture diameter. The aperture used had a diameter of 30 μm.

4.3 Measurements of Dust Concentration and Size

Dust size distribution measurements were performed on two sections of one meter each from the EPICA-DML ice core from the depth intervals 745-746 m and 1082-1083 m (thereafter referred to as EDML746-06 and EDML1083-06). The ice was melted using the melt head with a melt speed of about 1.5 cm · min^{-1} . An overview of the setup is given in Figure 4.1, but only the LS and the CC sample filling were used. The entire melt water from the inner part of the melt head passed the LS, where the size distribution was acquired with a frequency of 1 s^{-1}. This corresponds to a nominal depth resolution of about 0.2 mm. After passing the LS, the outflow was collected using an auto sampler with polystyrene (PS) beakers for the analysis with the CC. The regular filling interval was 30 seconds, and was increased to 15 seconds for selected intervals, which corresponds to a depth resolution of 6 and 3 mm, respectively. The CC aliquots had a volume between 0.9 and 2.0 mL. Since at

least 5 mL are needed for a CC measurement, freshly threefold filtered ultra pure water and threefold filtered NaCl was added to achieve 5 mL of diluted sample with a concentration of 1 % NaCl (used filter: Minisart, 0.2 μm, Nylon Membranfilter, Omnilab Bremen, Germany). The amount of added electrolyte and ultra pure water varied, depending on the amount of undiluted sample available, such that finally a solution of 1% NaCl in the sample was achieved. From each sample at least two, mostly three to five repetitions were performed and at least 500 μL were measured. The samples were measured as soon as possible after complete melting. The samples were measured after one meter of core was melted and aliquoted into samples. This resulted in a measuring delay of up to 36 h. To let particles not settle, the samples were kept on a shaker during this time. Measurements with the CC could not be performed under clean room conditions due to the infrastructure at AWI, but the lids of the sampling tubes were kept closed until the NaCl solution was added to avoid contamination. Possible contamination was quantified by regular blank measurements within a measurement session by measuring 1% NaCl solution of freshly threefold filtered ultra pure water and freshly threefold filtered NaCl (filter and solution as above). The blank levels during the measurements of EDML1083-06 samples were higher due to the much higher dust concentration in these samples and the therewith associated higher blank level in the system. Above 1 μm the blank was below 0.1 % of the lowest sample concentration for EDML1083-06 samples and below 4 % of the lowest concentration for EDML746-06 samples. For larger sizes the blank was even lower. Therefore the blank was not subtracted. For an overview of the obtained blank levels see Appendix G.1.

4.4 Calibration of the Laser Sensor

As mentioned in section 4.1, the LS calibration is performed by an intercalibration between the CC and the LS using identical ice samples. In this work the two sections EDML746-06 and EDML1083-06 were used for this calibration. It is crucial for the calibration to have exactly the same sample analyzed with both methods. The time needed for the water reaching from the LS to the filling of the CC aliquot was 40 seconds. This was manually determined before the measurements and checked later by maximizing the correlation of the two data sets.

The size distribution data measured by the LS were averaged on the respective time interval of the CC sampling (15 and 30 seconds). For the calibration only samples with a particle concentration < 350000 particle/mL were used. Above this concentration coincidences in the LS became more numerous and might therefore lead to an inaccurate calibration (Figure 4.9(b)). This limit was only exceeded for
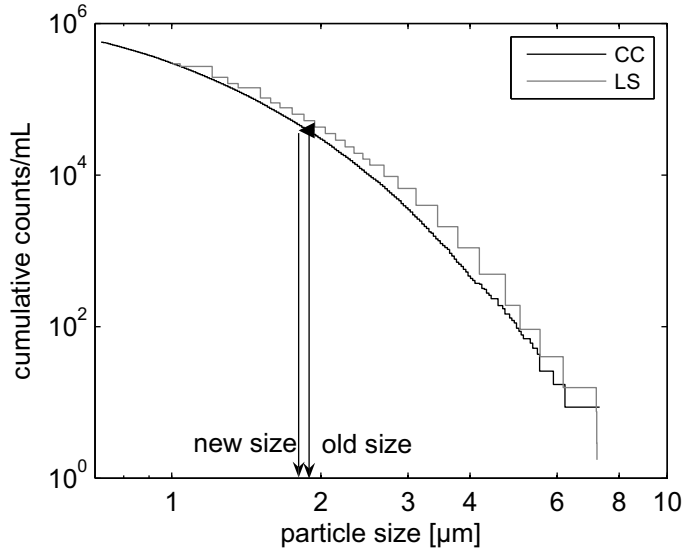
Figure 4.6: Example of a cumulative size distribution used for the calibration of the LS. To calibrate the LS, the cumulative LS size distribution was shifted on top of the cumulative CC size distribution.

some samples of EDML1083-06. Although the CC aliquots were filled in 15 or 30 second intervals, some of them with low dust concentrations were pooled together before the CC measurement to achieve better statistics. These samples were used for the data analysis, but excluded for the calibration. All together 144 samples from EDML1083-06 and 192 samples from EDML746-06 were available for the calibration with one data set measured by CC and one by LS.

Figure 4.6 shows an example of the uncorrected cumulative size distribution measured with LS and CC. For the calibration, the cumulative LS distribution of each sample was shifted onto the cumulative CC distribution starting from the largest particles, as it is indicated by the horizontal arrow in Figure 4.6 by the following procedure: Assuming n particles in the largest size bin of the LS, the counts in the CC spectrum were summed up starting in the largest size bin, until n particles were accumulated and the corresponding size d_{32} was determined. Assuming m particles in the second largest size bin of the LS, the counts in the CC spectrum were summed up starting at d_{32}, until m particles were accumulated and the corresponding size d_{31} was determined. Thus consecutive all 32 new size bins d_{32} to d_1 for the LS were determined. This corresponding size might not always meet a bin boundary in the CC spectrum. To account for the fact, that generally more particles are counted at the lower bin boundary, the CC spectrum was interpolated between the bin boundaries generating a continuous CC size spectrum. However, this interpolation might lead to errors in the calibration. The measured CC bin width is logarithmical distributed, with broader bins for larger sizes. The broader the bin width, the larger
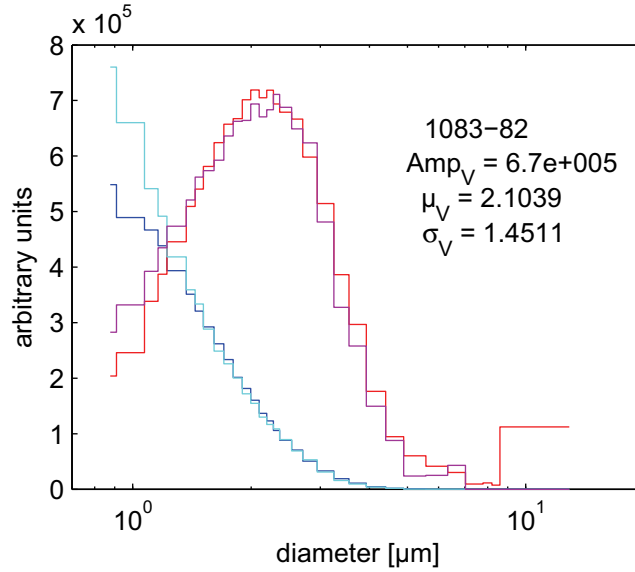
Figure 4.7: Example of a distributive cumulative size distribution after the intercalibration. LS spectrum is shown in red (volume distribution) and dark blue (number distribution), CC spectrum is shown in violet (volume distribution) and cyan (number distribution).

the error induced by the interpolation of the CC spectrum before performing the calibration. Thus the induced error of this interpolation increases with the bin size.

Thus, for each sample the new upper and lower bin boundaries of all size bins of the LS were determined. Afterwards, the overall new bin boundaries were calculated as the mean value of the bin boundaries of all 336 samples. The relationship between the old and the new bin boundaries is almost linear up to 8 μm for the EDML1083-06 samples ($R^2 = 0.999$, see Figure 4.8(a)) and up to 5 μm for the EMDL746-06 samples ($R^2 = 0.999$, not shown). The difference in the linearity range is attributed to the lower concentration in the EMDL746-06 samples. EDML1083-06 originates from the last glacial and contains about 100 fold more particles that EDML746-06 originating from the Antarctic Cold Reversal ([Blunier et al., 1998]). As can be seen in Figure 4.8(a) the uncertainty of the developed calibration line increases significantly above 6 μm. For larger particles the error inferred by the interpolation of the CC size spectrum is larger. That this is not an effect of non geometric scattering can be explained by the theory of light scattering: Light scattering for $\frac{\pi \lambda}{d} \gg 1$ can be described by Rayleigh Scattering, for $\lambda \approx d$ the theory of Mie scattering has to be applied and for $\frac{\pi \lambda}{d} \ll 1$ the geometric scattering occurs, were the integral cross section is proportional to d^2 ([Vogel, 1997]). In this work the laser wavelength is 670 nm, which might cause Mie scattering for particles close to the detection limit of 0.8 μm, but not for particles > 5 μm. In this size range geometric scattering occurs. It seems very unlikely that the initial calibration developed from spherical particles

(a) Correction for large particles

(b) comparison of the two datasets
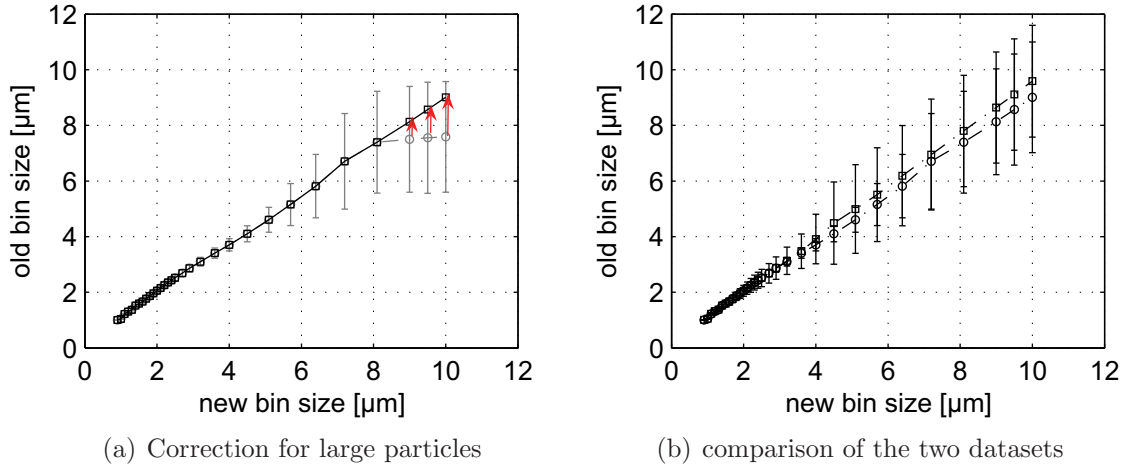
Figure 4.8: Calibration of the LS by intercomparison with the CC. (a) New channel boundaries obtained from the data from EDML1083-06. The grey line with circles gives the bin sizes obtained by the measurement. The black line with squares gives the bin sizes obtained by extrapolating the linearity. Error bars give 1 σ for the 144 samples (see text). The bin sizes were shifted as indicated by the red arrows. (b) New channel boundaries obtained from the data from EDML1083-06 (circles), EDML746-06 (squares). For the data analysis the mean value was taken. Error bars give 1 σ for the 144 and 192 samples (see text).

get worse for bigger particles, where Mie scattering does not occur. Taking the assumption the linearity of the calibration is still valid for particles with diameter for EDML1083-06 and > 5 μm for EDML746-06 the size bins were aligned with the linear fit, as it is indicated in Figure 4.8(a) with red arrows. However, the deviation from linearity appears above 5 μm and 8 μm, respectively, well above the size size of Antarctic dust. The fraction of particles larger than 8 μm do not exceed 0.26 % of the total counts for the EDML1083-06 samples and the fraction of particles larger than 5 μm do not exceed 2.5 % of the total counts for the EDML746-06 samples. For most samples the fraction is much lower. Therefore, the influence of this correction in this calibration is negligible for Antarctic ice samples.

The calibration was conducted separately for the EDML1083-06, EDML746-06 samples and for both samples together, but reveal the same calibration within the 1-σ error bars (Figure 4.8(b)). The difference between the calibration lines obtained from the two data sets increases with particle size up to 0.6 μm at a diameter of 10 μm. In the size range of the particles in Antarctic ice (< 3.7 μm) the difference is smaller than 0.1 μm. Figure 4.7 shows an example for a size distribution measured by CC and the respective size distribution measured by LS and evaluated with the calibration line obtained by the CC-LS intercalibration.

Figure 4.9 shows the comparison of the total mass concentration (4.9(a)), the total particle concentration (4.9(b)) and the mode (4.9(c)) of the log-normal distribution obtained by LS and CC after the calibration of the LS as described above. For the

(a) Mass concentration

(b) Number concentration

(c) Mode μ
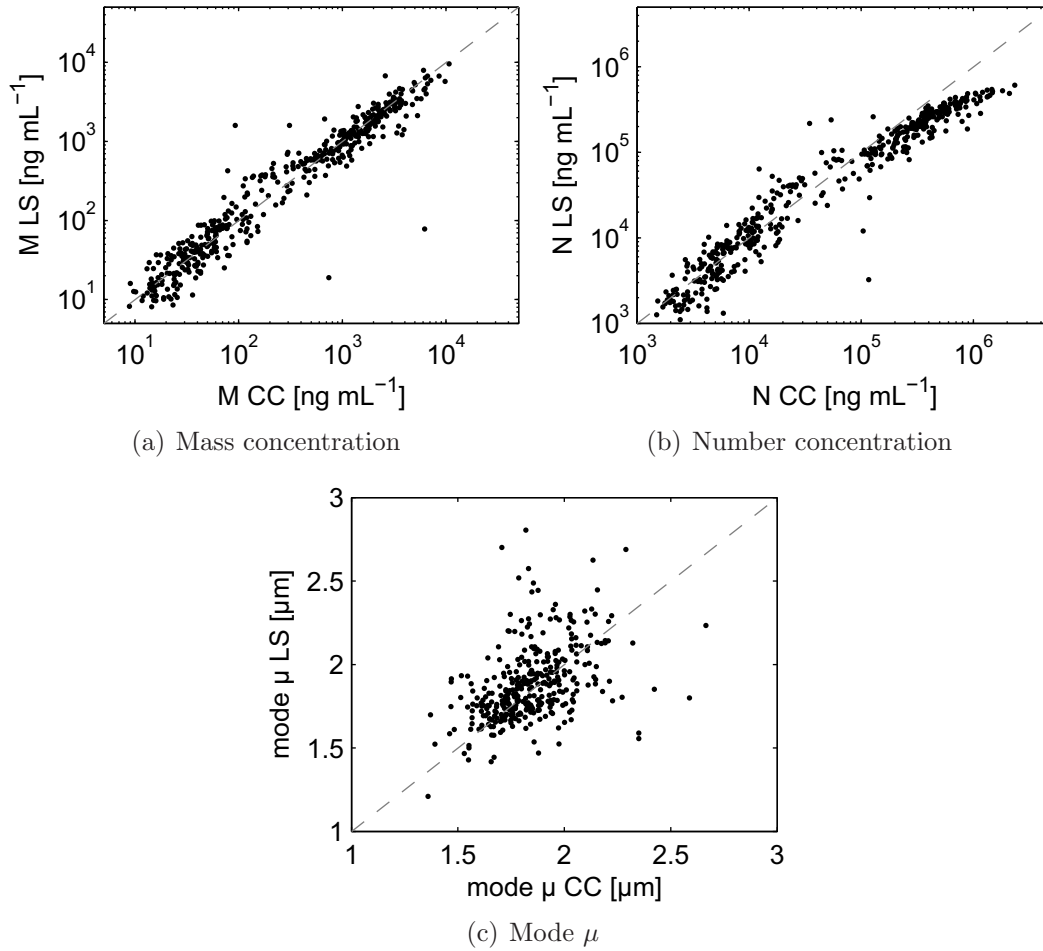
Figure 4.9: Comparison of the LS and CC measurements after the calibration. The dashed line is the bisecting line as a guide to the eye. Clearly observable is the deflection in the number concentration caused by coincidences in the LS in higher concentrated samples.

mass concentration the two methods agree well (R = 0.93, slope = 1.04). For the particle concentration the calibration does not work for high concentration above a certain threshold. In this study a threshold of 350000 part $\cdot$ mL^{-1} was identified as an upper limit for the validity of the calibration (R = 0.92, slope = 1.3). The non-linearity of the calibration for higher concentrations is attributed to a higher occurrence of coincidences in the LS, since the samples were diluted for the CC measurements. For the mode, the calibration does not give a convincing relationship between the two methods (R = 0.41), although no systematic difference in the mode is found for LS and CC measurements after careful calibration. Irregular shape of the particles, the fitting error and the coincidences in the LS, as mentioned for the number concentration, are supposed to be the main reason for this mismatch. Previous studies have already shown that different measurement techniques yield different results depending on the shape of the particles ([Hayakawa et al., 1995b],

[Hayakawa et al., 1995c], [Hayakawa et al., 1995a]). To achieve also a calibration for the mode μ further more complex investigations have to be performed. In the following, only the mode μ determined from the CC measurements is taken into account, due to the more reliable measuring principle.

5 Dust Concentration and Size in the EPICA-DML Ice Core

5.1 Sampling Sites

The measurements were conducted on sections from the EPICA-DML ice core. The drilling was performed at Kohnen Station located in DML (see Figure 5.1) from 2000 to 2006. The EPICA-DML ice core lies adjacent to the Atlantic sector on the Antarctic plateau with a recent accumulation rate of 64 kg $\cdot$ m$^{-2}\cdot$ year^{-1} ([Oerter et al., 2000])). Details about the location are given in Table 5.1. The second core drilled within EPICA is located at Dome C in the Indian sector on the Antarctic plateau with an accumulation rate of only one third of EPICA-DML (recent accumulation rate 25 kg $\cdot$ m$^{-2}\cdot$ year^{-1} ([EPICA Community Members, 2004])).

5.2 Core Sections

For this study, two depth intervals of the EPICA-DML ice core were analyzed. From each depth interval, the section indicated in Figure 4.2 with "CFA" and parts from the section indicated with "Discontinuous samples" were available for analysis. On the former the regular CFA-analysis ([Röthlisberger et al., 2000]) was performed, including major ions (e.g. Ca^{2+}, Na^+ and NH_4^+), electrical conductivity, air content and dust concentration using the LS. The latter was used for measurements of dust concentration using the LS and the CC, electrical conductivity and air content. The first section was chosen at the depth of 745-746 m corresponding to an age of approximately 13200 yr BP ([Ruth et al., 2007b]) in the interval of the Antarctic cold reversal (ACR, [Blunier et al., 1998]), herein after referred to as EDML746-04 (CFA-

position	75°00'S, 00°04'E
altitude	2892 m a.s.l.
mean annual surface temperature	-44.6°C
mean annual accumulation rate	64 kg $\cdot$ m$^{-2}\cdot$ year^{-1} [a]
ice thickness	2774.15 m
age at 87% of depth	150 000 a [b]

Table 5.1: Details of the EPICA-DML drill site. Data are taken from a [Oerter et al., 2004], b [Ruth et al., 2007b].
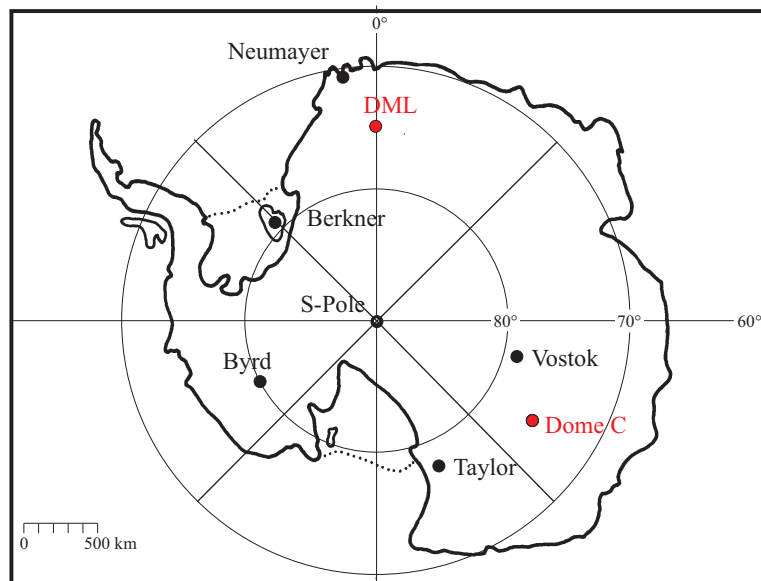
Figure 5.1: Overview about different drill sites and stations in Antarctica

cut) and EDML746-06 (Discontinuous samples-cut). The second section was taken from a depth of 1082-1083 m corresponding to an age of about 25600 yr BP in the last glacial ([Ruth et al., 2007b]), herein after referred to as EDML1083-04 (CFA-cut) and EDML1083-06 (Discontinuous samples-cut). The measured parameters were the same as for EDML746-04 and EDML746-06.

For EDML746-04 and EDML1083-04 the piece indicated with "CFA" in Figure 4.2 and an additional 32×32 mm cut from the part indicated with "discontinuous samples" was used. The procedure for the measurements of EDML746-06 and EDML1083-06 is described in Chapter 4.3, the procedure for the measurements of EDML746-04 and EDML1083-04 is described by [Ruth, 2002].

5.3 Seasonal Variability of Glacial Dust

Figure 5.2 shows the dust concentration for the EDML depth of 1082-1083 m. In the interval 1082.46 - 1082.67 m the depth resolution is 3 mm, hereafter referred to as high resolution (HR). The rest of the core section was measured in 6 mm resolution. The dust mass concentration varies between $100 \, \text{ng} \cdot \text{mL}^{-1}$ and $10000 \, \text{ng} \cdot \text{mL}^{-1}$ (300 $\text{ng} \cdot \text{mL}^{-1}$ and $11000 \, \text{ng} \cdot \text{mL}^{-1}$ for HR) with a mean of $2000 \, \text{ng} \cdot \text{mL}^{-1}$ (2900 ng · mL^{-1} for HR). In terms of fluxes, this is in agreement with previous measurements at Dome C ($1000 \, \text{ng} \cdot \text{mL}^{-1}$, [EPICA Community Members, 2004], accumulation rate $1.5 \, \text{kg} \cdot \text{m}^{-2} \cdot \text{year}^{-1}$, [Schwander et al., 2001]) and Vostok ($850 \, \text{ng} \cdot \text{mL}^{-1}$ average LGM, [Delmonte et al., 2002b], accumulation rate $1.2 \, \text{kg} \cdot \text{m}^{-2} \cdot \text{year}^{-1}$, [Parrenin et al., 2001]). The biggest variations are in the HR part (1082.4 m - 1082.7 m). That
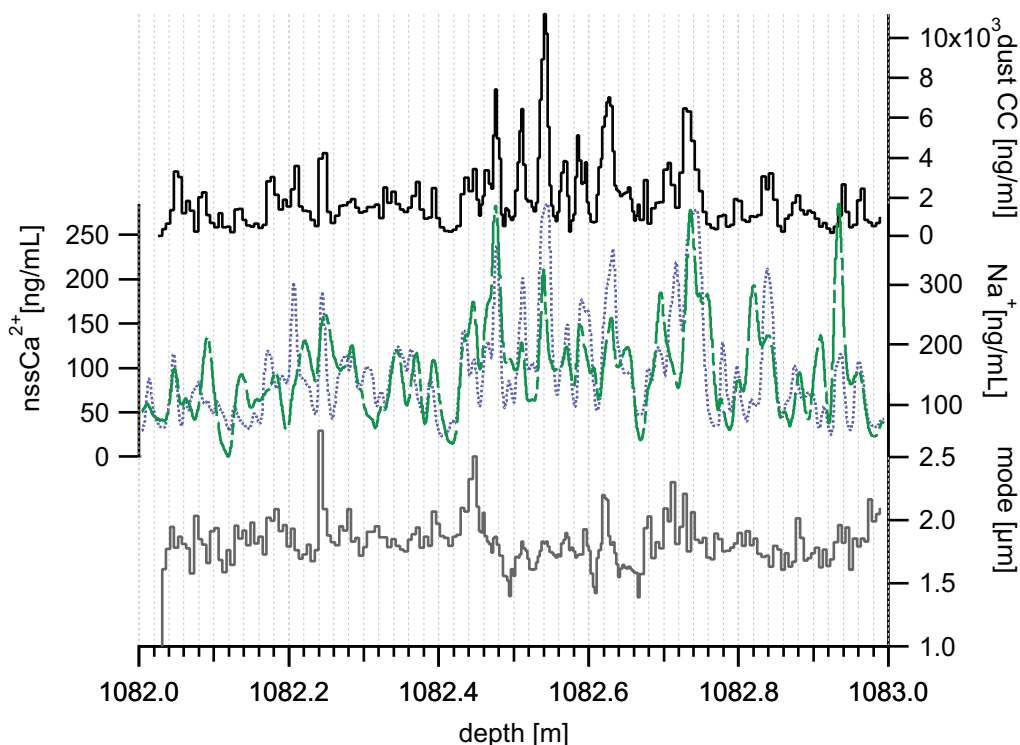
Figure 5.2: Dust in the EDML1083 ice core section. Insoluble mass concentration measured by Coulter Counter (top, solid black line), $nssCa^{2+}$ (dotted blue) and Na^+ (dashed green) concentration measured by CFA (center, data kindly provided by P. Kaufmann, University of Bern), mode μ of the log-normal distribution, fitted to the mass distribution (bottom, grey line).

this deviation is not only caused by the higher sampling resolution, but mainly due to the actual higher variations becomes apparent in the $nssCa^{2+}$ profile, which also has the highest variability in this depth interval, but was measured in constant resolution over the whole meter. The dust signal varies in phase with $nssCa^{2+}$, which in turn is in phase with Na^+. Recent aerosol measurements from the drilling station in DML record a maximum in the Na^+ concentration during winter ([Weller and Wagenbach, 2007]). Therefore, the maximum in the dust concentration can be related to a winter signal, under the assumption the timing of the maxima of Na^+ and $nssCa^{2+}$ did not change simultaneously. The mode μ varies between a minimum of 1.4 μm and a maximum of 2.7 μm. In the HR part, where the resolution suffices to resolve seasonal cycles, a minimum of 1.5 μm and a maximum of 2.0 μm is found. The typical seasonal amplitude in the HR part of μ is 0.2 - 0.3 μm. The maxima and the minima in the profile of μ coincide with the maxima and minima of the concentration profile (Figure 5.3). In analogy, the season of the arrival of larger particles is winter. The values of μ obtained for DML are roughly in the same range as previous measurements of μ in glacial ice at Dome C (1.91 $\pm$ 0.02 μm, [Delmonte et al., 2002b]). The error of μ is controlled by the count-statistical error of each
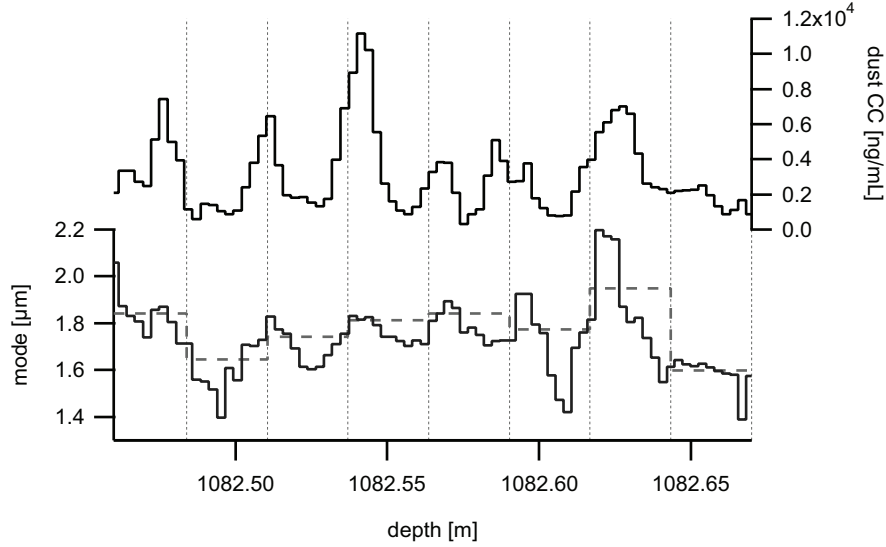
Figure 5.3: Dust mode μ in the Glacial in different resolution: 3 mm resolution (black solid line) and 3 cm resolution (grey dashed line).

size bin $\sqrt{N}$ (with the number of counts N) and the interval chosen for fitting. The influence of the counting statistics was determined by a Monte Carlo technique as follows: 1000 size spectra were calculated, where the counts in each size bin were varied, that the mean of the 1000 values for this size bin equaled the measured value N and the 1 σ interval the count-statistical error $\sqrt{N}$ for this size bin. This was done for all size bins yielding 1000 size spectra. The mode obtained by performing a log-normal fit on all those spectra varied within 1 σ of less than 0.02 μm for the glacial samples. The influence of the interval chosen for fitting was determined by changing the fitting interval. The range for reasonable values for μ by changing the range of the fitting interval was 0.05 μm and thus the dominant error.

To investigate the influence of the seasonality the mode of 3 mm resolution sampling intervals (μ_3) is shown in comparison with the mode fitted on 30 mm resolution sampling intervals (μ_{30}) (Figure 5.3). To obtain μ_{30} ten consecutive samples were summed up and afterwards the log-normal function was fitted on the mass distribution. The mean value for μ_{30} emerges as $1.88 \pm 0.15 \ \mu m$.

Interestingly, μ_{30} is always higher than the mean of μ_3 in the respective interval. This observation can be explained by combining two findings. First, maxima and minima in mass and mode are in phase and second, mass concentration changes within one year between maxima and minima on average by a factor of about 7.6. By measuring samples covering several years, the obtained mode is dominated by events of high mass input and represents in glacial time the size distribution during winter.

(a) no correction for deposition   (b) correction for deposition
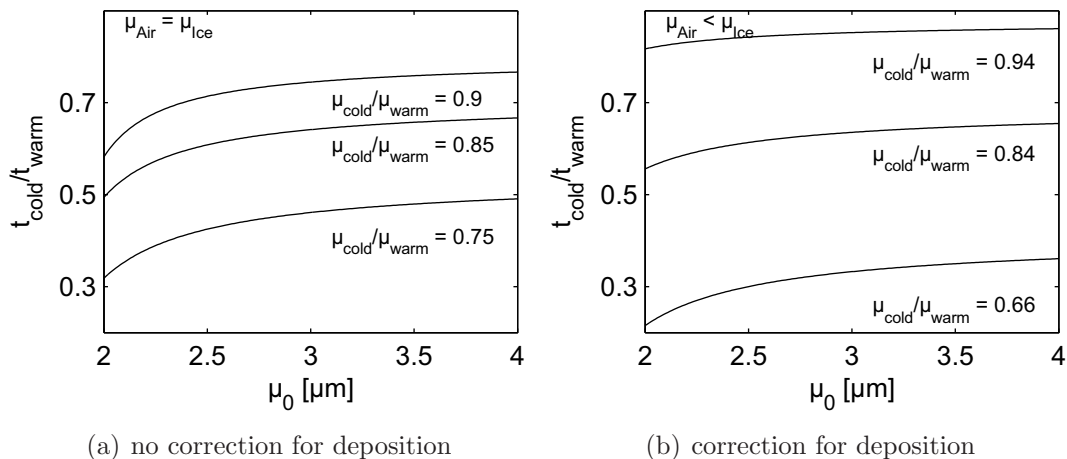
Figure 5.4: Seasonal changes in transport efficiency for glacial dust depending on the mode of the initial dust at the source.

5.4 Dust Transport to DML in the Last Glacial

In the following chapter the observed changes in dust concentration and size are used to quantify the contribution of changes inferred by transport and the source.

Invented by [Ruth, 2002] and improved by [Fischer et al., 2007b] a one dimensional model to describe the dust transport to Greenland ice cores is used to quantify the changes in transport time and efficiency to DML (see also chapter 2.5). It yields a relation between dust size and effective transport time (equation 2.4).

$$
log\frac{\mu_{air}^{I}}{\mu_{air}^{II}} = log\frac{\mu_{air}^{I}}{\mu_0}(1 - \frac{\mu_{air}^{II}{}^{2}}{\mu_{air}^{I}{}^{2}}\frac{t^{II}}{t^{I}})
$$

or

$$
\frac{t^{II}}{t^{I}} = (1 - \frac{log\frac{\mu_{air}^{I}}{\mu_{air}^{II}}}{log\frac{\mu_{air}^{I}}{\mu_0}}) \cdot \frac{\mu_{air}^{I}{}^{2}}{\mu_{air}^{II}{}^{2}} \tag{5.1}
$$

In high resolution the ratio between maxima and minima in the mode varies in the Glacial between 0.75 and 0.9 with a mean of 0.85 ± 0.06. Equation 5.1 with the mode of the initial dust at the source of 2.5 μm ([Schulz et al., 1998]) yields an effective transport time ratio between 0.4 and 0.7. Figure 5.4(a) illustrates the effect of a variation in μ_0. A larger μ_0 than the assumed 2.5 μm would not have a large effect on $\frac{t^{II}}{t^{I}}$, whereas a smaller μ_0 would have a larger effect. Equation 2.4 describes only the changes of the mode in the atmosphere. Instead, the values used here are measured in ice. In DML, where aerosol is deposited by wet and dry processes, the enrichment in larger particles due to dry deposition onto the snow has to be taken

into account. The relation between dust size distribution in air $V_{ice}(logd)$ and in ice $V_{ice}(logd)$ is described by [Fischer et al., 2007b] with

$$V_{ice}(logd) = V_{air}(t, logd)[kd^2 + \varepsilon A] \tag{5.2}$$

Therewith the relation 2.4 changes to

$$log\frac{\mu_{ice}^I}{\mu_{ice}^{II}} = [log\frac{\mu_{ice}^I}{\mu_{air,0}} - 2kln10log^2\sigma_0\frac{\mu_{ice}^{II\,2}}{k\mu_{ice}^{II\,2} + \varepsilon A_{ice}^{II}}] \cdot [\frac{t^{II}}{t^I}\frac{\mu_{air}^{II\,2}}{\mu_{air}^{I\,2}} - 1]+ \tag{5.3}$$

$$2kln10log^2\sigma_0 \cdot [\frac{\mu_{ice}^{I\,2}}{k\mu_{ice}^{I\,2} + \varepsilon A_{ice}^I} - \frac{\mu_{ice}^{II\,2}}{k\mu_{ice}^{II\,2} + \varepsilon A_{ice}^{II}}]$$

The mode corrected according to Equation 5.3 varies between 1.4 and 1.7, with changes in the ratio $\frac{\mu_{air}^I}{\mu_{air}^{II}}$ between 0.66 and 0.94 with a mean of 0.83. For this calculation the glacial accumulation $A = 30$ kg $\cdot$ m$^{-2}\cdot$ year^{-1} ([Ruth et al., 2007a]) was assumed to be constant throughout the year and $k = 83$ $\mu m^{-1}s^{-1}$ and $\varepsilon = 10^6$ was used as by [Ruth et al., 2003]. Figure 5.4(b) shows the effective transport time changes using this relation, depending on the initial mode at the source $\mu_{air,0}$. The curves for the uncorrected data (Figure 5.4(a)) are more bent, indicating a larger consequence of a change in the initial mode on the calculated effective transport time. The variation in accumulation corrected ratios $\frac{\mu_{air}^I}{\mu_{air}^{II}}$ is larger than in the uncorrected ratios, but the mean effective transport time change is 0.6 and does not alter after correcting for deposition processes. However, the variation becomes larger ($\frac{t_{cold}}{t_{warm}} = $ 0.3 - 0.85). In the following $\frac{t_{cold}}{t_{warm}} = 0.6$ will be used for the effective transport time change ratio.

Now we can estimate the influence of changes in transport and source on the dust concentration in the ice core.

If we apply equation 2.1

$$C_{air}(t) = C_{air}(0)e^{-\frac{t}{\tau}}$$

for a warm stage corresponding to summer and a cold stage corresponding to winter conditions, they are related to each other as follows:

$$\frac{C_{air}(t_{warm})}{C_{air}(t_{cold})} = \frac{C_{air}(0)_{warm}}{C_{air}(0)_{cold}} \cdot e^{-\frac{t_{warm}}{\tau} + \frac{t_{cold}}{\tau}} \tag{5.4}$$

Assuming the atmospheric transport time τ as constant throughout the year and using $\frac{t_{cold}}{t_{warm}} \approx 0.6$ and $\frac{C_{air}(t_{cold})}{C_{air}(t_{warm})} \approx 7.6$, which is the mean value of the ratio between the maximum and minimum concentrations in the HR-part of EDML1083, the relations emerges as

$$\frac{C_{air}(t_{cold})}{C_{air}(t_{warm})} = \frac{C_{air}(0)_{cold}}{C_{air}(0)_{warm}} \cdot e^{0.4 \cdot \frac{t_{warm}}{\tau}} = 7.6. \tag{5.5}$$

To calculate $\frac{C_{air}(0)_{cold}}{C_{air}(0)_{warm}}$, $\frac{t_{warm}}{\tau}$ has to be estimated. There are only few studies about the atmospheric residence time of dust in the last Glacial. Measurements of modern global atmospheric residence time of dust do not exist ([Zender et al., 2003]). Model estimates for modern atmospheric residence time vary between 2.7 days ([Mahowald et al., 2006]) and 7.1 days [Ginoux et al., 2001] with most of the estimates between 4 and 5.5 days ([Luo et al., 2003], [Miller et al., 2006], [Zender et al., 2003], [Tegen and Fung, 1994]). However, glacial residence times are longer. The increase varies from very slight increases of 5 % ([Lunt and Valdes, 2002]) to higher values of 30 % ([Werner et al., 2002]). This leads to glacial residence times of 4.2 - 7.1 days based on a modern residence time of 4 - 5.5 days. For the transport time no direct measurements in the Glacial are available. Backward trajectory studies for modern times yield transport times from Patagonia to DML of 5 - 10 days except events accompanied by very high snow fall, which are shorter ([Reijmer and van den Broeke, 2001]). Even if similar data is not available for glacial climate, it might serve as a rough estimate for transport times during the Glacial. Taking 5 days as a lower limit for the summer transport time (implying a winter transport time of 3 days) this would lead to a source ratio $\frac{C_{air}(0)_{warm}}{C_{air}(0)_{cold}}$ between 4.6 (for τ =4 days) and 5.3 (for τ =5.5 days). This estimation means, that maximal 60 - 70 % of the subannual dust concentration changes can be explained by the source. Assuming 10 days as an upper limit for the summer transport time (implying a winter transport time of 6 days) would lead to a source ratio $\frac{C_{air}(0)_{warm}}{C_{air}(0)_{cold}}$ between 2.8 (for τ =4 days) and 3.7 (for τ =5.5 days). Under this conditions 37 - 49 % of the subannual dust concentration changes can be explained by the source. This conclusion implies depending on transport time estimations, 30 - 63 % of the seasonal dust concentration changes must be explained by transport changes.

On the other extreme, to explain 100 % of the subannual dust concentration changes by transport only, implies values for t_{warm} between 20 days (for τ =4 days) and 28 days (for τ =5.5 days) and for t_{cold} between 12 days (for τ =4 days) and 17 days (for τ =5.5 days). This is up to a factor of 3 higher, than the estimates by [Reijmer et al., 2002]. Further, LGM backward trajectory studies have to be run using high resolution atmospheric transport models to validate this reasoning.

Seasonal changes in dust sources are observed by satellite imagery for recent times ([Prospero et al., 2002]) and are very likely to occur during the Glacial as well caused by changing wind speed, vegetation cover, soil moisture or changes in the areas, which supply the source with erodible material.
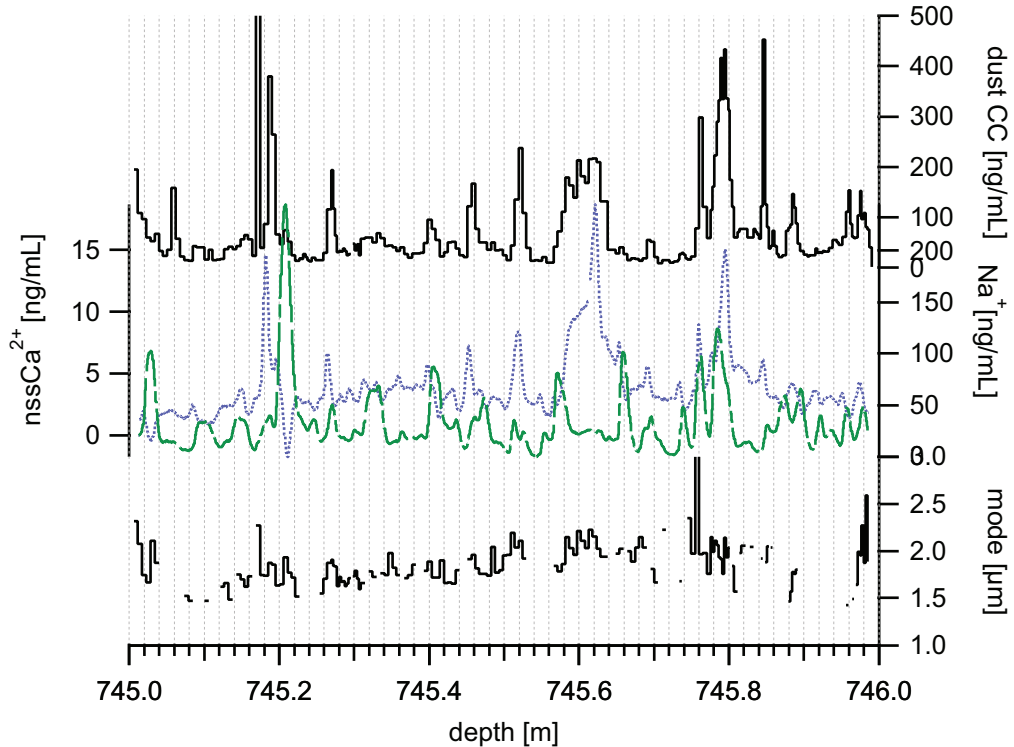
Figure 5.5: Dust in the EDML746 ice core section. Insoluble mass concentration measured by Coulter Counter (top, solid black line), $nssCa^{2+}$ (dotted blue) and Na^+ (dashed green) concentration measured by CFA (center, data kindly provided by P. Kaufmann, University of Bern), mode of the log-normal distribution, fitted to the mass distribution (bottom, black line). Values are missing in the mode where the log-normal fit could not be applied due to insufficient counting statistics.

Summing up the study, the dust concentration changes by a factor of 7.6 and the particle mode typically changes by 0.2 - 0.3 μm within a year during the last Glacial. Using a one dimensional model, the effective transport time was found to be lower in winter by a factor of 0.6 than in summer. The contribution of the source was deduced to be between 37 % and 70 % leaving a contribution of the transport of 30 - 63 %, respectively. This means, that the dust concentration changes in DML on subannual time scales can be explained by transport and source more or less with the same contribution.

5.5 Seasonal Variability of Dust in the Antarctic Cold Reversal

The second depth interval analyzed in this work (EDML746) lies in the ACR. Figure 5.5 shows the dust concentration in terms of insoluble particles and $nssCa^{2+}$, the Na^+ concentration and the size distribution expressed with the mode measured in the EDML746 core section. The dust mass concentration varies between 10 $ng \cdot mL^{-1}$ and 500 $ng \cdot mL^{-1}$ with a mean of 75 ± 75 $ng \cdot mL^{-1}$. This is higher than previous
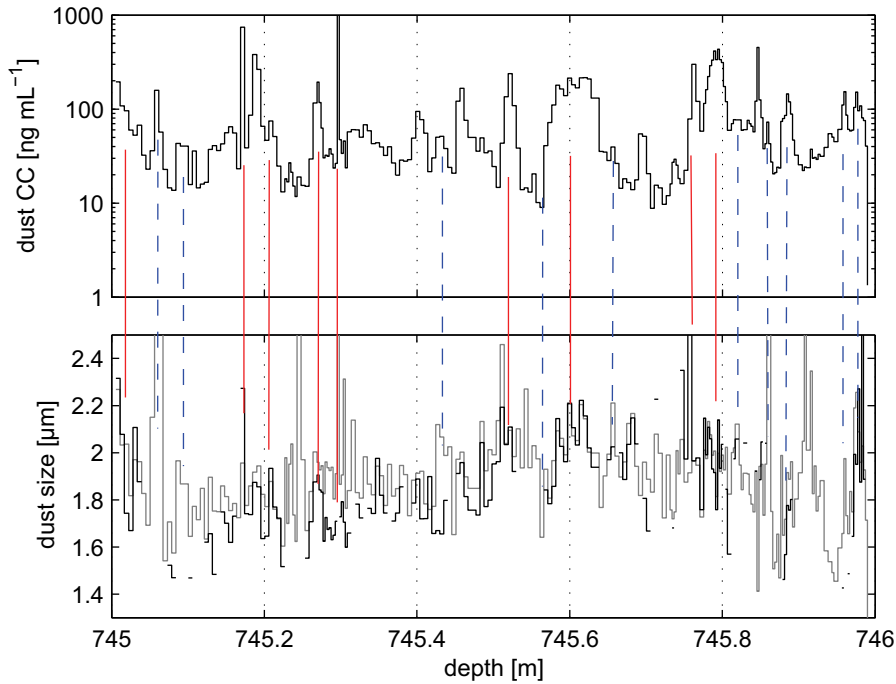
Figure 5.6: Dust in the EDML746 ice core section. Top: Mass concentration, bottom: size distribution expressed by Mean mass diameter (MMD) grey dashed line and mode in black solid line. The vertical lines indicate coinciding maxima or minima in mass and mode (red solid lines) and in mass and MMD (blue dashed lines).

measurements in other Antarctic ice cores (EPICA Dome C 25 $ng \cdot mL^{-1}$, KMS 25 $ng \cdot mL^{-1}$, Dome B 46 $ng \cdot mL^{-1}$ ([Delmonte et al., 2004b])). Even in terms of fluxes the highest values are found in DML (EPICA-DML: 12.5 $ng \cdot cm^{-2}yr^{-1}$, EPICA Dome C: 8.3 $ng \cdot cm^{-2}yr^{-1}$, KMS: 8.3 $ng \cdot cm^{-2}yr^{-1}$, DOME B: 9 $ng \cdot cm^{-2}yr^{-1}$). This difference can be explained by the closer proximity of DML to the dust source (see Chapter 6 and [Delmonte et al., 2004a]). The profile of the insoluble particles closely follows the nssCa^{2+}-profile. Unlike in Glacial times the Na^{+} and nssCa^{2+}-profile are not well correlated. Therefore it is hard to determine the timing of the dust maximum.

The particle mode does not follow the mass as closely as in glacial ice. It varies between 1.4 μm and 2.4 μm, but shows two cluster around 1.75 μm and 2.05 μm. The maxima of the mode usually are in line with dust concentration maxima. The variance of the mode induced by changing the fitting range is the same as for glacial samples ($\pm$ 0.05 μm). The count-statistical error, obtained as described in Section 5.3 is up to 0.1 μm and therewith the controlling error for the lower concentrated samples from the ACR. In any case, values for the mode have to be considered very carefully, since the limited counting statistics did not allow reliable determination of

the mode for all samples. To get a continuous record also in the mode, a log-normal fit was performed on averages of 10 consecutive samples as explained in Section 5.3. Seasonal resolution could not be obtained by this average but a reliable mean value for the mode could be calculated as $1.96 \pm 0.13 \ \mu m$. This value is only slightly higher than the dust size at Dome C ice core ($1.94 \ \mu m \pm 0.17 \ \mu m$ ([Delmonte et al., 2002b])). A higher value in DML than at Dome C is expected due to the closer proximity to the source in South America. One possible explanation for the small difference could be different transport routes from the source to DML and Dome C. Here again, one has to keep in mind that the values both in DML and at Dome C are governed by the high dust mass concentration events.

Additionally to the mode, the mean mass diameter (MMD) was calculated. It shows a reasonable correlation with the mode: R=0.74, slope 1.03 for ACR and R=0.93, slope 1.26 for glacial dust. The difference in R is probably due to better statistics in glacial ice, the difference in the slope indicates a higher skewness of the glacial distributions towards larger sizes. The advantage of the MMD is the possibility to calculate it even for low-concentration samples, where the low counting statistics does not allow a determination of the mode. In order to investigate if the seasonal cycle is as pronounced as in glacial ice, Figure 5.6 shows mass, MMD and mode. The correlation between the logarithmic mass and the mode is weak (R=0.3). The calculated correlation between MMD and mass is only slightly higher (R=0.33). However, even if the correlation is low, many of the maxima and minima of the mass and mode (MMD) coincide as indicated with red (blue dashed) lines in Figure 5.6.

5.6 Dust Transport to DML during the Antarctic Cold Reversal

The above described coincidences between mode μ and mass point to a relationship between mass concentration and size, that allows to apply the linear transport model described in Section 5.4 also in the ACR. Since consecutive clear seasonal cycles could not be obtained in the ACR, selected slices of the mass concentration and size profile are used instead. Those parts of the profile, where an uninterrupted transition from a higher to a lower mass concentration coincides with a transition from larger to smaller values for the mode and vice versa, are used in the following to estimate changes in the effective transport time during the year. 16 of those slices were identified. The mean value for the respective larger mode is $2.07 \pm 0.16 \ \mu m$, for the respective smaller mode $1.74 \pm 0.15 \ \mu m$, the difference between maximum and minimum is generally 0.2 - 0.35 μm with three outliers of 0.6 μm. The corresponding maxima and minima in the mass concentrations are 260 ± 160 $ng \cdot mL^{-1}$ and $74 \pm 45 \ ng \cdot mL^{-1}$. For each pair of large and small mode the change

in the effective transport time $\frac{t^{II}}{t^{I}}$ can be calculated using Equation 5.1

$$\frac{t^{II}}{t^{I}} = (1 - \frac{log\frac{\mu_{air}^{I}}{\mu_{air}^{II}}}{log\frac{\mu_{air}^{I}}{\mu_{0}}}) \cdot \frac{\mu_{air}^{I}{}^{2}}{\mu_{air}^{II}{}^{2}}$$

The mean effective transport time ratio between summer and winter deduced from the above mentioned 16 events is 0.4 ± 0.15. Here like for the calculation of the Glacial a μ_{0} of 2.5 μm was assumed ([Schulz et al., 1998]). 13 of these 16 events give very similar effective transport time ratios of 0.46 ± 0.07, the other 3 are lower with 0.12 (twice) and 0.16.

Now the changes in the dust concentration in the EPICA-DML ice core can be divided in changes caused by the source and changes caused by transport for the ACR as well (Equation 5.4).

$$\frac{C_{air}(t_{warm})}{C_{air}(t_{cold})} = \frac{C_{air}(0)_{warm}}{C_{air}(0)_{cold}} \cdot e^{-\frac{t_{warm}}{\tau} + \frac{t_{cold}}{\tau}}$$

As in the Glacial, τ is assumed to be constant throughout the year. With $\frac{t_{cold}}{t_{warm}} \approx$ 0.4 and $\frac{C_{air}(t_{cold})}{C_{air}(t_{warm})} \approx 3.5$ the relation emerges as

$$\frac{C_{air}(t_{cold})}{C_{air}(t_{warm})} = \frac{C_{air}(0)_{cold}}{C_{air}(0)_{warm}} \cdot e^{0.6 \cdot \frac{t_{warm}}{\tau}} \approx 3.5 \tag{5.6}$$

As discussed in Section 5.4 model predictions for τ vary from 4 to 5.5 days. Modern transport times based on back trajectory calculations are 5-10 days ([Reijmer et al., 2002]). These values will be used for the ACR as well. During summer the transport time is 2.5 times longer than during winter. Assuming 10 days of summer transport time the second term in Equation 5.6 describing changes in transport varies between ≈ 3 (for $\tau = 5.5$ days) and 4.5 (for $\tau = 4$ days). This means, depending on the assumed transport time and atmospheric residence time τ, between 70 and 100 % of the dust variation in DML can be explained by transport changes during the ACR. The remaining less than 30 % are attributed to the source. Assuming a transport time less than 10 days for summer, the contribution of the source rises. A longer transport time would lower the contribution of the source.

Modern back trajectory calculations indicate a shorter transport time from South America to DML during autumn (March - April - May) and spring (September - October - November) than during summer (December - January - February). Winter (June - July - August) trajectories are similar to those in spring and autumn, but have a slightly more northern origin ([Reijmer et al., 2002]). This is explained by the authors by a weaker cyclonic activity during summer. This is in line with the results of the present work for the ACR.

	Glacial	ACR
mean mass concentration [$ng \cdot mL^{-1}$]	2000	70
factor of mean subannual mass variation	7.6	3.5
size (mode [μm])	1.4 - 2.7	1.4 - 2.4
mean size (determined in samples covering several years [μm])	1.88 ± 0.15	1.96 ± 0.13
typical subannual mode shift [μm]	0.2 - 0.3	0.2 - 0.35
contribution source [%]	37 - 70	< 30
factor of mean subannual mass variation explained by transport	2.8 - 5.3	3 - 4.5
contribution transport [%]	63 - 30	70 - 100

Table 5.2: Variation of dust parameter during glacial times and during the ACR on subannual time scales.

Summing up this section, the dust concentration during the ACR changes by a factor of ≈ 3.5 with some larger excursions. The mode μ could not be determined for all samples, especially those with low dust concentration, due to insufficient counting statistics. For all other samples the mode generally varies between maxima and minima by 0.2 - 0.35 μm. Using a simple transport model the transport time was found to be lower by a factor of 0.4 in winter than in summer. 70 - 100 % of the dust concentration changes in the ACR could be explained by transport, the remaining less than 30 % are attributed to changes in the source.

5.7 Comparison of Glacial and Antarctic Cold Reversal

After investigating in detail two depth intervals from the EPICA-DML ice core, the variability of dust size and concentration on Glacial-Interglacial timescales will be discussed in the following section.

The main characteristics of dust concentration and size during the ACR and the Glacial are summarized in Table 5.2. The mean mass concentration is higher during the Glacial than during the ACR by a factor of ≈ 28. The respective nssCa^{2+} concentration ratio is ≈ 25 ([Fischer et al., 2007a]). A higher ratio of insoluble dust particle between Glacials and Interglacials compared to the nssCa^{2+} ratio is already observed by [Ruth et al., 2007a]. One possible explanation for this discrepancy could be a change in the mineralogical composition of the dust in the EPICA-DML ice core during the transition from the Glacial to the Holocene. This could be caused by a change in the source of the dust reaching DML. Another possibility to explain the higher ratio of insoluble dust compared to nssCa^{2+} could be a different recovery efficiency for nssCa^{2+} in glacial ice and ice from the ACR.

The seasonal dust concentration changes are more than a factor of 2 higher during

the Glacial than during the ACR. During the ACR almost the entire dust concentration changes of 3.5 can be explained by transport (Section 5.6). The variability inferred by the transport are in the same range during the Glacial as during the ACR. However, to explain the observed seasonal dust concentration changes an additional contribution from the source is required during the Glacial. The contribution from the source has to be approximately as large as the contribution explained by transport. The mean values for μ during Glacial and ACR are in agreement within the 1-σ interval, with a slightly higher value for the ACR. The typical shift of μ during the year is approximately the same during the Glacial and the ACR.

Accepting the values given in Table 5.2 for the mean size determined in samples covering several years at face values for the dust size during the Glacial at the ACR, the change in effective transport time can be estimated. Again, the simple conceptual transport model described in Section 2.5 is used for the calculation, yielding the relations

$$\frac{t^{ACR}}{t^{Glacial}} = (1 - \frac{log\frac{\mu_{air}^{Glacial}}{\mu_{air}^{ACR}}}{log\frac{\mu_{air}^{Glacial}}{\mu_0}}) \cdot \frac{\mu_{air}^{Glacial^2}}{\mu_{air}^{ACR^2}}$$

and

$$\frac{C_{air}(t_{ACR})}{C_{air}(t_{Glacial})} = \frac{C_{air}(0)_{ACR}}{C_{air}(0)_{Glacial}} \cdot e^{-\frac{t_{ACR}}{\tau_{ACR}} + \frac{t_{Glacial}}{\tau_{Glacial}}}$$

Note, the atmospheric residence time τ does not have to be constant. Model simulations yield a longer residence time τ of up to 30 % in the Holocene than in the Glacial ([Lunt and Valdes, 2002], [Werner et al., 2002]). However, assuming in a first (unrealistic) step $\tau = \tau_{ACR} = \tau_{Glacial}$ constant between Glacial and ACR , with $\mu_{ACR} = 1.96$ μm, $\mu_{Glacial} = 1.88$ μm, the transport term $e^{-\frac{t_{ACR}}{\tau_{ACR}} + \frac{t_{Glacial}}{\tau_{Glacial}}}$ is calculated ≤ 1. This indicates a possibly intensification of the transport during the Glacial-Interglacial transition. By assuming in a second more realistic step a longer atmospheric dust residence time during the Glacial than during the ACR, the factor given by the transport term would decrease even more indicating an even stronger intensification of the transport from the Glacial to the ACR. There are previous publications supporting this findings. A pollen and diatom record obtained out of a sediment core in southern South America (51°58' S, 70°23' W) reveals relatively calm winds during the late Glacial and an increase of the wind speed after 15440 yr BP ([Wille et al., 2007]).[Toggweiler and Russell, 2008] argues, that lower atmospheric CO_2 concentrations during LGM cause smaller temperature gradients in the middle of the atmosphere between low and high latitudes. This temperature gradient drives the westerly winds, which therefore would have increased during the

Glacial-Holocene transition. If transport would be indeed less effective during the Glacial than during the ACR, more than the observed dust concentration difference between Glacial and ACR has to be explained entirely by the source, implying a large increase of the source intensity. A record of three lake sediment cores from Lago Cardiel (49° S, 71° W) shows a significant increase in the lake level coinciding with the low dust concentration between 11600 and 11500 yr BP in Antarctic ice cores ([Gilli, 2003]). The authors explain the lake level increase with a strong positive hydrological balance at that time and an accompanying higher washout of dust from the atmosphere in the source region resulting in a lower dust concentration in Antarctica.

A combination of changes in glacial outwash, aridity and wind speed in the source are suggested to be mainly responsible for the required weakening of the source during the transition from Glacial to the Holocene ([Fischer et al., 2007a]). The shelf exposed adjacent to Argentina in the Atlantic is ruled out as a major contribution to the glacial dust source by [Wolff et al., 2006].

Based on nssCa^{2+}-fluxes in the EPICA-DML and EPICA-Dome C ice cores [Fischer et al., 2007a] found, that the observed changes in dust fluxes between Holocene and Glacial of 1-2 orders of magnitude predominantly reflect changes in source strength. The results of the presented work suggest actually an extend of the findings by [Fischer et al., 2007a], that the source intensification could have been stronger than the Glacial-Interglacial dust concentration changes in the EPICA-DML ice core. There, one has to keep in mind, that in this study Glacial-ACR changes are presented and [Fischer et al., 2007a] addresses Glacial-Holocene changes.

Admittedly, the values obtained for μ are mean values for one meter during each time interval representing only one data point each in the Glacial and the ACR. The seasonal as well as the interannual variability of μ is much larger than the difference between the obtained ACR-Glacial difference. To confirm the obtained findings on more depth intervals dust size measurements have to be performed.

[Delmonte et al., 2004b] explains observed changes of dust size during the transition from the last Glacial in the Indian sector of Antarctica with different pathways for different size classes. A gradual change of the eccentricity of the polar vortex is proposed to govern the transport of particles of different sizes onto the Antarctic plateau. Larger particles are transported over the lower troposphere, whereas smaller particles are transported in higher altitude and dominated by the subsidence of air masses over the east Antarctic ice sheet. This hypothesis was derived based on measurements in ice cores in the Indian sector of Antarctica and may therefore not be valid for DML. These regional distinctions indicate, that the different drill

sites of the EPICA-DML and the EPICA-Dome C ice cores, even if they are both located on the East Antarctic plateau, appear to be influenced by different changes during the Glacial-Interglacial transition.

6 Sources of Dust in Dronning Maud Land

The sources of dust in the EPICA-DML ice core are identified by a new approach using REE. In a first step the REE fingerprints are determined in samples from the PSAs. Afterwards the REE fingerprints in the EPICA-DML ice core sample are determined and compared to the REE fingerprints in the PSA samples.

6.1 Measurements of Rare Earth Elements

Due to the large differences in REE concentration and different matrices in the PSA and ice core samples two different procedures were applied to the two sets of samples. Figure 6.1 gives an overview of the two processing procedures. Processing and measurement of the PSA samples was performed at AWI and is described in Section 6.1.1. The EPICA-DML samples were processed and measured at the University of Venice. A detailed description is given in Section 6.1.2. An intercomparison study proving the consistency of both systems will be submitted soon ([Dick, et al. in preparation]).

6.1.1 Samples from the Potential Source Areas

The samples collected from the PSAs span a wide size spectrum differing from sample to sample. For the analysis only the $< 5 \ \mu m$ fraction was used. This corresponds to the typical size of the particles found in Antarctic ice cores (see Chapter 5, [Delmonte et al., 2002a], [Delmonte et al., 2004a]). The bulk of the sample (a few grams) was poured into 45-50 mL of ultra pure water. After 10 minutes of ultra sonication the sample was left to separate by settling due to Stokes law. The supernatant was taken with a pipette and checked with the CC to achieve a fraction of 95 % of the total number of particles in a size range $< 5 \ \mu m$. This aliquot may also include the soluble fraction of REE dissolved from coarser particles with a size $> 5 \ \mu m$. Due to the low solubility of the REE ([Humphris, 1983]), this contribution can be neglected. The size separation was performed within a cooperation with the University of Milan, Italy. Most of the samples were kindly provided by Barbara Delmonte. For detailed information about the samples see [Delmonte, 2003] and [Delmonte et al., 2004a].
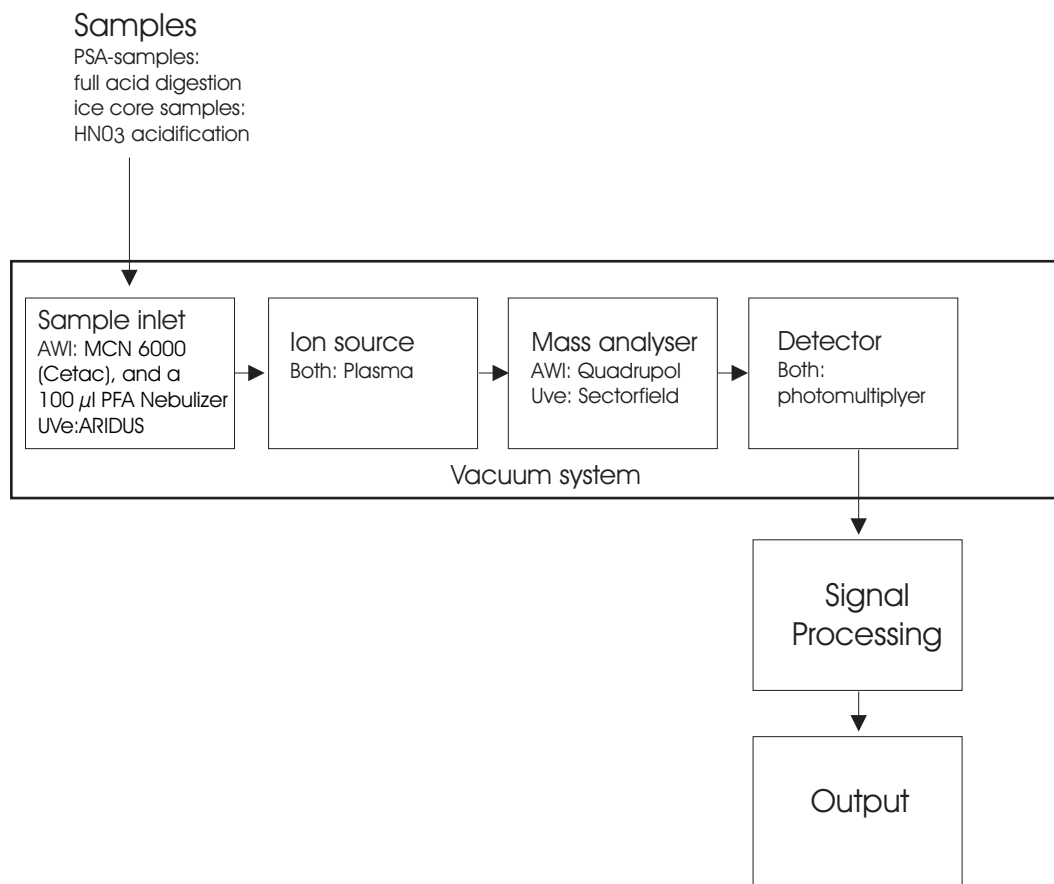
Figure 6.1: Schematic overview of the two processing and measurement setups used in this work. PSA samples are treated with a full acid digestion and measured using the ICP-QP-MS at AWI. Ice core samples are acidified with 1 % HNO_3 and measured at the University of Venice (UVe) using the ICP-SF-MS.

The aliquots containing the dust fraction $< 5 \ \mu m$ are treated with a full acid digestion. The samples added with HNO_3 (twofold distilled, 65 %, p.A., Merck), HF (distilled, 40 %, suprapur, Merck) and H_2O_2 (suprapur, Fa. SCP Science) are pressurized using polytetrafluoroethylen (PTFE) beakers to completely solubilize the sample matrix. The full digestion protocol is given in Appendix A.

At AWI all lab ware used to contain the samples, standards and used to prepare the solutions are cleaned following the procedure given in Appendix B.1. The digestion and the measurement of the samples are performed under a clean bench (US Class 100) in the clean room facilities at AWI, classified as US Class 10000, but presently U.S. Class 100-1000 is achieved. To each sample 10 μg·L^{-1} Rh are added to provide an internal standard to correct for instrumental drift during the measurements. Possible interferences of the Rh standard from ArCu, RbO and Pb^{2+} were not found to be significant. In any case through an interference on the Rh signal all REE concentration would be subjected to the same error, that vanishes, when considering relative changes among REE. Only the absolute concentration, which is

	ICP-QP-MS	ICP-SF-MS
ICP-MS		
RF Power [W]	1350	1250
Plasma gas [L·min^{-1}]	15	15.5
Auxiliary gas [L·min^{-1}]	0.8	1.8
Nebulizer gas [L·min^{-1}]	0.62	0.8-1.1
Nebulizer (with desolvatisation)	MCN 6000	Aridus I
Sweep gas [L·min^{-1}]	2.35	3.4 - 4.15
Nitrogen [L·min^{-1}]	12	15
T (spray chamber) [°C]	110	95
T (desolvating unit) [°C]	160	175
sample uptake [μ·min^{-1}]	100	100
Data aquisition		
Isotopes analyzed	≈ 40	19
Replicates	3	40
Integration time [s]	0.1	
Sweeps	20	
Measuring time per sample [min]	7	
Oxids [%]	0.03	
Double charged Ions [%]	5.7	

Table 6.1: Settings of the two ICP-MS used for ice core samples and PSA samples.

not discussed in this work, would be effected. Therefore, interferences on Rh do not affect the result of this work, anyways.

Blanks were prepared using ultra pure water, treated by the same procedure as the samples and measured regularly during data collection. The median of the blank values is subtracted from the sample concentration. The blank samples contain less than 0.5 % of the mean concentration in the samples and less than 10 % of the concentration in the lowest concentrated sample. The blanks for the REE are given in Appendix B.2. Calibration standards were prepared from a 10 μg · L^{-1} multi-element stock solution (Multielement Calibration Standard 2 and 3, Perkin-Elmer). The measurements were performed with a ICP-QP-MS ELAN 6000 built by Perkin Elmer/Sciex 1997 coupled with a micro concentric nebulizer and a desolvation unit MCN-6000 built by Cetac. The MCN-6000 is equipped with a heated membrane to separate the aerosol and the solvent. Thus the oxygen of the water available for oxid formation is minimized yielding an oxid formation rate for the REE of about 0.02 %. The uptake rate of sample is 100 μL · min^{-1}. The mean sensitivity obtained during the measurements is 490000 $\pm$ 200000 counts per second for a 10 μg · L^{-1} Rh solution. Instrumental conditions and measurement settings are summarized in Table 6.1.

-	La	Ce	Pr	Nd	Sm	Eu
detection limit [ppt]	0.303	0.523	0.087	0.296	0.055	0.075
melt head blank [ppt]	0.353	0.639	0.085	0.267	0.077	0.026
acid blank [ppt]	0.5509	0.9769	0.0837	0.2625	0.0653	0.0159

Gd	Tb	Dy	Ho	Er	Tm	Yb	Lu
0.044	0.018	0.039	0.019	0.029	0.022	0.034	0.023
0.075	0.019	0.044	0.009	0.024	0.006	0.02	0.01
0.0281	0.0041	0.0221	0.0046	0.0133	0.0032	0.0127	0.0024

Table 6.2: Detection limits and procedural blanks of the REE measurements in ice core samples. Calculations are described in the text.

6.1.2 Ice Core Samples

The ice core samples were taken from the innermost part of the core assigned to the CFA-analysis (see Figure 4.2 in Chapter 4). They were decontaminated using the melt head (Figure 4.1). Thus only the inner uncontaminated ice was used for the analysis. For the first time the sample decontamination using the melt head was performed for REE measurements. One line from the melt head filled 15 mL PS vials, that were also used for ion chromatography analysis (IC) providing continuous 1 m averages (Figure 4.1). These samples were immediately frozen after filling, once melted to take an aliquot for the IC and refrozen immediately afterwards. In a previous study, using a chiseling method, the ice core was decontaminated by removing ice in different layers from the outside to the inside. It was proved in that study, that the inner part of the ice core is not contaminated in REE by the drilling fluid ([Gabrielli et al., 2006]).

At least 24 h before the REE measurements, the samples were melted, filled into polypropylene vials (Greiner Bio-One), acidified with 100 μL HNO_3 (twofold distilled, p.a. 65 %, Fa. Merck) per 10 mL sample and afterwards kept frozen until the measurement. All sample handling was performed under class 100 clean room conditions. The cleaning scheme of the vials is given in Appendix B.1.

The measurements of the REE in the ice core samples were performed at the University of Venice, Italy, with an ICP-SFMS (Element2, Thermo Finnigan MAT, Bremen) coupled with a microflow/desolvation sample introduction system (Aridus, Cetac Technology). The Aridus consists of a microflow PFA nebulizer, a heated PFA spray chamber and a heated microporous PTFE tabular membrane. Interferences induced by oxides were highly reduced by this setup. The measurements were performed in low resolution mode with a nominal mass resolution of $\frac{\Delta m}{m} \approx 400$. The sample uptake by the system was 100 μL $\cdot$ min^{-1}. The maximum sensitivity in low

resolution mode (LRM) was $3 \cdot 10^6$ counts $\cdot$ s^{-1} for a 1 μg $\cdot$ L^{-1} Indium solution. The instrument stability was checked every seventh sample with a 1 μg $\cdot$ L^{-1} Indium solution. Additionally ^{129}Xe and ^{131}Xe was measured. Xe is included as an impurity in the used Argon and Nitrogen. If needed, the measurements are corrected for instrumental drift using the ^{129}Xe signal. The use of an internal standard like for the samples from the PSA was not possible due to the much lower REE concentration in the ice core samples associated with a much higher risk of contamination by the internal standard.

The blanks of the acid and the vials were determined with a series of blank samples with decreasing acidity (Figure B.1). The blanks of the CFA-melt head were determined with artificial ice bars cut out of artificial ice cores made of ultra pure water. These artificial ice bars were handled in the same way as the samples. Blanks were determined as the median of 10 samples. Both blank level values and detection limits are given in Table 6.2. The melt head blank is in the same range as the acid blank. The detection limit was calculated as three times the standard deviation of 10 replicates of 1 % HNO$_3$ in ultra pure water.

For La, Ce, Pr, Nd, Sm, Gd, and Dy measured in the EPICA-DML ice core samples from Holocene lie three to ten times above the detection limit and 10-200 times for glacial samples. For Tb, Ho, Er, and Yb the concentrations lie in the range of the detection limit for Holocene samples and 5-200 times above the detection limit for glacial samples. For Eu, Tm and Lu the concentrations lie below the detection limit for most of the Holocene samples and about ten times above the detection limit for glacial samples. The total blank (melt head blank) was subtracted from the concentration measured in the sample.

For the measurements the following isotopes, which are most abundant and less affected by interferences, are chosen: ^{139}La, ^{140}Ce, ^{141}Pr, ^{144}Nd, ^{151}Eu, ^{152}Sm, ^{157}Gd, ^{158}Gd, ^{160}Gd, ^{159}Tb, ^{164}Dy, ^{165}Ho, ^{166}Er, ^{169}Tm, ^{172}Yb and ^{175}Lu. Xe^{129} and Xe^{131} is recorded and used as a control for instrumental stability. These isotopes are the same as used by [Gabrielli et al., 2006], except Gd. Quantifying ^{155}Gd, ^{157}Gd, ^{158}Gd and ^{160}Gd yields the same concentration for ^{158}Gd and ^{160}Gd and elevated concentration for ^{155}Gd and ^{157}Gd. These results indicate interferences on the latter isotopes, whereas the agreement of ^{158}Gd and ^{160}Gd supports the absence of interferences on these isotopes.

54
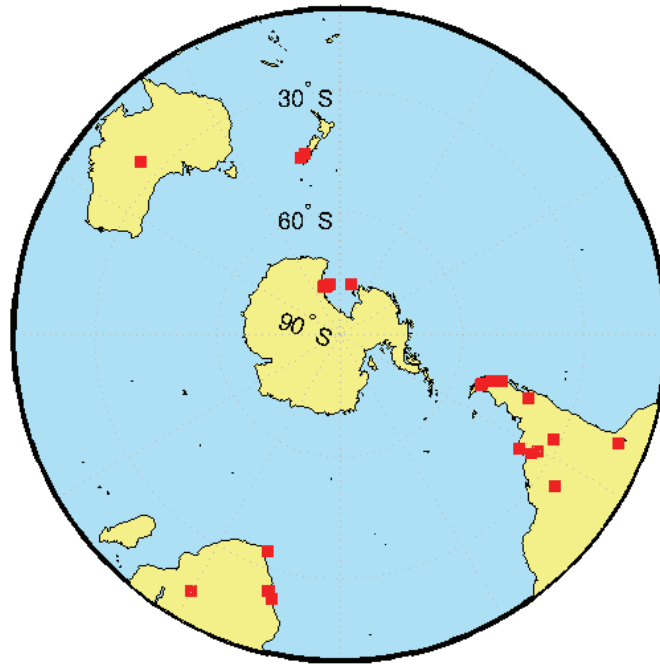
Figure 6.2: Locations of the sampling sites in the potential source areas of Antarctic ice core dust. The exact positions are given in Appendix D.

6.2 Rare Earth Element Composition in the Potential Source Areas

In this study 33 new samples from PSA with a particle size $< 5~\mu m$, most of them kindly provided by Barbara Delmonte, were analyzed for REE. Fourteen originate from South America, four from New Zealand, eight from ice free areas in Antarctica, five from Southern Africa and one sample from Australia (Figure 6.2 and Appendix D). The isotopic ratios of Sr and Nd were already analyzed earlier in these samples by [Delmonte, 2003]. Detailed information about these samples and previous measurements is given in [Delmonte, 2003].

The analyzed samples of this study are compared with literature data. Figure 6.3 shows the sample locations in South America and additional sampling sites available from literature data. Figure 6.4 shows a comparison with data from the literature of three samples from South America ([Gaiero et al., 2004], [Smith et al., 2003]). The concentrations are normalized to the upper continental crust (UCC). In order to eliminate the absolute concentration and to compare only the shape of the pattern, an additional normalization by dividing by one element is useful. [Tobler et al., 2007] uses Cer. Cer has the drawback to be subjected to an anomaly, due to the tendency
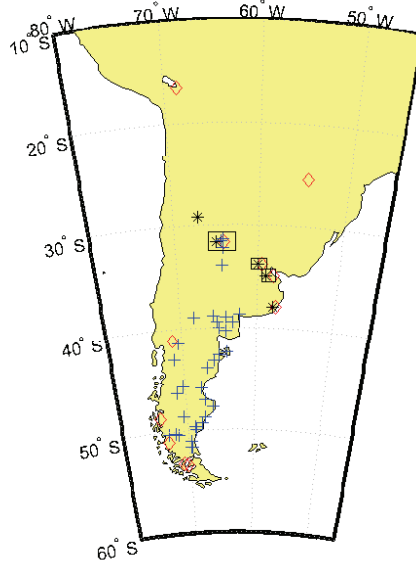
Figure 6.3: Sampling locations in South America. Samples analyzed in this study are marked with a red diamond, literature data are indicated with blue crosses ([Gaiero et al., 2003]) and black asterixes ([Smith et al., 2003]). The three samples taken for comparison between this study and literature data are marked with a rectangle.

to form the +4 oxidation state. Another possibility is to normalize by deviding by the mean value of all UCC-normalized concentrations. This normalization was earlier used by [Marx et al., 2005a] and has the advantage not to give too high influence to one single element. As an example the normalization of La is given in Equation 6.1.

$$La_{norm} = \frac{La_{conc}}{La_{UCC} \cdot mean(REE_{UCC})} \qquad (6.1)$$

with La_{norm} the normalized value, La_{conc} the La concentration in the sample, La_{UCC} the La concentration in the upper continental crust ([Wedepohl, 1995]) and $mean(REE_{UCC})$ the mean concentrations of all REE in the sample normalized on the UCC. The additional normalization on the mean value was performed for the following reason: The samples were fractionated by size using stokes settling in ultra pure water (see Section 6.1.1). The absolute amount of the dust $< 5 \ \mu m$ is not known exactly. To eliminate this uncertainty, the normalization was applied. Since for the PSA samples only the pattern and not the absolute value will be discussed, this procedure does not change any of this works results.

Three samples of the 33 were compared with three datasets from literature, which are not from exactly the same location, however in close proximity. The location of the samples is indicated by the three rectangles in Figure 6.3. In general, the
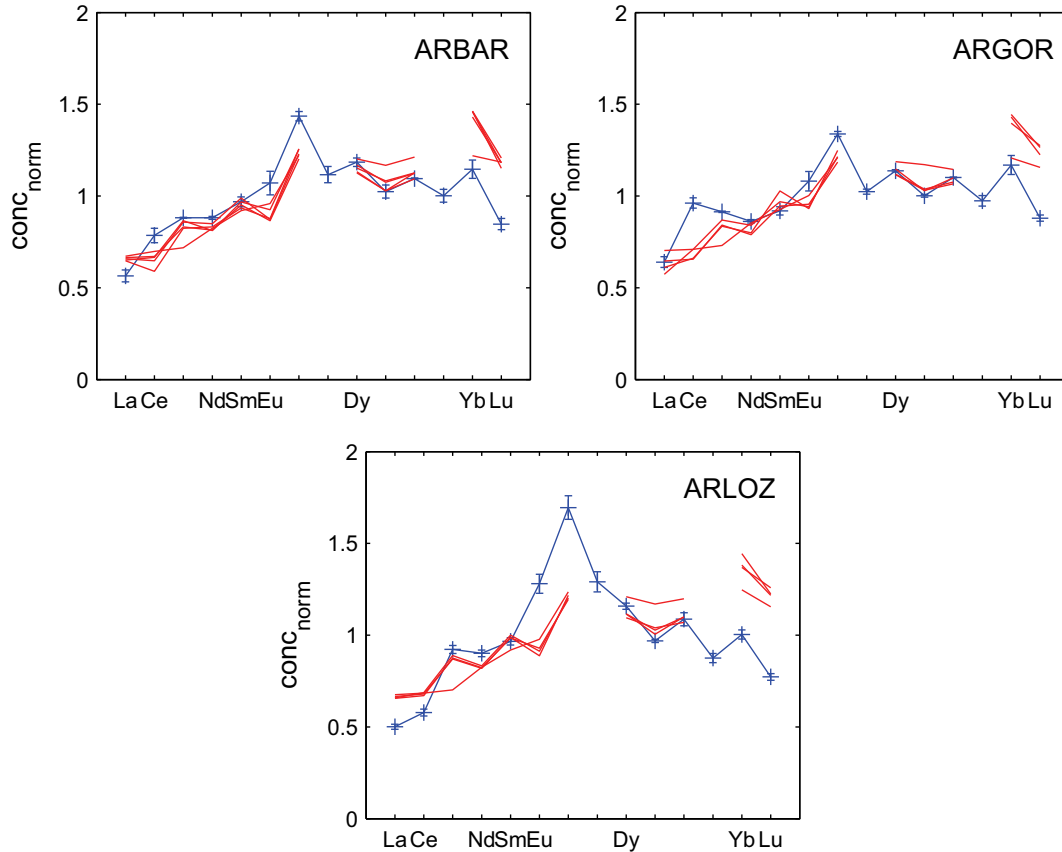
Figure 6.4: Comparison of the measurements with data from the literature: The locations indicated with an rectangle in Figure 6.3 are taken for comparison. Literature data (red) are taken from [Smith et al., 2003]. Data of this study are marked in blue. The concentration is normalized on the UCC ([Wedepohl, 1995]) and divided by each samples mean value according to Equation 6.1.

agreement in the pattern of the samples ARBAR and ARGOR with literature data is good (Figure 6.4). For the sample ARGOR Ce is elevated and in Lu there is a depletion for the sample measured in this study compared with literature data. For the sample ARBAR Lu is also lower in this study. For the third position considered for comparison (ARLOZ), the agreement in the pattern is not as good as in the other two cases. The enhancement in the MREE is higher than in the samples from literature data. One explanation of this difference might be the fact, that the samples are not from exactly the same locations. Maybe even more importantly, the concentrations in the literature are measured on the bulk sample, which has a bimodal size distribution with one maximum around 8 μm and another one around 80 - 100 μm ([Smith et al., 2003]), whereas the concentrations in this study are measured on the < 5 μm - fraction. These results indicate, that for a direct comparison with the ice core samples the separation of particles smaller than 5 μm is crucial and a comparison with literature values measured on the bulk could be misleading.
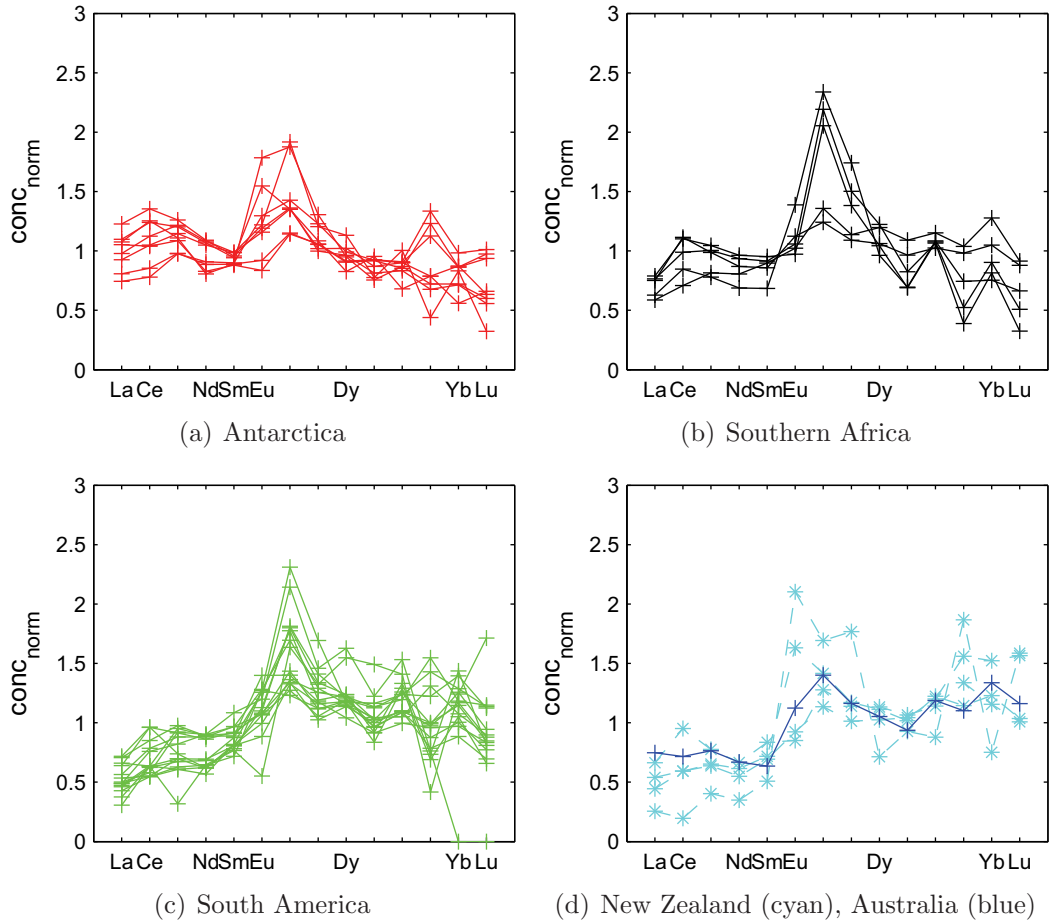
Figure 6.5: REE pattern for different continents. The concentration is normalized on the UCC ([Wedepohl, 1995])) and divided by each samples mean value according to Equation 6.1.

Figure 6.5 shows the REE pattern for different continents (concentrations are normalized according to Equation 6.1).

Some characteristics of the REE pattern in the PSA can already be seen in these graphs: The samples from Antarctica generally show a decrease from LREE to HREE ($\frac{LREE}{HREE} = 1.7$) and a variable enhancement of the Eu-concentration. The samples from southern Africa have also higher concentrations of LREE compared to HREE ($\frac{LREE}{HREE} = 1.4$), but much more pronounced is the elevated concentrations in the MREE. The highest Eu anomaly are found in the samples from New Zealand, in combination with an elevated HREE concentration compared to LREE ($\frac{LREE}{HREE} = 0.6$). Most of the samples are from South America. They all show a slightly increased concentration of MREE and a small enrichment of HREE compared to LREE ($\frac{LREE}{HREE} = 0.9$).

To get a more quantitative view about these differences and to test wether these differences are sufficient to provide separation of different PSAs Figure 6.6 shows the Eu-anomaly $\frac{Eu^*}{Eu}$ versus the ratio $\frac{LREE}{HREE}$ calculated as
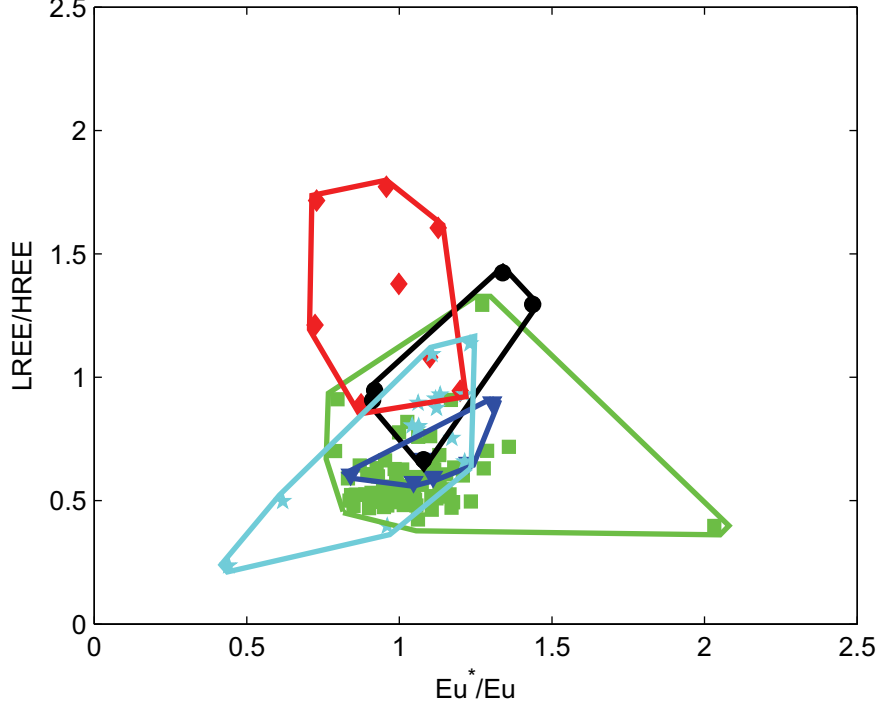
Figure 6.6: Comparison of $\frac{Eu^*}{Eu}$ vs. $\frac{LREE}{HREE}$ of the different source regions. New Zealand (cyan stars), Antarctica (red diamonds), Australia (blue triangles), South America (green rectangles), southern Africa (black circles). Calculation of $\frac{Eu^*}{Eu}$ and $\frac{LREE}{HREE}$ see text. The REE concentration are normalized on the UCC ([Wedepohl, 1995].

$$\frac{Eu^*}{Eu} = \frac{\sqrt{Sm_{UCC} \cdot Gd_{UCC}}}{Eu_{UCC}} \tag{6.2}$$

and

$$\frac{LREE}{HREE} = \frac{La_{UCC} + Ce_{UCC} + Pr_{UCC} + Nd_{UCC}}{Er_{UCC} + Tm_{UCC} + Yb_{UCC} + Lu_{UCC}} \tag{6.3}$$

with REE_{UCC} the respective element concentration normalized on the concentration in the UCC ([Wedepohl, 1995]). The features already identified in Figure 6.5 are also clearly apparent in Figure 6.6. Australia can be separated from Antarctica by different values for $\frac{LREE}{HREE}$. Furthermore the overlap between the New Zealand and the Antarctic field is small as well as the South African and the Australian field. The South American field, which was identified as the main source for dust in the EPICA-Dome C and Vostok ice core based on Sr/Nd isotopes ([Delmonte et al., 2002a]), overlaps with all other fields. Whether the areas are sufficiently separated to identify sources of dust in Antarctic ice cores will be discussed in Section 6.3. In any case, this approach does not use the full REE fingerprint. In particular the Eu-anomaly $\frac{Eu^*}{Eu}$ depends only on the three elements Sm, Eu and Gd. Even if the major variability is expected in Eu and in the ratios between LREE, MREE and HREE, using the full REE fingerprint could deliver additional information.

(a) Principle Component 1

(b) Principle Component 2

(c) Principle Component 3

(d) Principle Component 4
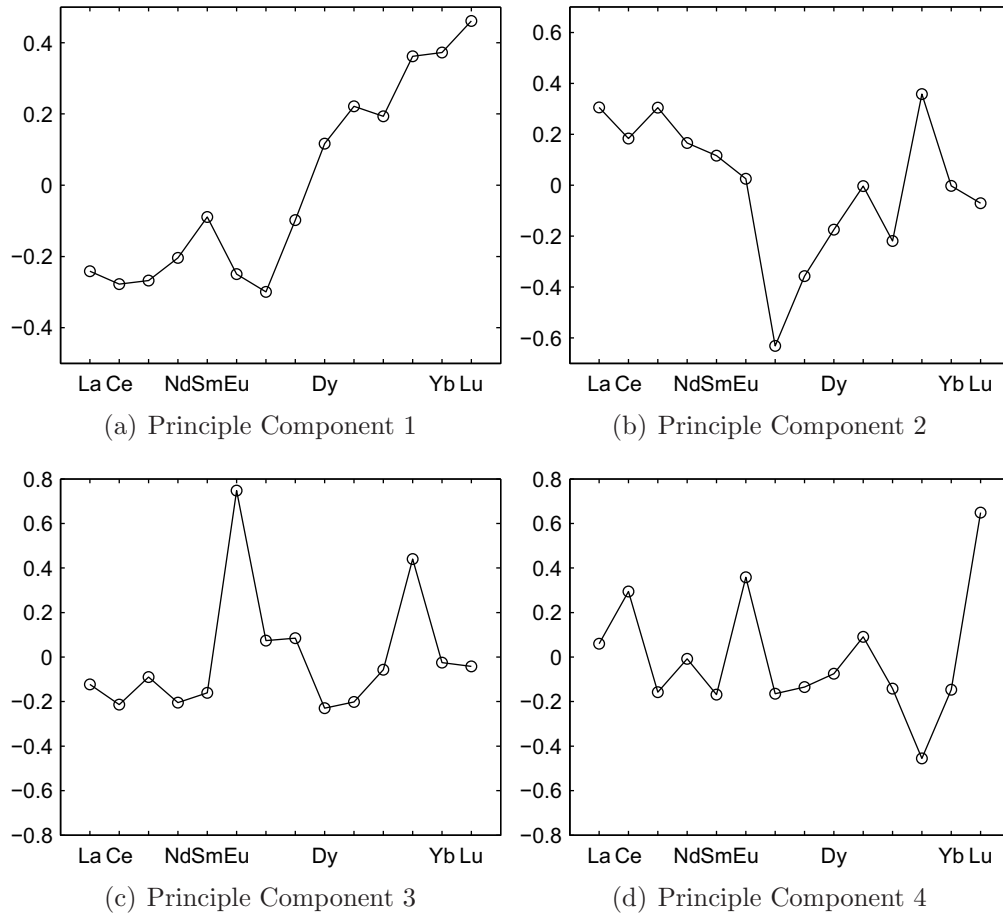
Figure 6.7: The principal components PC1 to PC4 of the PCA performed on the REE pattern of the samples from the PSA. PC1 to PC3 explain 88 % of the total variance.

To use the complete REE spectrum a principal component analysis (PCA) was performed. The REE span a 14-dimensional space, where each REE spans one dimension. The REE fingerprint of each sample represents a vector in this 14-dimensional space with the base (coordinate system) of the REE concentrations (CS_{REE}). With the principal components (PCs) a new coordinate system with a new base was established. The PSA samples were transformed from the old coordinate system CS_{REE} to the new coordinate system spanned by the principal components (CS_{PC}).

In order not to overweight one continent within the PCA analysis, the number of samples incorporated in the PCA should be equal and five samples were taken from each continent. Therefore, the samples from the continents with more than five samples (South America and Antarctica) were averaged into five groups, where samples with similar REE pattern were grouped. For continents with less than five samples available (New Zealand and Australia), literature data were used to fill the missing positions in the PCA.
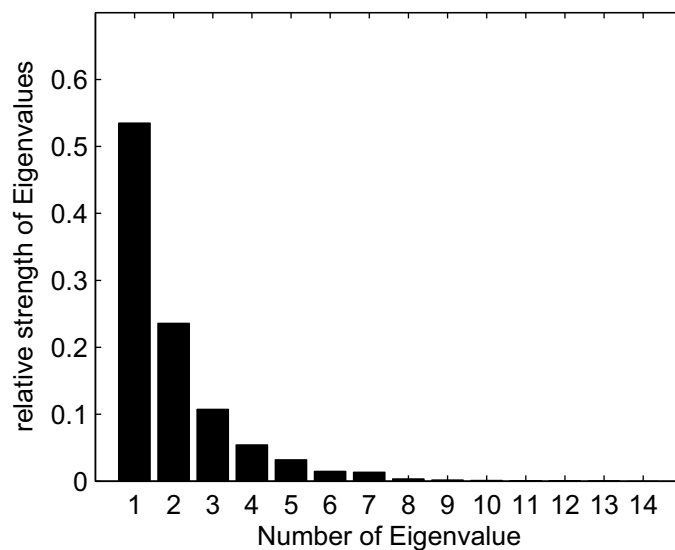
Figure 6.8: Eigenvalue spectrum of the PCA of the PSA. PC1 to PC3 explain 88 % of the total variance.

The PCA generated the eigenfunction matrix F and the principal components PC1 to PC14 (PC1 - PC4 are shown in Figure 6.7). The detailed mathematic description is given in Appendix E.

The main features of the REE fingerprint as seen in Figure 6.5 are apparent. PC1 explains the differences between LREE, MREE and HREE. By this principal component 53 % of the variance is explained. PC2 shows the enrichment in MREE and explains 24 % of the variance. PC3 shows a very strong peak in Eu and explains 11 % of the variance. PC2 and PC3 show also little variance in Ce. All together PC1 to PC3 explain 88 % of the total variance. PC4 to PC14 do not show a signal that obeys any obvious geochemical explanation and account all together only for 12 % of the total variance (Figure 6.8). Therefore, PC4 to PC14 are assigned as noise and will not be considered further in this study.

One difficulty arises in the determination of the error bars of the PCs. To get a measure for the dependency of the choice of the samples taken for the PCA, the PCA was repeated 50 times in the following way: The PCA was performed with 5 samples taken randomly out of the 14 samples of South America. From the other continents the samples were taken as described before. This was repeated 50 times. The 50 different PC1 to PC3 obtained in this way are shown in Figure 6.9. In some cases PC2 and/or PC3 changed their sign (i.e. the direction of the eigenvalue). In these cases the PC3 is shown in red. Despite this effect the first three PCs do not show any significant differences, indicating that the selection of the South American samples for the PCA does not affect the results. In the further work the PC1 to

(a) Principle Component 1

(b) Principle Component 2

(c) Principle Component 3
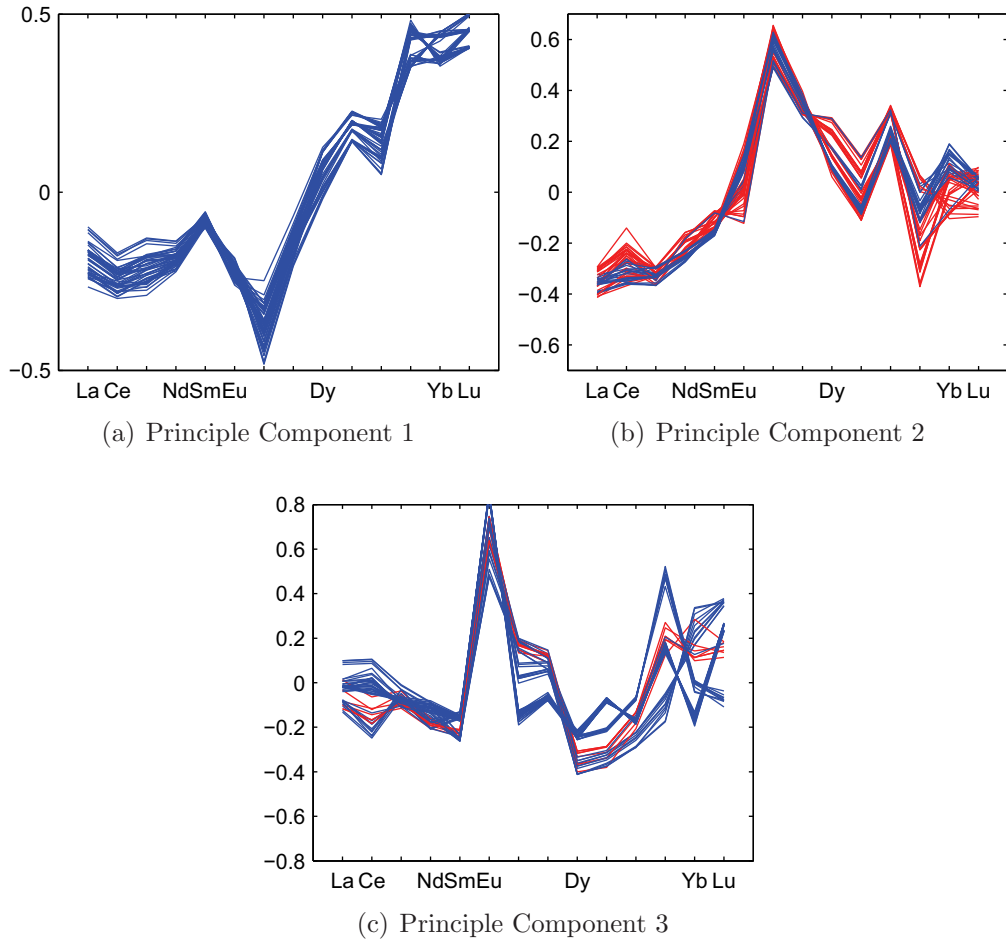
Figure 6.9: The first 3 principal components of the PCA performed on the REE pattern of the samples from the potential source areas. The PCA was repeated 50 times with 5 randomly chosen samples out of the South America samples each time. In some cases the sign of PC2 and/or PC 3 was reversed (see text). These cases are shown in red.

PC3 shown in Figure 6.7 are used.

In a next step all the other samples, which were not taken into account for the PCA, were transformed into the new coordinate system CS_{PC} according to Equation 6.4

$$B_{PC} = B_{REE} \cdot F \tag{6.4}$$

with B_{PC} the coordinates in CS_{PC}, B_{REE} the coordinates in CS_{REE} and the eigenfunction matrix F (see also Appendix E). Literature data were also included: 77 from South America ([Gaiero et al., 2004]), eleven from New Zealand and five from Australia ([Marx et al., 2005a]). Since they cover a larger size spectrum than the Antarctic ice core dust, the data from literature have to be interpreted with caution. In the PCA-analysis only samples with the full REE-pattern could be
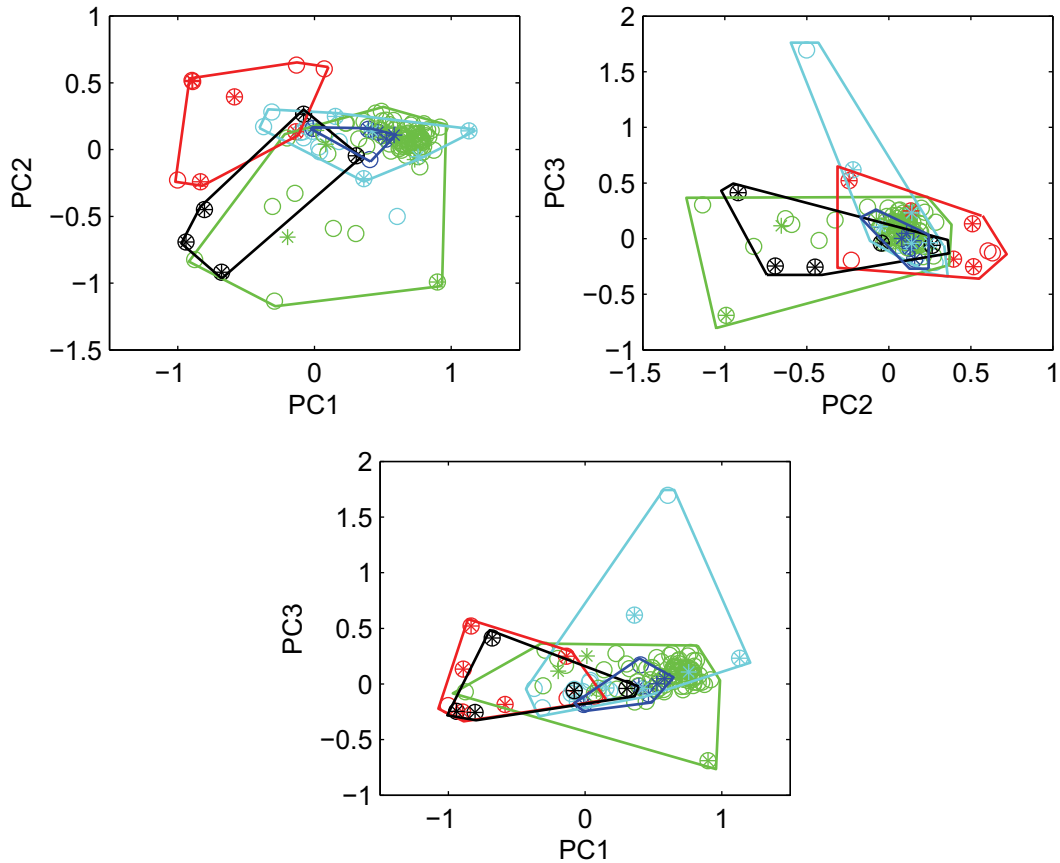
Figure 6.10: Principal component analysis of the REE concentration in the potential source area samples. New Zealand (cyan stars), Antarctica (red diamonds), Australia (blue triangles), South America (green rectangles), southern Africa (black circles). Samples used for the PCA are marked with filled symbols, samples that are transformed using Equation 6.4 are marked with open symbols.

included. Samples with one or more element missing could not be taken into account.

Figure 6.10 shows the first three principal components of the PSA samples plotted against each other. The separation of the different continents is not perfect. They do have a considerable overlap. PC2 vs. PC1 separates the Antarctic source totally from the Australian source and relatively well from the other sources. The samples from Australia form the narrowest cluster, which falls in all three cases in the New Zealandic field. Large areas in the in all three plots show an overlap and further analysis will show, if the ice core samples display a sufficiently distinct pattern to be placed in a distinct area in the CS_{PC}.

6.3 Rare Earth Element Composition in the EPICA-DML Ice Core

For the first time a quasi continuous REE profile is measured on an ice core in a depth interval covering the transition from the last Glacial to the Holocene. Around
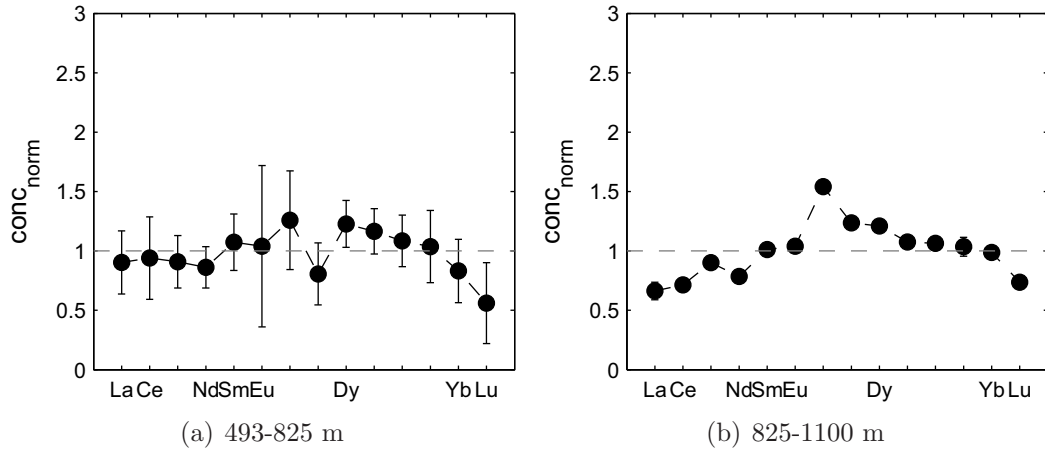
Figure 6.11: Mean REE pattern from different depth intervals from the EPICA-DML ice core. Mean values of the concentrations are normalized according to Equation 6.1. The errorbars give the standard deviation from the mean value. Data from the depth intervals 808 - 810 m, 1042 - 1043 m and 942 - 945 m are excluded (see text).

350 samples of the EPICA-DML ice core are analyzed for REE and several other TE (for details see Appendix C). They are taken from a depth interval ranging from 1100 m to 500 m covering the time span of the transition from the last Glacial to the Holocene (26500 - 7700 yr BP ([Ruth et al., 2007b])). In Appendix C all REE fingerprints are plotted. Generally the patterns in samples lower than ca. 825 m are very uniform. In this depth interval in almost all samples the full spectrum could be evaluated. Above 825 m the patterns become more variable and in several samples the less abundant elements could not be evaluated, in particular in the depth interval between 625 m and 725 m where the dust concentration is very low (Figure 6.14). Variations in the relative concentration and deviations from the flat pattern occur especially for Ce and Eu, consistent with the geochemical behaviour of the REE (Section 3). In some samples La and Tm show an enhancement.

Figure 6.11(a) shows the averaged REE spectrum of the depth interval from 493 to 825 m, that corresponds to the Holocene and the ACR. The error bars give the standard deviation from the mean value. Since for different elements the number of samples with a concentration below the detection limit is different, the number of samples for each elements mean value is also different. Least values were available for the less abundant REE (Eu, Tb, Ho, Tm, Yb, Lu). Aside from Lu, all mean values are within the standart deviation equal one and neither LREE nor HREE are clearly enriched. A decreasing trend from Dy to Lu is observable. Eu shows the largest scatter due to the highly variable enhancement or depletion in Eu.

The samples from lower than 825 m are characterized by a very uniform REE pattern. Figure 6.11(b) shows the mean REE spectrum of the depth interval from
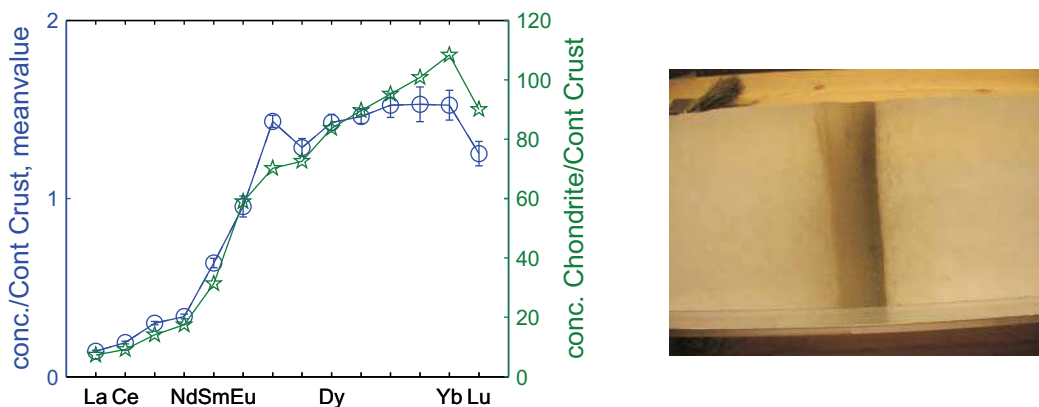
Figure 6.12: REE concentration in sample EDML809 (circles) and chondrites ([Palme, 2004]) (left). The REE concentration in this sample is dominated by the ash layer at a depth between 808.2 m and 808.3 m shown in the photograph (right).

825 to 1100 m, that corresponds to the last Glacial and the transition from the last Glacial to the Holocene. This pattern shows an enhancement in MREE compared to LREE and HREE, HREE are slightly enriched compared to LREE. In MREE and HREE occurs a decreasing trend from Gd to Lu. A small negative Eu-anomaly and a slightly depleted Nd concentration interrupts the in other respects smooth pattern.

These first findings suggest, that the dust supply to DML was more uniform during the Glacial than during the Holocene. The variable REE pattern during the Holocene points to a contribution of different sources to the EPICA-DML ice core dust. In contrast the uniform Glacial patterns indicate a permanently active single source or a constant mixing of more than one source.

Note, there are some samples, that differ from the others (see Figures 6.12 and 6.13) and these will be discussed separately:

The first eye-catching sample is found at a depth of 808 - 809 m (Figure 6.12, left). The concentration in HREE is strongly increased LREE are strongly depleted. For comparison, the chondritic REE concentration is shown. Between 808.2 m and 808.3 m is the best visible ash layer, in the whole EPICA-DML core caused by a volcanic eruption (Figure 6.12, right). The REE concentration is strongly dominated by this ash layer. During the volcanic eruption, the ejected ash originates not from the earth upper crust, but from lower crust or from the upper mantle, which has a chemical composition more similar to the chondritic composition than to the upper crust. Also in the sample from 809 - 810 m the HREE concentration is increased (not shown). The sample EDML810 was processed after EDML809 during the CFA, where also the REE sample filling took place. This enrichment is caused by the contamination of the CFA-system by the prominent ash layer in sample EDML809.
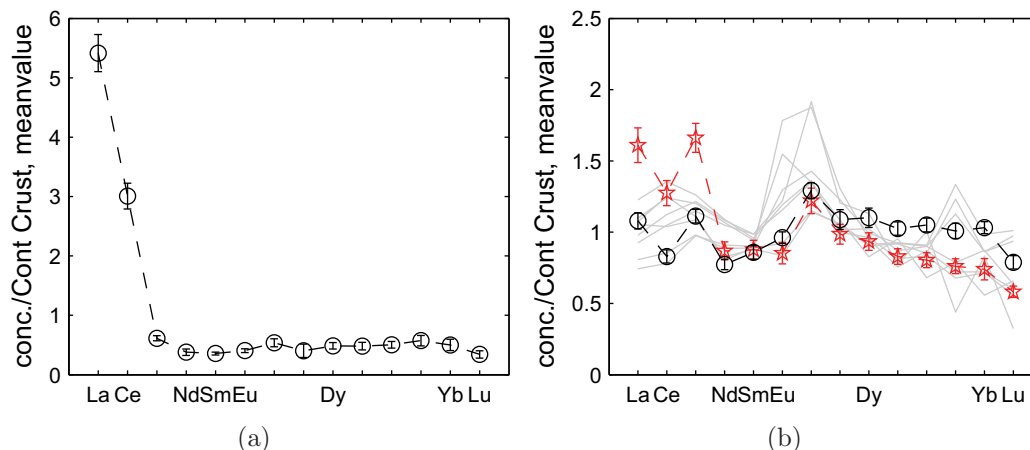
Figure 6.13: Samples, that are deviating from the common REE fingerprint during the glacial: Sample EDML1043 shows an strong enrichment in La and Ce (a). The reason for these enrichments is unclear. Sample EDML942 and 944 show an enrichment in LREE (b). For comparison the REE fingerprints of the Antarctic PSA samples are plotted in grey.

Despite intense rinsing of the system the strong REE pattern was carried over in the samples EDML810.

The next noticeable sample is from a depth of 1042 - 1043 m (Figure 6.13(a)). This sample shows extremely high values in La and Ce. To exclude an artefact emerging during the measurement, the samples was remeasured, but showed the same result. The other chemical species obtained from CFA and IC in this sample do not show any conspicuities, that would point to any anomaly. Since LREE are of all REE the most sensitive for contamination, it might also be a possibility, that this sample was contaminated during filling or during the sample treatment.

There are two other samples in the time interval of the last glacial showing a noticeable enrichment in LREE. These are from depth 942 - 943 m and 944 - 945 m. The sample from 943 - 944 m was not measured. Therefore it is not clear, if the pattern is persistent over 3 meters of ice or if it arises from two different events. The fingerprint of these samples bears resemblance to the fingerprint of the Antarctic PSA samples (Figure 6.13(b)) indicating that the dust in these two samples originates from ice free areas on the Antarctic continent. An enrichment in LREE like in these samples occurs frequently in Holocene samples from the EPICA Dome C ice core (pers. comm. Paolo Gabrielli), pointing to an Antarctic source for those samples as well. In contrast to the EPICA Dome C Holocene samples, where the Antarctic source seems to last for a longer time period, it would be restricted to the two (or one, if it is persistent over 3 m of ice core) events in the EPICA-DML ice core during the Glacial.

For the further analysis of dust provenance the above mentioned samples will not
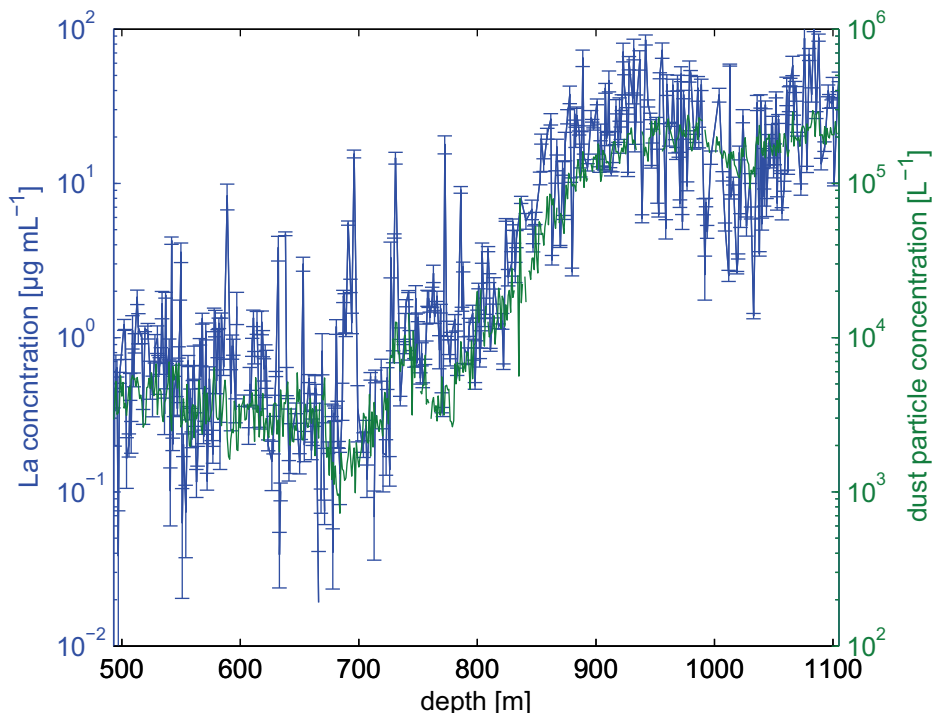
Figure 6.14: Dust (blue line) and La (green line) concentration in the EPICA-DML core in a depth interval from 493 to 1104 m. The continuous dust profile gives the number concentration measured using the LS (unpublished data, Urs Ruth, Patrik Kaufmann). The La is concentration measured in 1 m bag mean samples. This profile consists of 370 samples taken out of 600.

be taken into account.

In Figure 6.14 the La profile from the EPICA-DML ice core is shown as an example of the REE in comparison to the dust profile determined with the laser sensor (personal communication Urs Ruth, Patrik Kaufmann).

REE concentration in ice cores originates from dust in ice cores. The REE concentration in seawater is lower than in the crust by 6 orders of magnitude ([Nozaki et al., 1997]). Therefore marine contributions to the REE concentration in the samples can be neglected.

The dust concentration during the last Glacial is about two orders of magnitude higher than during the Holocene. This is consistent with the dust concentration obtained by CC (Section 5.7) and with other ice cores from Greenland and Antarctica (e.g. [Fischer et al., 2007a], [Ruth et al., 2003], [EPICA community members, 2006]). In general the La profile follows closely the dust profile. The La concentration is about 4 orders of magnitude below the dust number concentration profile, in accord with the mean La concentration in the UCC. The scatter is higher in the La concentration, due to the larger error of the measurement.

6.4 Identification of the DML Dust Provenance

In the following section the REE fingerprints obtained in ice core dust are compared to those of the PSA samples in order to identify the sources of dust in DML. In a first step the rations of LREE, MREE and HREE and the Eu*-anomaly are discussed. Thereafter, the PCA already presented for the PSA in Section 6.2 is used to refine the results. In a final step the fingerprints of the South American PSAs are investigated in more detail.

$\frac{LREE}{REE}$, $\frac{MREE}{REE}$ and $\frac{HREE}{REE}$ are used to exclude or confirm certain continents as a dust source for DML. Figure 6.15 shows $\frac{LREE}{REE}$, $\frac{MREE}{REE}$ and $\frac{HREE}{REE}$ and $\frac{Eu^*}{Eu}$ calculated according to equation 6.2 and 6.3. The black dots give the values in the ice core samples in the given depth. The colored lines give the upper and lower limit of the different PSA samples (green: South America, black: Southern Africa, red: Antarctica, blue: Australia, cyan: New Zealand). Ice core dust lying inside the range spanned by the colored lines could originate from the source indicated by the respective color. For samples, with one or more elements below the detection limit, the values were corrected as follows: In the case one element of the HREE below the detection limit (e.g. Lu), the remaining sum of HREE (Er + Tm + Yb) would be approximately 3/4 of the sum of all HREE (Er + Tm + Yb + Lu). Therefore 1/3 of the remaining sum of HREE (Er + Tm + Yb) was added. For two elements below the detection limit the remaining sum was doubled and for three elements below the detection limit tripled. For LREE, MREE and the total sum of all REE the correction was analogue. For samples with all HREE or MREE missing, no value is given in the respective plot. For the samples with Sm, Eu or Gd below the detection limit, no value for $\frac{Eu^*}{Eu}$ is given. The scattering of all values increase from the Glacial to the Holocene. Some of the Holocene values lie above the uppermost or below the lowermost line. This is attributed to an overcorrection of elements below the detection limit. Above 825 m corresponding to 15200 yr BP ([Ruth et al., 2007a]) a lot of samples lie outside the $\frac{LREE}{REE}$ range spanned by the South American PSA samples indicating that during the warm period dust cannot be solely from South America. $\frac{MREE}{REE}$, $\frac{HREE}{REE}$ and $\frac{Eu^*}{Eu}$ do not allow a conclusion of a dust provenance during the Holocene.

In the following the part below 825 m will be discussed. Considering $\frac{LREE}{REE}$, the lower limit for the PSAs in Antarctica is 0.24. There is only one single event out of 166 in the ice core dust with $\frac{LREE}{REE}$ larger than 0.24. Therefore, Antarctica can be excluded as a major source for DML dust. The PSA samples from Southern Africa reach a lower limit of $\frac{LREE}{REE} = 0.21$, that is in the range of the ice core dust (0.18 - 0.24). A non negligible amount of sample have a $\frac{LREE}{REE}$ value below the lower limit of
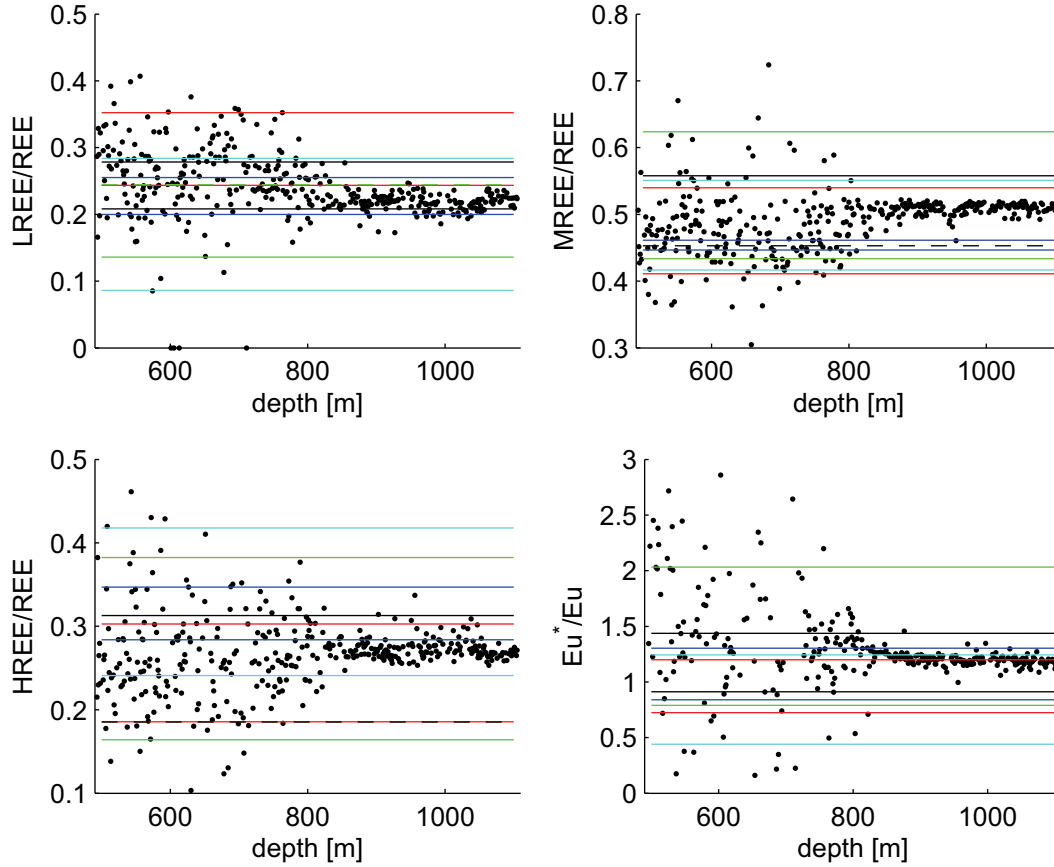
Figure 6.15: $\frac{LREE}{REE}$, $\frac{MREE}{REE}$, $\frac{HREE}{REE}$ and $\frac{Eu^*}{Eu}$ of the EPICA-DML ice core dust (black dots) and in the PSA. The colored lines give the upper and lower range of the samples from the respective PSA: New Zealand - cyan, Antarctica - red, Australia - blue, South America - green, Southern Africa - black. Calculation of the ratios are given in the text.

the Southern African PSAs, which therefore can not act as the only source for dust in DML. The interval covered by $\frac{MREE}{REE}$ in the Australian samples ranges from 0.44 to 0.46, which is well below the ice core dust ($\frac{MREE}{REE}$ = 0.46 - 0.52). Also regarding $\frac{HREE}{REE}$ Australia seems very unlikely as source, since most of the ice core dust values are below the lower limit of Australia. The mean $\frac{Eu^*}{Eu}$ in the ice core samples is 1.3, which is in the range of the upper limit of Antarctic dust and just below the upper limit for New Zealandic dust, excluding Antarctica and New Zealand as the only sources for the ice core dust.

In summary, analyzing the ratios of LREE, MREE, HREE and the Eu-anomaly, Antarctica and Australia can be excluded as a source for dust in DML in the time between 26500 and 15200 yr BP and Southern Africa or New Zealand can be excluded as the only source. The potential of areas in South America to act as sources is not confined by these investigations. For the time 15200 to 7500 yr BP no source is clearly identifiable and the dust input to DML is likely a mixture from different
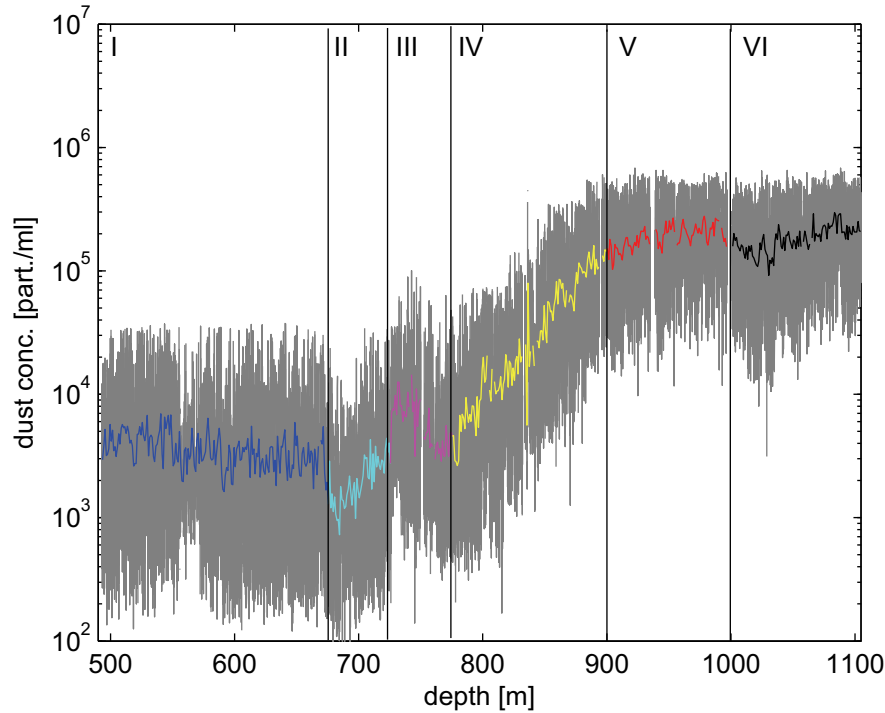
Figure 6.16: Dust profile in the EPICA-DML ice core, measured with the CFA laser sensor. The grey data represents 1 cm mean values, the colored data represents 1 m mean values and are colored according to the depth intervals I - VI, that are discussed in the text: mid holocene (I), early Holocene (II), ACR (III), transition (IV), LGM (V), before LGM (VI).

source areas. At least, the dust input to DML cannot originate solely from South America in contrast to the time between 26500 and 15200 yr BP.

In order to refine these findings, the PCA, already presented for the PSA in Section 6.2, was applied to the ice core samples.

For the further discussion the profile was divided into six depth intervals, which will be evaluated separately. In Figure 6.16 these six different depth sections are marked in different colors and labeled with I to VI.

To identify the provenance of the dust, the REE pattern of the remaining REE profile were transformed into the new coordinate system CS_{PC} as described in Section 6.2. In Figure 6.17 the first two components of the EPICA-DML ice core samples in the new coordinate system CS_{PC} are plotted separately in the six intervals defined in Figure 6.16.

Section I - III: Holocene and Antarctic Cold Reversal (ACR)

In these three sections, covering the time period of the Holocene and the ACR, the concentration of the most samples are below the detection limit for at least one element. Those samples, where the full REE fingerprint could be evaluated scatter widely in the coordinate system CS_{PC}. Some of them do not fall in any of the fields of the PSA, particularly in the Holocene. This is attributed to the large analytical

uncertainty due to the very low REE concentrations in the Holocene samples.

(a) I: Holocene

(b) II: Early Holocene

(c) III: ACR

(d) IV: Transition

(e) V: LGM

(f) VI: Glacial before LGM
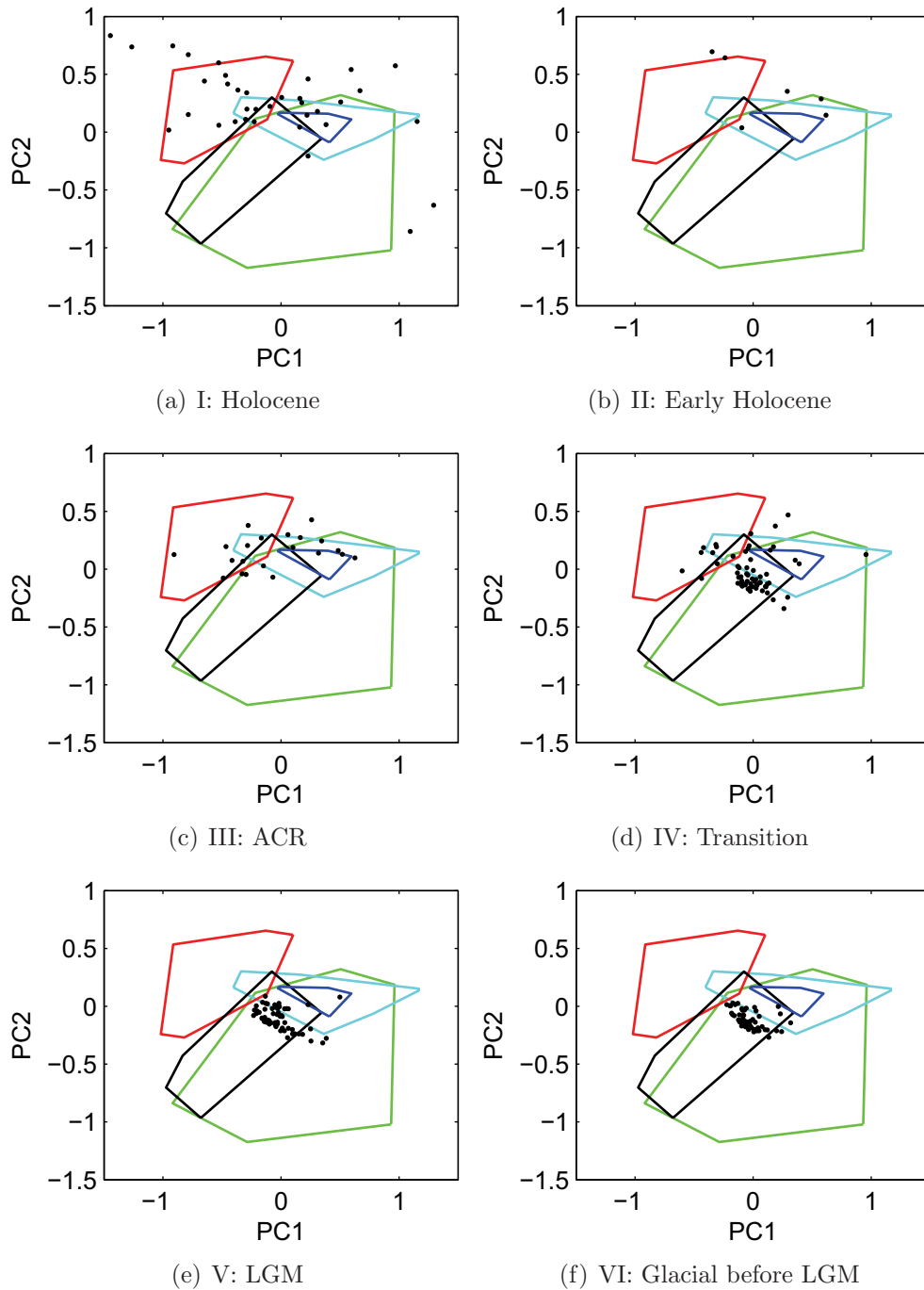
Figure 6.17: EPICA-DML ice core samples in the new coordinate system CS_{PC}: PC2 vs. PC1. EPICA-DML samples from the LGM are marked with red circles, from Glacial times before the LGM with black dots. The continents are marked with fields in different colors: New Zealand - cyan, Antarctica - red, Australia - blue, South America - green, Southern Africa - black.

Section IV: Transition

For section IV, corresponding to the transition from the Glacial to the Holocene, for more than half of the samples the full REE spectrum could be evaluated. Most
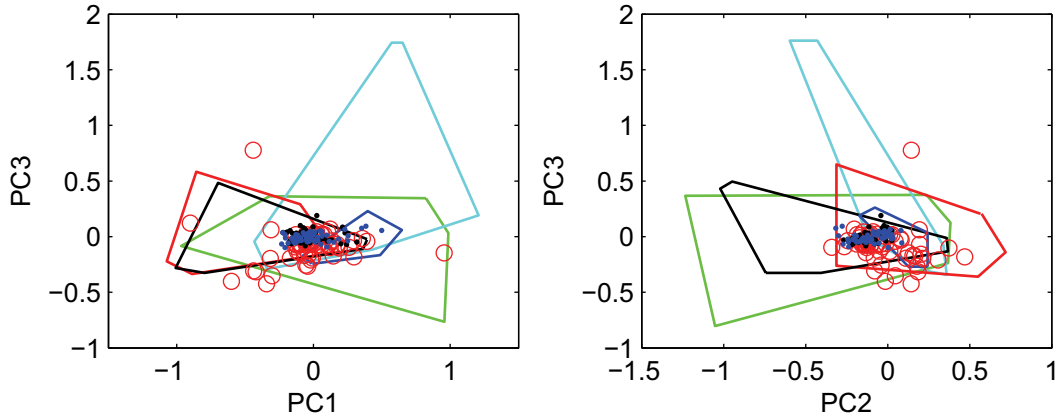
Figure 6.18: EPICA-DML ice core samples in the new coordinate system CS_{PC}. left: PC3 vs. PC1. right: PC3 vs. PC2. EPICA-DML ice core samples of the different time intervals are marked with black dots (section VI), blue dots (section V) and red circles (section IV). The continents are marked with fields in different colors: New Zealand - cyan, Antarctica - red, Australia - blue, South America - green, Southern Africa - black.

of the data fall into the area, were Southern Africa and South America overlap, while just a very few datapoints lie outsite of the South American field.

Section V - VI: Glacial

In the depth interval 900 - 1105 m, corresponding to the last Glacial, all data points lie within the South American and African field, very few of them also in the area of New Zealand. For the LGM one sample falls into the Australian area. No samples lie within the Antarctic area.

By evaluating only PC1 and PC2, the source areas of Southern Africa and South America cannot be sufficiently separated. For the Glacial and the transition (section IV to VI), PC3 vs. PC1 and PC3 vs. PC2 are shown in Figure 6.18. These plots can neither distinguish between South America and Africa.

Summarizing the results obtained from the PCA, Antarctica, Australia and New Zealand can be excluded as a considerable source region for dust in the EPICA-DML ice core during the last Glacial and termination I. Southern Africa and South America cannot be separated and cover both the area of the ice core dust in th PC2 vs PC1 plot.

Putting together all results from the PCA and LREE, MREE, HREE ratios and the Eu-anomaly, the following conclusions can be drawn:

Between 26500 and 15200 yr BP the REE fingerprints reveal no changes in the dust source area. For this time interval Antarctica, Australia and New Zealand can be excluded as a major source. However, ice free areas in Antarctica may contribute dust to DML during single events (depth interval 941-944 m). Dust cannot origin solely from Southern Africa according to this investigations. Isotopic measurements

on Sr and Nd exclude Southern Africa as a source of dust in the EPICA-Dome C and Vostok ice cores (Figure 6.20 taken from [Delmonte et al., 2004a]), suggesting that for DML Southern Africa might also account for a minor contribution of the dust input. Therewith the results of this work point to South America as the provanance of dust in the EPICA-DML ice core.

Between 15200 and 7500 yr BP the source cannot be identified. However, the source must have changed, since the $\frac{LREE}{REE}$-ratio of a lot of ice core dust samples in this time do not fit into the range spanned by the samples from South America. The dust concentration between 15200 and 7500 yr BP is very low with a minimum around 14000 yr BP (680 m). The PCA requires the full REE spectrum. As this is not given for a lot of samples from this time interval a larger sample volume would help to obtain full REE spectra even for samples with very low dust concentrations. A full REE fingerprint could be evaluated in almost all samples below 825 m, where the dust concentration is about 20 fold higher than in the minumum at 680 m. Less than 10 mL of sample were used in this study. An increase in sample volume by a factor of 20 is expected to deliver full REE spectra even for Holocene samples.

Recapitulatory, the REE fingerprint in combination with a PCA is a promising tool for the evaluation of REE fingerprints. The amount of samples from the PSA has to be increased to allow a more representative picture, especially for the Southern Africa region. The ice core samples volume has to be increased for the Holocene samples. A necessary volume of 200 mL would be still far below the volume used for isotopic measurements of Sr and Nd.

In a last stage the samples from South America are investigated in more detail to refine a South American source between 26500 and 15200 yr BP.

A closer look on the South American samples reveals three differing fingerprints (Figure 6.19). The samples from the Argentinian Pampas at the northern edge of Patagonia (shown in blue) are characterized by an enrichment of MREE ($\frac{LREE}{MREE}$ = 0.4), a light enrichment in HREE ($\frac{LREE}{HREE}$ = 0.7) and a very small positive Eu-anomaly ($\frac{Eu^*}{Eu}$ = 1.07). The second group of samples include samples from the central and southern part of Patagonia (shown in red). They are characterized by a variable positive Eu-anomaly varying between $\frac{Eu^*}{Eu}$ = 1 and $\frac{Eu^*}{Eu}$ = 2, a stronger enrichment in MREE ($\frac{LREE}{MREE}$ = 0.3) and again a slight enrichment in HREE ($\frac{LREE}{HREE}$ = 0.75). The third group of samples is from Tierra del Fuego from the southermost tip of the South America continent (shown in yellow). They show an increasing slope from LREE to HREE ($\frac{LREE}{MREE}$ = 0.4, LREE/HREE = 0.5) and a small negative Eu-anomaly ($\frac{Eu^*}{Eu}$ = 0.9). One sampling site at Bahia Blanca (white dot) has a very similar fingerprint to the samples from Tierra del Fuego.
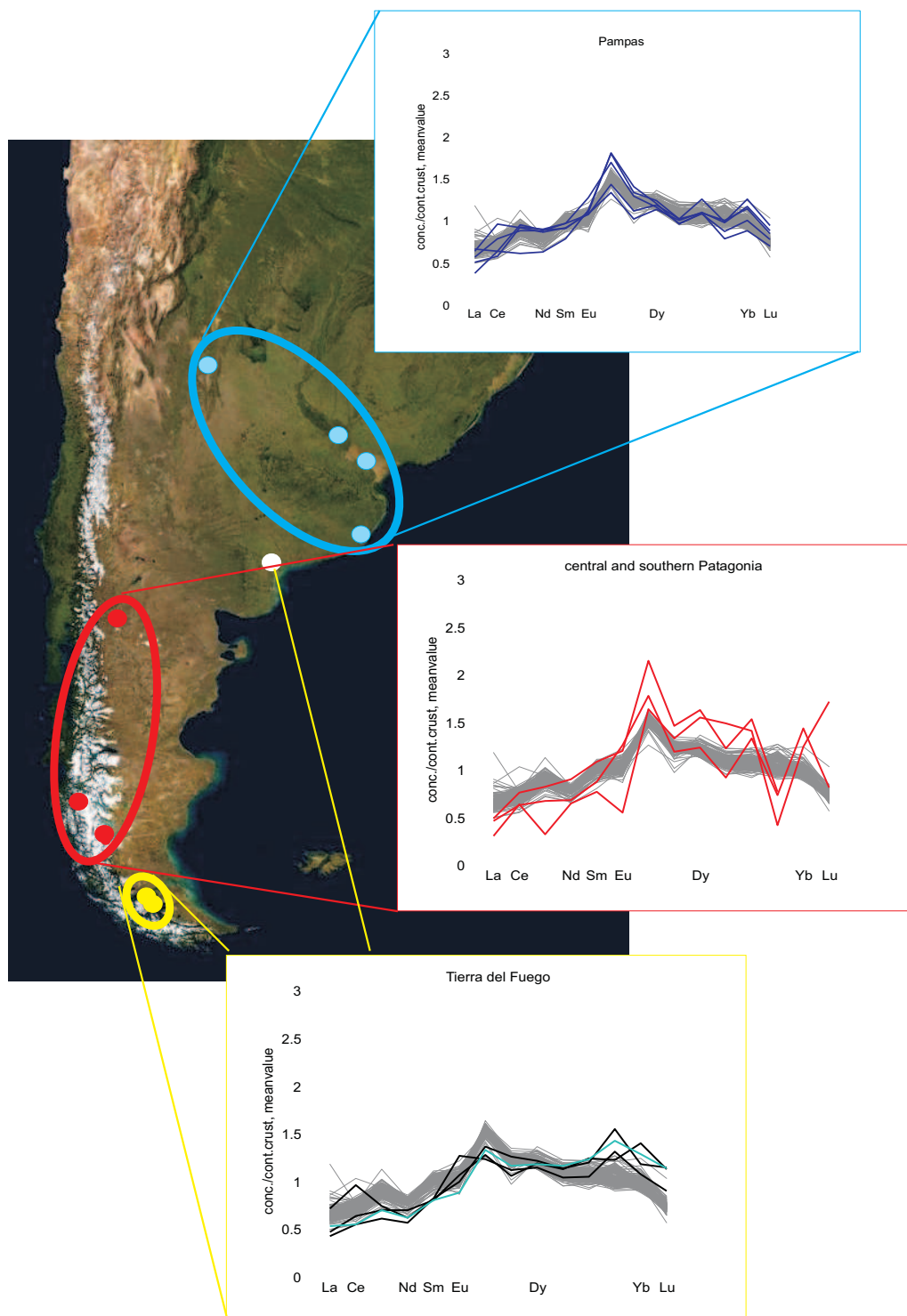
Figure 6.19: Comparison of REE fingerprints from the South American PSA samples and the EPICA-DML ice core samples. REE fingerprints of the PSA samples are shown in different colors: Pampas region blue, central and southern Patagonia red, Southermost tip and Bahia Blanca region (yellow, white). The light blue fingerprint in the plot representing Tierra del Fuego is obtained in the Bahia Blanca sample. The REE fingerprints from the EPICA-DML ice core representing a time between 26500 and 15200 yr BP are shown in grey for comparison.

For comparison the REE fingerprints of the EPICA-DML ice core dust in a depth
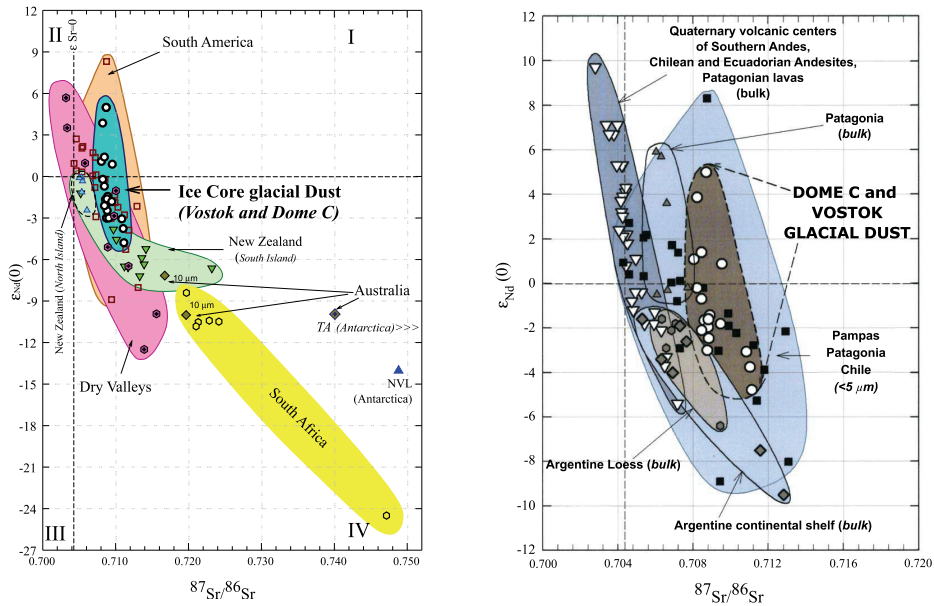
Figure 6.20: $^{87}Sr/^{86}Sr$ versus $\varepsilon_{Nd}(0)$. Comparison between ice core dust data from Vostok and EPICA-Dome C and the signature of the $< 5\ \mu m$ fraction of PSA samples (taken from [Delmonte et al., 2004a]).

from 825 to 1100 m are shown. The REE fingerprint of the ice core dust is very similar to the fingerprint of the samples from the Pampas suggesting that this region might have acted as a source for Glacial dust for DML. Isotopic measurements on Sr and Nd reveal the same region as the source for the dust at Dome C and Vostok during Glacials (Figure 6.20, [Delmonte et al., 2004a]). However, this region is not considered as a present day dust source ([Prospero et al., 2002]). Therefore, the distribution of dust sources in South America must have been changed since the last Glacial.

There are several parameters that may form a strong dust source: Firstly, a large amount of material available to be outblown, secondly, strong winds and thirdly, arid climatic conditions. During the last Glacial the Andean glaciers were much further advanced than today ([Mercer, 1976]), delivering much more clay size material. Dryer conditions were observed in Patagonia between 18000 and 14000 yr BP followed by a moderate increase in precipitation ([Markgraf et al., 2007]). A significant increase in windspeed could be explained by a more northward position of the westerly wind belt. At present times the westerly wind belt in the southern hemisphere is located between 45° and 55° S. The Pampas region is located at a latitude of 35° S. The results of this work would imply a significant northward shift. A shift of the Southern Westerlies have been discussed controversial (e.g. [Lamy et al., 1999], [Heusser, 1990], [Hemming et al., 2007], [Kim et al., 2002], [Wardle, 2003], [Wyrwoll et al., 2000]). The estimates of a possible shift range between up

to 10° northward and a few degree southward. To meet the Pampas region with the westerly wind belt a northward shift of at least 10° would be required, which is questionable. The amount of samples available from central and southern Patagonia is low. A more detailed sampling in this region is essential to scrutinize this explanation.

As deduced from size distribution measurements the dust concentration changes between the last Glacial and the ACR in the EPICA-DML ice cores cannot be explained by transport (Section 5.4 and 5.6), requiring a source change of a factor of about 28. It is likely that a combination of increased glacial outwash, higher aridity and an increase of the wind speed in the source area account for this changes. A more detailed sampling in Patagonia and the Pampas is needed, to investigate, if a position of the westerly wind belt reaching 35°S can be confirmed.

7 Conclusions and Outlook

The presented work investigates mineral dust in the EPICA-DML ice core. Dust concentration and size changes were analyzed in seasonal resolution during the Glacial and the ACR. The dust provenance was identified for the time between 26500 and 15200 yr BP.

Dust concentrations were found larger during the Glacial than during the ACR by a factor of 28. On seasonal timescale the dust concentration during the Glacial varies on average by a factor of 7.6, during the ACR by a factor of 3.5. The mean dust size spectrum reaching DML during the ACR has a modal value of $\mu = 1.96 \pm 0.13$ μm and is only slightly, but not significantly larger compared to the mean size spectrum reaching DML in Glacial times ($\mu = 1.88 \pm 0.15$ μm). The seasonal variability in the size is significantly larger. Typical seasonal changes of μ are 0.2 - 0.3 μm during the Glacial and 0.2 - 0.35 μm during the ACR.

A conceptual model ([Ruth et al., 2003], [Fischer et al., 2007b]) using the changes in dust size to calculate changes in the effective transport time is applied to the different time slices. According to this model, the mean effective transport time does not significantly change between the Glacial and the ACR. In contrary on a seasonal scale, changes in the effective transport time by a factor of 0.6 during the Glacial and 0.4 during the ACR are observed.

By knowing the variation in effective transport time, a quantification of transport and source contributions to the dust concentration changes in the ice core can be calculated. According to this simple model, the observed dust concentration changes from the Glacial to the ACR cannot be explained by transport and must therefore be explained by changes in the source. In contrast on a seasonal scale, during the ACR between 70 % and 100 % of the seasonal dust variations can be explained by transport, implying a rather constant source strength throughout the year during that time. During the Glacial the dust concentration changes arising from transport changes are in the same range, but explain only 30 - 63 % of the higher dust concentration variations found in the EPICA-DML ice core. Thus, an additional contribution from the source is necessary to explain the remaining 37 - 70 %.

These results are based on size distribution measurements in two core section of 1 m each. To confirm these findings, equal investigations have to be performed in other depth intervals. During Interglacials with low dust concentrations a larger

sample volume is needed to obtain better statistics and a continuous profile of the mode μ. In order not to loose the 3 mm resolution, a larger cross section than $32 \cdot 32$ mm from the CFA-cut (Figure 4.2) is needed. Additionally, the same investigations have to be performed on ice cores from different drill sites.

The use of REE is a promising tool to identify dust provenances. In the EPICA-DML ice core in a depth interval from 493 to 1105 m REE concentrations are measured using ICP-SF-MS. Less than 10 mL sample volume was used. For samples with low dust concentrations not the full REE spectrum could be obtained, as especially the less abundant elements are below the detection limit.

To identify the dust provenance by use of the REE, 33 samples from the PSA are analyzed and compared to the ice core samples. Considering the relative enrichment and depletion of LREE, MREE and HREE Antarctica and Australia could be excluded as a source before 15200 yr BP. If Southern Africa acts as a source, it cannot be the only one. By applying a PCA, New Zealand could be excluded as a major source. The results suggest South America as the major dust source before 15200 yr BP, whereas after 15200 yr BP a mixture of different sources seems more likely. At least one other source region is needed besides South America to explain the observed fingerprints. A direct comparison of the REE fingerprints indicates that the Glacial dust source for DML before 15200 yr BP is located in the Argentinean Pampas, which could be explained by a significant northward shift of the southern westerly wind belt during the last Glacial. Indeed, this implication is rather preliminary, since the number of samples from the PSAs used in the presented study is very limited. More samples are needed to get a clearer picture, especially from southern Africa and from South America. To investigate the source areas during warm stages a larger volume of ice core samples of up to 200 g is needed. Therewith a reduction in samples volume for provenance analysis using REE instead of isotopic measurements of Sr and Nd by a factor of $\approx$10 would be reached. REE fingerprints have shown their potential to serve as a tool for provenance analysis of dust in ice cores.

Appendix

A Preparation of the Samples from the Potential Source Areas

The samples from the potential source areas were digested according to the scheme given in the following Table.

step	duration [h]	temperature [°C]	comment
sample volume 2 or 5 mL			
addition of 10 mL HNO$_3$, 5 mL HF, 5 mL H$_2$O$_2$			
digestion according to the following procedure			
0		20	
1	1	100	heat
2	12	100	hold
3	end		let cool to room temperature
close beakers tightly			
0		20	
1	1	100	heat
2	5	100	hold
3	1	120	heat
4	2	120	hold
5	1	140	heat
6	2	140	hold
7	1	160	heat
8	2	160	hold
9	1	180	heat
10	2	180	hold
11	1	210	heat
12	5	210	hold
13	1.5	170	cool
14	1	160	cool
15	1.5	140	cool
16	1	140	hold
17	1	120	cool
18	1	100	cool
19	end		let cool to room temperature
add 10 mL ultra pure water to reduce Al and CaF			
0		20	
1	1	100	heat
2	4	100	hold
3	end		let cool to room temperature

		subboiling to 5 - 10 mL to reduce the acid	
step	duration [h]	temperature [°C]	comment
0		20	lower heating plate
1	2	160	heat
2	1.5	160	hold
3	end		let cool to room temperature
0		20	upper heating plate
1	1.33	110	heat
2	4	110	hold
3	end		let cool to room temperature
transfer sample to 25 mL vial, filling up to 25 mL with 2 % HNO_3			

Table A.1: Full acid digestion of the PSA samples.

B ICPMS Additional Information

B.1 Cleaning of lab ware at AWI

1 week	industrial cleaning agent (3 % Mucasol, 97 % ultra pure water
	rinsing with ultra pure water
1 week	HCl-bath (25 % HCl, 75 % ultra pure water)
	rinsing with ultra pure water
1 week	HNO_3-bath (25 % HNO_3, 75 % ultra pure water)
	rinsing with ultra pure water
1 week	HNO_3-bath (10 % HNO_3, 90 % ultra pure water)
	rinsing with ultra pure water
	drying under clean bench class 100
	sealing twice into PE-bags for storage

Table B.1: Cleaning procedure for the samples vials used for the ICP-MS analysis

Used reagents:

- ultra pure water: production by coupling a reverse osmosis system with a Purelab ultra system (Elga, High Wycombe, U.K.) (at AWI), production by coupling a Milli-Q (Millipore, Bedford, MA) water system with a Purelab Ultra system (Elga, High Wycombe, U.K.) (at University of Venice)

- industrial cleaning agent: MUCASOL, Fa. Merck

- HCl: HCl suprapur, Fa. Merck

- HNO_3: HNO_3 p.a. 65 %, Fa. Merck

B.2 Blank levels

element	La	Ce	Pr	Nd	Sm	Eu	Gd
blank level [ng/L]	1.61	2.27	1.48	3.44	0.95	0.56	0.74
element	Tb	Dy	Ho	Er	Tm	Yb	Lu
blank level [ng/L]	0.10	0.56	0.15	0.11	0.01	0.36	0.12

Table B.2: Procedural blanks of the samples from the potential source areas performed with the ICP-QP-MS determined by the median of 10 replicates
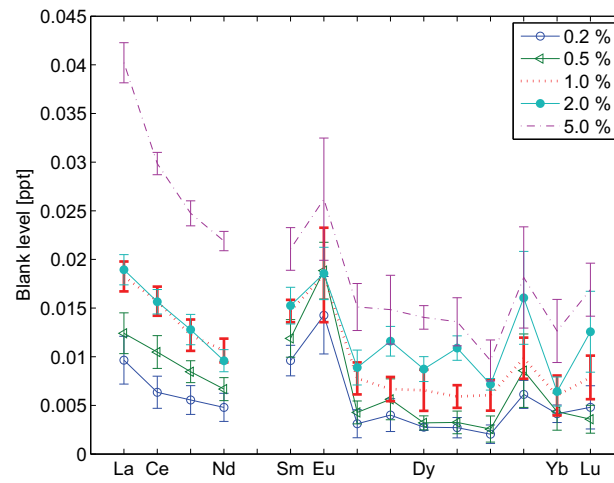
Figure B.1: Blank levels of the polypropylene sample vials used for the REE analysis in the EDML ice core samples. The different lines indicate different dilutions of HNO_3 in ultra pure water.

C EDML-samples analyzed on Rare Earth Elements

In the following REE fingerprints are plotted. Normalization was done according to Equation 6.1. The absolute value on the y-axis indicates the depth of the sample in the ice core. For example, the sample EDML800 from a depth of 800 m is plotted on the y-axis at 800. The relative deviation of the individual REE concentrations (e.g. La concentration, Ce concentration) from the mean value of 800 gives the fingerprint. Thereafter the measured concentrations are listed in [ng·L^{-1}].
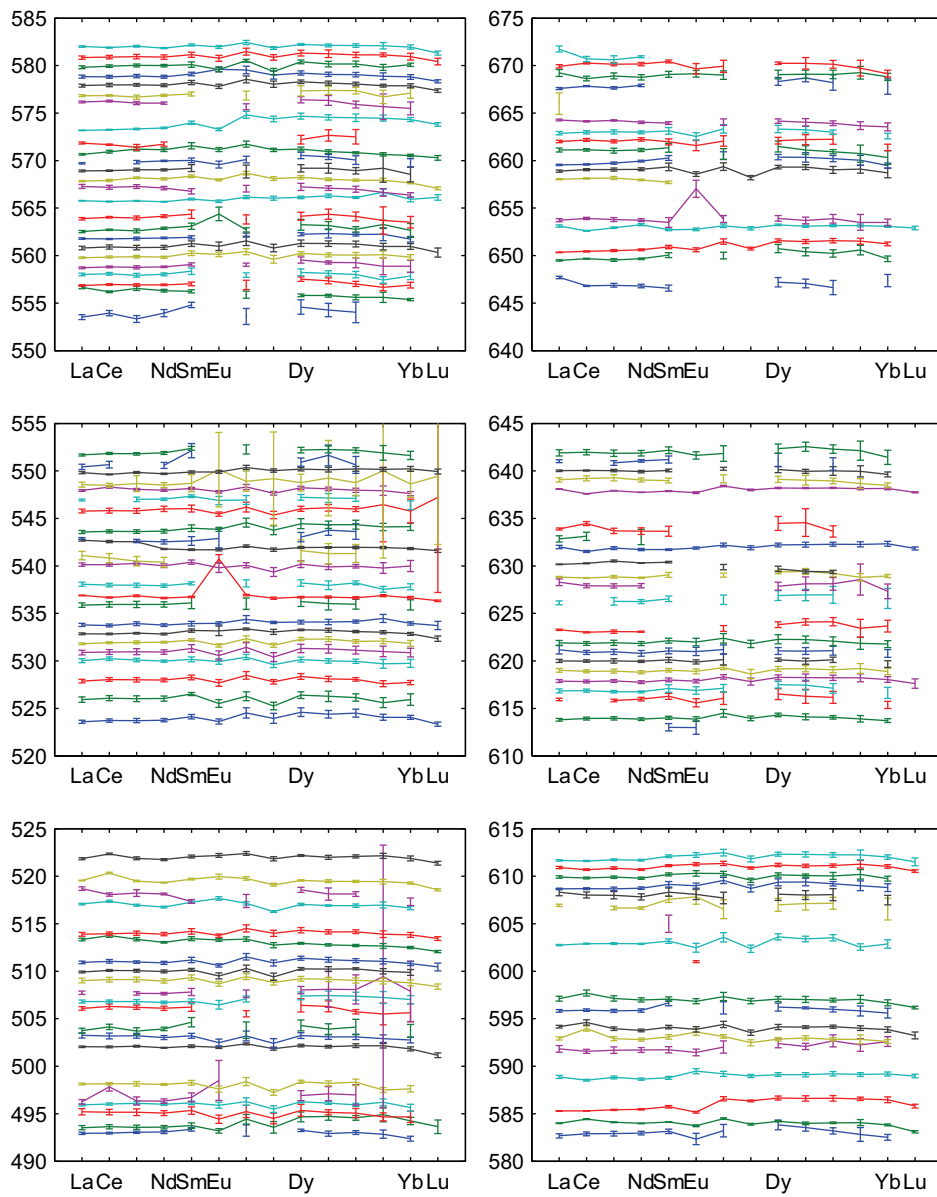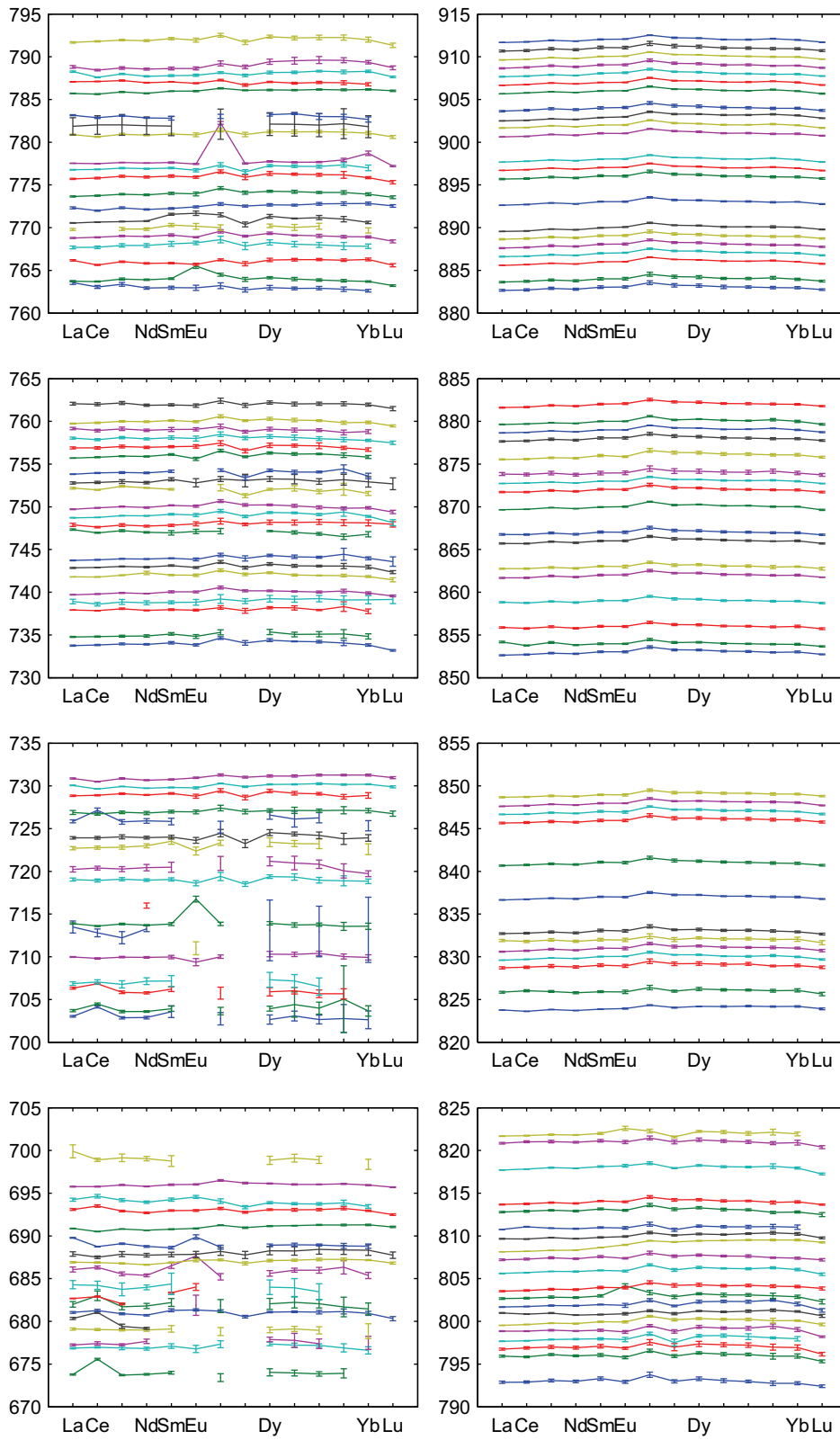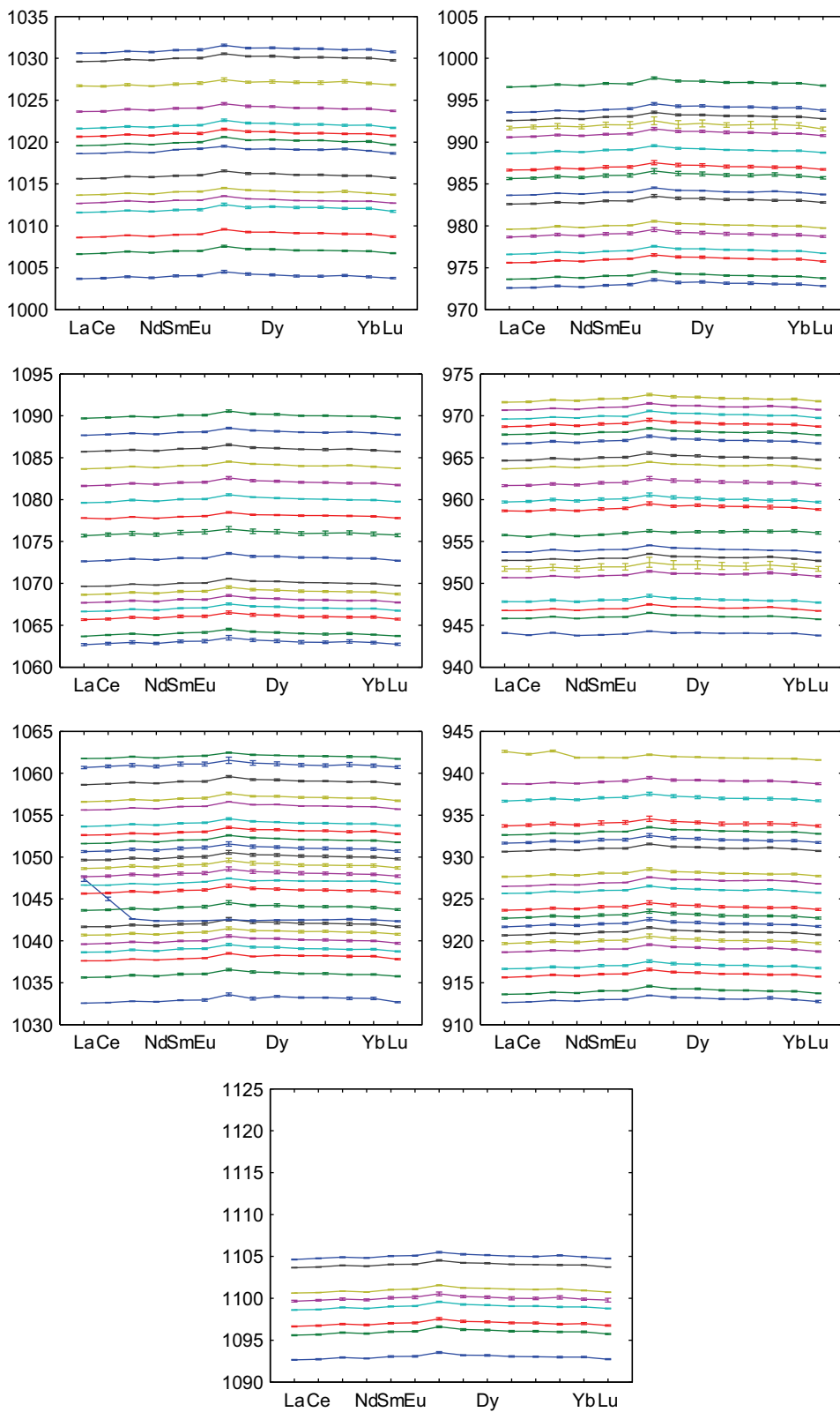
sample	depth [m]	La	Ce	Pr	Nd	Sm	Eu	Gd	Tb	Dy	Ho	Er	Tm	Yb	Lu
EDML493	493	0.3981	0.8368	0.0872	0.3665	0.0836	bdl	0.0451	bdl	0.0481	0.0074	0.0227	0.0027	0.0075	bdl
EDML494	494	0.3335	0.803	0.0707	0.2914	0.0684	0.0035	0.0774	0.0055	0.0938	0.0207	0.0509	0.0089	0.036	0.0033
EDML495	495	0.6081	1.1964	0.1137	0.4343	0.0981	0.0063	0.0538	0.0039	0.0613	0.011	0.0279	0.0025	0.0158	bdl
EDML496	496	0.6373	1.442	0.1482	0.5541	0.1138	0.0181	0.076	0.0052	0.0784	0.0147	0.0332	0.0062	0.0205	bdl
EDML497	497	0.0384	0.5585	0.0103	0.04	0.0158	0.0111	bdl	bdl	0.0122	0.0032	0.0076	bdl	bdl	bdl
EDML498	498	0.5506	1.1293	0.1093	0.4186	0.0891	0.0085	0.0583	0.0018	0.0596	0.0112	0.0328	0.0018	0.0141	bdl
EDML502	502	1.2138	2.447	0.2483	0.8629	0.1859	0.0339	0.1359	0.0151	0.1221	0.0236	0.0694	0.0099	0.0441	0.0015
EDML503	503	0.924	1.7901	0.1747	0.6106	0.1304	0.0107	0.0762	0.0048	0.0828	0.0154	0.0416	0.0049	0.026	bdl
EDML504	504	0.1649	0.5168	0.0301	0.1655	0.0526	bdl	0.0154	bdl	0.0258	0.0039	0.0129	bdl	0.0076	bdl
EDML506	506	0.2027	0.4925	0.0443	0.1654	0.0333	bdl	0.0085	bdl	0.0236	0.0047	0.0071	0.0007	0.0055	bdl
EDML507	507	0.4888	0.9751	0.0937	0.342	0.0732	0.0083	0.0562	bdl	0.0753	0.0166	0.0424	0.0055	0.0281	bdl
EDML508	508	0.2319	bdl	0.0413	0.1643	0.0373	bdl	0.0173	bdl	0.029	0.0066	0.0177	0.0057	0.0131	bdl
EDML509	509	1.1153	2.4986	0.2413	0.8561	0.2151	0.0223	0.137	0.0142	0.1196	0.0243	0.0583	0.0078	0.0394	0.0035
EDML510	510	0.5342	1.2999	0.1202	0.457	0.0975	0.0088	0.0657	0.0037	0.0661	0.0139	0.038	0.0043	0.0239	bdl
EDML511	511	0.9259	2.1149	0.1877	0.7018	0.1729	0.0177	0.1319	0.0135	0.1234	0.0231	0.0577	0.0077	0.0377	0.0038
EDML513	513	1.8328	4.9171	0.3678	1.1517	0.2868	0.0526	0.1655	0.016	0.1169	0.0205	0.0505	0.0067	0.0317	0.0009
EDML514	514	1.1683	2.4907	0.2565	0.9517	0.2277	0.0288	0.1696	0.0201	0.1548	0.0285	0.0785	0.0086	0.0506	0.0049
EDML517	517	0.9895	2.5831	0.1721	0.5571	0.1702	0.0455	0.0916	0.0041	0.0857	0.0163	0.0432	0.0067	0.0283	bdl
EDML518	518	0.3079	0.3946	0.0431	0.1647	0.0092	bdl	0.0062	bdl	0.0255	0.0039	0.0106	bdl	0.0026	bdl
EDML519-520	519.5	1.1383	4.052	0.2106	0.7106	0.1894	0.0462	0.1189	0.0101	0.1031	0.0202	0.0531	0.0075	0.0392	0.0007
EDML522	522	1.1065	3.6041	0.2252	0.7932	0.2034	0.046	0.1584	0.017	0.1393	0.0251	0.074	0.0112	0.0538	0.0042
EDML524	524	0.5504	1.3768	0.1311	0.5665	0.1546	0.0172	0.1243	0.0137	0.1346	0.0249	0.0729	0.0074	0.0459	0.0027
EDML526	526	0.4344	1.0171	0.092	0.3855	0.1018	0.007	0.0518	0.0018	0.0586	0.0113	0.0276	0.0021	0.0198	bdl
EDML528	528	0.8642	2.0923	0.1958	0.7791	0.1807	0.0196	0.1265	0.0123	0.1199	0.0209	0.054	0.0044	0.0334	bdl
EDML530	530	0.9904	2.4259	0.2072	0.7534	0.1642	0.0268	0.1177	0.0092	0.1	0.0186	0.0484	0.005	0.0338	bdl

sample	depth [m]	La	Ce	Pr	Nd	Sm	Eu	Gd	Tb	Dy	Ho	Er	Tm	Yb	Lu
EDML531	531	0.5972	1.2986	0.1281	0.5048	0.1297	0.0114	0.0839	0.0042	0.0798	0.0166	0.0396	0.005	0.0276	bdl
EDML532	532	0.6591	1.5342	0.1537	0.6377	0.1437	0.0153	0.0954	0.0082	0.0964	0.0205	0.0449	0.0066	0.0326	bdl
EDML533	533	0.7764	1.5723	0.1634	0.6099	0.1597	0.0315	0.108	0.0148	0.1041	0.0218	0.0512	0.0069	0.036	0.0026
EDML534	534	1.6575	3.075	0.3737	1.2858	0.2784	0.0582	0.2489	0.0337	0.2024	0.044	0.1224	0.0226	0.0911	0.0126
EDML536	536	0.3199	0.7037	0.068	0.2785	0.0596	bdl	0.0323	bdl	0.0412	0.0073	0.0184	bdl	0.0154	bdl
EDML537	537	1.8846	2.9109	0.3493	1.0388	0.2252	0.294	0.1718	0.0192	0.1331	0.0293	0.0704	0.0136	0.0642	0.0059
EDML538	538	0.5727	1.0702	0.1016	0.3937	0.0911	bdl	0.0536	bdl	0.0577	0.0099	0.0338	0.0021	0.0199	bdl
EDML540	540	0.8487	1.7167	0.185	0.6099	0.151	0.0178	0.0688	0.0041	0.0785	0.0129	0.0373	0.0043	0.0343	bdl
EDML541	541	0.1015	0.1555	0.009	0.0288	bdl	bdl	bdl	bdl	0.0133	0.0023	0.0063	bdl	bdl	bdl
EDML542	542	4.2564	7.9885	0.7526	1.5774	0.258	0.0524	0.2337	0.0278	0.2128	0.0458	0.1236	0.0174	0.0972	0.0125
EDML543	543	0.2038	bdl	0.0272	0.0955	0.0204	0.0059	bdl	bdl	0.0208	0.0076	0.0187	bdl	bdl	bdl
EDML544	544	0.4342	0.9947	0.0934	0.4047	0.1079	0.0193	0.1037	0.009	0.0994	0.0196	0.0534	0.0063	0.0401	bdl
EDML546	546	0.5582	1.1832	0.1113	0.5742	0.1074	0.0096	0.0742	0.004	0.065	0.0153	0.0359	0.0078	0.0258	0.0133
EDML547	547	0.3461	bdl	0.072	0.3008	0.0713	0.0096	0.03	bdl	0.0402	0.0081	0.0209	bdl	0.0066	bdl
EDML548	548	0.8044	2.2587	0.1799	0.6682	0.1443	0.0202	0.0981	0.0086	0.0941	0.0183	0.0427	0.0059	0.0245	bdl
EDML549	549	1.2036	2.1588	0.2809	0.8626	0.2192	0.1348	0.1709	0.0398	0.1478	0.0514	0.0853	0.0318	0.0612	0.026
EDML550	550	3.5845	5.6695	0.7304	2.5042	0.5723	0.1173	0.5227	0.0711	0.4755	0.0964	0.2773	0.0386	0.2502	0.0346
EDML551	551	0.0627	0.1989	bdl	0.0686	0.0457	bdl	bdl	bdl	0.0122	0.0046	0.0048	bdl	bdl	bdl
EDML552	552	0.2033	0.5074	0.0466	0.2131	0.0598	bdl	0.0329	bdl	0.0321	0.0072	0.0181	0.002	0.0087	bdl
EDML554	554	0.0738	0.2648	0.0089	0.1046	0.0368	bdl	0.0071	bdl	0.0198	0.0034	0.0074	bdl	bdl	bdl
EDML556	556	0.7065	1.0385	0.1282	0.4499	0.0773	bdl	0.033	bdl	0.0312	0.0064	0.0135	0.0019	0.0073	bdl
EDML557	557	0.325	0.7415	0.068	0.2826	0.0573	bdl	0.0304	bdl	0.0525	0.0099	0.0201	0.0019	0.016	bdl
EDML558	558	0.406	0.8853	0.0729	0.3312	0.0791	bdl	0.0327	bdl	0.0444	0.0087	0.0208	0.0013	0.0159	bdl
EDML559	559	0.2188	0.503	0.0454	0.2012	0.0475	bdl	0.0278	bdl	0.0422	0.0075	0.0197	0.002	0.0124	bdl
EDML560	560	0.5934	1.3132	0.1312	0.511	0.1397	0.0252	0.094	0.0072	0.0845	0.0159	0.0414	0.0062	0.0299	bdl

sample	depth [m]	La	Ce	Pr	Nd	Sm	Eu	Gd	Tb	Dy	Ho	Er	Tm	Yb	Lu
EDML561	561	0.7083	1.6404	0.1456	0.6172	0.1638	0.0258	0.1197	0.011	0.1039	0.0215	0.0561	0.0063	0.0396	0.0024
EDML562	562	0.2953	0.5714	0.0583	0.2577	0.0503	bdl	0.0377	bdl	0.042	0.0095	0.0238	0.0035	0.0127	bdl
EDML563	563	0.1158	0.3199	0.0259	0.1547	0.0347	0.0154	0.0135	bdl	0.0246	0.0049	0.0087	0.0021	0.0066	bdl
EDML564	564	0.1719	0.4122	0.0367	0.1797	0.0385	bdl	0.0137	bdl	0.0201	0.0051	0.0114	0.001	0.0047	bdl
EDML566	566	0.9411	1.7118	0.1793	0.6443	0.1683	0.0259	0.1226	0.0196	0.1228	0.0302	0.0693	0.0151	0.0524	0.0114
EDML567	567	0.5613	1.0531	0.1082	0.3868	0.0484	bdl	0.0396	bdl	0.0486	0.0092	0.0224	0.0021	0.0076	bdl
EDML568	568	1.3305	2.9216	0.3637	1.3673	0.3109	0.0448	0.2296	0.027	0.1757	0.0314	0.0762	0.011	0.0486	0.001
EDML569	569	0.2279	0.4735	0.0503	0.2034	0.0434	bdl	0.0182	bdl	0.0264	0.0057	0.0119	0.0022	0.0061	bdl
EDML570	570	0.2609	bdl	0.0596	0.2809	0.054	0.0061	0.0349	bdl	0.0502	0.0096	0.0197	bdl	0.013	bdl
EDML571	571	1.1039	3.1971	0.3989	1.539	0.3812	0.0577	0.2522	0.0295	0.1838	0.0304	0.0719	0.0082	0.0422	0.004
EDML572	572	0.1172	0.1887	0.0106	0.0814	bdl	bdl	bdl	bdl	0.015	0.0044	0.0108	bdl	bdl	bdl
EDML574	574	0.5403	1.5037	0.1913	1.061	0.4264	0.0262	0.4729	0.0645	0.4533	0.0892	0.2355	0.0327	0.1827	0.0202
EDML576	576	0.2325	0.5124	0.0409	0.169	bdl	bdl	0.0115	bdl	0.0252	0.0051	0.0093	0.001	0.0046	bdl
EDML577	577	0.1753	0.3678	0.0278	0.1487	0.0311	bdl	0.0155	bdl	0.0253	0.0056	0.0149	0.0011	0.0108	bdl
EDML578	578	1.3215	2.9071	0.2785	1.1021	0.2636	0.0354	0.1991	0.0239	0.1723	0.0328	0.0814	0.0097	0.0596	0.0044
EDML579	579	1.2578	2.5213	0.2671	1.002	0.246	0.0721	0.2018	0.0236	0.1654	0.0315	0.0828	0.01	0.0567	0.0044
EDML580	580	0.5251	1.2201	0.1265	0.5056	0.102	0.0109	0.083	0.0037	0.0798	0.0141	0.0386	0.0038	0.0321	bdl
EDML581	581	0.9334	2.0173	0.2054	0.8002	0.185	0.0252	0.1418	0.0149	0.1316	0.0266	0.065	0.0094	0.0489	0.0039
EDML582	582	1.2388	2.2384	0.2492	0.8241	0.2094	0.0349	0.153	0.0162	0.1359	0.0266	0.0704	0.01	0.0547	0.0032
EDML583	583	0.211	0.5622	0.0553	0.2415	0.0522	0.0031	0.0333	bdl	0.0516	0.0093	0.0195	0.0019	0.0075	bdl
EDML584	584	1.3896	4.0594	0.3011	1.0961	0.2286	0.0299	0.18	0.0193	0.1514	0.0265	0.0752	0.011	0.0531	0.0012
EDML586	586	0.6456	1.352	0.1767	0.8205	0.2374	0.0099	0.3031	0.0466	0.33	0.0688	0.1869	0.026	0.1522	0.015
EDML589	589	8.3119	10.2061	1.5193	4.9303	1.0684	0.4128	0.9829	0.1418	0.952	0.201	0.5871	0.0797	0.5218	0.0775
EDML592	592	0.4334	0.6082	0.0707	0.2971	0.0555	0.0069	0.0462	bdl	0.0654	0.0109	0.045	0.0048	0.0386	bdl
EDML593	593	0.8807	3.7983	0.1676	0.6157	0.151	0.0449	0.0938	0.007	0.0722	0.0178	0.0409	0.0059	0.0264	bdl

sample	depth [m]	La	Ce	Pr	Nd	Sm	Eu	Gd	Tb	Dy	Ho	Er	Tm	Yb	Lu
EDML594	594	0.8711	2.4452	0.1384	0.4633	0.1213	0.0195	0.0897	0.0062	0.0758	0.0161	0.0448	0.0056	0.0297	0.0015
EDML596	596	0.341	0.7552	0.0665	0.2853	0.0998	bdl	0.0407	bdl	0.045	0.009	0.021	0.0025	0.0113	bdl
EDML597	597	1.5892	4.9633	0.3192	1.1288	0.2223	0.0351	0.1655	0.0191	0.1384	0.0282	0.0711	0.011	0.0451	0.0021
EDML601	601	bdl	bdl	bdl	bdl	bdl	0.0827	bdl	bdl	bdl	bdl	bdl	bdl	bdl	bdl
EDML603	603	0.3909	0.9487	0.0925	0.3673	0.0877	0.0072	0.0705	0.003	0.0754	0.0139	0.0409	0.0021	0.021	bdl
EDML604-605-606	605	bdl	bdl	bdl	bdl	0.0088	bdl	bdl	bdl	bdl	bdl	bdl	bdl	bdl	bdl
EDML607	607	0.2319	bdl	0.0317	0.1289	0.0561	0.0132	0.0114	bdl	0.0218	0.0053	0.0144	bdl	0.0061	bdl
EDML608	608	0.4974	0.7894	0.0739	0.2508	0.0731	0.0122	0.0236	bdl	0.0373	0.0074	0.0208	bdl	0.0087	bdl
EDML609	609	0.4094	0.8852	0.0806	0.3723	0.1032	0.0184	0.0842	0.0069	0.0762	0.0166	0.0388	0.0046	0.0232	bdl
EDML610	610	0.8717	1.5758	0.167	0.6001	0.1651	0.0362	0.1054	0.0085	0.097	0.0196	0.0505	0.0084	0.033	bdl
EDML611	611	1.342	2.0497	0.2418	0.8123	0.2383	0.054	0.1693	0.0197	0.1539	0.0304	0.0846	0.0137	0.07	0.0066
EDML612	612	0.7433	1.3772	0.1595	0.6193	0.1805	0.0405	0.1435	0.0142	0.1316	0.0278	0.072	0.0104	0.0532	0.0047
EDML613	613	bdl	bdl	bdl	bdl	0.0362	0.0071	bdl	bdl	bdl	bdl	bdl	bdl	bdl	bdl
EDML614	614	1.2644	3	0.2927	1.0974	0.2305	0.0408	0.2034	0.0232	0.1854	0.0337	0.0861	0.0105	0.0519	bdl
EDML616	616	0.3037	bdl	0.0527	0.2528	0.0598	0.0056	0.0298	bdl	0.0439	0.0079	0.0196	bdl	0.0055	bdl
EDML617	617	0.339	0.7022	0.0594	0.2376	0.0644	0.0104	0.0392	bdl	0.0538	0.0112	0.0231	bdl	0.0117	bdl
EDML618	618	1.2634	2.4368	0.2476	0.8826	0.2085	0.0369	0.1634	0.0183	0.1632	0.0346	0.0901	0.0131	0.0696	0.0074
EDML619	619	0.9296	1.6668	0.1654	0.5911	0.1357	0.0245	0.103	0.0088	0.0949	0.0206	0.0509	0.0082	0.0378	bdl
EDML620	620	0.6253	1.2494	0.1236	0.4825	0.1012	0.0164	0.0624	bdl	0.0634	0.0117	0.0364	bdl	0.0199	bdl
EDML621	621	0.6533	1.017	0.1036	0.3579	0.0855	0.0163	0.0576	bdl	0.0526	0.0111	0.031	bdl	0.0205	bdl
EDML622	622	0.6474	1.2334	0.128	0.4751	0.119	0.0212	0.0865	0.0089	0.0826	0.0173	0.0402	0.0046	0.0259	bdl
EDML623-624	623.5	0.2007	0.2665	0.029	0.1188	bdl	bdl	0.0203	bdl	0.0302	0.0079	0.0216	0.0018	0.0139	bdl
EDML626-627	626.5	0.1573	bdl	0.0385	0.1542	0.0398	bdl	0.0214	bdl	0.0332	0.0074	0.0202	bdl	0.0131	bdl
EDML628	628	0.2426	0.3523	0.0332	0.1395	bdl	bdl	bdl	bdl	0.0147	0.0041	0.0109	0.0022	0.0029	bdl
EDML629	629	0.3934	0.7069	0.0789	0.2861	0.0725	bdl	0.0424	bdl	0.0573	0.0129	0.0298	0.0028	0.0206	bdl

sample	depth [m]	La	Ce	Pr	Nd	Sm	Eu	Gd	Tb	Dy	Ho	Er	Tm	Yb	Lu
EDML630	630	0.5807	1.2858	0.1468	0.525	0.1008	bdl	0.0376	bdl	0.0308	0.004	0.0093	bdl	bdl	bdl
EDML632	632	3.835	4.1059	0.6597	2.2278	0.4046	0.0994	0.4008	0.0545	0.4177	0.0916	0.2574	0.0364	0.2367	0.0269
EDML633	633	0.0392	0.1054	bdl	0.0385	bdl	bdl	bdl	bdl	bdl	bdl	bdl	bdl	bdl	bdl
EDML634	634	0.1007	0.3363	0.0151	0.0601	0.0107	bdl	bdl	bdl	0.015	0.0034	0.0037	bdl	bdl	bdl
EDML637	637	bdl	bdl	bdl	bdl	bdl	bdl	bdl	bdl	bdl	bdl	bdl	bdl	bdl	bdl
EDML638	638	4.7081	5.1896	0.7768	2.5861	0.5494	0.0907	0.5307	0.0665	0.4684	0.0986	0.2701	0.0367	0.2297	0.0269
EDML639	639	0.5306	1.2412	0.1242	0.4199	0.072	bdl	0.0506	bdl	0.0507	0.0099	0.0245	0.0025	0.0113	bdl
EDML640	640	0.3733	0.7721	0.0739	0.2711	0.0561	bdl	0.0388	bdl	0.0373	0.0067	0.0189	0.0026	0.0107	bdl
EDML641	641	0.1383	bdl	0.0224	0.1152	0.0238	bdl	bdl	bdl	0.0141	bdl	0.0051	bdl	bdl	bdl
EDML642	642	0.2041	0.443	0.038	0.1577	0.039	0.0042	0.0163	bdl	0.0272	0.0067	0.0151	0.0019	0.0046	bdl
EDML647	647	0.3491	0.3389	0.0351	0.1308	0.017	bdl	bdl	bdl	0.022	0.0042	0.0067	bdl	0.0131	bdl
EDML650	650	0.1535	0.4346	0.0328	0.1681	0.0479	bdl	0.0274	bdl	0.0492	0.0085	0.02	0.0037	0.0097	bdl
EDML651	651	0.2484	0.645	0.0739	0.3489	0.095	0.0131	0.0922	0.0082	0.1012	0.0203	0.0582	0.0081	0.0412	bdl
EDML653	653	3.0055	3.2832	0.4919	2.723	0.2793	0.0599	0.2634	0.0363	0.2994	0.0563	0.1608	0.0234	0.1339	0.0202
EDML654	654	0.2015	0.5121	0.0425	0.161	0.0196	0.0327	0.0204	bdl	0.0226	0.0037	0.0125	0.001	0.0061	bdl
EDML658	658	0.5434	1.202	0.1192	0.4055	0.0543	bdl	bdl	bdl	bdl	bdl	bdl	bdl	bdl	bdl
EDML659	659	0.3828	0.9182	0.0887	0.3741	0.084	0.0073	0.0509	0.0014	0.051	0.0109	0.0228	0.0035	0.0139	bdl
EDML660	660	0.1855	0.4047	0.048	0.2573	0.0624	bdl	0.0448	bdl	0.0415	0.0087	0.0211	0.0026	0.0076	bdl
EDML661	661	0.2479	0.509	0.0449	0.1986	0.0435	bdl	0.0133	bdl	0.0294	0.0047	0.0107	0.0012	0.0032	bdl
EDML662	662	0.3017	0.7111	0.0598	0.2935	0.0422	0.0051	0.0273	bdl	0.0294	0.0069	0.0192	bdl	0.0054	bdl
EDML663	663	0.4712	1.0653	0.107	0.4205	0.0877	0.0086	0.0623	bdl	0.0636	0.0129	0.0274	bdl	0.0142	bdl
EDML664	664	0.4614	0.8377	0.0871	0.2993	0.0499	bdl	0.033	bdl	0.0375	0.0072	0.0175	0.0018	0.0093	bdl
EDML666	666	0.0192	bdl	bdl	bdl	bdl	bdl	bdl	bdl	bdl	bdl	bdl	bdl	bdl	bdl
EDML667	667	bdl	bdl	bdl	bdl	bdl	bdl	bdl	bdl	bdl	bdl	bdl	bdl	bdl	bdl
EDML668	668	0.0885	0.2592	0.0191	0.1112	bdl	bdl	bdl	bdl	0.018	0.0049	0.0095	bdl	0.0056	bdl

sample	depth [m]	La	Ce	Pr	Nd	Sm	Eu	Gd	Tb	Dy	Ho	Er	Tm	Yb	Lu
EDML669	669	0.8179	0.8534	0.1193	0.4062	0.1048	0.0223	0.0573	bdl	0.0632	0.0138	0.0368	0.0062	0.025	bdl
EDML670	670	0.2357	0.6659	0.0571	0.239	0.0537	0.005	0.0207	bdl	0.0289	0.0061	0.0151	0.0014	0.0018	bdl
EDML671	671	0.0748	0.0612	0.0052	0.0318	bdl	bdl	bdl	bdl	bdl	bdl	bdl	bdl	bdl	bdl
EDML673	673	bdl	bdl	bdl	bdl	bdl	bdl	bdl	bdl	bdl	bdl	bdl	bdl	bdl	bdl
EDML674	674	0.1939	1.3121	0.0344	0.1613	0.0361	bdl	0.009	bdl	0.0231	0.0046	0.0109	0.0017	bdl	bdl
EDML676	676	bdl	bdl	bdl	bdl	bdl	bdl	bdl	bdl	bdl	bdl	bdl	bdl	bdl	bdl
EDML677	677	0.3391	0.7687	0.0684	0.2557	0.0635	0.0089	0.0452	bdl	0.0481	0.0091	0.0242	0.0026	0.011	bdl
EDML678	678	0.0405	0.1398	0.0087	0.0879	bdl	0.0239	bdl	bdl	0.0132	0.0025	0.0033	bdl	0.0037	bdl
EDML679	679	0.3235	0.6209	0.0569	0.2362	0.0478	bdl	0.0207	bdl	0.026	0.0062	0.0144	bdl	0.0117	bdl
EDML680	680	0.3188	0.9976	0.0195	0.0344	bdl	bdl	bdl	bdl	bdl	bdl	bdl	bdl	bdl	bdl
EDML681	681	1.1793	2.9181	0.1963	0.6478	0.2128	0.0445	0.117	0.0095	0.1103	0.0245	0.0627	0.0097	0.0492	0.003
EDML682	682	0.29	1.1996	0.0413	0.1897	0.0519	bdl	0.0205	bdl	0.0279	0.007	0.0163	0.0015	0.0062	bdl
EDML683	683	0.2017	0.5492	0.003	bdl	0.059	0.0179	bdl	bdl	bdl	bdl	bdl	bdl	bdl	bdl
EDML684	684	0.1314	0.2529	0.0148	0.0794	0.0205	bdl	bdl	bdl	0.0091	0.0018	0.0024	bdl	bdl	bdl
EDML686	686	0.3981	0.9878	0.04	0.1126	0.0818	0.029	0.007	bdl	0.0205	0.0071	0.0189	0.0037	0.0064	bdl
EDML687	687	1.8563	3.6427	0.3105	1.0038	0.2561	0.0683	0.2084	0.0246	0.2024	0.0449	0.1298	0.0186	0.11	0.0138
EDML688	688	1.4965	1.7038	0.2811	0.9925	0.2001	0.0412	0.173	0.02	0.1893	0.0393	0.1225	0.0168	0.1035	0.0105
EDML689	689	1.0415	0.8785	0.1242	0.3583	0.0528	0.032	0.0345	bdl	0.0484	0.0109	0.028	0.0036	0.0214	bdl
EDML691	691	5.5255	6.5955	1.0119	3.3662	0.7303	0.1625	0.6906	0.0955	0.6587	0.1464	0.4208	0.0606	0.3808	0.0558
EDML693	693	2.1744	6.0781	0.3595	1.1415	0.2839	0.0574	0.208	0.0238	0.1936	0.0407	0.1111	0.0182	0.0881	0.0083
EDML694	694	1.248	3.3864	0.2341	0.7612	0.1841	0.0463	0.093	0.0056	0.0805	0.0149	0.0387	0.0066	0.0213	bdl
EDML696	696	15.5203	31.7375	3.8122	13.013	2.9256	0.6165	2.6216	0.375	2.069	0.3992	1.0832	0.1638	0.889	0.1199
EDML699	699	0.3495	0.3398	0.0409	0.1528	0.0202	bdl	bdl	bdl	0.0141	0.0039	0.0086	bdl	0.0032	bdl
EDML703	703	0.1972	0.8252	0.0319	0.1347	0.0438	bdl	0.0123	bdl	0.0112	0.0039	0.0065	0.0011	0.0055	bdl
EDML704	704	0.2041	0.873	0.0338	0.1389	0.0391	bdl	0.0164	bdl	0.0242	0.0079	0.0149	0.0044	0.0089	bdl

sample	depth [m]	La	Ce	Pr	Nd	Sm	Eu	Gd	Tb	Dy	Ho	Er	Tm	Yb	Lu
EDML706	706	0.2676	0.7567	0.0334	0.1265	0.0357	bdl	0.0129	bdl	0.0166	0.004	0.007	0.001	bdl	bdl
EDML707	707	0.1205	0.2946	0.0208	0.1271	0.0233	bdl	bdl	bdl	0.0162	0.0031	0.0037	bdl	bdl	bdl
EDML710	710	0.5609	0.9401	0.1071	0.4275	0.0811	0.0063	0.0499	bdl	0.0675	0.014	0.0414	0.0044	0.0249	bdl
EDML711	711	bdl	bdl	bdl	bdl	bdl	0.0041	bdl	bdl	bdl	bdl	bdl	bdl	bdl	bdl
EDML712	712	bdl	bdl	bdl	bdl	bdl	bdl	bdl	bdl	bdl	bdl	bdl	bdl	bdl	bdl
EDML713	713	0.0687	0.0758	0.0021	0.0477	bdl	bdl	bdl	bdl	0.0045	bdl	0.0023	bdl	0.0025	bdl
EDML714	714	0.5618	0.7692	0.1024	0.3547	0.076	0.0696	0.0466	bdl	0.0518	0.0088	0.0251	0.0026	0.0169	bdl
EDML716	716	bdl	bdl	bdl	0.0525	bdl	bdl	bdl	bdl	bdl	bdl	bdl	bdl	bdl	bdl
EDML719	719	0.6222	1.131	0.1254	0.4642	0.0922	0.0108	0.0723	0.0046	0.0744	0.0154	0.0295	0.004	0.0232	bdl
EDML720-721	720.5	0.1781	0.4352	0.0362	0.1841	0.0349	bdl	0.0301	bdl	0.0366	0.0069	0.0168	0.001	0.0026	bdl
EDML723	723	0.1729	0.3821	0.0384	0.192	0.054	0.0027	0.0279	bdl	0.0308	0.0058	0.0152	bdl	0.0067	bdl
EDML724	724	0.5493	1.1082	0.1204	0.4505	0.0871	0.011	0.0757	0.0022	0.0816	0.0157	0.0373	0.0036	0.0253	bdl
EDML726	726	0.139	0.7134	0.025	0.1181	0.0198	bdl	0.0025	bdl	0.0233	0.0035	0.0107	bdl	0.0025	bdl
EDML727	727	3.2969	5.1921	0.6491	2.4204	0.5242	0.1026	0.448	0.0554	0.366	0.0797	0.2071	0.0312	0.1878	0.0229
EDML729	729	0.7537	1.6452	0.1905	0.6732	0.1458	0.0206	0.1128	0.0089	0.1129	0.0195	0.0498	0.0048	0.0366	bdl
EDML730	730	4.558	5.5386	0.7881	2.5253	0.5064	0.0974	0.4819	0.0601	0.4537	0.0977	0.2787	0.037	0.2379	0.0319
EDML731	731	14.6052	16.9387	2.8408	8.9244	1.8286	0.4674	1.8531	0.2631	1.7489	0.3737	1.1061	0.1577	0.9904	0.1357
EDML734	734	1.0623	2.36	0.2613	1.0222	0.2206	0.0346	0.2012	0.0233	0.1761	0.0336	0.0873	0.0111	0.0537	0.0024
EDML735	735	0.3883	0.8249	0.0841	0.3528	0.0818	0.0122	0.0572	bdl	0.061	0.0103	0.0282	0.0042	0.0195	bdl
EDML738	738	0.9204	1.7111	0.2083	0.7014	0.14	0.0266	0.1046	0.0128	0.1067	0.0224	0.0475	0.0098	0.0353	bdl
EDML739	739	1.1095	1.4855	0.2033	0.7436	0.1437	0.0292	0.1269	0.0178	0.1349	0.0272	0.078	0.0098	0.0628	0.0117
EDML740	740	1.6724	3.8335	0.4271	1.5969	0.3605	0.0724	0.3179	0.0423	0.2475	0.0497	0.1259	0.02	0.1001	0.0112
EDML742	742	1.9889	4.0196	0.4797	2.5389	0.3702	0.0732	0.3413	0.0426	0.2894	0.0488	0.1264	0.0177	0.0968	0.0096
EDML743	743	1.0413	2.2566	0.2467	0.9302	0.2013	0.0323	0.1641	0.0169	0.144	0.0257	0.0684	0.0098	0.0546	0.0036
EDML744	744	0.769	1.7383	0.1886	0.7576	0.152	0.0262	0.1271	0.0159	0.1253	0.0236	0.0606	0.0115	0.0483	0.0053

sample	depth [m]	La	Ce	Pr	Nd	Sm	Eu	Gd	Tb	Dy	Ho	Er	Tm	Yb	Lu
EDML747	747	0.686	1.0039	0.1209	0.417	0.0711	0.0168	0.0512	bdl	0.0539	0.0099	0.0222	0.0019	0.0188	bdl
EDML748	748	1.7938	2.5912	0.3433	1.2128	0.2455	0.06	0.2326	0.0299	0.2181	0.0452	0.1283	0.0173	0.1052	0.0161
EDML749	749	0.6851	1.4619	0.1779	0.7146	0.1565	0.0292	0.1242	0.0129	0.1139	0.0236	0.0541	0.0099	0.0396	0.0011
EDML750	750	1.3561	3.3554	0.3783	1.3837	0.321	0.06	0.2726	0.0353	0.2074	0.0404	0.0914	0.0115	0.0768	0.0062
EDML752	752	0.5454	0.9197	0.1264	0.4516	0.0711	bdl	0.0496	0.0022	0.0437	0.0102	0.0187	0.0036	0.0119	bdl
EDML753	753	0.7899	1.7341	0.1872	0.6588	0.1776	0.024	0.1094	0.0167	0.114	0.0238	0.0506	0.0088	0.0429	0.0058
EDML754	754	0.4912	1.1735	0.1191	0.4659	0.1009	bdl	0.0674	0.0036	0.0681	0.0123	0.0334	0.0064	0.0168	bdl
EDML756	756	0.6962	1.6095	0.1787	0.7044	0.1626	0.0176	0.1342	0.013	0.1155	0.0222	0.0605	0.0076	0.038	bdl
EDML757	757	1.0845	2.2167	0.251	0.9303	0.1827	0.0381	0.1516	0.0102	0.1295	0.027	0.0712	0.008	0.0388	bdl
EDML758	758	1.8085	3.0268	0.3719	1.3109	0.2754	0.0502	0.225	0.0284	0.1927	0.0368	0.0872	0.0111	0.0621	0.007
EDML759	759	1.7847	2.8806	0.3383	1.1628	0.2331	0.0485	0.1879	0.0187	0.1505	0.0291	0.0779	0.008	0.0577	bdl
EDML760	760	1.3508	3.0787	0.3587	1.4027	0.2907	0.0509	0.2515	0.0308	0.2109	0.0403	0.1024	0.0115	0.0742	0.007
EDML762	762	1.8483	3.5142	0.3881	1.2346	0.2357	0.0431	0.2131	0.0237	0.1869	0.0344	0.0959	0.0138	0.0769	0.0072
EDML763	763	2.61	3.5978	0.4484	1.2559	0.2363	0.0471	0.1752	0.0189	0.1463	0.0284	0.0798	0.0098	0.0487	bdl
EDML764	764	1.364	2.6373	0.3625	1.35	0.2831	0.1389	0.2439	0.0275	0.1935	0.0356	0.0846	0.011	0.0609	0.0034
EDML766	766	1.8553	2.0437	0.3125	1.0396	0.1958	0.0323	0.1682	0.019	0.1734	0.0381	0.1038	0.014	0.0937	0.0079
EDML768	768	0.8289	1.751	0.2224	0.9033	0.1968	0.0438	0.1702	0.0161	0.1398	0.0252	0.0621	0.0078	0.0469	bdl
EDML769	769	1.5415	3.4422	0.3867	1.502	0.3194	0.0495	0.2648	0.0301	0.2343	0.041	0.1043	0.0135	0.0825	0.0065
EDML770	770	0.3817	bdl	0.0803	0.324	0.0929	0.0166	0.0422	bdl	0.0535	0.0096	0.0294	bdl	0.0151	bdl
EDML771	771	0.3296	0.8005	0.0841	0.3751	0.1383	0.0301	0.0787	0.0036	0.0723	0.0126	0.0369	0.0045	0.0172	bdl
EDML772-773	772.5	17.9069	21.8248	3.5155	11.246	2.3855	0.6058	2.397	0.3533	2.3034	0.4807	1.4651	0.213	1.3522	0.1917
EDML774	774	1.148	2.6914	0.3187	1.2041	0.2632	0.0497	0.2495	0.0301	0.2018	0.0411	0.1027	0.0148	0.0751	0.0082
EDML776	776	0.87	2.0113	0.2436	0.9074	0.1864	0.0331	0.1671	0.0172	0.1481	0.0296	0.076	0.0108	0.0482	0.0034
EDML777	777	0.692	1.4825	0.1687	0.6392	0.1274	0.0188	0.1044	0.0075	0.1003	0.0205	0.0534	0.009	0.0411	bdl
EDML778	778	1.0255	1.9224	0.2381	0.8726	0.1739	0.0255	0.88	0.0154	0.13	0.024	0.0675	0.0134	0.1533	0.0035

sample	depth [m]	La	Ce	Pr	Nd	Sm	Eu	Gd	Tb	Dy	Ho	Er	Tm	Yb	Lu
EDML781	781	1.3154	1.9184	0.2721	1.0069	0.2042	0.038	0.1837	0.0208	0.1664	0.0346	0.0958	0.0132	0.0743	0.0077
EDML782	782	0.5076	1.2224	0.1176	0.4398	0.0761	bdl	0.0564	bdl	0.0589	0.0125	0.0304	0.0051	0.0222	bdl
EDML783	783	0.601	0.9116	0.1122	0.3509	0.0607	bdl	0.0458	bdl	0.0565	0.0134	0.0268	0.0038	0.0158	bdl
EDML786	786	9.074	16.34	2.192	7.4206	1.8091	0.3718	1.453	0.214	1.2831	0.2671	0.772	0.1076	0.6989	0.1088
EDML787	787	1.525	3.2066	0.3385	1.1	0.2189	0.0376	0.1551	0.0151	0.1351	0.0247	0.0732	0.0102	0.0514	bdl
EDML788	788	2.8728	2.7654	0.4411	1.3147	0.2597	0.0562	0.2254	0.0289	0.2369	0.0515	0.1551	0.0208	0.138	0.0122
EDML789	789	0.8457	0.9349	0.141	0.4671	0.0941	0.0196	0.1105	0.0131	0.134	0.0307	0.0874	0.0124	0.0662	0.0062
EDML792	792	0.7637	1.8332	0.2076	0.7916	0.1831	0.0311	0.148	0.0118	0.136	0.0256	0.073	0.0104	0.0522	0.0031
EDML793	793	1.1748	2.4407	0.2795	1.0441	0.2544	0.036	0.2044	0.0203	0.1543	0.0274	0.067	0.0074	0.0471	0.0045
EDML796	796	1.4379	2.6448	0.3397	1.196	0.2396	0.0364	0.2099	0.0226	0.1824	0.0349	0.0902	0.0106	0.0678	0.0041
EDML797	797	0.8443	2.0314	0.219	0.8352	0.1815	0.0286	0.1521	0.0173	0.1376	0.0274	0.0709	0.0082	0.0487	0.0016
EDML798	798	0.4862	1.0669	0.1238	0.5363	0.1021	0.0186	0.0973	0.0058	0.0859	0.0188	0.0459	0.0058	0.0329	bdl
EDML799	799	0.9058	1.8634	0.2012	0.752	0.1496	0.0238	0.1377	0.0135	0.1302	0.0247	0.0662	0.0114	0.0517	0.0018
EDML800	800	1.4213	3.4582	0.4166	1.5819	0.3734	0.0731	0.3695	0.0493	0.3163	0.0635	0.1697	0.0213	0.1346	0.0141
EDML801	801	2.1615	3.7892	0.414	1.2929	0.254	0.0582	0.2369	0.0308	0.2412	0.0469	0.1367	0.0213	0.1181	0.0119
EDML802	802	0.6873	1.5329	0.1688	0.6656	0.1438	0.026	0.1301	0.0126	0.1188	0.026	0.0689	0.0111	0.0493	0.0025
EDML803	803	0.9811	2.1214	0.24	0.9272	0.2083	0.093	0.174	0.0197	0.1617	0.0307	0.0831	0.0108	0.0601	0.0037
EDML804	804	3.5661	8.2718	0.9882	3.8284	0.9428	0.1844	0.8912	0.1261	0.7685	0.1499	0.4152	0.0556	0.3315	0.0476
EDML806	806	1.2547	2.9352	0.3427	1.3657	0.2897	0.0543	0.2866	0.0324	0.2418	0.0473	0.1238	0.0195	0.102	0.0089
EDML807-808	807.5	1.6079	3.6161	0.4207	1.5125	0.3586	0.0587	0.2954	0.0397	0.2559	0.05	0.1336	0.0162	0.0947	0.0135
EDML809	809	3.7504	10.2624	1.5454	7.1427	2.4475	0.7405	3.2758	0.525	3.3786	0.739	2.0771	0.2995	1.8662	0.2759
EDML810	810	2.4356	4.6528	0.5663	1.9516	0.4386	0.0995	0.4367	0.0609	0.3978	0.0804	0.238	0.0367	0.2091	0.0233
EDML811	811	0.8341	2.4035	0.1956	0.7414	0.1563	0.0302	0.1315	0.0122	0.1142	0.0228	0.0604	0.009	0.0525	bdl
EDML813	813	1.4934	3.4099	0.3697	1.3902	0.3183	0.0552	0.2657	0.0329	0.2209	0.0399	0.1031	0.0105	0.0705	0.0079
EDML814	814	2.2566	5.0602	0.578	2.1522	0.5236	0.0969	0.4434	0.0621	0.3673	0.0695	0.1878	0.0224	0.1511	0.0183

sample	depth [m]	La	Ce	Pr	Nd	Sm	Eu	Gd	Tb	Dy	Ho	Er	Tm	Yb	Lu
EDML818	818	1.1839	2.7466	0.315	1.212	0.2682	0.0586	0.2155	0.0237	0.1847	0.0349	0.0904	0.0142	0.072	0.0035
EDML821	821	1.2822	3.1331	0.3092	1.1811	0.2513	0.0442	0.193	0.0235	0.1716	0.0324	0.0801	0.0097	0.0647	0.005
EDML822	822	0.6479	1.4452	0.1576	0.625	0.1379	0.0445	0.1054	0.0087	0.1058	0.0211	0.0489	0.0081	0.0415	bdl
EDML824	824	5.7968	9.2964	1.2056	4.282	0.949	0.2089	0.8746	0.1229	0.8015	0.1709	0.4775	0.0657	0.4149	0.0571
EDML826	826	2.4646	6.0638	0.5271	1.8307	0.3865	0.0754	0.3514	0.0434	0.3192	0.0627	0.1657	0.0221	0.1441	0.0155
EDML829	829	3.0575	6.7453	0.7629	2.7671	0.6349	0.1177	0.5497	0.0787	0.4667	0.0908	0.2592	0.0297	0.1947	0.0275
EDML830	830	5.6208	13.5363	1.5783	6.0031	1.3994	0.2929	1.2473	0.1784	1.0485	0.1938	0.5097	0.0796	0.4346	0.0543
EDML831	831	4.5263	10.7205	1.291	4.5641	1.1009	0.2165	0.9963	0.1377	0.8438	0.1599	0.4201	0.0601	0.3513	0.045
EDML832	832	2.6751	4.7941	0.5639	1.9307	0.4294	0.0847	0.3633	0.0464	0.3209	0.062	0.1705	0.0223	0.1443	0.016
EDML833	833	4.3815	9.3928	1.0683	3.8983	0.9604	0.1848	0.8243	0.1096	0.6568	0.1276	0.3483	0.0463	0.2608	0.0339
EDML837	837	7.8204	17.8425	2.0057	7.4896	1.7912	0.3496	1.59	0.2318	1.3368	0.2508	0.6841	0.0914	0.5548	0.0767
EDML841	841	5.7117	12.8713	1.4534	5.402	1.324	0.2566	1.1651	0.167	0.9137	0.1793	0.4566	0.0617	0.3701	0.0513
EDML846	846	6.7985	14.9415	1.6901	6.2488	1.461	0.2948	1.3854	0.1951	1.162	0.2286	0.614	0.0816	0.4978	0.0669
EDML847	847	3.8285	8.1257	0.9782	3.5778	0.8463	0.1599	0.7878	0.108	0.6374	0.1231	0.3326	0.0462	0.2654	0.034
EDML848	848	4.9914	11.2453	1.3558	4.9472	1.145	0.2314	1.0698	0.1531	0.9105	0.1817	0.4749	0.068	0.3996	0.0489
EDML849	849	5.9489	12.7299	1.4405	5.4106	1.2495	0.2453	1.1561	0.166	0.9713	0.193	0.5215	0.0687	0.4251	0.0593
EDML853	853	10.8121	24.5685	2.9344	10.9594	2.5791	0.5178	2.3617	0.3352	1.9349	0.3631	0.954	0.1241	0.8113	0.1039
EDML854	854	19.3864	25.6194	3.6086	10.7793	2.3199	0.468	2.0866	0.2849	1.6881	0.3173	0.8265	0.1121	0.6923	0.0918
EDML856	856	13.2012	23.3747	2.8425	9.5164	2.2201	0.4404	1.9304	0.2853	1.608	0.3041	0.7973	0.1055	0.7031	0.0921
EDML859	859	21.0101	38.0808	4.5774	16.0717	3.7304	0.7516	3.2931	0.4737	2.6688	0.4936	1.3496	0.1774	1.1145	0.1541
EDML862	862	26.118	53.676	6.7751	24.0416	5.6531	1.1797	5.0826	0.7369	4.3099	0.7909	2.085	0.278	1.7844	0.2437
EDML863	863	3.1818	6.4891	0.7389	2.702	0.6413	0.1236	0.5454	0.0767	0.4657	0.0862	0.2332	0.0298	0.1955	0.0267
EDML866	866	11.0335	21.8357	2.7672	9.8268	2.2671	0.461	2.0488	0.2979	1.7079	0.3273	0.8257	0.1116	0.7282	0.0913
EDML867	867	17.2696	34.5528	4.1175	14.4668	3.4322	0.6859	3.0448	0.4315	2.4179	0.4615	1.2081	0.1627	1.0098	0.137
EDML870	870	3.8925	8.4532	1.0276	3.7167	0.8254	0.1778	0.8145	0.1099	0.6692	0.1261	0.3448	0.0442	0.2787	0.0318

sample	depth [m]	La	Ce	Pr	Nd	Sm	Eu	Gd	Tb	Dy	Ho	Er	Tm	Yb	Lu
EDML872	872	12.5424	25.4853	3.037	11.044	2.6293	0.5145	2.3401	0.3281	1.8581	0.35	0.9145	0.1259	0.7692	0.1045
EDML873	873	6.0139	13.149	1.4289	5.1454	1.2009	0.2367	1.07	0.1519	0.8916	0.1714	0.4554	0.0677	0.3777	0.0498
EDML874	874	17.7185	33.7674	3.9018	12.9518	2.9241	0.605	2.7075	0.3887	2.2193	0.4291	1.1326	0.1842	0.9325	0.1314
EDML876	876	27.1834	59.4804	7.1733	27.6468	7.2375	1.2683	6.8843	1.0407	5.9379	1.1263	2.9978	0.4018	2.5062	0.3336
EDML878	878	37.8117	83.1797	10.1751	36.8641	8.8298	1.798	7.7017	1.1297	6.2345	1.1851	3.0935	0.4129	2.5984	0.3624
EDML879	879	10.4988	23.261	2.7187	9.8579	2.3091	0.4662	2.12	0.3065	1.7345	0.3252	0.8917	0.1408	0.7363	0.098
EDML880	880	2.663	5.8878	0.6762	2.5704	0.6104	0.1241	0.5826	0.0757	0.4786	0.0913	0.2344	0.0371	0.1938	0.0228
EDML882	882	28.1916	62.2603	7.7741	28.6419	6.8283	1.4526	6.1332	0.9088	5.0964	0.9629	2.5279	0.3491	2.1251	0.2982
EDML883	883	20.0832	43.792	5.3118	19.4872	4.5934	0.9434	4.0969	0.5882	3.3158	0.6214	1.6438	0.221	1.3623	0.187
EDML884	884	27.5267	63.4142	7.4761	27.3417	6.4147	1.3146	5.8841	0.8508	4.7539	0.8875	2.3621	0.3672	1.9412	0.272
EDML886	886	21.1921	49.2803	5.919	21.876	5.2226	1.0818	4.8323	0.7179	3.9827	0.7582	2.0073	0.3091	1.6845	0.2326
EDML887	887	11.8038	25.6132	3.1148	11.5377	2.835	0.604	2.5736	0.3807	2.2038	0.4112	1.0936	0.1508	0.9152	0.1233
EDML888	888	19.8061	45.229	5.6	20.7057	4.9852	1.0404	4.4005	0.6356	3.6226	0.6815	1.7455	0.2351	1.4715	0.2029
EDML889	889	65.1431	149.184	17.6439	66.2306	15.5838	3.213	13.5251	1.9761	10.8957	2.0434	5.4314	0.7264	4.5944	0.6287
EDML890	890	14.8558	33.5581	4.385	16.2382	3.8314	0.843	3.6117	0.5314	2.9752	0.5641	1.5171	0.2173	1.3009	0.1771
EDML893	893	12.7072	29.4945	3.5485	12.7709	3.1078	0.6192	2.7388	0.3919	2.2177	0.4224	1.1257	0.1474	0.9716	0.1297
EDML896	896	26.5988	58.6113	6.9815	25.3658	6.0104	1.1866	5.2605	0.7513	4.1428	0.7722	2.0526	0.2715	1.6731	0.2426
EDML897	897	25.4526	57.7759	6.9806	24.3638	5.4238	1.138	4.7702	0.683	3.7385	0.6981	1.896	0.295	1.6155	0.2077
EDML898	898	22.5296	52.496	6.1553	22.5105	4.9973	1.0343	4.3976	0.6341	3.5746	0.6765	1.7812	0.2866	1.5161	0.194
EDML901	901	33.7903	75.8891	9.6376	34.8845	8.2654	1.6404	7.3536	1.0914	5.9432	1.0997	2.979	0.3928	2.4716	0.3436
EDML902	902	14.9	33.2638	4.0621	14.8111	3.2717	0.6695	3.0662	0.4294	2.3549	0.4462	1.1997	0.1876	1.0134	0.1266
EDML903	903	12.2949	28.2564	3.5092	13.3012	3.2031	0.7074	3.383	0.4958	2.8966	0.5652	1.533	0.2347	1.3094	0.1699
EDML904	904	21.5264	51.0771	6.1304	22.1817	5.0459	1.0655	4.6793	0.6688	3.6879	0.6983	1.8138	0.2449	1.5488	0.2048
EDML906	906	12.6121	29.7194	3.4015	12.6974	2.7722	0.5734	2.5286	0.358	2.0388	0.3878	1.0124	0.1644	0.8708	0.1101
EDML907	907	12.551	28.8913	3.4308	12.4775	2.7426	0.5588	2.5102	0.3516	1.9786	0.3765	1.0201	0.1596	0.8811	0.1088

sample	depth [m]	La	Ce	Pr	Nd	Sm	Eu	Gd	Tb	Dy	Ho	Er	Tm	Yb	Lu
EDML908	908	41.4045	93.3617	11.0328	40.4588	9.7788	2.1007	8.4502	1.2175	6.7776	1.2552	3.3273	0.4453	2.8374	0.3881
EDML909	909	19.4281	46.0107	5.548	19.6327	4.5311	0.9303	4.1022	0.5744	3.1886	0.5954	1.6382	0.2094	1.3435	0.1746
EDML910	910	21.159	47.0017	5.8279	21.277	5.0317	1.0475	4.5062	0.648	3.6513	0.6966	1.8174	0.2449	1.511	0.2011
EDML911	911	46.3362	102.6809	12.7931	45.7449	11.0002	2.1768	9.3973	1.3481	7.3839	1.3766	3.6257	0.4907	3.0343	0.4179
EDML912	912	12.3125	27.5197	3.2589	12.1211	2.7367	0.574	2.4076	0.3448	1.9344	0.3554	0.9437	0.1501	0.8202	0.1068
EDML913	913	11.5255	26.0701	3.1386	11.5119	2.5455	0.5359	2.327	0.3451	1.9181	0.3664	0.9567	0.16	0.8214	0.1142
EDML914	914	12.7643	27.3419	3.4807	12.6946	3.0629	0.6293	2.8303	0.4014	2.3406	0.4314	1.1559	0.1521	0.9352	0.1262
EDML916	916	19.7274	46.8962	5.6806	20.2237	4.6386	0.9615	4.2138	0.605	3.3062	0.6213	1.6699	0.2202	1.3941	0.1869
EDML917	917	31.5316	68.4139	8.4269	30.6836	7.3149	1.4816	6.5557	0.9462	5.2294	0.9912	2.6643	0.3455	2.2244	0.304
EDML919	919	17.0795	38.6426	4.5252	16.8359	3.8943	0.7942	3.5347	0.5171	2.8326	0.5269	1.4111	0.2209	1.1942	0.1603
EDML920	920	30.5694	71.5652	8.3854	30.3677	7.0129	1.4374	6.2186	0.8975	4.8649	0.9141	2.4244	0.3374	2.011	0.2735
EDML921	921	21.2275	47.1353	5.8498	21.2458	4.9449	1.0184	4.4406	0.63	3.4036	0.6478	1.731	0.2416	1.433	0.1943
EDML922	922	33.6	78.5481	9.2248	33.0224	7.5023	1.612	6.821	0.975	5.331	1.0008	2.6668	0.3602	2.142	0.301
EDML923	923	71.0886	164.5641	19.6148	70.5037	16.1046	3.3552	13.7601	1.9823	10.6358	1.9882	5.2455	0.7402	4.3908	0.6144
EDML924	924	44.002	99.0319	11.704	42.9568	10.3907	2.1112	9.0202	1.3219	7.275	1.3549	3.577	0.4756	3.036	0.4151
EDML926	926	29.4963	62.73	7.9	28.5573	6.6176	1.3633	5.9278	0.8643	4.646	0.8951	2.3553	0.3764	1.9453	0.2741
EDML927	927	11.4253	25.7457	3.1958	12.1616	3.0627	0.6492	3.1572	0.4719	2.7134	0.5179	1.4128	0.2109	1.1756	0.1561
EDML928	928	60.3653	136.7724	16.3458	60.4391	14.58	2.9295	12.636	1.8103	9.9742	1.8731	4.9428	0.6621	4.1798	0.5762
EDML931	931	35.624	81.3572	9.6718	35.3304	8.2465	1.6668	7.4126	1.052	5.7972	1.0908	2.9162	0.4567	2.4325	0.3374
EDML932	932	74.5161	166.0224	20.1634	73.2976	17.6569	3.5675	15.3238	2.2079	12.0661	2.2553	5.9561	0.7897	4.9885	0.6933
EDML933	933	16.9446	36.7069	4.4505	16.4728	4.0508	0.8083	3.5945	0.5258	2.9608	0.5631	1.4846	0.1933	1.243	0.171
EDML934	934	31.1405	71.4757	8.2073	28.9713	6.8216	1.4567	5.9104	0.8364	4.4162	0.7978	2.1874	0.3213	1.8698	0.2618
EDML937	937	63.291	151.351	17.7682	62.9492	14.6442	3.1499	12.5678	1.8467	9.6427	1.8194	4.8387	0.6714	3.9678	0.5646
EDML939	939	5.9062	11.4816	1.375	4.8813	1.1096	0.2543	1.005	0.1443	0.8337	0.1645	0.4332	0.0637	0.3496	0.049
EDML942	942	85.2073	137.1363	17.1446	36.8453	6.7516	1.327	5.5935	0.8075	4.4374	0.842	2.1972	0.299	1.8178	0.2571

sample	depth [m]	La	Ce	Pr	Nd	Sm	Eu	Gd	Tb	Dy	Ho	Er	Tm	Yb	Lu
EDML944	944	32.9766	51.538	6.6286	18.9484	3.8145	0.864	3.4212	0.5148	3.0209	0.6012	1.6595	0.229	1.4633	0.2013
EDML946	946	27.1865	55.1286	6.6234	21.3199	4.7211	0.968	4.2547	0.6208	3.4054	0.6493	1.7534	0.2685	1.4192	0.197
EDML947	947	12.7975	26.376	3.1591	10.3826	2.3535	0.483	2.1895	0.3189	1.8326	0.3368	0.933	0.1475	0.7378	0.1012
EDML9X8	948	20.3553	41.0725	4.8996	15.8948	3.6585	0.7617	3.2545	0.4684	2.5807	0.4939	1.2924	0.1703	1.0844	0.1462
EDML951	951	25.5264	50.9537	6.3846	21.3187	4.8761	1.0673	4.6467	0.6771	3.865	0.7595	2.138	0.3487	1.8484	0.2622
EDML952	952	12.0263	24.6006	2.9348	9.93	2.3244	0.4761	2.1749	0.312	1.8023	0.3444	0.894	0.1434	0.7447	0.1014
EDML953	953	6.2299	12.7058	1.5212	5.264	1.2199	0.2477	1.121	0.1595	0.9012	0.1754	0.4635	0.0736	0.3727	0.0491
EDML954	954	49.8844	101.4985	13.4577	44.4879	10.0188	2.0945	9.0513	1.2945	7.0482	1.356	3.5801	0.4751	2.8934	0.3958
EDML956	956	73.0707	111.8845	15.7783	49.8556	11.2103	2.8479	10.4566	1.604	9.9055	2.1116	6.1247	0.8617	5.5344	0.828
EDML959	959	5.0824	9.5446	1.1996	4.0296	0.9757	0.2155	1.0068	0.1428	0.9056	0.1758	0.4642	0.0626	0.375	0.0525
EDML960	960	43.8245	98.3801	12.0654	41.4476	9.3675	1.953	8.318	1.1932	6.3584	1.2031	3.2915	0.4102	2.626	0.3574
EDML962	962	20.9	44.4819	5.3118	18.6817	4.5654	0.9485	4.1121	0.6152	3.4295	0.6623	1.7521	0.2344	1.4651	0.203
EDML964	964	24.1209	54.7132	6.4751	23.4155	5.1362	1.1115	4.633	0.6775	3.8064	0.7076	1.9306	0.2982	1.6566	0.2054
EDML965	965	43.4426	93.5646	12.0554	42.5619	9.9485	2.0735	8.9286	1.3133	7.2915	1.3643	3.6731	0.4845	3.0294	0.4189
EDML967	967	17.472	39.6641	4.8549	16.7854	3.8106	0.8181	3.5602	0.5135	2.8441	0.5344	1.4421	0.1918	1.1725	0.1569
EDML968	968	15.6959	33.8182	3.9458	13.4428	3.1817	0.6514	2.7224	0.3891	2.1252	0.4108	1.0636	0.1621	0.8977	0.1214
EDML969	969	44.9191	98.9718	12.1731	41.9018	9.5206	2.033	8.3691	1.2086	6.6548	1.2602	3.3451	0.4714	2.8283	0.3834
EDML970	970	15.3239	32.9913	4.1413	14.8246	3.5872	0.6833	3.4108	0.5032	2.8679	0.5464	1.4667	0.1909	1.1971	0.1551
EDML971	971	7.3967	15.6686	1.9217	6.7575	1.5894	0.3403	1.418	0.2067	1.1895	0.2247	0.5956	0.0952	0.522	0.0665
EDML972	972	51.3178	111.2046	14.5207	52.3158	12.1128	2.572	10.834	1.618	9.0385	1.7043	4.4802	0.5925	3.7705	0.5039
EDML973	973	5.6501	12.1763	1.5331	5.3121	1.2506	0.2778	1.2799	0.1829	1.114	0.2104	0.5667	0.0744	0.4572	0.0654
EDML974	974	37.6892	82.262	10.7233	37.8736	8.969	1.8827	8.0212	1.1747	6.606	1.2389	3.247	0.4369	2.7003	0.3793
EDML976	976	20.6391	44.2965	5.7804	20.8696	4.9273	1.0723	4.5609	0.6818	3.8641	0.7493	1.8909	0.2578	1.637	0.2186
EDML977	977	9.5848	21.6627	2.7154	9.6588	2.2367	0.4875	2.1588	0.3113	1.7912	0.3489	0.9208	0.1178	0.7389	0.0968
EDML979	979	53.7042	125.6441	14.9658	52.2863	12.2179	2.6006	10.9257	1.5401	8.4003	1.6119	4.247	0.565	3.4774	0.4891

sample	depth [m]	La	Ce	Pr	Nd	Sm	Eu	Gd	Tb	Dy	Ho	Er	Tm	Yb	Lu
EDML980	980	51.9878	114.4234	15.7562	54.2515	12.8007	2.6284	11.495	1.6904	9.2884	1.7854	4.6711	0.6223	3.8381	0.5234
EDML983	983	18.7013	39.8668	4.8557	17.6538	4.4368	0.8753	4.1742	0.6106	3.506	0.6763	1.8032	0.2395	1.4947	0.2052
EDML984	984	17.705	38.8549	4.7592	17.2832	3.9923	0.8176	3.6551	0.5206	2.9396	0.5526	1.4525	0.2277	1.234	0.1669
EDML986	986	41.6407	93.4313	11.4071	41.0725	9.6866	2.0092	8.783	1.2783	7.0805	1.3388	3.5387	0.5534	2.944	0.4066
EDML987	987	20.0285	43.0076	5.3254	19.099	4.5418	0.9261	4.053	0.5947	3.3524	0.6266	1.6677	0.2239	1.4032	0.1866
EDML989	989	43.6645	98.369	12.4724	44.6784	10.5893	2.2303	9.3813	1.3473	7.427	1.4217	3.6857	0.4891	3.1011	0.4276
EDML991	991	7.101	16.7634	2.0626	7.5356	1.7041	0.3631	1.7013	0.2449	1.4358	0.2765	0.7354	0.0965	0.595	0.0803
EDML992	992	2.5635	6.1693	0.6696	2.4885	0.589	0.117	0.5018	0.0646	0.4161	0.0746	0.2071	0.0315	0.1711	0.0178
EDML993	993	7.5121	17.0122	2.1447	7.7502	1.9061	0.4053	1.7556	0.25	1.4624	0.2808	0.7546	0.1008	0.6201	0.0846
EDML994	994	4.8641	10.6731	1.3217	4.7712	1.1178	0.2567	1.1919	0.1735	1.0375	0.1993	0.5417	0.0707	0.4555	0.0574
EDML997	997	14.7618	34.1141	4.35	15.5618	3.7434	0.718	3.6497	0.5164	2.9089	0.5505	1.4857	0.1956	1.2259	0.1581
EDML1004	1004	37.4833	83.0839	9.8081	34.8171	8.1088	1.668	7.1676	1.0401	5.6015	1.0541	2.7695	0.4366	2.3171	0.3433
EDML1007	1007	11.1303	25.3737	3.155	10.9371	2.5087	0.5103	2.355	0.3299	1.8871	0.3585	0.9675	0.1312	0.795	0.1066
EDML1009	1009	5.2197	11.8459	1.4472	5.1127	1.1649	0.2519	1.1765	0.1667	0.9586	0.1857	0.5008	0.0662	0.4058	0.0507
EDML1012	1012	2.5191	5.6562	0.695	2.4243	0.5542	0.117	0.5744	0.0792	0.4942	0.0972	0.2662	0.0346	0.2144	0.0261
EDML1013	1013	58.4368	137.046	16.364	57.4968	13.0531	2.6577	11.4556	1.6233	8.894	1.673	4.4354	0.6	3.725	0.5071
EDML1014	1014	8.1689	18.3905	2.1693	7.8054	1.9049	0.3996	1.6167	0.2413	1.2865	0.2456	0.638	0.103	0.5246	0.0736
EDML1016	1016	10.3527	22.6917	2.889	10.9673	2.363	0.5064	2.23	0.3183	1.8464	0.3458	0.9341	0.1206	0.7497	0.1004
EDML1019	1019	2.6349	5.7942	0.6778	2.4616	0.6755	0.1513	0.5549	0.0758	0.4559	0.0897	0.2394	0.0376	0.19	0.0234
EDML1020	1020	3.363	7.503	0.9406	3.3391	0.769	0.1696	0.8066	0.1102	0.6757	0.1315	0.3637	0.0452	0.2899	0.0334
EDML1021	1021	15.8238	35.2582	4.2699	15.5823	3.7205	0.7417	3.2405	0.4752	2.7181	0.4888	1.3496	0.1791	1.1238	0.1537
EDML1022	1022	5.7745	13.1033	1.5866	5.7507	1.3167	0.2789	1.3053	0.1839	1.0383	0.1988	0.5374	0.0704	0.4464	0.0549
EDML1024	1024	27.4021	58.5423	7.6847	27.6129	6.4206	1.3421	5.8063	0.8383	4.7273	0.8726	2.3391	0.3034	1.9274	0.2614
EDML1027	1027	5.2965	9.897	1.2189	4.0904	0.9908	0.228	0.9335	0.1321	0.8142	0.1623	0.4232	0.0684	0.3506	0.0517
EDML1030	1030	10.7743	23.3873	2.975	10.9123	2.593	0.535	2.3754	0.341	2.0168	0.3704	1.024	0.138	0.8427	0.113

sample	depth [m]	La	Ce	Pr	Nd	Sm	Eu	Gd	Tb	Dy	Ho	Er	Tm	Yb	Lu
EDML1031	1031	6.4423	13.6304	1.7293	6.3018	1.5004	0.3139	1.4134	0.1986	1.1791	0.2302	0.6173	0.0784	0.5156	0.0668
EDML1033	1033	1.3798	3.1582	0.3715	1.3925	0.322	0.0663	0.3353	0.0416	0.2968	0.0568	0.1527	0.0205	0.1268	0.0138
EDML1036	1036	33.3907	74.1202	9.4708	33.9027	8.0456	1.6625	7.2607	1.062	5.8254	1.1216	3.0382	0.3871	2.4645	0.3451
EDML1038	1038	3.4886	7.2976	0.9138	3.2634	0.7159	0.1572	0.7442	0.1003	0.6493	0.1341	0.3599	0.0486	0.3082	0.0385
EDML1039	1039	34.1156	73.7848	9.6768	34.1607	8.1528	1.6947	7.2222	1.0371	5.9045	1.0962	2.8808	0.3865	2.4775	0.3328
EDML1040	1040	5.464	12.7078	1.5499	5.6699	1.3087	0.2706	1.2383	0.1806	1.0336	0.1961	0.5206	0.0687	0.419	0.0547
EDML1041	1041	14.6432	30.4588	3.7012	12.86	3.009	0.6506	2.7341	0.4002	2.3021	0.4472	1.2435	0.1632	0.9911	0.1397
EDML1042	1042	8.1545	17.0242	2.1187	7.7329	1.7376	0.3677	1.6547	0.2337	1.3163	0.2524	0.6834	0.0916	0.5594	0.0684
EDML1043	1043	32.307	36.4972	0.7138	1.8109	0.3087	0.0712	0.2775	0.0372	0.2601	0.0551	0.1555	0.0254	0.1388	0.017
EDML1044	1044	7.0183	15.6408	1.8452	6.6197	1.6113	0.3492	1.4953	0.2093	1.2311	0.2316	0.6176	0.0891	0.4968	0.0681
EDML1046	1046	18.4924	42.2542	5.1121	18.1989	4.2584	0.907	3.8933	0.5628	3.0694	0.5938	1.5835	0.2121	1.3169	0.1849
EDML1047	1047	12.8661	25.4361	3.2356	11.6389	2.5999	0.6038	2.4656	0.3533	2.1412	0.43	1.1531	0.1642	1.0319	0.1381
EDML1048	1048	20.7535	47.6563	5.776	20.9434	4.8543	1.0204	4.3792	0.623	3.4375	0.6601	1.735	0.2318	1.3894	0.1943
EDML1049	1049	23.3529	53.1146	6.6625	23.5488	5.5809	1.1914	5.1536	0.727	4.0171	0.7379	2.0028	0.2705	1.7096	0.2198
EDML1050	1050	12.7328	27.1124	3.4031	12.195	2.8871	0.6108	2.7251	0.3943	2.2461	0.4321	1.1246	0.1523	0.9288	0.1305
EDML1051	1051	15.6058	35.0447	4.2844	15.3325	3.574	0.7931	3.2205	0.4598	2.5208	0.481	1.2654	0.1721	1.0543	0.1423
EDML1052	1052	37.5401	82.1608	10.8189	39.0419	9.1285	1.8937	8.4271	1.2333	6.7255	1.2722	3.3156	0.445	2.7675	0.3867
EDML1053	1053	7.4352	15.8916	1.9479	7.1671	1.6764	0.3577	1.5993	0.235	1.3655	0.2596	0.7016	0.0912	0.6011	0.0777
EDML1054	1054	26.1715	60.8603	7.2878	26.3065	6.0538	1.302	5.4904	0.7857	4.2286	0.8084	2.1726	0.2939	1.8279	0.2503
EDML1056	1056	11.8315	25.8319	3.2499	12.0122	2.8673	0.6046	2.6647	0.3742	2.2106	0.4043	1.089	0.1474	0.8968	0.1167
EDML1057	1057	6.374	14.8139	1.8172	6.5906	1.5457	0.328	1.4881	0.2098	1.2111	0.2312	0.6147	0.0823	0.5134	0.0648
EDML1059	1059	9.5978	23.1496	2.722	9.8239	2.2911	0.4639	2.1515	0.2984	1.6824	0.3173	0.8533	0.1129	0.7134	0.0924
EDML1061	1061	40.3454	98.7149	11.0717	38.1604	9.4653	1.9292	7.8908	1.118	5.9534	1.1092	2.7907	0.4566	2.4803	0.3576
EDML1062	1062	11.8205	25.122	3.0134	10.3992	2.334	0.502	2.0082	0.294	1.6183	0.3207	0.849	0.1162	0.7091	0.0933
EDML1063	1063	35.7217	85.6836	9.8074	34.5036	8.1267	1.6792	6.8549	0.9945	5.2678	0.984	2.5899	0.4113	2.2496	0.3208

sample	depth [m]	La	Ce	Pr	Nd	Sm	Eu	Gd	Tb	Dy	Ho	Er	Tm	Yb	Lu
EDML1064	1064	45.3679	115.2298	12.8403	44.2453	10.4659	2.2637	8.8147	1.2789	6.7795	1.3054	3.2387	0.5045	2.7451	0.3995
EDML1066	1066	58.2139	132.4508	16.095	58.6075	13.5044	2.7648	11.5389	1.6902	9.2935	1.7151	4.6043	0.6282	3.9687	0.5345
EDML1067	1067	25.8234	57.4226	7.2245	25.6712	6.0939	1.2607	5.3817	0.7829	4.3703	0.805	2.1775	0.2903	1.8511	0.251
EDML1068	1068	42.2729	98.1043	11.2538	40.8544	9.83	1.9292	8.255	1.1868	6.4746	1.213	3.2252	0.4281	2.7463	0.3722
EDML1069	1069	38.2718	87.5227	10.6168	38.2367	8.9405	1.8308	7.9004	1.1456	6.311	1.1993	3.1714	0.4308	2.6628	0.3571
EDML1070	1070	20.8416	44.05	5.6657	20.4734	4.7922	0.9873	4.3284	0.6318	3.5621	0.6779	1.7637	0.2369	1.4525	0.1987
EDML1073	1073	9.1388	21.679	2.6311	9.4921	2.1725	0.4273	1.9801	0.2759	1.5593	0.3034	0.8056	0.107	0.6618	0.0856
EDML1076	1076	87.0511	208.8407	23.4295	83.1602	19.6935	4.282	16.0615	2.3749	13.1535	2.29	6.389	0.9638	5.2625	0.7849
EDML1078	1078	12.3184	21.6476	2.8049	9.3683	2.1519	0.4602	1.9677	0.2843	1.5992	0.3221	0.8645	0.1192	0.7118	0.1013
EDML1080	1080	68.574	153.3802	20.533	72.426	16.8192	3.4709	15.1851	2.2298	11.8384	2.2968	5.9802	0.7964	4.8934	0.7017
EDML1082	1082	37.6605	86.5088	10.7372	39.0001	8.9529	1.8796	8.1626	1.1634	6.4172	1.2168	3.1963	0.4276	2.668	0.3674
EDML1084	1084	101.4322	237.0254	28.3482	100.544	23.0715	4.8969	20.2896	2.9863	16.1372	2.9847	8.0123	1.2459	6.5672	0.9576
EDML1086	1086	27.7224	64.4931	7.1298	25.6431	5.9892	1.288	5.1851	0.7259	3.944	0.7472	1.9388	0.3009	1.6043	0.2333
EDML1088	1088	88.1203	204.5831	23.3006	83.4666	19.7089	4.1279	17.2204	2.5109	13.4098	2.5965	6.7049	1.0408	5.677	0.8094
EDML1090	1090	13.3692	30.7903	3.509	12.8756	3.0193	0.6096	2.6104	0.3627	2.0221	0.3727	1.0104	0.1376	0.8272	0.1164
EDML1093	1093	17.331	38.6909	4.7668	17.157	4.0108	0.8238	3.4923	0.4903	2.7821	0.5322	1.3924	0.192	1.2039	0.1604
EDML1096	1096	39.9619	92.1794	11.9369	43.0608	9.918	2.0924	9.3237	1.3219	7.317	1.3781	3.6938	0.4958	3.1364	0.4164
EDML1097	1097	34.1287	79.802	9.5584	34.7638	7.8639	1.6583	7.1188	1.0236	5.6421	1.0838	2.8658	0.3606	2.4037	0.3353
EDML1099	1099	32.8417	72.2811	9.4331	33.7185	7.9102	1.6878	7.2696	1.0434	5.6792	1.0858	2.9359	0.385	2.4142	0.3463
EDML1100	1100	42.1562	100.2088	11.2904	41.9976	9.8704	2.1524	8.5344	1.214	6.5164	1.2349	3.2664	0.5282	2.6537	0.4206
EDML1101	1101	9.8256	21.9729	2.6237	9.5507	2.3591	0.5103	2.1239	0.301	1.6675	0.3281	0.8535	0.1301	0.684	0.0969
EDML1104	1104	37.6263	85.4863	10.3837	38.3066	8.7753	1.7977	7.5617	1.0926	6.1296	1.1607	3.0151	0.4135	2.6155	0.3502
EDML1105	1105	49.1481	120.1977	13.6118	50.5654	11.7038	2.472	10.0186	1.4967	7.994	1.516	3.9484	0.6445	3.3506	0.4795

Table C.1: Names, depths and REE concentration [ng·L^{-1}] of the ice core samples analyzed in this study. bdl: concentration was below detection limit.

D Samples from the Potential Source Areas

sample name	continent	geographical coordinates	remarks
A1	Antarctica	77°43' S, 161°23' E	-
A2	Antarctica	77°31' S, 169°24' E	-
A3	Antarctica	77°17' S, 193°15' E	-
A4	Antarctica	77°17' S, 163°15' E	-
A5	Antarctica	77°30' S, 165°0' E	-
A6	Antarctica	77°30' S, 165°0' E	-
A7	Antarctica	77°37' S, 163°11' E	-
A8	Antarctica	77°38' S, 162°51' E	-
A9	Antarctica	77°28' S, 161°42' E	-
A10	Antarctica	77°50' S, 164°30' E	-
NZ22	New Zealand	44°38' S, 168°59' E	-
NZ12	New Zealand	45°24' S, 167°42' E	-
NZ31	New Zealand	-	-
NZ32	New Zealand	-	-
NZ143	New Zealand	43°28' S, 172°31' E	-
Na1	Southern Africa	24°29' S, 15°48' E	-
Na2	Southern Africa	24°42' S, 15°17' E	-
Na3	Southern Africa	23°7' S, 14°30' E	-
Na4	Southern Africa	24°42' S, 15°17' E	-
Southafrican Aerosol	southern Africa	33.5°' S, 22°0' W	-

Table D.1: Samples from the PSA of Antarctic ice core dust analyzed in this study. Continued on next page.

sample name	continent	geographical coordinates	remarks
Aus	Australia	25°20' S, 131°2' E	Ayers Rock, Northern Territory
ARLOZ5	South America	31°39' S, 64°8' W	Cordoba area, 10 - 20 ka B.P
ARBAR4	South America	33°49' S, 59°31' W	Pampas, ca. 20 ka B.P
ARHUD3	South America	25 km NW from ARGOR2	Pampas, ¡ 23 ka B.P
ARGOR2	South America	34°54' S, 58°1' W	Pampas, 20 - 25 ka B.P
ARMDP1	South America	37°57' S, 57°38' W	Pampas, 20 - 25 ka B.P
CH1	South America	41°9' S, 71°18' W	San Carlos de Bariloche, Argentina yellow silt, loess-like
CH5	South America	48°38' S, 74°6' W	western coast of Isla Grande de Chiloe dark grey sand, modern aeolian deposit
CH6	South America	51°4' S, 73°9' W	frontal moraine, 50-60 m above the level of Lake Grey, torre del Paine National Park, grey sand
CH8	South America	-	
CH9	South America	53°9' S, 70°55' W	probable a bottom moraine buried under a 30-40 cm soil light olive brown silt with brownish patches
CH10	South America	53°18' S, 70°22' W	bottom moraine, Tierra del Fuego, light brownish gray silt with salty encrustations from marine aerosol
CH11	South America	53°9' S, 70°55' W	4.5 km west of Punta Arenas yellowish-brown sandy silt (loess-like)
Bahia Blanca	South America	28°44' S, 62°16' W	-
Patagonia	South America	-	-

Table D.2: Samples from the PSA of Antarctic ice core dust analyzed in this study. Continued from last page.

E Mathematics of the PCA

The PCA is performed on the REE without the element Pm, since Pm does not have any stable isotope and could therefore not be measured.

1. Center the matrix used for the PCA $X \rightarrow X_{mean} = X - mean(X)$

2. Compute the covariance matrix $S \rightarrow S = X'_{mean} \cdot X_{mean}$

3. Compute eigenvector matrix F and eigenvalues L of S.

4. Sort eigenvectors and eigenvalues in decreasing order of eigenvalues.

5. Calculate principal components $B \rightarrow B = X \cdot F$. B gives the coordinates in the new coordinate system CS_{PC}.

6. Transform the other samples, that were not used for the initial PCA X_{all}, in the new coordinate system CS_{PC}

   - Center the data $X_{all} \rightarrow X_{allcenter} = X_{all} - mean(X)$
   - Transform the samples into $CS_{PC} \rightarrow B_{all} = X_{allcenter} \cdot F$

F Derivation of Dust Size Distribution Changes During Transport

Change of the concentration within one size interval.
Assumptions:

- no interaction between individual size classes

- deposition is caused by wet and dry deposition and proportional to the particle concentration

$$H\frac{dc_{air}(d,t)}{dt} = -c_{air}[v_{dry} + v_{wet}] \tag{F.1}$$

$$v_{dry} = kd^2 \tag{F.2}$$

$$v_{wet} = \varepsilon A(t) \tag{F.3}$$

with Equation F.1, Equation F.2 and Equation F.3

$$H\frac{dc_{air}(d,t)}{dt} = -c_{air}[kd^2 + \varepsilon A(t)] \qquad | : H| \cdot dt| : c_{air} \tag{F.4}$$

$$\frac{dc_{air}(d,t)}{c_{air}} = -\frac{kd^2 + \varepsilon A(t)}{H}dt \qquad | \int \tag{F.5}$$

$$ln(c_{air(d,t)}) = -\frac{kd^2 t + \varepsilon \int A(t)dt}{H} \qquad |exp \tag{F.6}$$

$$c_{air(d,t)} = c_{air,0} \cdot e^{-\frac{kd^2 t + \varepsilon \int A(t)dt}{H}} \tag{F.7}$$

Assuming A(t) constant during en route simplifies $\int A(t)dt$ to εAt, leading to

$$c_{air(d,t)} = c_{air,0} \cdot e^{-\frac{kd^2 t + \varepsilon At}{H}} \tag{F.8}$$

Change of concentration in a log-normal size distribution with independent particle channels.

$$V(t, logd) = \frac{a_0}{\sqrt{2\pi}log\sigma_0}e^{-\frac{1}{2}\frac{(logd-log\mu_0)^2}{log^2\sigma_0}} \tag{F.9}$$

Change of the concentration during the transport according to Equation F.7

$$V(t, logd) = V(t = 0, logd)e^{-\frac{kd^2}{H}t - \frac{\varepsilon}{H}At} \tag{F.10}$$

With Equation F.9 and Equation F.10

$$V(t, logd) = \frac{a_0}{\sqrt{2\pi}log\sigma_0}e^{-\frac{1}{2}\frac{(logd-log\mu_0)^2}{log^2\sigma_0} - \frac{kd^2}{H}t - \frac{\varepsilon}{H}At} \tag{F.11}$$

The maximum of this equation ($d = \mu_{air}$) is deduced by setting the first derivative with respect to *logd* to zero.

$$\frac{dV(t, log(d = \mu_{air}))}{dlogd} = 0 \tag{F.12}$$

$$\frac{dV(t, log(d = \mu_{air}))}{dlogd} = \frac{P_0}{\sqrt{2\pi}log\sigma_0} \cdot e^{-\frac{1}{2}(\frac{log\mu_{air}-log\mu_0}{log\sigma_0})^2 - \frac{t}{H}(kd^2+\epsilon A)}. \tag{F.13}$$

$$[\frac{logd-log\mu_0}{log^2\sigma_0} - (2\frac{t}{H}kd^2ln10)] = 0$$

While generating the derivative of *d* with respect to *logd* the relation
$$d = 10^{logd} = e^{logd \cdot ln10}$$
was used.
In Equation F.13 $e^{-\frac{1}{2}(\frac{logd-log\mu_0}{log\sigma_0})^2 - \frac{t}{H}(kd^2+\epsilon A)}$ is always $\neq 0$. This means for fulfilling
$\frac{dV(t,logd)}{dlogd} = 0$ is obtained with

$$\frac{logd-log\mu_0}{log^2\sigma_0} - (2\frac{t}{H}kd^2ln10) = 0. \tag{F.14}$$

$$\frac{logd-log\mu_0}{log^2\sigma_0} = -2ln10kd^2\frac{t}{H} \qquad | \cdot log^2\sigma_0 \tag{F.15}$$

with $d = \mu_{air}$

$$log\mu_{air} - log\mu_0 = log\frac{\mu_{air}}{\mu_0} = -2ln10k\mu_{air}^2\frac{t}{H} \cdot log^2\sigma_0 \tag{F.16}$$

Taking 2 different stages *I* and *II* and subtracting Equation F.16 for stage *II* from Equation F.16 for stage *I*

$$log\frac{\mu_{air}^I}{\mu_0} - \frac{\mu_{air}^{II}}{\mu_0} = -2ln10k\mu_{air}^I{}^2\frac{t^I}{H} \cdot log^2\sigma_0 + 2ln10k\mu_{air}^{II}{}^2\frac{t^{II}}{H} \cdot log^2\sigma_0 \qquad \text{(F.17)}$$

Assuming H, μ_0, σ_0 and k to be constant from stage I and II

$$log\frac{\mu_{air}^I}{\mu_{air}^{II}} = -2ln10k\frac{log^2\sigma_0}{H}(\mu_{air}^I{}^2t^I - \mu_{air}^{II}{}^2t^{II}) \qquad \text{(F.18)}$$

Using Equation F.16

$$log\frac{\mu_{air}^I}{\mu_{air}^{II}} = log\frac{\mu_{air}^I}{\mu_0}(1 - \frac{\mu_{air}^{II}{}^2}{\mu_{air}^I{}^2}\frac{t^{II}}{t^I}) \qquad \text{(F.19)}$$

G Dust Concentration Blank Levels

Blank levels during the measurements with the Coulter Counter

sample	EDML1083		EDML746	
Particle Diameter	mean	stddev	mean	stddev
$[\mu m]$	[part/ml]	[part/ml]	[part/ml]	[part/ml]
< 1	354.1	249.6	52.2	48.5
1 - 2	316.0	224.3	58.4	53.5
2 - 3	40.3	34.8	9.2	13.4
3 - 4	9.6	12.1	1.6	4.8
4 - 5	3.3	8.1	1.1	3.7
5 - 6	0.8	2.6	0.4	1.9
6 - 7	0.4	1.9	0.4	1.9
7 - 8	0.0	0.0	0.2	1.3
8 - 9	0.3	1.9	0.0	0.0
9 - 10	0.3	1.9	0.1	0.4
10 - 11	0.0	0.0	0.1	1.0
11 - 18	0.0	0.0	0.4	1.9
number of blanks	41		55	

Table G.1: Blank levels of the Coulter Counter measurements

Bibliography

[Adam and Green, 1993] Adam, J. and Green, T. H. (1993). The effect of pressure and temperature on the partitioning of Ti, Sr and REE between amphibole, clinopyroxene and basaltic melts. *Chemical Geology*, 117:219–233.

[Albarede, 2003] Albarede, F. (2003). *Geochemistry: An Introduction.* Cambridge University Press, Cambridge.

[Alfaro and Gomes, 2001] Alfaro, C. A. and Gomes, L. (2001). Modeling mineral aerosol production by wind erosion: Emission intensities and aerosol size distributions in source areas. *Journal of Geophysical Research*, 106:18075–18084.

[Arimoto, 2001] Arimoto, R. (2001). Eolian dust and climate: relationships to sources, tropospheric chemistry, transport and deposition. *Earth-Science Reviews*, 54:29–42.

[Basile et al., 1997] Basile, I., Grousset, F., Revel, M., Petit, J. R., Biskaye, P. E., and Barkov, N. I. (1997). Patagonian origin of glacial dust deposited in East Antarctica (Vostok and Dome C) during glacial stages 2, 4 and 6. *Earth and Planetary Science Letters*, 146:573 – 589.

[Beer et al., 1988] Beer, J., Siegenthaler, U., Bonani, G., Finkel, R. C., Oeschger, H., Suter, M., and Wölfli, W. (1988). Information on past solar activity and geomagnetism from ^{10}Be in the Camp Century ice core. *Nature*, 331:675–679.

[Beer et al., 2006] Beer, J., Vonmoos, M., and Muscheler, R. (2006). Solar variability over the past several millennia. *Space Science Reviews*, 125:67–79.

[Biscaye et al., 1997] Biscaye, P. E., Grousset, F. E., Revel, M., Van der Gaast, S., Zielinski, G. A., Vaars, A., and Kukla, G. (1997). Asian provenance of glacial dust (stage 2) in the Greenland Ice Sheet Project 2 ice core, Summit, Greenland. *Journal of Geophysical Research*, 102:26765–26781.

[Blunier et al., 1998] Blunier, T., Chappellaz, J., Schwander, J., Dallenbach, A., Stauffer, B., Stocker, T. F., Raynaud, D., Jouzel, J., Clausen, H. B., Hammer, C. U., and Johnsen, S. J. (1998). Asynchrony of Antarctic and Greenland climate change during the last glacial period. *Nature*, 394:739–743.

[Buseck and Veblen, 1978] Buseck, P. R. and Veblen, D. R. (1978). Trace elements, crystal defects and high resolution electron microscopy. *Geochimica et Cosmochimica Acta*, 42(6):669–678.

[Claquin et al., 1999] Claquin, T., Schulz, M., and Balkanski, Y. J. (1999). Modeling the mineralogy of atmospheric dust sources. *Journal of Geophysical Research*, 104:22243–22256.

[Coulter, 1959] Coulter, W. (1959). Fluid metering apparatus. US. Patent No. 2869078.

[de Angelis et al., 1984] de Angelis, M., Legrand, M., Petit, J. R., Barkov, N. I., Korotkevitch, Y. S., and Kotlyalov (1984). Soluble and Isoluble Impurities Along the 950 m Deep Vostok Ice Core (Antarctica) - Climatic Implications. *Journal of Atmospheric Chemistry*, 1:215–239.

[Delmonte, 2003] Delmonte, B. (2003). *Quaternary variations and origin of continental dust in east Antarctica*. PhD thesis, Universita degli Studi di Milano-Bicocca.

[Delmonte et al., 2002a] Delmonte, B., Basile-Doelsch, I., Michard, A., Petit, J. R., Maggi, V., Gemmiti, B., and Revel-Rolland, M. (2002a). Sr-Nd signature of potential source areas for dust in East Antarctica: Preliminary results. *Geochimica et Cosmochimica Acta*, 66(15A):A175–A175.

[Delmonte et al., 2004a] Delmonte, B., Basile-Doelsch, I., Petit, J. R., Maggi, V., Revel-Rolland, M., Michard, A., Jagoutz, E., and Grousset, F. (2004a). Comparing the Epica and Vostok dust records during the last 220,000 years: stratigraphical correlation and provenance in glacial periods. *Earth-Science Reviews*, 66(1-2):63–87.

[Delmonte et al., 2004b] Delmonte, B., Petit, J. R., Andersen, K. K., Basile-Doelseh, I., Maggi, V., and Lipenkov, V. Y. (2004b). Dust size evidence for opposite regional atmospheric circulation changes over east Antarctica during the last climatic transition. *Climate Dynamics*, 23(3-4):427–438.

[Delmonte et al., 2005] Delmonte, B., Petit, J. R., Krinner, G., Maggi, V., Jouzel, J., and Udisti, R. (2005). Ice core evidence for secular variability and 200-year dipolar oscillations in atmospheric circulation over East Antarctica during the Holocene. *Climate Dynamics*, 24(6):641–654.

[Delmonte et al., 2002b] Delmonte, B., Petit, J. R., and Maggi, V. (2002b). Glacial to Holocene implications of the new 27000-year dust record from the EPICA Dome C (East Antarctica) ice core. *Climate Dynamics*, 18(8):647–660.

[Dentener et al., 1996] Dentener, F. J., R., C. G., Zhang, Y., Lelieveld, J., and Crutzen, P. J. (1996). Role of mineral aerosol as a reactive surface in the global troposphere. *Journal of Geophysical Research*, 101:22869–22890.

[Duce, 1995] Duce, R. A. (1995). *Aerosol forcing of Climate*, chapter Sources, Distributions, and Fluxes of Mineral Aerosol anf Their relationship to Climate, pages 43–72. Report of Dahlem Workshop.

[EPICA Community Members, 2004] EPICA Community Members (2004). Eight glacial cycles from an Antarctic ice core. *Nature*, 429(6992):623–628.

[EPICA Community Members, 2006] EPICA Community Members (2006). One-to-one coupling of glacial climate variability in Greenland and Antarctica. *Nature*, 444(7116):195–198.

[Feichter, 2003] Feichter, J. (2003). Aerosole und das Klimasystem. *Physik in unserer Zeit*, 34:72–79.

[Fischer et al., 2007a] Fischer, H., Fundel, F., Ruth, U., Twarloh, B., Wegner, A., Udisti, R., Becagli, S., Castellano, E., Morganti, A., Severi, M., Wolff, E., Littot, G., Röthlisberger, R., Mulvaney, R., Hutterli, M. A., Kaufmann, P., Federer, U., Lambert, F., Bigler, M., Hansson, M., Jonsell, U., de Angelis, M., Boutron, C., Siggaard-Andersen, M. L., Steffensen, J. P., Barbante, C., Gaspari, V., Gabrielli, P., and Wagenbach, D. (2007a). Reconstruction of millenial changes in the dust emission, transport and regional sea ice coverage using the deep EPICA ice cores from the Atlantic and the Indian sector of Antarctica. *Earth and Planetary Science Letters*, 260:340–354.

[Fischer et al., 2007b] Fischer, H., Siggaard-Andersen, M. L., Ruth, U., Röthlisberger, R., and Wolff, E. (2007b). Glacial/interglacial changes in mineral dust and sea-salt records in polar ice cores: Sources, transport, and deposition. *Reviews of Geophysics*, 45(1):–.

[Fung et al., 2000] Fung, I. Y., Meyn, S. K., Tegen, I., Doney, S. C., John, J. G., and Bishop, J. K. B. (2000). Iron supply and demand in the upper ocean. *Global Biogeochemical Cycles*, 14(1):281–295.

[Gabrielli et al., 2006] Gabrielli, P., Barbante, C., Turetta, C., Marteel, A., Boutron, C., Cozzi, G., Cairns, W., Ferrari, C., and Cescon, P. (2006). Direct determination of rare earth elements at the subpicogram per gram level in antarctic ice by ICP-SFMS using a desolvation system. *Analytical Chemistry*, 78(6):1883–1889.

[Gaiero et al., 2004] Gaiero, D. M., Depetris, P. J., Probst, J.-L., Bidart, S. M., and Leleyter, L. (2004). The signature of river- and wind-borne materials exported from Patagonia to the southern latitudes: a view from REEs and implications for paleoclimatic interpretations. *Earth and Planetary Science Letters*, 219:357–376.

[Gaiero et al., 2003] Gaiero, D. M., Probst, J. L., Depetris, P. J., Bidart, S. M., and Leleyter, L. (2003). Iron and other transition metals in patagonian riverborne and windborne materials: Geochemical control and transport to the southern south atlantic ocean. *Geochimica et Cosmochimica Acta*, 67(19):3603–3623.

[Gibbs et al., 1986] Gibbs, A. K., Montgomery, C. W., O'day, P. A., and Erslev, E. A. (1986). The Archean-Proterozoic transition: Evidence from the geochemistry of metasedimentary rocks of Guyana and Montana. *Geochimica et Cosmochimica Acta*, 50:2125–2141.

[Gilette, 1978] Gilette, D. (1978). A wind tunnel simulation of the erosion of soil: Effect of soil texture, sandblasting, wind speed, and soil consolidation on dust production. *Atmospheric Environment*, 12:1735–1743.

[Gillette, 1988] Gillette, D. A. (1988). Threshold friction velocities for dust production for agricultural soils. *Journal of Geophysical Research*, 93:12645–12662.

[Gilli, 2003] Gilli, A. P. (2003). *Tracking late Quaternary environmental change in southernmost South America using lake sediments of Lago Cardiel (49ºS), Patagonia, Argentina*. PhD thesis, Swiss Federal Institute of Technology Zurich.

[Ginoux et al., 2001] Ginoux, P., Chin, M., Tegen, I., Prospero, J. M., B., H., Dubrovnik, O., and Lin, S.-J. (2001). Sources and distributions of dust aerosols simulated with the GOCART model. *Journal of Geophysical Research*, 106:20255–20273.

[Greaves et al., 1999] Greaves, M., Elderfield, H., and Sholkovitz, E. (1999). Aeolian sources of rare earth elements to the Western Pacific Ocean. *Marine Chemistry*, 68:31–38.

[Grini et al., 2002] Grini, A., Zender, C. S., and Colarco, P. R. (2002). Saltation Sandblasting behavior during mineral dust aerosol production. *Geophysical Research Letters*, 29:1868.

[Grousset and Biscaye, 2005] Grousset, F. E. and Biscaye, P. E. (2005). Tracing dust sources and transport patterns using Sr, Nd and Pb isotopes. *Chemical Geology*, 222:149–167.

[Grousset et al., 2003] Grousset, F. E., Ginoux, P., Bory, A., and Biscaye, P. E. (2003). Case study of a Chinese dust plume reaching the French Alps. *Geophysical Research Letters*, 30:1277.

[Harrison et al., 2001] Harrison, S. P., Kohfeld, K. E., Roelandt, C., and Claquin, T. (2001). The role of dust in climate changes today, at the last glacial maximum and in the future. *Earth-Science Reviews*, 54(1-3):43–80. Times Cited: 61 Article English Cited References Count: 318 467tt Sp. Iss. SI.

[Hayakawa et al., 1995a] Hayakawa, O., Nakahira, K., and Tsubaki, J. (1995a). Comparison of Fine Ceramics Raw Powders with Particle Size Analysers Having Different Measuring Principles and Its Problem. *Journal of the Ceramic Society of Japan*, 103(6):586–592.

[Hayakawa et al., 1995b] Hayakawa, O., Nakahira, K., and Tsubaki, J. (1995b). Comparison of Particle Size Analysers and Evaluation of Its Measuring Technique with Fine Ceramics Powders (Part 1) - Oxide Powders. *Journal of the Ceramic Society of Japan*, 103(4):392–397.

[Hayakawa et al., 1995c] Hayakawa, O., Nakahira, K., and Tsubaki, J. (1995c). Comparison of Particle Size Analysers and Evaluation of Its Measuring Technique with Fine Ceramics Powders (Part 2) - Non-Oxide Powders. *Journal of the Ceramic Society of Japan*, 103(5):500–505.

[Hemming et al., 2007] Hemming, S. R., van de Flierdt, T.and Goldstein, S. L., Franzese, A. M., Roy, M., Gastineau, G., and Landrot, G. (2007). Strontium isotope tracing of terrigenous sediment dispersal in the Antarctic Circumpolar Current: Implications for constraining frontal positions. *Geochemistry Geophysics Geosystems*, 8:–.

[Heusser, 1990] Heusser, C. J. (1990). Ice age vegetation and climate of subtropical Chile. *Palaeogeography, Palaeoclimatology, Palaeoecology*, 80:107–127.

[Humphris, 1983] Humphris (1983). The Mobility of the Rare Earth Elements in the Crust. In *Rare Earth Element Geochemistry*. Elsevier Science Publishers.

[IPCC, 2007] IPCC (2007). Intergovernmental panel on climate change - fourth assessment report.

[Jickells et al., 2005] Jickells, T. D., An, Z. S., Andersen, K. K., Baker, A. R., Bergametti, G., Brooks, N., Cao, J. J., Boyd, P. W., Duce, R. A., Hunter, K. A., Kawahata, H., Kubilay, N., laRoche, J., Liss, P. S., Mahowald, N., Prospero, J. M., Ridgwell, A. J., Tegen, I., and Torres, R. (2005). Global iron connections between desert dust, ocean biogeochemistry, and climate. *Science*, 308(5718):67–71.

[Kim et al., 2002] Kim, J.-H., Schneider, R. R., Hebbeln, D., Müller, P. J., and Wefer, G. (2002). Last deglacial sea-surface temperature evolution in the Southeast Pacific compared to climate changes on the South American. *Quaternary Science Reviews*, 21:2085–2097.

[Koehler et al., 2005] Koehler, P., Fischer, H., Munhoven, G., and Zeebe, R. E. (2005). Quantitative interpretation of atmospheric carbon records over the last glacial termination. *Global Biogeochemical Cycles*, 19.

[Kohfeld and Harrison, 2001] Kohfeld, K. E. and Harrison, S. P. (2001). DIRTMAP: The geological record of dust. *Earth-Science Reviews*, 54:81–114.

[Koopmann, 2006] Koopmann, J. D. (2006). Calibration of a laser particle counter and mineral dust measurements in Antarctic snow pits. Master's thesis, Rheinisch-Westfälische Technische Hochschule Aachen.

[Lamy et al., 1999] Lamy, F., Hebbeln, D., and Wefer, G. (1999). High-resolution marine record of climatic change in mid-latitude chile during the last 28,000 years based on terrigenous sediment parameters. *Quaternary Research*, 51:83–93.

[Lau and Kim, 2007] Lau, K. M. and Kim, K. M. (2007). Cooling of the Atlantic by Saharan dust. *Geophysical Research Letters*, 34:L23811.

[Legrand and Mayewski, 1997] Legrand, M. and Mayewski, P. (1997). Glaciochemistry of polar ice cores: A Review. *Reviews of Geophysics*, 3:219 – 123.

[Lisiecki and Raymo, 2005] Lisiecki, L. E. and Raymo, M. E. (2005). A Pliocene-Pleistocene stack of 57 globally distributed benthic δ^{18}O records. *Paleoceanography*, 20:1003.

[Lunt and Valdes, 2002] Lunt, D. J. and Valdes, P. J. (2002). Dust deposition and provenance at the Last Glacial Maximum and present day. *Geophysical Research Letters*, 29:–.

[Luo et al., 2003] Luo, C., Mahowald, N., and del Corral, J. (2003). Sensitivity study of meteorological parameters on mineral aerosol mobilization, transport, and distribution. *Journal of Geophysical Research*, 108:4447.

[Mahowald et al., 2005] Mahowald, N. M., Baker, A. R., Bergametti, G., Brooks, N., Duce, R. A., Jickells, T. D., Kubilay, N., Prospero, J. M., and Tegen, I. (2005). Atmospheric global dust cycle and iron inputs to the ocean. *Global Biogeochemical Cycles*, 19(4):–.

[Mahowald and Kiehl, 2003] Mahowald, N. M. and Kiehl, L. M. (2003). Mineral aerosol and cloud interactions. *Geophysical Research Letters*, 30.

[Mahowald et al., 2006] Mahowald, N. M., Muhs, D. R., Levis, S., Rasch, P., Yoshioka, M., Zender, C. S., and Luo, C. (2006). Change in atmospheric mineral aerosols in response to climate: Last glacial period, preindustrial, modern, and doubled carbon dioxide climates. *Journal of Geophysical Research*, 111.

[Mahowald et al., 2002] Mahowald, N. M., Zender, C. S., Luo, C., Savoie, D., Torres, O., and del Corral, J. (2002). Understanding the 30-year Barbados desert dust record. *Journal of Geophysical Research*, 107:4561.

[Markgraf et al., 2007] Markgraf, V., Whitlock, C., and Haberle, S. (2007). Vegetation and fire history during the last 18,000 cal yr BP in Southern Patagonia: Mallin Pollux, Coyhaique, Province Aisen (45 degrees 41 ' 30 " S, 71 degrees 50 ' 30 " W, 640 m elevation). *Palaeogeography, Palaeoclimatology, Palaeoecology*, 254:492–507.

[Martinelli, 2004] Martinelli, N. (2004). Climate from dendrochronology: latest developments and results. *Global and Planetary Change*, 40:129–139.

[Martinez Cortizas et al., 2005] Martinez Cortizas, A., Mighall, T., Pontevedra Pombal, X., Novoa Munfoz, J., Peiteado Varelal, E., and Pifneiro Rebolol, R. (2005). Linking changes in atmospheric dust deposition, vegetation change and human activities in northwest Spain during the last 5300 years. *The Holocene*, 15:698–706.

[Marx et al., 2005a] Marx, S. K., Kamber, B. S., and McGowan, H. A. (2005a). Estimates of Australian dust flux into New Zealand: Quantifying the eastern Australian dust plume pathway using trace element calibrated Pb-210 as a monitor. *Earth and Planetary Science Letters*, 239(3-4):336–351.

[Marx et al., 2005b] Marx, S. K., Kamber, B. S., and McGowan, H. A. (2005b). Provenance of long-travelled dust determined with ultra-trace-element composition: a pilot study with samples from New Zealand glaciers. *Earth Surface Processes and Landforms*, 30(6):699–716.

[McGowan et al., 2005] McGowan, H. A., Kamber, B., McTainsh, G. H., and Marx, S. K. (2005). High resolution provenancing of long travelled dust deposited on the Southern Alps, New Zealand. *Geomorphology*, 69(1-4):208–221.

[McKay, 1989] McKay, G. (1989). Partitioning of rare earth elements between major silicate minerals and basaltic melt. In Lipin, B. R. and McKay, G. A., editors, *Geochemistry and Mineralogy of Rare Earth Elements*, volume 21 of *Reviews in Mineralogy*, pages 44 – 77. Mineral. Soc. Am.

[McLennan, 1989] McLennan (1989). Rare earth elements in sedimentary rocks: Influence of provenance and sedimentary processes. In Lipin, B. R., editor, *Geochemistry and mineralogy of rare earth elements*. Mineralogical Society of America, Washington.

[Mercer, 1976] Mercer, J. H. (1976). Glacial History of Southernmost South America. *Quaternary Research*, 6:125–166.

[Miller et al., 2006] Miller, R. L., Cakmur, R. V., Perlwitz, J., Geogdzhayev, I. V., Ginoux, P., Koch, D., Kohfeld, K. E., Prigent, C., Ruedy, R., Schmidt, G. A., and Tegen, I. (2006). Mineral dust aerosols in the NASA Goddard Institute for Space Sciences ModelE atmospheric general circulation model. *Journal of Geophysical Research*, 111.

[Naito et al., 1998] Naito, M., Hayakawa, O., Nakahira, K., Mori, H., and Tsubaki, J. (1998). Effect of particle shape on the particle size distribution measured with commercial equipment. *Powder Technology*, 100:52–60.

[NGRIP-Members, 2004] NGRIP-Members (2004). High-resolution record of Northern Hemisphere climate extending into the last interglacial period. *Nature*, 431:147–151.

[Nozaki et al., 1997] Nozaki, Y., Zhang, J., and Amakawa, H. (1997). The fractionation between Y and Ho in the marine environment. *Earth and Planetary Science Letters*, 148:329–340.

[Oerter et al., 2004] Oerter, H., Graf, W., Meyer, H., and Wilhelms, F. (2004). The EPICA ice core from Dronning Maud Land: First results from stable-isotope measurements. *Annals of Glaciology*, 39:307–312.

[Oerter et al., 2000] Oerter, H., Wilhelms, F., Jung-Rothenhausler, F., Goktas, F., Miller, H., Graf, W., and Sommer, S. (2000). Accumulation rates in Dronning Maud Land, Antarctica, as revealed by dielectric-profiling measurements of shallow firn cores. *Annals of Glaciology*, 30:27–34.

[Palme, 2004] Palme, H. (2004). Solar System Abundances of the Elements. In Holland, H. D. and Turekian, K. K., editors, *Treatise on Geochemistry*, volume 1. Elsevier-Pergamon, Oxford.

[Parrenin et al., 2001] Parrenin, F., Jouzel, J., Waelbroeck, C., Ritz, C., and Barnola, J. M. (2001). Dating the Vostok ice core by an inverse method. *Journal of Geophysical Research*, 106(D23):31837–31851.

[Philpotts, 1978] Philpotts, J. A. (1978). The law of constant rejection. *Geochimica et Cosmochimica Acta*, 42:909–920.

[Prospero et al., 2002] Prospero, J., Ginoux, P., Torres, O., Nicholson, E., and Gill, T. (2002). Environmental characterization of global sources of atmospheric soil dust identified with NIMBUS-7 Total Ozone Mapping Spectrometer (TOMS) absorbing aerosol products. *Reviews of Geophysics*, 40(1).

[Pye, 1987] Pye, K. (1987). *Aeolian dust and dust deposits*. Academic Press, London.

[Rea, 1994] Rea, D. K. (1994). The paleoclimatic record provided by eolian deposition in the deep sea; the geologic history of wind. *Reviews of Geophysics*, 32:159–195.

[Reijmer and van den Broeke, 2001] Reijmer, C. H. and van den Broeke (2001). Moisture source of precipitation in Western Dronning Maud Land, Antarctica. *Antarctic Science*, 13:210–220.

[Reijmer et al., 2002] Reijmer, C. H., van den Broeke, M. R., and Scheele, M. P. (2002). Air Parcel Trajectories and Snowfall Related to Five Deep Drilling Locations in Antarctica Based on the ERA-15 Dataset. *Journal of Climate*, 15:1957–1968.

[Revel-Rolland et al., 2006] Revel-Rolland, M., De Dekker, P., Delmonte, B., Hesse, P., Magee, J., Basile-Doelsch, I., Grousset, F., and Bosch, D. (2006). Eastern Australia: A possible source of dust in East Antarctica interglacial ice. *Earth and Planetary Science Letters*, 249:1–13.

[Ridgwell, 2002] Ridgwell, A. J. (2002). Dust in the Earth system: the biogeochemical linking of land, air and sea. *Phil. Trans. R. Soc. Lond. A*, 360(1801):2905–2924.

[Ridgwell and Watson, 2002] Ridgwell, A. J. and Watson, A. J. (2002). Feedback between aeolian dust, climate, and atmospheric CO_2 in glacial time. *Paleoceanography*, 17(4):–.

[Ringwood, 1955] Ringwood, A. E. (1955). The principles governing trace element distribution during magmatic crystallization. *Geochimica et Cosmochimica Acta*, 7:189 – 202.

[Royer et al., 1983] Royer, A., de Angelis, M., and Petit, J. R. (1983). A 30000 year record of physical and optical properties of the microparticles from an east antarctic ice core and implications for paleoclimate reconstruction models. *Climate Change*, 5:381–412.

[Röthlisberger et al., 2000] Röthlisberger, R., Bigler, M., Hutterli, M., Sommer, S., Stauffer, B., Junghans, H. G., and Wagenbach, D. (2000). Technique for continuous high-resolution analysis of trace substances in firn and ice cores. *Environmental Science & Technology*, 34(2):338–342.

[Röthlisberger et al., 2002] Röthlisberger, R., Mulvaney, R., Wolff, E. W., Hutterli, M. A., Bigler, M., Sommer, S., and Jouzel, J. (2002). Dust and sea salt variability in central East Antarctica (Dome C) over the last 45 kyrs and its implications for southern high-latitude climate. *Geophysical Research Letters*, 29(20):1963.

[Ruth, 2002] Ruth, U. (2002). Concentration and Size Distribution of Microparticles in the NGRIP Ice Core (Central Greenland) during the Last Glacial Period. *Berichte zur Polar- und Meeresforschung*, 428:146.

[Ruth et al., 2007a] Ruth, U., Barbante, C., Bigler, M., Delmonte, B., Fischer, H., Gabrielli, P., Gaspari, V., Kaufmann, P., Lambert, F., Maggi, V., Marino, F., Petit, J. R., Steffensen, J. P., Traversi, R., Udisti, R., Wagenbach, D., Wegner, A., and Wolff, E. (2007a). Proxies and measurement techniques for mineral dust in Antarctic ice cores. *submitted to Environmental Science & Technology*.

[Ruth et al., 2007b] Ruth, U., Barnola, J.-M., Beer, J., Bigler, M., Blunier, T., Castellano, E., Fischer, H., Fundel, F., Huybrechts, P., Kaufmann, P., Kipfstuhl, S., Lambrecht, A., Morganti, A., Oerter, H., Parrenin, F., Rybak, O., Severi, M., Udisti, R., Wilhelms, F., and Wolff, E. (2007b). "EDML1": A chronology for the EDML ice core, Antarctica, over the last 150 000 year. *Climate of the Past*, 3:475–484.

[Ruth et al., 2006] Ruth, U., Kaufmann, P., Delmonte, B., Bigler, M., Lambert, F., Petit, J. R., Wegner, A., Severi, M., Gersonde, R., Kunz-Pirrung, M., and Meyer, H. (2006). Climatic implications of the continuous dust record (200kyr) from the EPICA-DML ice core, Antarctica. In *EGU General Assembly 2006, 2-7 APR., Vienna, Austria., 2006*.

[Ruth et al., 2002] Ruth, U., Wagenbach, D., Bigler, M., Steffensen, P., Rothlisberger, R., and Miller, H. (2002). High-resolution microparticle profiles at North-GRIP, Greenland: case studies of the calcium-dust relationship. *Annals of Glaciology*, 35:237–242.

[Ruth et al., 2003] Ruth, U., Wagenbach, D., Steffensen, J. P., and Bigler, M. (2003). Continuous record of microparticle concentration and size distribution in the central Greenland NGRIP ice core during the last glacial period. *Journal of Geophysical Research*, 108(D3):–.

[Schulz et al., 1998] Schulz, M., Balkanski, Y. J., Guelle, W., and Dulac, F. (1998). Role of aerosol size distribution and source location in a three-dimensional simulation of a Saharan dust episode tested against satellite-derived optical thickness. *Journal of Geophysical Research*, 103:10579–10592.

[Schwander et al., 2001] Schwander, J., Jouzel, J., Hammer, C., Petit, J., Udisti, R., and Wolff, E. (2001). A tentative chronology for the EPICA Dome Concordia ice core. *Geophysical Research Letters*, 28(22):4243–4246.

[Severi et al., 2007] Severi, M., Becagli, S., Castellano, E., Morganti, A., Traversi, R., Udisti, R., Ruth, U., Fischer, H., Huybrechts, P., Wolff, E., Parrenin, F., Kaufmann, P., Lambert, F., and Steffensen, J. P. (2007). Synchronisation of the EDML and EDC ice cores for the last 52 kyr by volcanic signature matching. *Climate of the Past*, 3:367–374.

[Siegenthaler et al., 2005] Siegenthaler, U., Stocker, T., Monnin, E., Luthi, D., Schwander, J., Stauffer, B., Raynaud, D., Barnola, J., Fischer, H., Masson-Delmotte, V., and Jouzel, J. (2005). Stable carbon cycle-climate relationship during the late Pleistocene. *Science*, 310:1313–1317.

[Smith et al., 2003] Smith, J., Vance, D., Kemp, R. A., Archer, C., Toms, P., King, M., and Zarate, M. (2003). Isotopic constraints on the source of Argentinian loess - with implications for atmospheric circulation and the provenance of Antarctic dust during recent glacial maxima. *Earth and Planetary Science Letters*, 212(1-2):181–196.

[Sokolik et al., 2001] Sokolik, I. N., Winker, D., Bergametti, G., Gillette, D. A., Carmichael, G., Kaufman, Y. J., Gomes, L., Schuetz, L., and Penner, J. E. (2001). Introduction to special section: Outstanding problems in quantifying the radiative impacts of mineral dust. *Journal of Geophysical Research*, 106:18015–18028.

[Spahni et al., 2005] Spahni, R., Chappellaz, J., Stocker, T., Loulergue, L., Hausammann, G., Kawamura, K., Flückiger, J., Schwander, J., Raynaud, D., Masson-Delmotte, V., and Jouzel, J. (2005). Atmospheric methane and nitrous oxide of the late Pleistocene from Antarctic ice cores. *Science*, 310:1317–1321.

[Steffensen, 1997] Steffensen, J. P. (1997). The size distribution of microparticles from selected segments of the Greenland Ice Core Project ice core representing different climatic periods. *Journal of Geophysical Research*, 102 (C12):26755–26764.

[Swap et al., 1992] Swap, R., Garstang, M., Greco, S., Talbot, R., and Kallberg, P. (1992). Saharan dust in the Amazon Basin. *Tellus*, 44B:133–149.

[Taylor and McLennan, 1985] Taylor, S. R. and McLennan, S. M. (1985). *The continental crust: Its composition and evolution : An examination of the geochemical record preserved in sedimentary rocks*. Blackwell Scientific.

[Tegen and Fung, 1994] Tegen, I. and Fung, I. (1994). Modelling of mineral dust in the atmosphere: Sources, transport, and optical thickness. *Journal of Geophysical Research*, 99:22897–22914.

[Tegen et al., 1997] Tegen, I., Hollrig, P., Chin, M., Fung, I., Jacob, D., and Penner, J. (1997). Contribution of different aerosol species to the global aerosol extinction optical thickness: Estimates from model results. *Journal of Geophysical Research*, 102:23895–23915.

[Tegen and Lacis, 1996] Tegen, I. and Lacis, A. A.and Fung, I. (1996). The influence on climate forcing of mineral aerosols from disturbed soils. *Nature*, 380:419–422.

[Tie et al., 2005] Tie, X., Madronich, S., Walters, S., Edwards, D. P. andl Ginoux, P., Mahowald, N., Zhang, R., Lou, C., and Brasseur, G. (2005). Assessment of the global impact of aerosols on tropospheric oxidants. *Journal of Geophysical Research*, 110.

[Tobler et al., 2007] Tobler, L., Kellerhal, T., and Schwikowski, M. (2007). An approach to determine the provenance of dust in the different ice cores by principal component analysis of rare earth elements. *PSI, annual report*, page 32.

[Toggweiler and Russell, 2008] Toggweiler, J. R. and Russell, J. (2008). Ocean circulation in a warming climate. *Nature*, 451:286–288.

[Vogel, 1997] Vogel, H. (1997). *Gerthsen Physik*. Springer Verlag Berlin Heidelberg.

[Wardle, 2003] Wardle, R. (2003). Using anticyclonicity to determine the position of the Southern Hemisphere westerlies: Implications for the LGM. *Geophysical Research Letters*, 30:–.

[Watson et al., 2000] Watson, A. J., Bakker, D. C. E., Ridgwell, A. J., Boyd, P. W., and Law, C. S. (2000). Effect of iron supply on Southern Ocean CO_2 uptake and implications for glacial atmospheric CO_2. *Nature*, 407:730–733.

[Wedepohl, 1995] Wedepohl, H. K. (1995). The composition of the continental crust. *Geochimica et Cosmochimica Acta*, 59(7):1217–1232.

[Weller and Wagenbach, 2007] Weller, R. and Wagenbach, D. (2007). Year-round chemical aerosol records in continental Antarctica obtained by automatic samplings. *Tellus*, 59:775–765.

[Werner et al., 2002] Werner, M., Tegen, I., Harrison, S. P., Kohfeld, K. E., Prentice, I. C., Balkanski, Y., Rodhe, H., and Roelandt, C. (2002). Seasonal and interannual variability of the mineral dust cycle under present and glacial climate conditions. *Journal of Geophysical Research*, 107(D24):–.

[Wille et al., 2007] Wille, M., Maidana, N. I., Schäbitz, F. andl Fey, M., Haberzettl, T., Janssen, S., Lücke, A. Mayr, C., Ohlendorf, C., H., S. G., and Zolitschka, B. (2007). Vegetation and climate dynamics in southern South America: The microfossil record of Laguna Potrok Aike, Santa Cruz, Argentina. *Review of Palaeobotany and Palynology*, 146:234–246.

[Winckler and Fischer, 2006] Winckler, G. and Fischer, H. (2006). 30 000 years of cosmic dust in Antarctic ice. *Science*, 313:491.

[Wolff et al., 2006] Wolff, E. W., Fischer, H., Fundel, F., Ruth, U., Twarloh, B., Littot, G., Mulvaney, R., Röthlisberger, R., de Angelis, M., Boutron, C., Hansson, M., Jonsell, U., Hutterli, M.and Bigler, M., Lambert, F., Kaufmann, P., Stauffer, B., Steffensen, J. P., Siggaard-Andersen, M. L., Udisti, R., Becagli, S., Castellano, E., Severi, M., Wagenbach, D., Barbante, C., Gabrielli, P., and Gaspari, V. (2006). Southern Ocean sea-ice extent, productivity and iron flux over the past eight glacial cycles. *Nature*, 440:491–496.

[Wyrwoll et al., 2000] Wyrwoll, K.-H., Dong, B., and Valdes, P. (2000). On the position of southern hemisphere westerlies at the Last Glacial Maximum: an outline of AGCM simulation results and evaluation of their implications. *Quaternary Science Reviews*, 19:881–898.

[Yung et al., 1996] Yung, Y. L., Lee, T., Wang, C.-H., and Shieh, Y.-T. (1996). Dust: a diagnostic of the hydrologic cycle during the last glacial maximum. *Science*, 271:962–963.

[Zender et al., 2003] Zender, C. S., Bian, H., and Newman, D. (2003). Mineral Dust Entrainment and Deposition (DEAD) model: Description and 1990s dust climatology. *Journal of Geophysical Research*, 108:4416.

In the following four publications are appended, which evolved during this work:
The personal contribution was the following:

- Paper I and Paper II: laboratory work on the continuous flow analysis to obtain, ionic species, dust and other parameters and discussion of the results

- Paper III: measurements on the ICP-Sector Field-MS and on the ICP-Quadrupole-MS and discussion of the results

- Paper IV: calibration for the laser sensor system and discussion of the results

Paper I

One-to-one coupling of glacial climate variability in Greenland and Antarctica

nature

One-to-one coupling of glacial climate variability in Greenland and Antarctica

EPICA Community Members*

Precise knowledge of the phase relationship between climate changes in the two hemispheres is a key for understanding the Earth's climate dynamics. For the last glacial period, ice core studies[1,2] have revealed strong coupling of the largest millennial-scale warm events in Antarctica with the longest Dansgaard–Oeschger events in Greenland[3–5] through the Atlantic meridional overturning circulation[6–8]. It has been unclear, however, whether the shorter Dansgaard–Oeschger events have counterparts in the shorter and less prominent Antarctic temperature variations, and whether these events are linked by the same mechanism. Here we present a glacial climate record derived from an ice core from Dronning Maud Land, Antarctica, which represents South Atlantic climate at a resolution comparable with the Greenland ice core records. After methane synchronization with an ice core from North Greenland[9], the oxygen isotope record from the Dronning Maud Land ice core shows a one-to-one coupling between all Antarctic warm events and Greenland Dansgaard–Oeschger events by the bipolar seesaw[6]. The amplitude of the Antarctic warm events is found to be linearly dependent on the duration of the concurrent stadial in the North, suggesting that they all result from a similar reduction in the meridional overturning circulation.

The glacial climate in the North Atlantic region is characterized by rapid shifts from cold stadial to warmer interstadial conditions[3,4,9]. Greenland temperatures during these Dansgaard–Oeschger (D–O) events rise by 8–16 °C (refs 10, 11) within a few decades followed by a less rapid temperature decline back to stadial conditions. In contrast, glacial climate in the circum-Antarctic region exhibits slower millennial changes with smaller temperature amplitudes of only 1–3 °C (refs 1, 12, 13). After synchronization of Greenland and Antarctic ice core records[1,2] using the global atmospheric change in CH_4 concentrations, a conspicuous phase relationship between the largest Antarctic warmings (A1–A7; ref. 1) and the longest D–O events was observed with the south warming during the stadial conditions in the north, and starting to cool as soon as the D–O warming set in. This bipolar seesaw pattern was explained by changes in the heat and freshwater flux connected to the Atlantic Meridional Overturning Circulation (MOC), where a stronger MOC leads to increased drainage of heat from the Southern Ocean heat reservoir[6,7].

In principle, an interhemispheric climate coupling by the bipolar seesaw should also apply for all the short D–O events. However, to what extent this concept is also able to explain the higher-frequency climate variability in Antarctic ice cores remained unclear (as discussed for example, in ref. 14 and references therein). Here we report
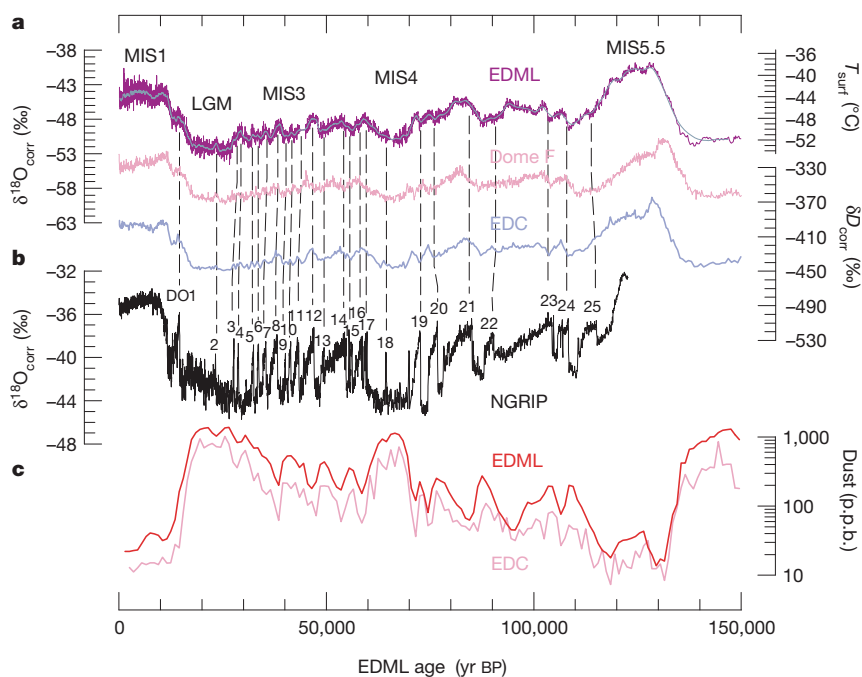
Figure 1 | Antarctic stable isotope records show synchronous millennial variations during the last glacial, whereas rapid variations are encountered in Greenland. a, EDML $\delta^{18}O$ record (purple, 0.5-m resolution; grey, 15-m running mean) after sea level and upstream correction (see Supplementary Information) over the past 150 kyr. The record shows features similar to those of the EDC[12] (blue) and the Dome F[13] (pink) isotope records but with more fine structure during MIS3 and MIS4. We note that EDML and EDC are plotted on the new common EDC3 timescale (see Supplementary Information) while Dome F is plotted on its individual timescale. The temperature axis on the right side indicates approximate surface temperatures at EDML as derived from the spatial $\delta^{18}O$/temperature gradient (see Supplementary Information). **b**, $\delta^{18}O$ record of the NGRIP ice core (grey)[9]. **c**, Mineral dust records of the EDML (red) and EDC[12] (pink) ice cores at 1,000-yr resolution; these dust records were used for synchronization of the cores.

on the climate record over the last glacial cycle from a new ice core drilled within the European Project for Ice Coring in Antarctica (EPICA) in the interior of Dronning Maud Land, hence denoted EDML, at 75° S, 0° E, 2,892 m.a.s.l. (metres above sea level), with a recent accumulation rate of 6.4 cm water equivalent (w.e.) per year[15]. This site was chosen to complement the long EPICA Dome C (EDC, 75° S, 123° E, 3,233 m.a.s.l., 2.5 cm w.e. yr^{-1}) record[12], because EDML is the first deep ice core in the Atlantic sector of the Southern Ocean region[16] and thus located near the southern end of the bipolar seesaw. The snow accumulation at EDML is two to three times higher than at other deep drilling sites on the East Antarctic plateau, so higher-resolution atmosphere and climate records can be obtained for the last glacial period, making the EDML core especially suitable for studying decadal-to-millennial climate variations in Antarctica.

In Fig. 1 the EDML $\delta^{18}O$ record as proxy for local temperature on the ice sheet is shown in 0.5-m resolution (equivalent to 15–30 yr during the marine isotope stage MIS3 and 100–150 yr during MIS5) after correction for upstream and glacial–interglacial ice sheet altitude effects (see Supplementary Information). The overall pattern closely resembles that recorded in most Antarctic ice cores previously covering this time period[12,13,17]. Also, very similar dust profiles (Fig. 1) are encountered at EDML and EDC, related to parallel changes in climate conditions in the Patagonian dust source region common to both cores[18]. Despite the high correlation of the EDML $\delta^{18}O$ and the EDC δD record over the last 150,000 yr ($r^2 = 0.94$ for 250-yr averages) some distinct differences exist. In the penultimate warm period (MIS5.5) the EDML $\delta^{18}O$ record indicates temperatures about 4–5 °C higher than those of the Holocene, in line with other ice cores from the East Antarctic plateau[12,13,17]. However, $\delta^{18}O$ at EDML exhibits persistently higher $\delta^{18}O$ values over the entire duration of MIS5.5 while other ice cores on the East Antarctic plateau show a substantial drop after an initial climate optimum[12,13]. We note that this difference is not due to the altitude corrections applied to the EDML $\delta^{18}O$ record (see Supplementary Information), because a similar temporal evolution during MIS5.5 is also seen in the uncorrected data. Instead, a smaller cooling at EDML in the course of MIS5.5 compared to EDC and Dome Fuji is consistent with marine sediment records from the Atlantic sector of the Southern Ocean revealing persistently warmer summer sea surface temperatures

and a reduced winter sea ice cover throughout MIS5.5 (ref. 19). This suggests that there were regional differences in temperature and sea ice evolution during this period for the Atlantic and Indian Ocean sector.

The most outstanding feature of the high-resolution EDML record is the pronounced millennial variability during the glacial. As indicated by the dashed lines in Fig. 1 each of the warming episodes in Antarctica can be related to a corresponding D–O event, but only synchronization of the age scales allows us to assign them unambiguously and to pinpoint the phase relationship between climate changes in Greenland and Antarctica. To do this, the EDML core has been synchronized (see Supplementary Information) to the layer counted NGRIP ice core[20,21] over MIS3, using high-resolution CH_4 profiles over the last 55 kyr from the NGRIP, GRIP and GISP2 ice cores[1,11]. The synchronized $\delta^{18}O$ records are shown in Fig. 2. Also plotted is the CH_4 synchronized $\delta^{18}O$ record from the Byrd ice core[1] and new high-resolution δD data from EDC[22] which closely resemble the temperature variability found at EDML during MIS3 and support an Antarctic-wide interpretation of these fluctuations. The higher glacial snow accumulation at EDML ($\sim$3 cm w.e. yr^{-1}) compared to that at EDC, Dome Fuji or Vostok ($\sim$1.4 cm w.e. yr^{-1}) implies a CH_4 synchronization two to three times better than at those sites. The synchronization uncertainty for MIS3 ranges from 400 to 800 yr for all events in the EDML record, making the synchronization error for EDML always much smaller than the duration of the events themselves.

This is important, because this allows an unequivocal one-to-one assignment not only of the well-known large warm events in Antarctica (A1, A2 and so on) but of each single isotope maximum indicated in Fig. 2 with a corresponding D–O event in the north. Although the exact timing of the temperature maxima relative to the stadial/interstadial transitions cannot be discerned more precisely than the synchronization error, it is evident that each Antarctic warming starts significantly before the respective D–O event. In addition, a synchronization of the stable water isotope records of the GRIP and EDC ice cores using the ^{10}Be production anomaly around 41,000 yr BP, which constrains the in-phase relationship of the onset of D–O 10 and the respective Antarctic δD maximum to better than 200 yr (ref. 23), supports our CH_4 match. Accordingly, we suggest a new Antarctic Isotope Maximum (AIM) nomenclature in Fig. 2
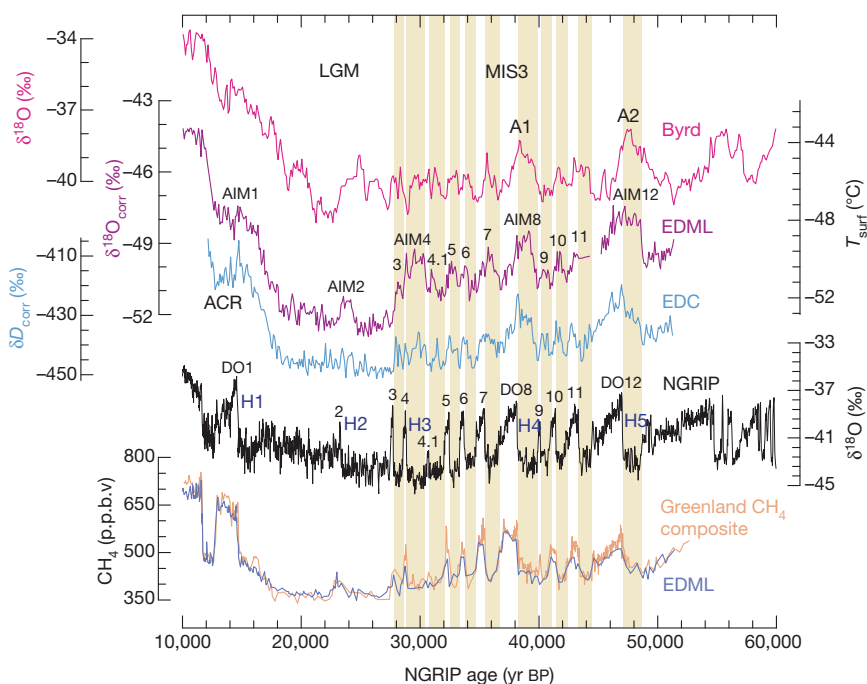
Figure 2 | Methane synchronization of the EDML and the NGRIP records reveals a one-to-one assignment of each Antarctic warming with a corresponding stadial in Greenland. Displayed are 100-yr averages during MIS3 in the EDML, EDC[26] and Byrd[1] ice core for the time interval 10–60 kyr BP in comparison with the NGRIP $\delta^{18}O$ record from Northern Greenland[9]. All records are CH_4 synchronized and given on the new GICC05 age scale for the NGRIP ice core, which has been derived by counting annual layers down to 41 kyr and by a flow model for older ages[9,21]. Yellow bars indicate the Greenland stadial periods that we relate to respective Antarctic temperature increases. The approximate timing of Heinrich layers in North Atlantic sediments is indicated as well[27]. The y axis on the right side indicates approximate temperature changes at EDML based on the modern spatial gradient between $\delta^{18}O$ and temperature.
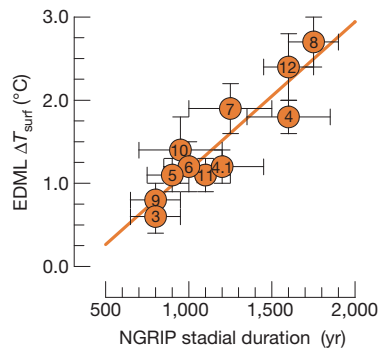
**Figure 3 | Amplitudes of Antarctic warmings show a linear relationship
($r^2 = 0.85$) with the duration of the accompanying stadial in Greenland
during MIS3.** The amplitude was determined from the Antarctic $\delta^{18}O$
maximum to the preceding minimum of each event; the stadial duration is
defined by the interval between the midpoint of the stepwise temperature
change at the start and end of a stadial on the extended GICC05 age scale[9,21].
Error bars reflect the estimated uncertainty in the definition of the maxima
and minima in $\delta^{18}O$ at EDML and in the duration of the concurrent stadial
period. Numbers indicate the corresponding AIMs and D–O events.

which reflects the connection of southern warming to reduced
oceanic heat transport into the North Atlantic during stadials. The
timing and duration of the AIMs relative to D–O events is also
indirectly supported by the comparison of changes in deep-water
masses linked to Antarctic Bottom Water formation and Atlantic
surface water changes, as archived in sediment records offshore of
Portugal[24].

Most striking is the varying amplitude of the AIMs, which is lin-
early dependent on the duration of stadials in the north, as shown in
Fig. 3. The only significant deviation from this linear relationship
during MIS3 is AIM4, in which the error in the stadial duration
estimate is quite large. We conclude that the duration of a reduced
MOC—and, hence, the duration of the warming period in the
Southern Ocean—determines the amount of heat accumulated in
the Southern Ocean heat reservoir, strongly supporting the general
applicability of the thermal bipolar seesaw[6] concept within the range
of stadial events encountered during MIS3. We note that for longer
cessations of the MOC a new equilibrium temperature in the
Southern Ocean would be reached and the warming would even-
tually have to cease. This linear relationship also implies that the
Antarctic warming rate—and thus the heat flux from the Southern
Ocean to the Atlantic—is similar for all warming events during MIS3.
If we assume the same spatial configuration of the overturning cell for
cold intervals in MIS3, this would suggest that the strength of the
MOC is approximately constant for all stadials, challenging the
notion of different overturning rates[25] for stadials in which massive
iceberg discharges into the North Atlantic (the so-called Heinrich
events in Fig. 2: H1–H5) occurred compared to stadials without
Heinrich events. Note however, that the stadials before D–O 8 and
D–O 12 in which Heinrich events occurred were the longest and the
related Antarctic warmings the largest. This may be due to the longer
time needed to mix away the large freshwater anomalies during
Heinrich events. There is, however, a less clear relationship for other
Heinrich events. Comparison of the millennial climate variability
during MIS3 at EDML and EDC shows no significant difference in
the amplitude of the isotopic change in the Atlantic and Indian Ocean
sectors of the Southern Ocean. This implies a uniform ocean heat
reservoir controlling temperature changes at both sites and reflects
the rapid mixing of the Southern Ocean by the Antarctic
Circumpolar Current.

In the EDML $\delta^{18}O$ record a major warm event (AIM2, connected
to D–O 2) is seen during the Last Glacial Maximum, which cannot be
clearly identified in the EDC core but is present in the Dome F record
(Fig. 1). AIM2 also shows a decrease in high-resolution mineral dust
concentrations at EDC, as do all the other AIMs[26]. We therefore

conclude that AIM2 is a warm event comparable to the other AIMs
in MIS3 but is not sufficiently resolved in the EDC record owing to its
lower accumulation. The corresponding D–O 2 event in the North
Atlantic is preceded by the longest cold period in the NGRIP record
(Fig. 2) and accordingly, a higher temperature amplitude of AIM2 is
to be expected if the same bipolar seesaw concept holds as for D–O
events during MIS3. However, sea level and temperature conditions
were significantly different during the Last Glacial Maximum, poten-
tially affecting the spatial configuration and strength of the overturn-
ing cell in the North Atlantic. The fact that AIM2 is only 2,000 yr long
suggests that the strength of the MOC was not significantly reduced
for the entire cold period in the North, but collapsed only about
1,000 yr before D–O 2, which would be in line with significant iceberg
discharge depositing ice-rafted debris in the North Atlantic during
H2 (ref. 27).

In summary, a strong interhemispheric coupling of all bipolar
climate variations during MIS3 via the MOC is supported by the
new high-resolution $\delta^{18}O$ record from EDML indicating that
Antarctic warming rates and potentially also overturning rates have
been similar for all events in MIS3. The question of what triggers the
switch from stadial to interstadial conditions remains. Transitions in
the strength of the MOC and its effect on the Atlantic Southern
Ocean heat exchange are simulated in response to changes in the
North Atlantic freshwater balance[7,8]; however, the origin of such
variations in freshwater input are still not ascertained for all indi-
vidual D–O events. In addition, large iceberg discharge from the
Laurentide ice sheet does not systematically coincide with either
the onset or the end of stadials[27,28]. Recently, the potential role of a
change in Southern Ocean sea-ice cover for reinstalling a stronger
MOC has been identified for the onset of the Bølling/Allerød warm-
ing[29,30]. The intrinsic feedback of a reduced sea-ice cover in the
Southern Ocean during AIMs, followed by a delayed onset of deep-
water formation in the North, could potentially explain the interhe-
mispheric climate coupling seen in our records during MIS3.

1. Blunier, T. & Brook, E. J. Timing of millennial-scale climate change in Antarctica
    and Greenland during the last glacial period. *Science* **291**, 109–112 (2001).
2. Blunier, T. *et al.* Asynchrony of Antarctic and Greenland climate change during the
    last glacial period. *Nature* **394**, 739–743 (1998).
3. Johnsen, S. J. *et al.* Irregular glacial interstadials recorded in a new Greenland ice
    core. *Nature* **359**, 311–313 (1992).
4. Bond, G. *et al.* Correlations between records from North Atlantic sediments and
    Greenland ice. *Nature* **365**, 143–147 (1993).
5. McManus, J. F., Oppo, D. W. & Cullen, J. L. A 0.5-million-year record of millennial
    climate variability in the North Atlantic. *Science* **283**, 971–975 (1999).
6. Stocker, T. F. & Johnsen, S. J. A minimum thermodynamic model of the bipolar
    seesaw. *Paleoceanography* **18**, art. no. 1087 (2003).
7. Knutti, R., Flückiger, J., Stocker, T. F. & Timmermann, A. Strong hemispheric
    coupling of glacial climate through freshwater discharge and ocean circulation.
    Nature **430**, 851–856 (2004).
8. Ganopolski, A. & Rahmstorf, S. Rapid changes of glacial climate simulated in a
    coupled climate model. *Nature* **409**, 153–158 (2001).
9. North Greenland Ice Core Project members. High resolution climate record of the
    northern hemisphere reaching into the last interglacial period. *Nature* **431**, 147–151
    (2004).
10. Landais, A. *et al.* Quantification of rapid temperature change during DO event 12
    and phasing with methane inferred from air isotopic measurements. *Earth Planet.
    Sci. Lett.* **225**, 221–232 (2004).
11. Huber, C. *et al.* Isotope calibrated Greenland temperature record over Marine
    Isotope Stage 3 and its relation to CH₄. *Earth Planet. Sci. Lett.* **245**, 504–519
    (2006).
12. EPICA community members. Eight glacial cycles from an Antarctic ice core.
    Nature **429**, 623–628 (2004).
13. Watanabe, O. *et al.* Homogeneous climate variability across East Antarctica over
    the past three glacial cycles. *Nature* **422**, 509–512 (2003).
14. Roe, G. H. & Steig, E. J. Characterization of millennial-scale climate variability. *J.
    Clim.* **17**, 1929–1944 (2004).
15. Oerter, H. *et al.* Accumulation rates in Dronning Maud Land, Antarctica, as
    revealed by dielectric-profiling measurements of shallow firn cores. *Ann. Glaciol.*
    30, 27–34 (2000).
16. Reijmer, C. H., van den Broeke, M. R. & Scheele, M. P. Air parcel trajectories to five
    deep drilling locations on Antarctica, based on the ERA-15 data set. *J. Clim.* **15**,
    1957–1968 (2002).

17. Petit, J. R. *et al.* Climate and atmospheric history of the past 420,000 years from the Vostok ice core, Antarctica. *Nature* **399**, 429–436 (1999).

18. Basile, I. *et al.* Patagonian origin of glacial dust deposited in East Antarctica (Vostok and Dome C) during glacial stages 2, 4 and 6. *Earth Planet. Sci. Lett.* **146**, 573–589 (1997).

19. Bianchi, C. & Gersonde, R. The Southern Ocean surface between Marine Isotope Stage 6 and 5d: Shape and timing of climate changes. *Palaeogeogr. Palaeoclimatol. Palaeoecol.* **187**, 151–177 (2002).

20. Rasmussen, S. O. *et al.* A new Greenland ice core chronology for the last glacial termination. *J. Geophys. Res.* **111**, D06102 (2006).

21. Andersen, K. K. *et al.* The Greenland ice core chronology 2005, 15–42 kyr. Part 1: Constructing the time scale. *Quat. Sci. Rev.* (in the press).

22. Stenni, B. *et al.* A late-glacial high-resolution site and source temperature record derived from the EPICA Dome C isotope records (East Antarctica). *Earth Planet. Sci. Lett.* **217**, 183–195 (2003).

23. Raisbeck, G., Yiou, F. & Jouzel, J. Cosmogenic [10]Be as a high resolution correlation tool for climate records. *Geochim. Cosmochim. Acta* **66**, abstr. A623 (2002).

24. Shackleton, N. J., Hall, M. A. & Vincent, E. Phase relationships between millennial-scale events 64,000–24,000 years ago. *Paleoceanography* **15**, 565–569 (2000).

25. Rahmstorf, S. Ocean circulation and climate during the past 120,000 years. *Nature* **419**, 207–214 (2002).

26. Röthlisberger, R. *et al.* Dust and sea-salt variability in central East Antarctica (Dome C) over the last 45 kyrs and its implications for southern high-latitude climate. *Geophys. Res. Lett.* **29**, article no. 1963 (2002).

27. Bond, G. & Lotti, R. Iceberg discharges into the North Atlantic on millennial time scales during the last glaciation. *Science* **267**, 1005–1010 (1995).

28. de Abreu, L., Shackleton, N. J., Joachim Schönfeld, J., Hall, M. & Chapman, M. Millennial-scale oceanic climate variability off the Western Iberian margin during the last two glacial periods. *Mar. Geol.* **196**, 1–20 (2003).

29. Knorr, G. & Lohmann, G. Southern Ocean origin for the resumption of Atlantic thermohaline circulation during deglaciation. *Nature* **424**, 532–536 (2003).

30. Stocker, T. F. & Wright, D. G. Rapid transitions of the ocean's deep circulation induced by changes in surface water fluxes. *Nature* **351**, 729–732 (1991).

EPICA Community Members (listed in alphabetical order): C. Barbante[1,2], J.-M. Barnola[3], S. Becagli[4], J. Beer[5], M. Bigler[6,7], C. Boutron[3], T. Blunier[6], E. Castellano[4], O. Cattani[8], J. Chappellaz[3], D. Dahl-Jensen[7], M. Debret[3], B. Delmonte[9], D. Dick[10], S. Falourd[8], S. Faria[10,11], U. Federer[6], H. Fischer[10], J. Freitag[10], A. Frenzel[10], D. Fritzsche[12], F. Fundel[10], P. Gabrielli[2,3], V. Gaspari[1], R. Gersonde[10], W. Graf[13], D. Grigoriev[14], I. Hamann[10], M. Hansson[15], G. Hoffmann[8], M. A. Hutterli[6,16], P. Huybrechts[10,17], E. Isaksson[18], S. Johnsen[7], J. Jouzel[8], M. Kaczmarska[18], T. Karlin[15], P. Kaufmann[6], S. Kipfstuhl[10], M. Kohno[10], F. Lambert[6], Anja Lambrecht[10], Astrid Lambrecht[10], A. Landais[8], G. Lawer[10], M. Leuenberger[6], G. Littot[16], L. Loulergue[3], D. Lüthi[6], V. Maggi[9], F. Marino[9], V. Masson-Delmotte[8], H. Meyer[12], H. Miller[10], R. Mulvaney[16], B. Narcisi[19], J. Oerlemans[20], H. Oerter[10], F. Parrenin[3], J.-R. Petit[3], G. Raisbeck[21], D. Raynaud[3], R. Röthlisberger[16], U. Ruth[10], O. Rybak[10], M. Severi[4], J. Schmitt[10], J. Schwander[6], U. Siegenthaler[6], M.-L. Siggaard-Andersen[7], R. Spahni[6], J. P. Steffensen[7], B. Stenni[22], T. F. Stocker[6], J.-L. Tison[23], R. Traversi[4], R. Udisti[4], F. Valero-Delgado[10], M. R. van den Broeke[20], R. S. W. van de Wal[20], D. Wagenbach[24], A. Wegner[10], K. Weiler[6], F. Wilhelms[10], J.-G. Winther[18] & E. Wolff[16]

[1]Department of Environmental Sciences, University Ca' Foscari of Venice, [2]Institute for the Dynamics of Environmental Processes-CNR, Dorsoduro 2137, 30123 Venice, Italy. [3]Laboratoire de Glaciologie et Géophysique de l'Environnement (LGGE), CNRS-UJF, BP96 38402 Saint-Martin-d'Hères cedex, France. [4]Department of Chemistry, University of Florence, Via della Lastruccia 3, 50019 Sesto Fiorentino, Florence, Italy. [5]EAWAG, PO Box 611, 8600 Dübendorf, Switzerland. [6]Climate and Environmental Physics, Physics Institute, University of Bern, Sidlerstrasse 5, 3012 Bern, Switzerland. [7]Niels Bohr Institute, University of Copenhagen, Juliane Maries Vej 30, 2100 Copenhagen OE, Denmark. [8]Laboratoire des Sciences du Climat et de l'Environnement (LSCE/IPSL), CEA-CNRS-UVSQ, CE Saclay 91191, Gif sur Yvette, France. [9]Environmental Sciences Department, University of Milano Bicocca, Piazza della Scienza 1, 20126 Milano, Italy. [10]Alfred-Wegener-Institute for Polar and Marine Research, Columbusstrasse, D-27568 Bremerhaven, Germany. [11]Max Planck Institute for Mathematics in the Sciences, Inselstrasse 22, 04103 Leipzig, Germany. [12]Alfred Wegener Institute for Polar and Marine Research, Research Unit Potsdam, Telegrafenberg A 43, 14473 Potsdam, Germany. [13]GSF National Center for Environment and Health, Ingolstädter Landstrasse 1, 85764 Neuherberg, Germany. [14]University College London, Gower Street, London WC1E 6BT, UK. [15]Department of Physical Geography and Quaternary Geology, Stockholm University, 106 91 Stockholm, Sweden. [16]British Antarctic Survey, High Cross, Madingley Road, Cambridge CB3 0ET, UK. [17]Departement Geografie, Vrije Universiteit Brussel, Pleinlaan 2, 1050 Brussel, Belgium. [18]Norwegian Polar Institute, 9296 Tromsø, Norway. [19]ENEA, C. R. Casaccia, Via Anguillarese 301, 00060 Roma, Italy. [20]Utrecht University, Institute for Marine and Atmospheric Research, PO Box 80005, 3508 TA Utrecht, The Netherlands. [21]CSNSM/IN2P3/CNRS, Bat. 108, 91405 Orsay, France. [22]Department of Geological, Environmental and Marine Sciences, University of Trieste, Via E. Weiss 2, 34127 Trieste, Italy. [23]Département des Sciences de la Terre, Université Libre de Bruxelles, CP160/03, 1050 Brussels, Belgium. [24]Institute for Environmental Physics, University of Heidelberg, INF229, 69120 Heidelberg, Germany.

Paper II

Reconstruction of millenial changes in the dust emission, transport and regional sea ice coverage using the deep EPICA ice cores from the Atlantic and the Indian sector of Antarctica

Fischer, H., Fundel, F., Ruth, U., Twarloh, B., Wegner, A., Udisti, R., Becagli, S., Castellano, E., Morganti, A. and Severi, M., Wolff, E., Littot, G., Röthlisberger, R., Mulvaney, R., Hutterli, M. A., Kaufmann, P., Federer, U., Lambert, F., Bigler, M., Hansson, M., Jonsell, U., de Angelis, M., Boutron, C., Siggaard-Andersen, M. L., Steffensen, J. P., Barbante, C., Gaspari, V., Gabrielli, P. and Wagenbach, D. (2007), Earth and Planetary Science Letters, 260, 340-354.

Reconstruction of millennial changes in dust emission, transport and regional sea ice coverage using the deep EPICA ice cores from the Atlantic and Indian Ocean sector of Antarctica

Hubertus Fischer [a,*], Felix Fundel [a], Urs Ruth [a], Birthe Twarloh [a], Anna Wegner [a],
Roberto Udisti [b], Silvia Becagli [b], Emiliano Castellano [b], Andrea Morganti [b],
Mirko Severi [b], Eric Wolff [c], Genevieve Littot [c], Regine Röthlisberger [c],
Rob Mulvaney [c], Manuel A. Hutterli [d,c], Patrik Kaufmann [d],
Urs Federer [d], Fabrice Lambert [d], Matthias Bigler [d,g],
Margareta Hansson [e], Ulf Jonsell [e], Martine de Angelis [f],
Claude Boutron [f], Marie-Louise Siggaard-Andersen [g],
Jorgen Peder Steffensen [g], Carlo Barbante [h,i],
Vania Gaspari [h], Paolo Gabrielli [i], Dietmar Wagenbach [j]

[a] *Alfred-Wegener-Institute for Polar and Marine Research, Columbusstrasse, D-27568 Bremerhaven, Germany*
[b] *Department of Chemistry, University of Florence, Via della Lastruccia 3, 50019 Sesto Fiorentino (Florence), Italy*
[c] *British Antarctic Survey, High Cross, Madingley Road, Cambridge CB3 0ET, UK*
[d] *Climate and Environmental Physics, Physics Institute, University of Bern, Sidlerstr.5, 3012 Bern, Switzerland*
[e] *Department of Physical Geography and Quaternary Geology Stockholm University, 106 91 Stockholm, Sweden*
[f] *Laboratoire de Glaciologie et Géophysique de l'Environnement (LGGE), CNRS-UJF, BP96 38402 Saint-Martin-d'Hères Cedex, France*
[g] *Niels Bohr Institute, University of Copenhagen, Juliane Maries Vej 30, 2100 Copenhagen OE, Denmark*
[h] *Department of Environmental Sciences, University Ca' Foscari of Venice, Dorsoduro 2137, 30123 Venice, Italy*
[i] *Institute for the Dynamics of Environmental Processes-CNR, Dorsoduro 2137, 30123 Venice, Italy*
[j] *Institute for Environmental Physics, University of Heidelberg, INF229, 69120 Heidelberg, Germany*

Abstract

Continuous sea salt and mineral dust aerosol records have been studied on the two EPICA (European Project for Ice Coring in Antarctica) deep ice cores. The joint use of these records from opposite sides of the East Antarctic plateau allows for an estimate of changes in dust transport and emission intensity as well as for the identification of regional differences in the sea salt aerosol source. The mineral dust flux records at both sites show a strong coherency over the last 150 kyr related to dust emission changes in the glacial Patagonian dust source with three times higher dust fluxes in the Atlantic compared to the Indian Ocean sector of the Southern Ocean (SO). Using a simple conceptual transport model this indicates that transport can explain only 40% of the atmospheric dust concentration changes in Antarctica, while factor 5–10 changes occurred. Accordingly, the main cause for the

* Corresponding author.
E-mail address: hubertus.fischer@awi.de (H. Fischer).

strong glacial dust flux changes in Antarctica must lie in environmental changes in Patagonia. Dust emissions, hence environmental conditions in Patagonia, were very similar during the last two glacials and interglacials, respectively, despite 2–4 °C warmer temperatures recorded in Antarctica during the penultimate interglacial than today. 2–3 times higher sea salt fluxes found in both ice cores in the glacial compared to the Holocene are difficult to reconcile with a largely unchanged transport intensity and the distant open ocean source. The substantial glacial enhancements in sea salt aerosol fluxes can be readily explained assuming sea ice formation as the main sea salt aerosol source with a significantly larger expansion of (summer) sea ice in the Weddell Sea than in the Indian Ocean sector. During the penultimate interglacial, our sea salt records point to a 50% reduction of winter sea ice coverage compared to the Holocene both in the Indian and Atlantic Ocean sector of the SO. However, from 20 to 80 ka before present sea salt fluxes show only very subdued millennial changes despite pronounced temperature fluctuations, likely due to the large distance of the sea ice salt source to our drill sites.

1. Introduction

Antarctic glacial/interglacial temperature changes have been reconstructed over up to eight glacial cycles using deep ice cores drilled on the Antarctic plateau (Petit et al., 1999; Watanabe et al., 2003; EPICA community members, 2004; Brook et al., 2005; EPICA community members, 2006; Jouzel et al., in press) and on coastal ice domes (Steig et al., 1998; Morgan et al., 2002). Such climate records are generally interpreted as being representative for the whole SO region, which plays a key role in glacial/interglacial climate changes (Blunier et al., 1997; Knorr and Lohmann, 2003; Stocker and Johnsen, 2003) and the global carbon cycle (Archer et al., 2001; Köhler et al., 2005; Toggweiler et al., 2006). However, while the large-scale glacial/interglacial

Fig. 1. Map of the Antarctic continent indicating the EPICA drill sites in Dronning Maud Land (EDML) facing the Atlantic sector of the SO and at Dome C (EDC) facing the Indian Ocean sector of the SO together with previously drilled deep ice cores on the Antarctic plateau.

changes are imprinted in all those records (Watanabe et al., 2003) the influence of different air mass origin allows us to reconstruct also regional differences in climate evolution (Morgan et al., 2002). Moreover, while temperature changes have been documented in many Antarctic ice cores, regional information on accompanying environmental changes is still limited. Especially, temporally resolved information on a dust induced iron fertilization of marine phytoplankton productivity (Martin, 1990) and on reduced gas exchange and decreased mixing of the ocean due to an increase in sea ice cover (Toggweiler, 1999; Stephens and Keeling, 2000; Köhler et al., 2005) is needed to constrain the carbon cycle/climate feedback. Independent information on mineral dust deposition and sea ice coverage in different regions of Antarctica can be deduced from aerosol records in deep Antarctic ice cores (Petit et al., 1990; Delmonte et al., 2002; Röthlisberger et al., 2002; Wolff et al., 2003; Udisti et al., 2004; Wolff et al., 2006; Fischer et al., 2007).

Within the European Project for Ice Coring in Antarctica (EPICA) two deep ice cores have recently been drilled (Fig. 1). The core at Dome C (EPICA community members, 2004) (EDC: 75°06′S, 123°21′E, 3233 m above sea level) in the Indian Ocean sector of Antarctica comprises undisturbed ice core records over the last approximately 800 kyr (Jouzel et al., in press). The second ice core was drilled at Kohnen station in Dronning Maud Land (EPICA community members, 2006) (EDML: 75°00′S, 00°04′E, 2882 m above sea level). With a snow accumulation rate 2–3 times higher than at EDC it provides higher resolution records down to Marine Isotope Stage (MIS) 4. Moreover, due to its location it represents the first ice core closely linked to climate changes in the Atlantic sector of the SO.

In the following, we report on mineral dust (represented by non-sea salt calcium ($nssCa^{2+}$)) and sea salt aerosol (represented by sea salt sodium ($ssNa^+$)) records derived from both ice cores in decadal to centennial
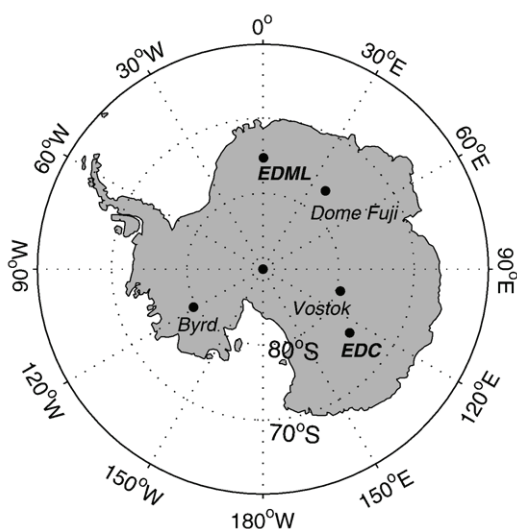
resolution. The change of these parameters in the EDC ice core has been previously discussed for the last 45 kyr in high resolution (Röthlisberger et al., 2002) and in millennial resolution over the last 740 kyr (Wolff et al., 2006). Here we extend the discussion of the centennial sea salt and mineral dust record from EDC to the last 150 kyr. More importantly, we contrast the EDC data to the first continuous aerosol records from the Atlantic sector of the Antarctic ice sheet as archived in the deep EDML ice core. This way we can make use of the coherencies and differences between the two records located on opposite sides of the East Antarctic plateau allowing for an estimate of changes in transport intensity and for the identification of regional differences in aerosol source strengths.

2. Methods

2.1. Age scales

The age scale (called EDC3) for the EDC core was derived using an accumulation and ice flow model constrained by independent age markers (Parrenin et al., 2007). For internal coherence, a dependent EDML age scale (called EDML1) has been derived for the last 150 kyr by synchronizing the EDC and EDML ice core (Ruth et al., 2007; Severi et al., 2007) using volcanic horizons in sulfate, in the dielectric profile as well as electrolytic conductivity down to a depth of 2366 m (equivalent to 128 ka before present (BP) where present is defined as 1950). Below this depth no unambiguous volcanic synchronization could be established and we relied on a few pronounced dust match points to synchronize both cores. Due to the hemispheric and often global impact of volcanic eruptions on sulfuric acid deposition and due to the common glacial dust source for EDML and EDC in Patagonia (Grousset et al., 1992; Basile et al., 1997; Delmonte et al., 2004a,b) this procedure provides unambiguous isochrones in both ice cores and allows for direct comparison of regional differences in the two cores independent of absolute dating uncertainties. Below 150 ka BP no unambiguous matching has been accomplished yet (Ruth et al., 2007). Accordingly, we will restrict the discussion of the EDML chemistry data to the last 150 kyr.

For this time period the absolute dating uncertainty of the EDC3 age scale is always better than 6000 yr (Parrenin et al., 2007). During MIS 3 the absolute uncertainty of the age scale is less than 1500 yr. More important for our comparison of the EDC and EDML ice cores is the internal consistency of the EDC3 and the EDML1 age scale, which is defined by the synchronization uncertainty. The

maximum synchronization uncertainty at 130 ka BP is 450 yr and even larger for older ages. However, during most of the record the maximum synchronization uncertainty is smaller and on average about 40 yr (Ruth et al., 2007). Note, that this maximum synchronization uncertainty is a conservative estimate and the typical synchronization uncertainty is even smaller (on average 6 yr over the last 130 kyr). Thus, the interpolation error is always small compared to the absolute dating uncertainty and allows for unprecedented synchronization of these two independent climate archives. Among others, this becomes crucial when directly comparing aerosol fluxes at both sites at a given point in time.

2.2. Chemical analyses

Samples for chemical analyses have been taken using a continuous flow melting device, which precludes contact of the melt water with contaminated ice core surfaces (Röthlisberger et al., 2000). EDML Concentrations of Ca^{2+} and Na^+ presented here have been determined using ion chromatography (IC), while the top 580 m of Ca^{2+} data at Dome C have been determined using continuous flow analysis (CFA) (Röthlisberger et al., 2002; Wolff et al., 2006). Analytical details for the EDC chemistry data set are summarized in Wolff et al. (2006). The uncertainty in IC analyses is mainly determined by the lab dependent blank contribution, while the instrument detection limit is one order of magnitude lower. The average blank contribution for EDML lies between 3 and 50% of the Ca^{2+} concentration for average glacial and interglacial conditions, respectively, and between 2 and 5% in the case of Na^+. The reproducibility of the Ca^{2+} and Na^+ data is typically better than 10% and even better than 5% during glacial conditions. During interglacial periods the reproducibility of Ca^{2+} concentrations lower than 2 ppb deteriorates to around 50%. The CFA based EDC Holocene record is not affected by this blank contribution. For the EDML ice core the top 113 m were not sampled. The depth interval 113–450 m in the EDML ice core covering the time period from 1200 to 6700 a BP has been sampled in 5 cm resolution and then averaged to 1 m intervals for this study. Analyses of these 6400 high-resolution samples were done in 4 continuous batches in 4 different laboratories. Due to different lab procedures blank values and reproducibility of the different batches vary from lab to lab. To account for the interlaboratory differences in mean blank contribution and to gain a homogeneous record throughout the Holocene, the concentration values have been corrected by subtracting the mean concentration difference in neighboring 5 m depth intervals in each of the adjacent

batches with the depth interval 273–450 m taken as reference interval. To avoid a bias by high concentration peaks we used the median to estimate the mean concentration level. In doing so, all data are corrected to the same average blank contribution, assuming that no change in average atmospheric concentrations occurred in the adjacent 5 m intervals used for the correction, representing a time interval of approximately 150 yr. With this procedure we are able to avoid interlaboratory offsets between the batches while retaining as much long-term variability in the individual batches as possible. For the sodium record the average correction was −0.8 ppb (the maximum correction was −2.4 ppb applied to one batch) which is less than 5% (maximum 14%) of the average concentration. For the calcium record the correction was on average 0.2 ppb (maximum correction −3.0 ppb applied to one batch), i.e. about 9% (maximum 130%) of the average concentration. Note, that these interlaboratory corrections affect only the Holocene record and are rather small for Na^+. For Holocene samples with low Ca^{2+} concentrations these corrections are significant and we have to state that we cannot determine the lower envelope of Holocene Ca^{2+} concentrations with certainty using IC. Note however, that these corrections do not affect any of our conclusions on glacial

aerosol variability, where Ca^{2+} concentrations are more than one order of magnitude higher. The depth interval 450–2774 m has been analyzed entirely in one lab in 1 m resolution and no interlaboratory offsets had to be corrected.

The contributions of sea salt and mineral dust to the total Ca^{2+} and Na^+ content have been corrected using the sea salt Ca^{2+}/Na^+ and the average crustal Ca^{2+}/Na^+ ratio of $R_m = 0.038$ and $R_t = 1.78$ (Bowen, 1979) (in bulk weight units), respectively (Röthlisberger et al., 2002). While this correction is of minor importance for interglacial sea salt aerosol (on average 10%) it becomes important for mineral dust in the Holocene where approximately 24% of the total Ca^{2+} content in the EDML core is derived from sea salt aerosol. In the peak glacial (20–30 ka BP) this effect is reversed. Here $nssCa^{2+}$ is on average only 5% lower than total Ca^{2+} while about 28% of the total sodium is of crustal origin. The composition of crustal tracers as recorded in ionic ice core data may differ from R_t which is based on the bulk elemental composition of insoluble crustal material. Note, that R_t may vary dependent on the composition of crustal material as well as on size dependent fractionation processes of different minerals during the formation of mineral dust aerosol. Ice core observations at EDC point to an R_t which may be
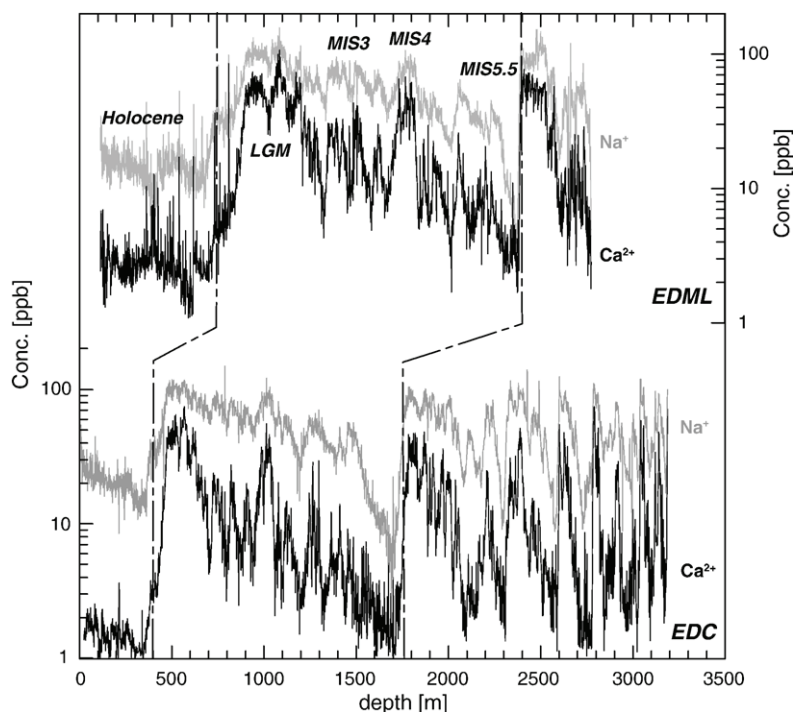
Fig. 2. Na^+ (grey line) and Ca^{2+} (black line) concentration records (logarithmic scale) as measured on the EDML (top) and EDC ice cores (bottom) on their individual depth scale in 1 m resolution. The dashed-dotted lines indicate pronounced isochronous dust changes during the last two glacial/interglacial transitions in both records.
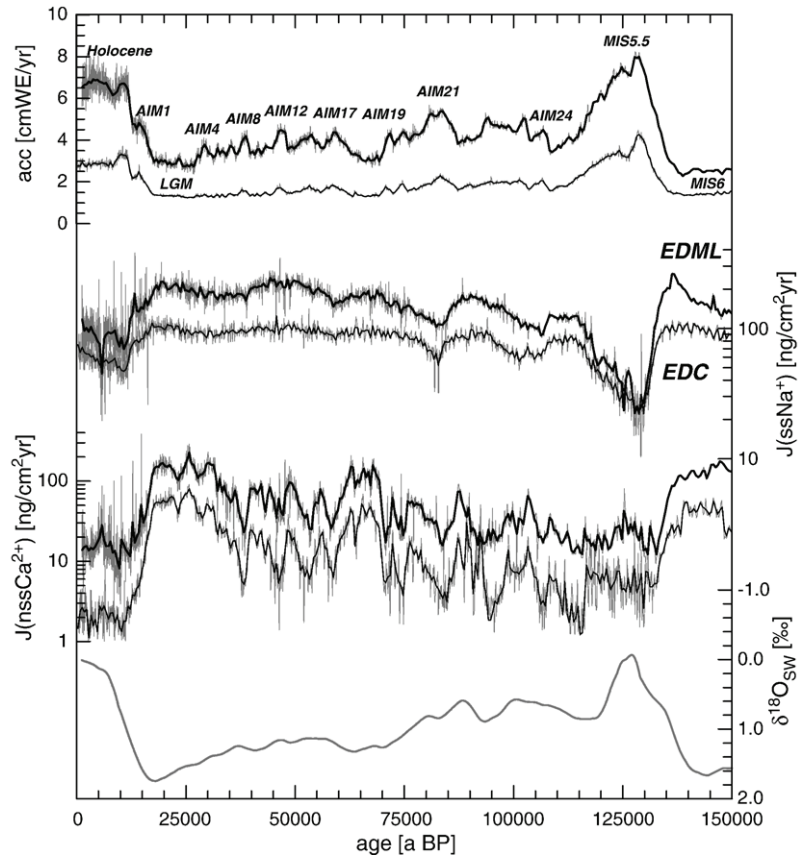
Fig. 3. Sea salt Na$^+$ (ssNa$^+$) and non-sea salt Ca^{2+} (nssCa^{2+}) flux records (logarithmic scale) over the last 150 kyr at EDML and EDC on the common EDML1/EDC3 age scale (Parrenin et al., 2007; Ruth et al., 2007). For comparison past accumulation rates at the site of deposition are given as derived from isotope temperature changes (δ^{18}O, δD) at EDML and EDC (EPICA community members, 2004, 2006) which have been used for flux calculations. Data are shown in 1 m resolution (thin grey lines) and 500 yr averages (thick black line for EDML and thin black line for EDC), the latter accounting for the loss in temporal resolution down core. Also depicted are reconstructed changes in benthic δ^{18}O representative of long-term sea level changes on the new EDML1/EDC age scale (Bintanja et al., 2005).

closer to 1 (Bigler et al., 2006). While the effect of such a variability in R_t changes the nssCa^{2+} estimate only by a few percent, its effect on ssNa$^+$ is considerable. For instance reducing R_t within reasonable bounds to 1 (Bigler et al., 2006) or increasing it to 3.5 changes the ssNa$^+$ estimate by 10–30% for glacial conditions in Antarctica (Fischer et al., 2007). Note, that R_t may also change from glacials to interglacials due to potentially shifting sources and weathering conditions, however, within reasonable limits of R_t this effect is too small to significantly affect our conclusions.

2.3. Accumulation rates and deposition fluxes

The total average deposition flux J_{tot} at an ice core site (Fischer et al., 2007) can be approximated by

$$J_{tot} = C_{ice}A = v_{dry}C_{air} + W/\rho_{air}C_{air}A.$$

The first term on the right hand side of this equation parameterizes the dry deposition and the second term the wet deposition flux with v_{dry} the total mean dry deposition velocity, W the scavenging ratio, ρ_{air} the density of air, C_{air} the atmospheric aerosol concentration and A the average accumulation rate. In low accumulation areas dry deposition dominates and the total flux is essentially independent of changes in accumulation and almost proportional to the atmospheric aerosol concentrations. Accordingly, we will discuss aerosol flux records in this study, which are more representative of atmospheric aerosol concentrations. Knowledge of the latter is a prerequisite for quantitative estimates of source strength or transport changes in the past. The total deposition flux was calculated by multiplying the measured ice concentration C_{ice} with reconstructed accumulation rates (Figs. 2 and 3). Both at EDC and EDML the accumulation rate is estimated from the

stable water isotope (δ^{18}O, δD) profiles (after correction for changes in the isotopic composition of sea water due to continental ice mass changes) essentially assuming thermodynamic control of the water vapor saturation pressure (EPICA community members, 2006; Parrenin et al., 2007). Second order corrections of non-thermodynamic effects on the accumulation rate at EDML have been made using the spatial variability in accumulation rates upstream of the drill site (EPICA community members, 2006) derived from firn cores and an extended surface radar survey (Oerter et al., 2000; Steinhage et al., 2001; Graf et al., 2002; Rybak et al., 2005) and at EDC by a one-dimensional flow model (Parrenin et al., 2007). The error of the reconstructed accumulation rates is estimated to be 30% for glacial times and significantly less for warm periods, where the precipitation regime is similar to today. This is also supported by comparing these continuous thermodynamically derived accumulation rates at EDML with discrete accumulation rates derived from the unstrained layer thickness between volcanic match points (Severi et al., 2007). Both accumulation estimates agree typically within ±20%. Because the accumulation information based on δ^{18}O can be calculated continuously in high resolution over the entire length of the core, we will use the thermodynamically derived accumulation rate in the following to derive aerosol fluxes. Based on the errors in accumulation rates and ion concentrations, the aerosol fluxes are constrained to better than 30% for the large majority of the samples and to better than 60% for very low Holocene Ca^{2+} concentrations. Note, that although these errors are considerable they are small compared to the order of magnitude change in glacial/interglacial Ca^{2+} concentrations and cannot explain systematic glacial variations on millennial time scales in concentration and flux records.

2.4. Upstream correction

In contrast to the EDC ice core, which is located on a dome position, the EDML ice core lies at a saddle position of the ice divide with small (about 1 m/yr) horizontal flow velocities. Accordingly, while the ice at Dome C originates at the current drill site, deeper ice at EDML originates from upstream positions at higher altitudes, where temperatures and accumulation rates are lower and the atmospheric aerosol concentrations may be slightly different. E.g. ice with an age of 150 ka BP has been deposited 160 km upstream (EPICA community members, 2006; Huybrechts et al., 2007). Note, that geographic effects in aerosol concentrations are small compared to the glacial/interglacial changes (Sommer

et al., 2000; Göktas et al., 2002). As outlined above the true total aerosol flux at the site of deposition should be almost independent from the local snow accumulation rate in low accumulation areas where dry deposition prevails. Accordingly, we used the local accumulation rate at the site of initial deposition to calculate total aerosol fluxes.

3. Results

The Ca^{2+} and Na^+ concentration records for both ice cores are shown on a depth scale in Fig. 2. The EDC record provides unprecedented data over 8 full glacial cycles, while the EDML record shows only 2 unambiguous glacial maxima. In return, the EDML record exhibits higher annual layer thicknesses down to a depth of 1900 m, allowing for higher resolution records down to an age of approximately 80 ka BP. The concentration records show comparable glacial/interglacial variations both at EDML and EDC with 1–2 orders of magnitude higher sea salt and mineral dust concentrations during glacial periods and significant millennial dust variability during marine isotope stage 2–4. Similar glacial/interglacial variability has been also reported from Vostok (de Angelis et al., 1997) and Taylor Dome (Mayewski et al., 1996) as far as temporal resolution allowed.

One major achievement for the EPICA ice cores is the unambiguous stratigraphic link between the two EPICA ice cores (Ruth et al., 2007; Severi et al., 2007). This common EDML1/EDC3 age scale allows for direct comparison of aerosol flux records and their interpretation in terms of atmospheric aerosol concentrations. In Fig. 3 the ssNa$^+$ and nssCa^{2+} flux records are plotted. The accompanying changes in the snow accumulation rate are given for comparison. Clearly, both records show a very high covariance between both sites in each of the aerosol species. However, nssCa^{2+} fluxes at EDML are about 3 times higher than at EDC showing that atmospheric nssCa^{2+} concentrations are substantially higher at EDML than at EDC. Isotopic fingerprinting for Dome C samples showed that Patagonia is the dominant source of mineral dust deposited at that site in the glacial (Basile et al., 1997; Delmonte et al., 2007) as also supported by dust modeling (Lunt and Valdes, 2001; Mahowald et al., 2006). In the interglacial an additional Australian dust source may be possible at Dome C (Revel-Rolland et al., 2006; Delmonte et al., 2007). Isotopic fingerprinting of mineral dust has not been accomplished yet at EDML, but a strong influence of Australian dust sources to EDML appears to be very unlikely, given its geographic location which is much closer to South America and downwind of the

cyclonically curved atmospheric pathway from Patagonia (Reijmer et al., 2002). Accordingly, we attribute the higher atmospheric $nssCa^{2+}$ concentrations at EDML to the greater proximity of EDML to the Patagonian dust source.

Also sea salt fluxes are about a factor of 2 higher at EDML than at EDC indicating higher atmospheric sea salt aerosol concentrations in Dronning Maud Land. Note, that in the case of sea salt wet deposition may have a stronger influence than is the case for dust. Transport of sea salt aerosol is closely linked to cyclonic activity and a higher contribution by wet deposition of sea salt aerosol may be expected. This holds especially at EDML, where large parts of the recent annual accumulation is derived from a few single snow fall events per year (Reijmer and van den Broeke, 2001), while at EDC only non-frontal diamond dust is observed. Model studies show that circum-Antarctic cyclone activity in the glacial was most likely reduced (Krinner and Genthon, 1998) due to the extended sea ice cover and an accompanying northward shift of the atmospheric polar front, reducing the effect of single precipitation events on sea salt transport to EDML at that time. Given the high covariance between both records and the extremely low glacial accumulation of 1–3 cm WE/yr at both sites a dominant influence of wet deposition during cold climate periods appears to be unlikely. This implies that glacial sea salt fluxes are largely representative of the true variations in atmospheric concentrations.

Most striking are the substantial changes in dust and sea salt fluxes over the last glacial cycle similarly found at both sites. The $nssCa^{2+}$ flux decreased by a factor of about 10 during the last two glacial/interglacial transitions (Fig. 3) at both sites. At the same time the $ssNa^+$ flux decreased at EDC by a factor of 2 and at EDML by a factor of 3 from the Last Glacial Maximum (LGM) to the Holocene and by a factor of 4–8 during the penultimate transition, essentially due to much lower $ssNa^+$ fluxes during the interglacial MIS 5.5. Apart from the glacial/interglacial changes in dust emissions, strong millennial variations in the $nssCa^{2+}$ flux are also observed, while such variations are very subdued in the sea salt record.

4. Discussion

4.1. Mineral dust

A key question is, how much of the glacial/interglacial and millennial variations in the glacial is due to changes in the aerosol transport or changes in aerosol source strength. Using the coherent change in glacial dust fluxes at both EPICA sites from opposite sides of the East Antarctic

plateau ($r^2 = 0.82$ for 100 yr averages), we are now able to constrain the influence of transport changes on the changes in mineral dust flux in Antarctica. Assuming the atmospheric aerosol concentration close to the source is given by $C_{air}(0)$ and an air parcel is transported away from the source, the atmospheric aerosol concentration C_{air} at any time t along the transport trajectory can to first order be approximated by

$$C_{air}(t) = C_{air}(0)\exp(-t/\tau) \quad \text{or}$$

$$\log[C_{air}(t)/C_{air}(0)] = -t/\tau$$

where t is the transport time and the average atmospheric residence time τ along the transport route is controlled by wet and dry deposition (Hansson, 1994). τ is typically on the order of a few days to weeks (Mahowald et al., 1999; Gong et al., 2002; Reijmer et al., 2002; Werner et al., 2002). If two sites with transport times t_1 and t_2 (e.g. EDML and EDC) are considered, the logarithmic air concentration at site 2 can be expressed by the concentration at site 1 according to

$$\log[C_{air}(t_2)] = \log[C_{air}(t_1)] - \Delta t/\tau \tag{1}$$

where $\Delta t = t_2 - t_1$ is the transport time difference along the two trajectories and where we assume that the atmospheric residence time along both transport routes is comparable.
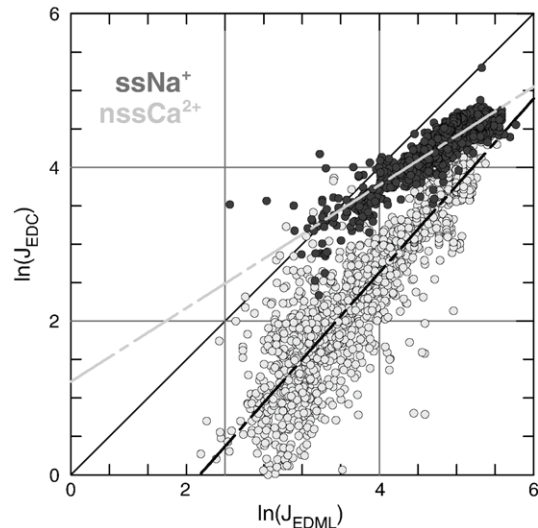
Fig. 4. Scatter plot of logarithmic $nssCa^{2+}$ (light grey dots) and $ssNa^+$ (dark grey dots) fluxes in the EDC vs. EDML ice cores in 100 yr resolution according to Eq. (1). If transport remains unchanged the difference of the data points from the first bisecting line should stay constant. For visual guidance a linear regression through all data points has been added which shows a slope close to 1 for $nssCa^{2+}$ (dark grey line) and around 0.6 for $ssNa^+$ (light grey line).

Accordingly, if the aerosol is derived from the same source at both sites (as is the case for glacial Patagonian dust in Antarctica) the difference in the logarithmic atmospheric aerosol concentration (thus, the deposition flux in Antarctic low accumulation areas), should be $\Delta t/\tau$. The offset $\Delta t/\tau$ may change for different climate conditions. For example if transport velocities intensify as hypothesized for colder climate conditions (Petit et al., 1999), Δt and, thus, the logarithmic offset should become smaller. If the atmospheric residence time τ is considerably lengthened as hypothesized for cold periods (Yung et al., 1996; Petit et al., 1999) the offset should also be reduced.

As shown in Fig. 4 the difference of logarithmic $nssCa^{2+}$ fluxes in the ice (representative of atmospheric $nssCa^{2+}$ concentrations) at EDC and EDML stayed rather constant, providing observational evidence that transport parameters for dust transport from Patagonia to Antarctica have not changed strongly over the last glacial cycles. Alternatively, both Δt and τ may have changed in the same way compensating each other's transport effect. However, it seems unlikely that this was the case during all time periods over the last 150 kyr. In any case the change in atmospheric concentration at the drill site is only dependent on the joint effect of transport time and residence time which, based on our results, was limited. In Table 1 the average differences (representative of $\Delta t/\tau$) of logarithmic fluxes between EDML and EDC are summarized for individual time periods. Based on our conceptual model it becomes clear that $\Delta t/\tau$ is between 1 and 2 for all time periods over the last glacial cycle, implying that the difference in transport time is similar to the atmospheric residence time and is on the order of a week approximately in line with back trajectory studies (Reijmer et al., 2002). For the glacial intervals, where Patagonian dust is dominant (Grousset et al., 1992; Basile et al., 1997; Delmonte et al., 2004a), the offset lies between 1 and 1.5 with the lower values for peak glacial conditions (LGM, MIS6). This points to a somewhat faster transport or a larger residence time during the coldest periods but the decrease in $\Delta t/\tau$ from MIS3 to the LGM is still within the uncertainty in Table 1. Taking the values in Table 1 at face value a LGM decrease in $\Delta t/\tau$

compared to MIS3 could explain increases in the atmospheric $nssCa^{2+}$ concentration of approximately 40% assuming that this change were entirely due to changes in atmospheric residence time and if we assume both an average atmospheric residence time and a transport time to EDML of approximately a week during MIS 3 (Gong et al., 2002). Only if we use an unrealistically long transport time, which is 6 times larger than the atmospheric residence time, can we explain the observed factor of 5 changes in the glacial $nssCa^{2+}$ flux records with our simple conceptual transport model. The largest difference in Table 1 is found between the Holocene and the LGM. Taken at face value this would point to a slower transport or a reduced atmospheric residence time during the Holocene, which could explain a glacial increase by 70%. However, the Holocene Ca^{2+} flux at EDML has to be regarded as an upper limit due to the relatively high blank contribution in this time interval and accordingly the real difference in $\Delta t/\tau$ in Table 1 is significantly smaller. E.g. reducing the average Holocene concentration at EDML for a blank contribution of only 1 ppb would reduce $\Delta t/\tau$ to 1.5, i.e. a value similar to MIS3 and 4.

Interestingly, the scatter of the $nssCa^{2+}$ flux data in Fig. 4 decreases with increasing flux values, i.e. for colder climate conditions. This can only partly be explained by the larger measurement uncertainty for low Ca^{2+} concentrations during warm periods. Accordingly, this suggests a higher transport variability or a variable input of Australian dust export to Antarctica for warm climate conditions. In summary, we conclude that both transport intensity as well as variability changed over time but played only a secondary role for the observed dust changes in line with atmospheric circulation models (Krinner and Genthon, 1998; Reader and McFarlane, 2003; Mahowald et al., 2006). Thus, the observed changes in $nssCa^{2+}$ fluxes predominantly reflect changes in source strength.

For glacial dust this implies strongly increased dust emissions in Patagonia, which are most pronounced during the LGM. The penultimate glacial but also the cold interval between 60–70 ka BP show extraordinarily high $nssCa^{2+}$ fluxes comparable to the environmental

Table 1
Average±standard deviation of the difference in logarithmic $nssCa^{2+}$ fluxes in 100 yr resolution at EDML and EDC representing the average ratio of the transport time difference between the two sites and the atmospheric residence time as controlled by wet and dry deposition en route

Time period	Holocene	LGM	MIS3	MIS4-5.4	MIS5.5	MIS6
	1–10 ka BP	20–30 ka BP	30–60 ka BP	60–120 ka BP	120–130 ka BP	130–150 ka BP
$\Delta t/\tau$	(2.01±0.47)	0.96±0.17	1.41±0.40	1.56±0.84	(1.45±0.51)	1.16±0.39

The Holocene value represents an upper limit due to the larger blank contribution to ion chromatographically determined Ca^{2+} concentrations at EDML compared to the CFA data used at EDC. During MIS5.5 both EDML and EDC are affected by the blank level.

conditions during the LGM. Parallel to the nssCa^{2+} flux maxima in Antarctica, terrigenous records in marine sediments in the northern Scotia Sea also point to higher mineral dust input from southern Patagonian sources (Diekmann et al., 2000), however this study did not distinguish between aeolian and lateral transport of suspended particles to the sediment. The rest of the last glacial is characterized by intermediate nssCa^{2+} fluxes, hence mineral dust emissions in Patagonia, which are strongly but not linearly related to temperature changes recorded in Antarctica (Fig. 5) (Wolff et al., 2006). Especially, each of the Antarctic Isotope Maxima (AIM) (EPICA community members, 2006) indicated in Fig. 3 is accompanied by a significant decline in nssCa^{2+} fluxes at EDML and EDC. This points to synchronous changes (reduced aridity and/or lower wind speeds) in the Patagonian source regions during AIMs. Of special importance in Fig. 3 are also the apparently comparable environmental conditions during the last two interglacials. This points to similar precipitation rates and wind speeds in Patagonia while temperatures in Antarctica were 2–4 °C higher in MIS5.5 than in the Holocene (EPICA community members, 2006).

Little is known about the long-term change in local Patagonian climate beyond the LGM. For the LGM, terrestrial records ((Markgraf et al., 1992) and references therein) and climate models (Wainer et al., 2005) suggest increased aridity leeside of the Andes and a northward expansion and potential strengthening of the westerlies (Moreno et al., 1999). The latter is connected to the

northward expansion of sea ice found in marine sediment records (Gersonde et al., 2005) and in line with our sea salt reconstructions discussed in Section 4.2. Model simulations on the change in the southern hemisphere westerlies are inconsistent (Shin et al., 2003; Butzin et al., 2005; Otto-Bliesner et al., 2006). While an idealized atmospheric model without continents shows a clear glacial northward shift of peak westerly winds (Williams and Bryan, 2006), one model study with a complex coupled ocean/atmosphere climate model (Shin et al., 2003) shows even a slight southward shift of the peak wind stress in the SO. Interestingly, a northward expansion of the westerlies is also observed for recent winter conditions compared to summer in NCEP/NCAR reanalysis data (Kalnay et al., 1996), while the core of the westerlies in the SO does not shift in latitude.

Another possible factor acting on dust emission may be the reduction of sea level exposing substantial shelf areas especially on the Atlantic side off Patagonia. Comparison of the EDC nssCa^{2+} record with coast line reconstructions for the Argentinian shelf (Wolff et al., 2006) showed that the major glacial/interglacial nssCa^{2+} decrease occurred prior to any significant sea level rise. In addition the millennial climate variability during MIS 3 is also accompanied by significant nssCa^{2+} flux variations (Fig. 3), but has not been accompanied by sea level changes at similar high frequencies. In contrast to the delayed global sea level rise relative to the mineral dust decrease, an early glacier retreat before 17 ka BP has been reported from Tierra del Fuego and other mid-
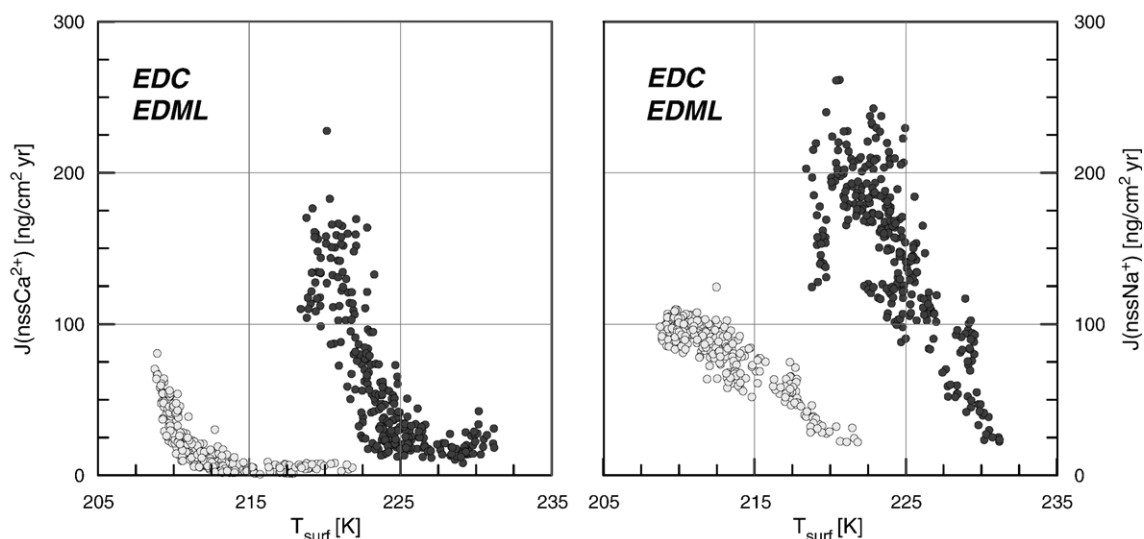
Fig. 5. Temperature dependence of nssCa^{2+} (left) and ssNa^{+} (right) fluxes in 500 yr resolution at EDML (dark grey dots) and EDC (light grey dots). Surface temperatures have been derived from δ^{18}O (EDML) and δD (EDC) using the spatial isotope/temperature gradient in the respective region (EPICA community members, 2004, 2006).

latitude glaciers (Sugden et al., 2005; Schaefer et al., 2006), supporting a close connection of glaciation and continental dust sources in southern South America. Outwash of mineral dust material has been strongly enhanced during glacial expansion of southern Andean ice masses, providing a potential active source for mineral dust mobilization in the glacial. In summary we suggest that a combination of changes in glacial outwash, aridity and wind speed are mainly responsible for the glacial/interglacial mineral dust changes recorded in Antarctica (Mahowald et al., 2006) while the influence of sea level changes is small for the rapid decrease in dust fluxes at the beginning of the termination and during MIS 3.

4.2. Sea salt

A quantification of transport changes for sea salt aerosol is even more difficult as in the case of dust. Sea salt concentration increases more strongly at EDML than at EDC for colder climate conditions leading to an increase in the difference of logarithmic sea salt concentration in Fig. 4. However, this cannot be used to quantify transport changes as in the case of glacial dust because the sea salt source regions for the Atlantic and Indian Ocean sector of Antarctica are not the same and sea salt source strength as well as transport may have changed independently in both regions. In view of the largely expanded sea ice coverage around Antarctica a longer transport time from the open ocean to the Antarctic plateau is expected in glacial periods and any intensification of transport from the open ocean would have to overcompensate that effect. An increased inflow of marine air masses from the open ocean leading to an increased sea salt aerosol flux seems also in contradiction with the strongly depleted stable water isotope (δ^{18}O, δD) levels (EPICA community members, 2004, 2006) and reduced snow accumulation rates at both sites, pointing to a stronger depletion of marine air masses in water vapor and most likely also sea salt aerosol during transport.

Also an explanation of the site dependent glacial increase in sea salt fluxes in terms of sea salt source strength is not straightforward. The canonical interpretation of changes in sea salt aerosol is an increased sea/air particle flux at the open ocean surface due to increased wind speeds. This, however, is in contradiction to the greatly increased sea ice cover (Gersonde et al., 2005) during glacial periods. Aerosol formation from brine water, as for example experienced during the formation of frost flowers in sea ice leads and polynyas, has recently been identified as an additional effective source

for sea salt aerosol (further on referred to as "sea ice salt"). Precipitation of mirabilite ($Na_2SO_4 \cdot 10H_2O$) from sea water during brine formation leads to a characteristic sulfate depletion compared to the average sea water composition. This fractionation has been regularly observed in atmospheric sea salt aerosol concentrations at coastal Antarctic sites in winter (Wagenbach et al., 1998; Rankin et al., 2000) showing the importance of the brine water source for the local sea salt aerosol budget. Brine and frost flower formation was also suggested as a possible mechanism for the glacial/interglacial increase in sea salt concentrations in ice cores on the high Antarctic plateau (Wolff et al., 2003, 2006). Only recently, year-round aerosol sampling on the East Antarctic plateau revealed evidence of sulfate depleted sea salt aerosol during austral winter (Hara et al., 2004), which we interpret as significant influence of sea ice formation on the sea salt aerosol budget also for the interior of Antarctica (Wolff et al., 2006; Fischer et al., 2007). In the following we will explore whether we can explain the observed changes in sea salt fluxes, if we take sea ice salt formation into account, while recognizing that there remains some controversy about this interpretation as long as we have no quantitative source estimate for sea ice salt production.

Due to wind driven opening of leads this sea ice salt aerosol formation process occurs throughout the sea ice cover and continuously in coastal polynyas. Based on diatom evidence in SO sediment records it was shown that the circum-Antarctic winter sea ice cover during the LGM was enhanced by approximately a factor of two from 19 to $39 \cdot 10^6$ km^2 (Gersonde et al., 2005). Although the reconstruction of the summer sea ice edge is hampered by the lack of siliceous sediments in regions of second year sea ice, some evidence for substantial summer sea ice exists for the LGM in the Atlantic and Indian Ocean sector of the SO (Gersonde et al., 2005). This indicates that the glacial summer sea ice was as large as recent winter sea ice coverage in the Atlantic sector while it was not extended in the Indian Ocean sector of the SO. Sea surface temperatures in summer sea ice regions (e.g. in coastal polynyas in the Weddell Sea) have been well below the freezing point during the LGM (Gersonde et al., 2005), allowing for considerable sea ice formation also during summer. This summer sea ice salt formation would add to the sea ice salt aerosol emission in winter and further enhance the annually averaged aerosol source strength of this process. If we take at first order the sea ice salt contribution to the Antarctic sea salt budget to be proportional to the total sea ice cover in winter and summer we expect a factor of 2 increase in the Indian ocean and a factor up to 3

increase in the Atlantic sector of the SO, favorably in line with our observations in the EDC and EDML ice cores.

Concentrating on the variability in sea salt flux in parallel to millennial climate variations during MIS 3 (Fig. 4) it becomes clear that a warming during AIMs does not lead to a clear response in sea salt fluxes. This casts doubt on a quantitative use of sea salt in ice cores as sea ice proxy. During peak glacial times the potential sea ice salt formation zone extends as far north as 50°S. Sea ice salt produced in areas at the outer edge of the sea ice cover has to travel a very long distance before it reaches an ice core site on the Antarctic plateau. Due to this long transport time it experiences substantial depletion by wet and dry deposition en route. Accordingly, we suggest that the farther north the sea ice salt formation zone extends during cold periods the less efficient is this edge

area to add to the sea salt aerosol budget at Antarctic ice core drill sites. Looking at the sea salt variations in MIS 3 in more detail (Fig. 6) we see that at EDC no imprint on sea salt fluxes can be found during AIMs whatsoever while the record at EDML suggests a tendency to rapidly reduced sea salt fluxes at the onset of most of the warming events and a gradual recovery thereafter. Although this effect is rather weak it may point to a decline in the summer sea ice extent in the Weddell Sea sector which may react more sensitively to the warming events during MIS 3.

A major difference in ssNa⁺ fluxes exists for the penultimate warm period. During MIS 5.5 the sea salt flux in the EDML ice core was reduced by a factor of 4 while it was lowered by a factor of 2–3 at EDC compared to Holocene conditions in line with significantly warmer temperatures at EDC and EDML (EPICA
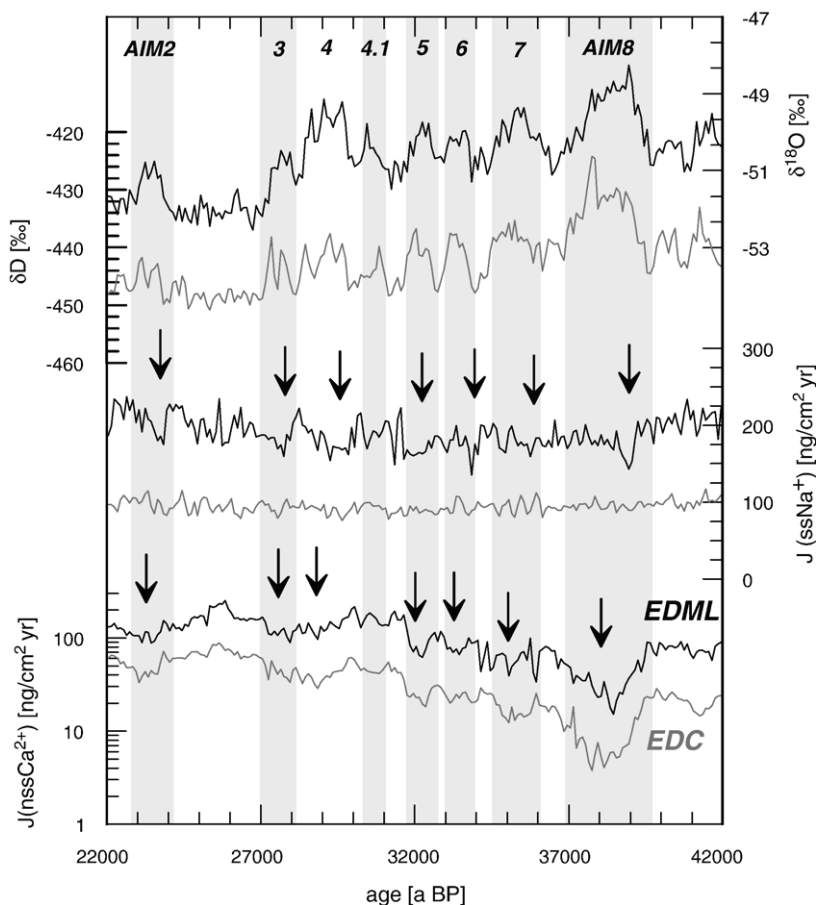
Fig. 6. High-resolution (100 yr averages) plots of stable water isotopes, ssNa⁺ fluxes and nssCa²⁺ fluxes in the EDML (black line) and EDC (grey line) ice cores during the time interval 22–42 ka BP on the common EDML1/EDC3 age scale (Parrenin et al., 2007; Ruth et al., 2007). Isotope temperatures show Antarctic Isotope Maxima (AIM) during this period (EPICA community members, 2006) which are also reflected in lowered nssCa²⁺ fluxes at both sites (indicated by arrows in the bottom panel, note the logarithmic y-scale). Sea salt aerosol at EDML tends to a rapid decline at the onset of most of the AIMs (indicated by arrows in the middle panel) while no significant changes in sea salt aerosol can be observed at EDC.

community members, 2006). Because summer sea ice is nearly absent in the Indian Ocean sector for Holocene conditions, this implies that only a reduction in the winter sea ice salt source could explain the sea salt decrease in this region during the warmer MIS 5.5. In the Atlantic sector of the SO an even stronger decline in sea ice coverage during MIS 5.5 is indicated by our ssNa$^+$ data, possibly related to a reduction of both winter and summer sea ice in the Weddell Sea. This is also supported by changes in marine sediments, indicating a southward shift of the opal deposition belt by 3–5° latitude (Bianchi and Gersonde, 2002) at that time.

5. Conclusions

Sea salt and mineral dust aerosol records are representative for basin-wide atmospheric catchment areas of aerosol transported onto the East Antarctic ice sheet. The records allow us to draw a clearer picture on the timing of environmental changes in Patagonia and the SO and their influence on aerosol formation in parallel to climate variations in Antarctica over the last 150 kyr.

Sea salt records at both sites allow for the first time a basin-wide estimate of sea salt aerosol emissions, which support an accompanying change in sea ice cover over the complete time interval from the penultimate glacial to the present. The coherence of the two sea salt records from opposite sides of the Antarctic ice sheet indicates a waxing and waning of sea ice, which was generally synchronous in the Atlantic and the Indian Ocean sector of the SO on glacial/interglacial time scales. The sensitivity of sea salt fluxes to temperature changes (Fig. 5), however, is higher in the Weddell Sea sector, a fact which we attribute to a more vigorous change in sea ice cover and the additional role of summer sea ice extent on sea ice salt formation in this area. We note, that for very cold climate conditions sea salt changes become increasingly insensitive to temperature changes probably related to the long transport distance of aerosol formed at the northern margin of the sea ice cover. Accordingly, the use of sea salt as quantitative proxy for sea ice coverage is hampered and requires a rigorous calibration against marine sediment data for different time slices, experimental studies of the modern sea ice salt source as well as refined model studies about its change in the past.

Using our dust records from sites facing different sectors of the SO with greatly different distances to Patagonia and using a simple conceptual transport model we can rule out a substantial variation in transport as being the main factor being responsible for the observed nssCa^{2+} changes during glacial times as also supported by atmospheric circulation models (Krinner and Gen-

thon, 1998; Reader and McFarlane, 2003). Instead our results point to temporal changes in the strength of the Patagonian mineral dust source in parallel to temperature variations in Antarctica. The three times higher nssCa^{2+} fluxes at EDML also point to a threefold higher aeolian dust input into the Weddell Sea sector of the SO, potentially related to a stronger dust fertilization in this region. This effect may be amplified by a potential dust storage effect of the greatly extended winter and summer sea ice coverage as indicated in our ssNa$^+$ record. The extension of summer and winter sea ice in this region is also expected to have a strong effect on bottom water formation, gas exchange and wind shear of the surface ocean likely related to a reduced ventilation of the deep SO with strong impacts on the global carbon cycle (Köhler et al., 2005). Accordingly, our data will allow for a better time resolved, basin-wide quantification of potential dust fertilization on marine export productivity and investigation of the effect of the sea ice extent on gas exchange and water mass formation.

Acknowledgments

Appendix A. Supplementary data

Supplementary data associated with this article can be found, in the online version, at doi:10.1016/j. epsl.2007.06.014.

References

Archer, D., Winguth, A., Lea, D., Mahowald, N., 2001. What caused the glacial/interglacial atmospheric pCO$_2$ cycles? Rev. Geophys. 38, 159–189.

Basile, I., Grousset, F.E., Revel, M., Petit, J.R., Biscaye, P.E., Barkov, N.I., 1997. Patagonian origin of glacial dust deposited in East Antarctica (Vostok and Dome C) during glacial stages 2, 4 and 6. Earth Planet. Sci. Lett. 146, 573–589.

Bianchi, C., Gersonde, R., 2002. The Southern Ocean surface between Marine Isotope Stage 6 and 5d: Shape and timing of climate changes. Palaeogeogr. Palaeoclimatol. Palaeoecol. 187, 151–177.

Bigler, M., Röthlisberger, R., Lambert, F., Stocker, T.F., Wagenbach, D., 2006. Aerosol deposited in East Antarctica over the last glacial cycle: detailed apportionment of continental and sea salt contributions. J. Geophys. Res. 111. doi:10.1029/2005JD006469.

Bintanja, R., van de Wal, R.S.W., Oerlemans, J., 2005. Modelled atmospheric temperatures and global sea levels over the past million years. Nature 437, 125–128.

Blunier, T., Schwander, J., Stauffer, B., Stocker, T., Dällenbach, A., Indermühle, A., Tschumi, J., Chappellaz, J., Raynaud, D., Barnola, J.-M., 1997. Timing of the Antarctic Cold Reversal and the atmospheric CO_2 increase with respect to the Younger Dryas event. Geophys. Res. Lett. 24, 2683–2686.

Bowen, H.J.M., 1979. Environmental Chemistry of the Elements. Academic Press, London.

Brook, E.J., White, J.W.C., Schilla, A.S.M., M.L.B., Barnett, B., Severinghaus, J.P., Taylor, K.C., Alley, R.B., Steig, E.J., 2005. Timing of millenial-scale climate change at Siple Dome, West Antarctica, during the last glacial period. Quat. Sci. Rev. 24, 1333–1343.

Butzin, M., Prange, M., Lohmann, G., 2005. Radiocarbon simulations for the glacial ocean: the effects of wind stress, Southern Ocean sea ice and Heinrich events. Earth Planet. Sci. Lett. 235, 45–61.

de Angelis, M., Steffensen, J.P., Legrand, M., Clausen, H., Hammer, C., 1997. Primary aerosol (sea salt and soil dust) deposited in Greenland ice during the last climatic cycle: comparison with east Antarctic records. J. Geophys. Res. 102, 26681–26698.

Delmonte, B., Petit, J.R., Maggi, V., 2002. Glacial to Holocene implications of the new 27000-year dust record from the EPICA Dome C (East Antarctica) ice core. Clim. Dyn. 18, 647–660.

Delmonte, B., Basile-Doelsch, I., Petit, J.R., Maggi, V., Revel-Rolland, M., Michard, A., E.J., Grousset, F., 2004a. Comparing the EPICA and Vostok dust records during the last 220,000 years: stratigraphical correlation and provenance in glacial periods. Earth-Sci. Rev. 66, 63–87.

Delmonte, B., Petit, J.R., Andersen, K.K., Basile-Doelsch, I., Maggi, V., Lipenkov, V., 2004b. Dust size evidence for opposite regional atmospheric circulation changes over East Antarctica during the last climatic transition. Clim. Dyn. 23, 427–438.

Delmonte, B., Petit, J.R., Basile-Doelsch, I., Jagoutz, E., Maggi, V., 2007. Late Quaternary Interglacials in East Antarctica from ice core dust records. In: Sirocko, F., Claussen, M., Sanchez-Goni, M.F., Litt, T. (Eds.), The Clim. Past interglacials. Elsevier, Amsterdam, pp. 53–73.

Diekmann, B., Kuhn, G., Rachold, V., Abelmann, A., Brathauer, U., Fütterer, D.K., Gersonde, R., Grobe, H., 2000. Terrigenous sediment supply in the Scotia Sea (Southern Ocean): response to late Quaternary ice dynamics in Patagonia and on the Antarctic Peninsula. Palaeogeogr. Palaeoclimatol. Palaeoecol. 162, 357–387.

EPICA community members, 2004. Eight glacial cycles from an Antarctic ice core. Nature 429, 623–628.

EPICA community members, 2006. One-to-one coupling of glacial climate variability in Greenland and Antarctica. Nature 444, 195–198.

Fischer, H., Siggaard-Andersen, M.-L., Ruth, U., Röthlisberger, R., Wolff, E., 2007. Glacial/interglacial changes in mineral dust and sea salt records in polar ice cores: sources, transport, deposition. Rev. Geophys. 45. doi:10.1029/2005RG000192.

Gersonde, R., Crosta, X., Abelmann, A., Armand, L., 2005. Sea-surface temperature and sea ice distribution of the Southern Ocean at the EPILOG Last Glacial Maximum — a circum-Antarctic view based on siliceous microfossil records. Quat. Sci. Rev. 24, 869–896.

Göktas, F., Fischer, H., Oerter, H., Weller, R., Sommer, S., Miller, H., 2002. A glacio-chemical characterisation of the new EPICA deep drilling site on Amundsenisen, Dronning Maud Land, Antarctica. Ann. Glaciol. 35, 347–354.

Gong, S.L., Barrie, L.A., Lazare, M., 2002. Canadian Aerosol Module (CAM): a size segregated simulation of atmospheric aerosol processes for climate and air quality models 2. Global sea-salt aerosol and its budgets. J. Geophys. Res. 107. doi:10.1029/2001JD002004.

Graf, W., Oerter, H., Reinwarth, O., Stichler, W., Wilhelms, F., Miller, H., Mulvaney, R., 2002. Stable isotope records from Dronning Maud Land, Antarctica. Ann. Glaciol. 35, 195–201.

Grousset, F.E., Biscaye, P.E., Revel, M., Petit, J.-R., Pye, K., Joussaume, S., Jouzel, J., 1992. Antarctic (Dome C) ice core dust at 18 k.y. B.P.: isotopic constraints on origins. Earth Planet. Sci. Lett. 111, 175–182.

Hansson, M.E., 1994. The Renland ice core. A Northern Hemisphere record of aerosol composition over 120000 years. Tellus 46, 390–418.

Hara, K., Osada, K., Kido, M., Hayashi, M., Matsunaga, K., Iwasaka, Y., Yamanouchi, T., Hashida, G., Fukatsu, T., 2004. Chemistry of sea-salt particles and inorganic halogen species in Antarctic regions: compositional differences between coastal and inland stations. J. Geophys. Res. 109. doi:10.1029/2004JD004713.

Huybrechts, P., Rybak, O., Pattyn, F., Ruth, U., Steinhage, D., 2007. Ice thinning, upstream advection, and non-climatic biases for the upper 89% of the EDML ice core from a nested model of the Antarctic ice sheet. Clim. Past Disc. 3, 693–727.

Jouzel, J., Masson-Delmotte, V., Cattani, O., Dreyfus, G., Falourd, S., Hoffmann, G., Minster, B., Nouet, J., Barnola, J.-M., Chappellaz, J., Fischer, H., Gallet, J.C., Johnsen, S., Leuenberger, M., Loulergue, L., Luethi, D., Oerter, H., Parrenin, F., Raisbeck, G., Raynaud, D., Schwander, J., Spahni, R., Souchez, R., Selmo, E., Schilt, A., Steffensen, J.P., Stenni, B., Stauffer, B., Stocker, T.F., Tison, J.-L., Werner, M., Wolff, E.W., in press. Orbital and millennial Antarctic climate variability over the last 800 000 years. Science.

Kalnay, E., Kanamitsu, M., Kistler, R., Collins, W., Deaven, D., Gandin, L., Iredell, M., Saha, S., White, G., Woollen, J., Zhu, Y., Chelliah, M., Ebisuzaki, W., Higgins, W., Janowiak, J., Mo, K.C., Ropelewski, C., Wang, J., Leetmaa, A., Reynolds, R., Jenne, R., Joseph, D., 1996. The NCEP/NCAR 40-year reanalysis project. Bull. Am. Meteorol. Soc. 77, 437–471.

Knorr, G., Lohmann, G., 2003. Southern Ocean origin for the resumption of Atlantic thermohaline circulation during deglaciation. Nature 424, 532–536.

Köhler, P., Fischer, H., Munhoven, G., Zeebe, R.E., 2005. Quantitative interpretation of atmospheric carbon records over the last glacial termination. Glob. Biogeochem. Cycles 19. doi:10.1029/2004GB002345.

Krinner, G., Genthon, C., 1998. GCM simulation of the Last Glacial Maximum surface climate of Greenland and Antarctica. Clim. Dyn. 14, 741–758.

Lunt, D.J., Valdes, P.J., 2001. Dust transport to Dome C, Antarctica, at the Last Glacial Maximum and present day. Geophys. Res. Lett. 28, 295–298.

Mahowald, N., Kohfeld, K., Hansson, M., Balkanski, Y., Harrison, S.P., Prentice, I.C., Schulz, M., Rodhe, H., 1999. Dust sources and deposition during the last glacial maximum and current climate: a comparison of model results with paleodata from ice cores and marine sediments. J. Geophys. Res. 104, 15895–15916.

Mahowald, N.M., Muhs, D.R., Levis, S., Rasch, P.J., Yoshioka, M., Zender, C.S., Luo, C., 2006. Change in atmospheric mineral aerosols in response to climate: last glacial period, preindustrial, modern, and doubled carbon dioxide climates. J. Geophys. Res. 111. doi:10.1029/2005JD006653.

Markgraf, V., Dodson, J.R., Kershaw, A.P., McGlone, M.S., Nicholls, N., 1992. Evolution of late Pleistocene and Holocene climates in the circum-South Pacific land areas. Clim. Dyn. 6, 193–211.

Martin, J., 1990. Glacial–interglacial CO_2 change: the iron hypothesis. Paleoceanography 5, 1–13.

Mayewski, P.A., Twickler, M.S., Whitlow, S.I., Meeker, L.D., Yang, Q., Thomas, J., Kreutz, K., Grootes, P.M., Morse, D.L., Steig, E.J., Waddington, E.D., Saltzman, E.S., Whung, P.-Y., Taylor, K.C., 1996. Climate change during the last deglaciation in Antarctica. Science 272, 1636–1638.

Moreno, P.I., Lowell, T.V., Jacobson Jr., G.L., Denton, G.H., 1999. Abrupt vegetation and climate changes during the last glacial maximum and last termination in the Chilean Lake District. A case study from Canal de la Puntilla (41°S). Geogr. Ann. 81A, 285–311.

Morgan, V., Delmotte, M., van Ommen, T., Jouzel, J., Chappellaz, J., Woon, S., Masson-Delmotte, V., Raynaud, D., 2002. Relative timing of deglacial climate events in Antarctica and Greenland. Science 297, 1862–1864.

Oerter, H., Wilhelms, F., Jung-Rothenhäusler, F., Göktas, F., Miller, H., Graf, W., Sommer, S., 2000. Accumulation rates in Dronning Maud Land, Antarctica, as revealed by dielectric-profiling measurements of shallow firn cores. Ann. Glaciol. 30, 27–34.

Otto-Bliesner, B.L., Brady, E.C., Clauzet, G., Tomas, R., Levis, S., Z.K., 2006. Last Glacial Maximum and Holocene climate in CCSM3. J. Clim. 19, 2526–2544.

Parrenin, F., Barnola, J.-M., Beer, J., Blunier, T., Castellano, E., Chappellaz, J., Dreyfus, G., Fischer, H., Fujita, S., Jouzel, J., Kawamura, K., Lemieux-Dudon, B., Loulergue, L., Masson-Delmotte, V., Narcisi, B., Petit, J.-R., Raisbeck, G., Raynaud, D., Ruth, U., Schwander, J., Severi, M., Spahni, R., Steffensen, J.P., Svensson, A., Udisti, R., Waelbroeck, C., Wolff, E., 2007. The EDC3 agescale for the EPICA Dome C ice core. Clim. Past Disc. 3, 575–606.

Petit, J.R., Mounier, L., Jouzel, J., Korotkevich, Y.S., Kotlyakov, V., Lorius, C., 1990. Paleoclimatological and chronological implications of the Vostok core dust record. Nature 343, 429–436.

Petit, J.R., Jouzel, J., Raynaud, D., Barkov, N.I., Barnola, J.-M., Basile, I., Bender, M., Chappellaz, J., Davis, M., Delaygue, G., Delmotte, M., Kotlyakov, V.M., Legrand, M., Lipenkov, V.Y., Lorius, C., Pepin, L., Ritz, C., Saltzman, E., Stievenard, M., 1999. Climate and atmospheric history of the past 420,000 years from the Vostok ice core, Antarctica. Nature 399, 429–436.

Rankin, A.M., Auld, V., Wolff, E.W., 2000. Frost flowers as a source of fractionated sea salt aerosol in the polar regions. Geophys. Res. Lett. 27, 3469–3472.

Reader, M.C., McFarlane, N., 2003. Sea-salt aerosol distribution during the Last Glacial Maximum and its implications for mineral dust. J. Geophys. Res. 108. doi:10.1029/2002JD002063.

Reijmer, C.H., van den Broeke, M.R., 2001. Moisture sources of precipitation in Western Dronning Maud Land, Antarctica. Antarct. Sci. 13, 210–220.

Reijmer, C.H., van den Broeke, M.R., Scheele, M.P., 2002. Air parcel trajectories to five deep drilling locations on Antarctica, based on the ERA-15 data set. J. Clim. 15, 1957–1968.

Revel-Rolland, M., De Dekker, P., Delmonte, B., Hesse, P.P., Magee, J.W., Basile-Doelsch, I., Grousset, F., Bosch, D., 2006. Eastern Australia: a possible source of dust in East Antarctica interglacial ice. Earth Planet. Sci. Lett. 249, 1–13.

Röthlisberger, R., Bigler, M., Hutterli, M., Sommer, S., Stauffer, B., Junghans, H.G., Wagenbach, D., 2000. Technique for continuous high-resolution analysis of trace substances in firn and ice cores. Environ. Sci. Technol. 34, 338–342.

Röthlisberger, R., Mulvaney, R., Wolff, E.W., Hutterli, M., Bigler, M., Sommer, S., Jouzel, J., 2002. Dust and sea-salt variability in central East Antarctica (Dome C) over the last 45 kyrs and its implications for southern high-latitude climate. Geophys. Res. Lett. 29. doi:10.1029/2002GL015186.

Ruth, U., Barnola, J.-M., Beer, J., Bigler, M., Blunier, T., Castellano, E., Fischer, H., Fundel, F., Huybrechts, P., Kaufmann, P., Kipfstuhl, S., Lambrecht, A., Morganti, A., Oerter, H., Parrenin, F., Rybak, O., Severi, M., Udisti, R., Wilhelms, F., Wolff, E., 2007. "EDML1": A chronology for the EDML ice core, Antarctica, over the last 150 000 year. Clim. Past Disc. 3, 549–574.

Rybak, O., Huybrechts, P., Steinhage, D., Pattyn, F., 2005. Dating and accumulation rate reconstruction along the Dome Fuji — Kohnen radio-echo-sounding profile. Geophys. Res. Abstr. 7, 05421.

Schaefer, J.M., Denton, G.H., Barrell, D.J.A., Ivy-Ochs, S., Kubik, P.W., Andersen, B.G., Phillips, F.M., Lowell, T.V., Schlüchter, C., 2006. Near synchronous interhemispheric termination of the Last Glacial Maximum in mid-latitudes. Science 312, 1510–1513.

Severi, M., Castellano, E., Morganti, A., Udisti, R., Ruth, U., Fischer, H., Huybrechts, P., Wolff, E., Parrenin, F., Kaufmann, P., Lambert, F., Steffensen, J.P., 2007. Synchronisation of the EDML1 and EDC3 timescales for the last 52 kyr by volcanic signature matching. Clim. Past Disc. 3, 409–433.

Shin, S.-I., Liu, Z., Otto-Bliesner, B., Brady, E.C., Kutzbach, J.E., Harrison, S.P., 2003. A simulation of the Last Glacial Maximum climate using the NCAR-CCSM. Clim. Dyn. 20, 127–151.

Sommer, S., Wagenbach, D., Mulvaney, R., Fischer, H., 2000. Glacio-chemical study covering the past 2 kyr on three ice cores from Dronning Maud Land, Antarctica 2. Seasonally resolved chemical records. J. Geophys. Res. 105, 29423–29433.

Steig, E.J., Brook, E.J., White, J.W.C., Sucher, C.M., Bender, M.L., Lehman, S.J., Morse, D.L., Waddington, E.D., Clow, G.D., 1998. Synchronous climate changes in Antarctica and the North Atlantic. Science 282, 92–95.

Steinhage, D., Nixdorf, U., Meyer, U., Miller, H., 2001. Subglacial topography and internal structure of central and western Dronning Maud Land, Antarctica, determined from airborne radio echo sounding. J. Appl. Geophys. 47, 183–189.

Stephens, B.B., Keeling, R.F., 2000. The influence of Antarctic sea ice on glacial–interglacial CO_2 variations. Nature 404, 171–174.

Stocker, T., Johnsen, S., 2003. A minimum thermodynamic model of the bipolar seesaw. Paleoceanography 18. doi:10.1029/2003PA000920.

Sugden, D.E., Bentley, M.J., Fogwill, C.J., Hulton, N.R.J., McCulloch, R.D., Purves, R.S., 2005. Late-glacial glacier events in southernmost South America. Geogr. Ann. 87A, 273–288.

Toggweiler, J.R., 1999. Varition of atmospheric CO_2 by ventilation of the ocean's deepest water. Paleoceanography 14, 571–588.

Toggweiler, J.R., Russell, J.L., Carson, S.R., 2006. Midlatitude westerlies, atmospheric CO_2, and climate change during the ice ages. Paleoceanography 21. doi:10.1029/2005PA001154.

Udisti, R., Becagli, S., Benassai, S., de Angelis, M., Hansson, M.E., Jouzel, J., Schwander, J., Steffensen, J.P., Traversi, R., Wolff, E., 2004. Sensitivity of chemical species to climatic changes in the last 45 kyr as revealed by high-resolution Dome C (East Antarctica) ice-core analysis. Ann. Glaciol. 39, 457–466.

Wagenbach, D., Ducroz, F., Mulvaney, R., Keck, L., Minikin, A., Legrand, M., Hall, J.S., Wolff, E.W., 1998. Sea-salt aerosol in coastal Antarctic regions. J. Geophys. Res. 103, 10961–10974.

Wainer, I., Clauzet, G., Ledru, M.-P., Brady, E.C., Otto-Bliesner, B., 2005. Last Glacial Maximum in South America: paleoclimate proxies and model results. Geophys. Res. Lett. 32. doi:10.1029/2004GL021244.

Watanabe, O., Jouzel, J., Johnsen, S., Parrenin, F., Shoji, H., Yoshida, N., 2003. Homogeneous climate variability across East Antarctica over the past three glacial cycles. Nature 422, 509–512.

Werner, M., Tegen, I., Harrison, S.P., Kohfeld, K., Prentice, I.C., Balkanski, Y., Rodhe, H., Roelandt, C., 2002. Seasonal and inter-annual variability of the mineral dust cycle under present and glacial conditions. J. Geophys. Res. 107. doi:10.1029/2002JD002365.

Williams, G.P., Bryan, K., 2006. Ice age winds: an aquaplanet model. J. Clim. 19, 1706–1715.

Wolff, E.W., Rankin, A.M., Röthlisberger, R., 2003. An ice core indicator of Antarctic sea ice production? Geophys. Res. Lett. 30. doi:10.1029/2003GL018454.

Wolff, E.W., Fischer, H., Fundel, F., Ruth, U., Twarloh, B., Littot, G.C., Mulvaney, R., de Angelis, M., Boutron, C.F., Hansson, M., Jonsell, U., Hutterli, M., Bigler, M., Lambert, F., Kaufmann, P., Röthlisberger, R., Steffensen, J.P., Siggaard-Andersen, M.-L., Udisti, R., Becagli, S., Castellano, E., Severi, M., Wagenbach, D., Barbante, C., Gabrielli, P., Gaspari, V., 2006. Southern Ocean sea ice, DMS production and iron flux over the last eight glacial cycles. Nature 440, 491–496.

Yung, Y., Lee, T., Wang, C.-H., Shieh, Y.-T., 1996. Dust: a diagnostic of the hydrological cycle during the last glacial maximum. Science 271, 962–963.

Paper III

ICP-Time of Flight-MS as a versatile tool for ultra trace element analysis in Antarctic ice

ICP-Time of Flight-MS as a versatile tool for ultra trace element analysis in Antarctic ice

D. Dick, A. Wegner, P. Gabrielli[+,t], C. Barbante[+], U. Ruth, M. Kriews[*]

Alfred Wegener Institute for Polar and Marine Research, Am Handelshafen 12, 27570 Bremerhaven

[+]Institute for the Dynamics of Environmental Processes – CNR, I-30123 Venice, Italy

[t]School of Earth Science and Byrd Polar Research Center, Ohio State University,

Columbus, OH 43210-1002, USA

1   Abstract

The importance of trace element analysis in natural samples for climate reconstruction has increased in recent years. Oftentimes the available sample amount is very restricted. Therefore high sensitive detection systems with fast data acquisition are required. The inductively coupled plasma time of flight mass spectrometer (ICP-TOF-MS) meets these demands. Here we present accuracy and precision studies of the ICP-TOF-MS for element analysis. Therefore reference materials SPS-SW1, SLRS-4 and NIST 1640 were analysed. Further accuracy studies for rare earth elements (REE) were accomplished with low concentrated molten ice core samples from Antarctica. Results obtained by ICP-TOF-MS are compared with results obtained by ICP-Quadrupol-MS and ICP-Sector Field-MS. The presented ICP-TOF-MS correlates very well with ICP-Q-MS and ICP-SF MS as long as analysed concentrations are higher 4 ng L^{-1}. Below that concentrations the results have to be looked at carefully.

Keywords: ultra trace element analysis, ICP-TOF-MS, rare earth elements, Antarctic ice

2   Introduction

The earth climate is mainly driven by complex processes between the Arctic and Antarctic. Mineral dust and sea salt have been deposited on polar ice caps over several thousands of years. Because of the stratigraphic deposition of snow these chronologically deposited compounds reflect various aspects of climate change [1-4]. Owing to large distances between South America – Antarctica (~1100 km), South Africa – Antarctica (~4000 km) and New Zeeland / Australia Antarctica (~2500 km, ~3000 km), Antarctica is one of the cleanest areas of the world. Therefore highest demands are posted on sampling of snow and ice cores, sample preparation and

[*] Correspondance author tel.: +49-(0)471-4831-1420; fax: +49-(0)471-4831-1149; email: Michael.Kriews@awi.de

finally the analysis of low concentrations [5-7]. The complexity of sampling in the isolated Antarctica implicates restricted sample volumes available for trace element analysis.

Several methods for trace element analysis in polar snow and ice are performed. Analytical techniques such as atomic absorption spectrometry (AAS) [8-9], cold vapour atomic fluorescence spectrometry (CVAFS) [10-11] are used for single element analysis. Isotope dilution mass spectrometry (IDMS) [12] and mass spectrometry (MS) in general are used for multielement analysis. Information about sea salt, mineral dust and anthropogenic compounds should be obtained prefereably out of one sample. This is important if high spatial resolution analysis is accomplished. Thereby, errors generated by assigning the sample to its originating depth are eliminated. Hence MS is most suitable for multielement analysis.

MS are made up of different components; the mass analyzer determines the type of spectrometer. Sector field mass spectrometers (SF-MS) [5] and quadrupol mass spectrometers (Q-MS) [7] are the most common MS types used for investigations of polar ice core samples. These MS measure in the sequential mode. Owing to low sample volumes a delimited amount of isotopes can be analysed. In contrast to these MS systems the time of flight-MS (TOF-MS) analyses in the "simultaneous" mode. Major advantages of this system are: no limitations in the number of analysed isotopes, fast data acquisition and consequently the possibility for numerous replicate analysis. [13] gives a brief overview on the application of TOF-MS. Until now there is only a spare number of literature available on the use of TOF-MS for element analysis [14-17] and none publication for element analysis at the ultra trace concentration level.

The aim of this work is to assess the accuracy and precision of the inductively coupled plasma- TOF-MS (ICP-TOF-MS) [17-18] developed at the Institute for Analytical Science in Berlin. Therefore reference materials SPS-SW1, SLRS-4 and NIST 1640 were analysed. Detection limits, the recovery rate and precision, the sample consumption and analysing time will be presented.

For intercomparison studies natural ice core samples, drilled within the EPICA project (European Project for Ice Coring in Antarctica) [19] were analysed by ICP-TOF-MS, ICP-Q-MS (Elan 6000, Perkin Elmer/Sciex) and ICP-SF-MS (Element 2, Thermo Finnigan). Owing to the limitation of analysed isotopes, especially by ICP-SF-MS, only rare earth element (REE) concentrations are compared. The presented ICP-TOF-MS correlates very well with ICP-Q-MS and ICP-SF MS as long as analysed concentrations are higher 4 ng L^{-1}. Below that concentrations the results have to be looked at carefully.

3 Experimental

3.1 Standards and Labware

At the Alfred Wegener Institute (AWI) in Bremerhaven, ultrapure water was produced by coupling a reverse osmosis system with a Purelab ultra system (Elga, High Wycombe, U.K.). Commercial available ICP-MS multielement stock solutions (Perkin Elmer) were used for external calibration of the ICP-MS systems. At the Department of Environmental Science (DES) in Venice, the ultrapure water was produced by coupling a Milli-Q (Millipore, Bedford, MA) water system with a Purelab Ultra system (Elga, High Wycombe, U.K.). Matrix matched calibration was done at DES obtained by adding different amounts of multielement standard spikes to a surface snow sample. At AWI all standards were acidified to pH 1-2 with subboiled HNO_3 (distilled 65 % HNO_3, pro analysis, Merck) and contained 1 μg L^{-1} Rh ($RhCl_3$, Merck) as internal standard. Eppendorf Pipettes with polypropylene (PP) tips were used for sample and standard preparation. Steps for standard preparation were done under a clean bench (US Class 100) which was located inside a clean room laboratory, classified as US Class 10,000, but presently U.S. Class 100-1000 is achieved. At AWI all labware which came into contact with samples and standards were run through a special cleaning procedure in the following way:

- 1 week treatment with 3 % Mucasol solution (Merck) to degrease all labware, thereafter rinsing all parts with ultrapure water

- 1 week treatment with 1:4 diluted HCL (30 %, suprapur, Merck) , thereafter rinsing all parts with ultrapure water

- 1 week treatment with 1:4 diluted HNO_3 (distilled 65 %, p.a., Merck) , thereafter rinsing all parts with ultrapure water

- 1 week treatment with 1:10 diluted HNO_3 (65 %, suprapur, Merck) , thereafter rinsing all parts with ultrapure water

- Drying of all parts in a clean room under a clean bench, US Class 100.

- Packing of all parts in 2 polyethylene (PE) bags for storage

3.2 Sample collection and preparation

3.2.1 Reference material

Three reference materials were used to validate the quality of the ICP-TOF-MS as well as the ICP-Q-MS measurements.

- SPS-SW1: Spectrapure Standards as, Reference Material for measurements of Elements in Surface Waters

- SLRS-4: National Research Council Canada, River Water Reference Materials for Trace Metals

- NIST 1640: National Institute for Standards and Technology, Trace Elements in Natural Water

Due to the expected REE concentrations in Antarctic ice the SPS-SW1 standard was diluted 1:100. REE from La to Nd in SLRS-4 were analysed out of a 1:10 dilution, all other REE were analysed without any dilution. In NIST1640 all REE concentrations were analysed using a 1:10 dilution.

3.2.2   *Antarctic Ice Core samples*

Within the EPICA a 2774.15 m long ice core (diameter: 98 mm) was drilled in a fluid filled hole at Kohnen station (Dronning Maud Land (DML), Position: 75°00'S, 0°04'E) and a 3189.45 m long (diameter: 98 mm) was drilled in a fluid filled hole at Dome C station (Position: 75°06'S, 123°21'E) [19-20]. For shipping and handling the ice cores are cut in 1 m long sections at Kohnen station and 0.55 m long sections at Dome C station. One section is called bag, they are consecutively numbered. 22 bags were chosen from each ice core for REE analysis. Bags from Kohnen station cover the time from the last glacial / interglacial transition. The top of the youngest bag was 5.78 kyr old and the bottom of the oldest ice core was 48.7 kyr old [21]. Instead the transition between these two stages is not such good represented by Dome C ice core bags. The top of the youngest ice core bag was 10.5 kyr old and the bottom of the oldest ice core was 21.5 kyr old [22]. During glacial times the dust transport is expected to be 4 to 7 times higher compared to warm periods [23], which should also be reflected in REE- and mineral dust components concentrations.

Each bag of an ice core is used for several ice core studies, therefore a section from the inner part of the ice core was available for REE analysis. From the top of each bag 30 cm long sections were cut by a band saw and used for further steps. The sample surface was decontaminated in a first step by sawing 1 cm of the surface with a band saw. The 30 cm long section was divided in three 10 cm long parts. Each part was rinsed with 1 to 2 L ultrapure water for three times. In consequence of this procedure the weight of each part was reduced by 50 %. The three 10 cm long parts of each section were placed in pre-cleaned high density polyethylene (HDPE) bottles and melted at room temperature. Samples were dispersed by pivoting; aliquots were filled in polystyrene (PS) CC-accuvettes and finally stored at -20 °C.

Under a clean bench (US-Class 100) which was situated in a clean room laboratory (US-Class 10,000) samples were molten and transferred into pre-cleaned polyfluor alkoxy (PFA) vessels. The CC-accuvettes were rinsed with 10 ml subboiled HNO_3 (1 Mol L^{-1}) and added into the PFA vessels. Diluted samples were contentrated to 0.5 to 2 ml with a pressure digestion system (Druckaufschlusssystem DAS, Picotrace GmbH, Germany). Afterwards samples were digested using 2 ml subboiled HNO_3 (distilled 65 %, p.a., Merck), 1 ml subboiled HF (40 %, suprapur, Merck) and 2 ml H_2O_2 (30 %, suprapur, Merck). Subsequently samples were concentrated to a

maximum volume of 1.75 mL. Detailed information about the concentration and digestion of samples is given as supplementary material. Finally samples were quantitatively transferred into polypropylene (PP) vials, Rh was added (final concentration 1 μg L^{-1}) and the samples were filled up to a volume of 2 ml with subboiled HNO_3 (1 Mol L^{-1}). Out of these 2 ml multielement analysis by ICP-TOF-MS, ICP-Q-MS and ICP-SF MS were accomplished. Ten blank solutions have been processed in the same way to obtain information about the digestion quality.

3.3   Instrumentations

The analytical measurements were conducted at AWI by ICP-TOF-MS (Analytik Jena, Jena, Germany) and ICP-Q-MS (Elan 6000, Perkin Elmer/Sciex, Waltham, Massachussets). Analysis by ICP-SF-MS (Element2, Thermo Finnigan MAT, Bremen, Germany) was done at DES. The experimental setup for the ICP-TOF-MS is shown elsewhere [17]. The ICP-TOF-MS and the ICP-Q-MS were situated in clean room laboratories, US-Class 10,000; the ICP-SF-MS is equipped with a class 100 clean bench as a clean sample introduction area.

To minimize spectral interferences and oxide forming microflow nebulization systems with desolvating units were used (Aridus II (for ICP-TOF-MS), MCN6000 (for ICP-Q-MS), Aridus I (for ICP-SF-MS); all: Cetac Technologies, Omaha, Nebraska). These 3 systems were all equipped with a 100 μL PFA nebulizer, a heated PFA spray chamber, and a heated microporous PTFE membrane. Besides reducing the oxide formation the signal intensities increased by a factor of about 10 compared to analysis with cross flow nebulisation as sample introduction system for ICP-TOF-MS and ICP-Q-MS and by a factor of 5 for ICP-SF-MS. The instrument settings were optimized daily and are given in Table 1. The oxide forming rates of all systems were optimized daily by tuning with a Ce solution.

4   Results and discussion

4.1   Calibration studies, detection limits and blank contributions for the ICP-TOF-MS

External calibration was performed for quantification. Standards were prepared from 10 mg L^{-1} stock solutions with HNO_3, Rh as internal standard and ultrapure water. Due to sensitivity drifts of the detector system three calibrations were run per day. Calibration standards ranged from 1 ng L^{-1} to 500 ng L^{-1}, 7 standards inclusive blank, were analysed 10 times per calibration. Table 2 shows averaged calibration data from 5 calibrations, that include the number of standards used for calibration, the slope with standard deviation (SD), the intercept with SD, the standards error of replicate measurements (values for blank and 50 ng L^{-1} are shown exemplarily), the correlation coefficient (r^2) and the instrumental detection limit (IDL, 3 σ criteria). The tuned ICP-TOF-MS

system was very sensitive which is represented by an average slope of 1.9 (Table 2). A very low intercept was obtained for all REE (average 4.6 x 10^{-4}) except Ce which showed an average intercept of 25.7 x 10^{-4}. Generally the SD for the intercept is high (average 120 %). The calibration range was chosen according the expected concentrations in Antarctic ice cores. The resulting correlation coefficients for REE are higher than 0.9992. No IDL is inferior than 1 ng L^{-1}. The linearity of calibration curves was checked by analysing standards with known concentrations at the end of an analysis cycle.

Antarctic ice core samples were digested for analysis. Hence it is of importance to carefully look at the blank contributions. 10 blank standards (2 ml HNO_3, 1 ml HF, 2 ml H_2O_2) were digested parallel to the digestion of natural samples. The REE concentrations were always found to be below the IDL except for La, Ce, Pr and Nd (Table 2).

4.2 Accuracy and Precision of the ICP-TOF-MS and ICP-Q-MS

Three reference materials, SPS-SW1, SLRS-4 and NIST 1640, have been analysed. Certified REE concentrations are only available for SPS-SW1, each concentrations amounts 500 ng L^{-1}. Table 3 summarizes all REE concentrations obtained by ICP-TOF-MS, ICP-Q-MS, certified values for SPS-SW1 as well as literature data available for SLRS-4 [24] and NIST 1640 [25]. For SPS-SW1 the recovery rate obtained by ICP-TOF-MS studies amounts 103 ± 8.4 % whereas the recovery rate for ICP-Q-MS amounts 104 ± 12 %. Both MS systems showed distinct differences for Dy. The recovery rate for La and Ce obtained by ICP-TOF-MS amounts 117%. For the ICP-TOF-MS it is known that Ba concentrations exceeding 1 μg L^{-1} influence the analysis of La and Ce. SPS-SW1 contains 50 μg L^{-1} Ba, in a 1:100 dilution only 0.5 μg L^{-1}. This should not influence the analysis of La and Ce, therefore we can not explain the reason for high recovery rates yet. SLRS-4 contains 12.2 μg L^{-1} Ba but La and Ce analysis are not as strong influenced as in SPS-SW1. REE concentrations of SLRS-4 obtained by ICP-TOF-MS, ICP-Q-MS and literature data [24] fit very well (relative standard deviation (RSD) 7.6 ± 4.4 %). This good correlation could not be achieved for NIST 1640. The average RSD for all REE obtained by ICP-TOF-MS, ICP-Q-MS and literature data [25] is 36 ± 23 %. Higher concentrations obtained by ICP-TOF-MS can be explained by high matrix load. NIST 1640 contains e.g. 29.4 mg L^{-1} Na and 7 mg L^{-1} Ca. The ICP-TOF-MS works with a multi channel plate as detector system (MCP). Each time a channel has to process an incoming ion this channel needs 10 ms to recover. The RSD of replicate analysis, representing the precision, is similar for both MS systems. It amounts 4.1 % for ICP-TOF-MS analysis and 4.5 % for ICP-Q-MS analysis.

4.3   Interference studies

To exclude problems with spectral interferences in ICP-TOF-MS, for REE mainly represented by oxides, the described desolvation unit was used. Nevertheless equations were compiled to calculate fractions of interfering species. Formula 1 is an example to correct isobaric interferences of ^{142}Nd by ^{142}Ce. Spectral interferences by oxides are considered by formula 2, as example the correction of the ^{155}Gd signal is shown.

$$^{142}Nd_{corr} = {}^{142}Nd - \frac{11.08}{88.48} \cdot {}^{140}Ce \tag{1}$$

$$^{155}Gd_{corr} = {}^{155}Gd - 0.9967 \cdot {}^{139}La \cdot MO^+ \tag{2}$$

Isobaric interference are present for isotopes ^{142}Nd (^{142}Ce, 11.08 %), ^{144}Nd (^{144}Sm, 3.1 %) and ^{164}Dy (^{164}Er, 1.61 %). For isotopes exceeding mass 155 corrections due to oxide forming has to be accomplished (formula 2). Table S 1 shows analysed isotopes with its natural abundance and potential interefence species, which are taken into account for evaluating ICP-TOF-MS data. Problems caused by polyatomic species including Ba can be neglected due to high Ba^{2+} forming rates 14.7 ± 0.3 %. Where possible several isotopes of one element were analysed to check the quality of the correction equations. The very good agreement of concentrations obtained by two or more different isotopes suggests that, isobaric and spectroscopic interferences were eliminated or rendered negligible.

Ba concentrations exceeding 1 μg L^{-1} lead to high background signals (10 cps) in the ICP-TOF-MS on mass 139 (La) and 140 (Ce). Therefore, in the majority of cases, La and Ce concentrations were taken from diluted samples.

Adequate equations are integrated within the evaluation system of the ICP-Q-MS. Interference studies of the used ICP-SF-MS at DES are reported in [5].

4.4   Long term stability of the ICP-TOF-MS

200 measurements à 7 s integration time and 5.4 s relaxation time (Σ41.3 minutes) have been conducted for long term stability tests of ICP-TOF-MS. Several standards were tested and showed very convincing results. For example the relative standard deviation (RSD) of Er, as it is the REE with lowest signal sensitivity, is: 12.9 % for a blank standard, 11.7 % for a 1 ng L^{-1} standard, 5.9 % for a 10 ng L^{-1} standard, 3.4 % for a 0.1 μg L^{-1} standard, 1.0 % for a 0.5 μg L^{-1} standard and 0.8 % for a 1 μg L^{-1} standard. This is in a good agreement with data obtained by coupling the Aridus II to a Multi-Collector ICP-MS and analyzing a 0.5 μg L^{-1} multielement solution [26].

4.5 Concentrations in Antarctic ice core samples

Intercomparison studies between 3 different ICP-MS (2 different labs) should clarify the performance of the ICP-TOF-MS, particular in terms of the analysis on ultra trace level. Due to the limitations of isotopes analysed by ICP-Q-MS and ICP-SF-MS only concentrations of REE are available for all 3 devices.

Depending on the age of ice cores samples contain more or less mineral dust. During glacial periods the dust transport into Antarctica increases, therefore REE concentrations are higher compared to interglacial periods [23]. The authors report that the amount of dust and its source varies within the Antarctic. An overview of average interglacial REE concentrations, glacial concentrations as well as the proportion of glacial / interglacial is given in Table 4 for DML and EDC ice core samples. All concentrations of Antarctic samples represent concentrations, which were obtained by calculations due to concentration after digestion and after subtracting blank concentrations. Except few samples concentrations were higher then blank levels. Depending on the mass spectrometry system used most concentrations are above the detection limit. If one of these two criteria fails the sample is not being considered for the associated MS system. Minimum concentrations are observed during warm periods whereas high REE concentrations are observed during glacial periods. On average the concentration of REE concentrations during glacial periods is 8 ± 3 times higher for DML ice core samples and 3 ± 1 times higher for EDC samples. This increase of dust transport during glacial periods compared to interglacial periods is consistent with data obtained by [23]. [5] report about REE concentrations in Antarctic ice from Dome C station. During interglacial stages they found lower concentrations compared to data reported here. Concentrations during glacial stages fit very well. Perhaps contamination took place during sample preparation which influences low concentrated samples much more than high concentrated samples. This does not have any influence when comparing the three different MS systems.

Mainly depending on the concentrations of the samples, the results obtained by three different MS systems coincide or differ from each other. As example Figure 1 shows exemplarily correlation diagrams (ICP-Q-MS vs ICP-TOF-MS, ICP-SF-MS vs ICP-TOF-MS, ICP-SF-MS vs ICP-Q-MS) for Ce, Dy and Lu. These elements were chosen as they represent light, middle and heavy REE. Correlation diagrams of all REE are shown in the supplementary material section (Figure S 2). For the linear fit function the errors of each REE were taken as weighing parameter. 12 samples analysed by ICP-TOF-MS show distinct different concentrations compared to the other two MS systems which can not be explained yet. These samples are symbolized as grey dots with their standard deviation (SD) in the correlation diagrams ICP-Q-MS vs ICP-TOF-MS and ICP-SF-MS vs ICP-TOF-MS. They are ignored for linear fit studies. All other samples are marked as black dots with SD.

In general the SD obtained by ICP-Q-MS is much higher compared to the other two MS systems. ICP-Q-MS data fit very well to ICP-SF-data with slightly higher concentrations obtained by ICP-Q-MS. The ICP-TOF-MS system obtains higher concentrations for nearly all REE compared to the other two systems. The higher the concentrations are, the better the correlation between the three systems is. For the presented ICP-TOF-MS system one can say, as long as the REE concentrations of a sample amounts 4 ng L^{-1} the correlation with ICP-Q-MS and ICP-SF-MS is very good. Below that concentration results have to be looked at carefully.

5   Conclusions

Analysis of reference materials showed that the used ICP-TOF-MS is best suitable for the determination of trace element concentration as long as the concentrations amount 1 ng L^{-1} to 250 ng L^{-1}. Within this concentration range the accuracy and precision is very good (recovery rate 103 %, RSD of replicate analysis 4.1 %). Intercomparison studies between three different types of mass spectrometers showed that the ICP-TOF-MS is able to detect trace elements in the sub ng L^{-1} range with the tendency to find higher concentrations than other MS systems. If analysed concentrations are below 4 ng L^{-1} the accuracy of the ICP-TOF-MS gets worse, but the distribution pattern of concentrations of different samples is similar. Therefore, trace element concentration patterns obtained by ICP-TOF-MS can be used for interpreting signal progressions covering long time periods in ice cores from remote areas like Antartica.

Until now there is no literature available on the investigation of such low element concentrations with ICP-TOF-MS. This indicates that the presented ICP-TOF-MS is much more sensitive compared to other devices. Improvements could be achieved by further preconcentration of the samples before analysis. Further a different generator system for the inductively coupled plasma system will stabilize the plasma and reduces the oxide forming rate.

6   Acknowledgement

7   Literature

1. M. Revel-Rolland, P. De Deckker, B. Delmonte, P.P. Hesse, J.W. Magee, I. Basile-Doelsch, F. Grousset, D. Bosch, EPSL, 249 (2006) 1

2. M. Legrand, P. Mayewski, Rev. Geophys., 35(1997) 219

3. E. Wolff, H. Fischer, F. Fundel, U. Ruth, B. Twarloh, G.C. Littot, R. Mulvaney, R. Röthlisberger, M. de Angelis, C.F. Boutron, M. Hansson, U. Jonsell, M.A. Hutterli, F. Lambert, P. Kaufmann, B. Stauffer, T.F. Stocker, J.P. Steffensen, M. Bigler, M.L. Siggaard-Andersen, R. Udisti, S. Becagli, E. Castellano, M. Severi, D. Wagenbach, C. Barbante, P. Gabrielli, V. Gaspari, Nature, 440 (2006) 491

4. I. Basile, F.E. Grousset, M. Revel, J.R. Petit, P.E. Biscaye, N.I. Barkov, EPSL, 146 (1996) 573

5. P. Gabrielli, C. Barbante, C. Turetta, A. Marteel, C. Boutron, G. Cozzi, W. Cairns, C. Ferrari, P. Cescon, Anal. Chem., 78 (2006) 1883

6. S. Hong, J.P. Candelone, C. Turetta, C.F. Boutron, EPSL, 143 (1996) 233

7. G. Tao, R. Yamada, Y. Fujikawa, A. Kudo, J. Zheng, D.A. Fisher, R.M. Koerner, Talenta, 55 (2001) 765

8. J.P. Candelone, S. Hong, C. Pellone, C.F. Boutron, JGR, 100(D8) (1995) 16605

9. S.M. Hong, C.F. Boutron, C. Barbante, S.D. Hur, K. Lee, P. Gabrielli, G. Capodaglio, C.P. Ferrari, C . Turetta, J.R. Petit, V.Y. Lipenkov, J. Environ. Monit., 7(12) (2005) 1326

10. G.M. Vandal, W.F. Fitzgerald, C.F. Boutron, J.P. Candelone, Nature, 362 (1993) 621

11. R. Capelli, V. Minganti, C. Chiarini, R. De Pellegrini, Int. J. Environ. Anal. Chem., 71(3-4) (1998) 289

12. K. Van de Velde, P. Vallelonga, J.P. Candelone, K.J.R. Rosman, V. Gaspari, G. Cozzi, C. Barbante, R. Udisti, P. Cescon, C.F. Boutron, EPSL, 232(1-2) (2005) 95

13. M. Balcerzak, Anal. Sci., 19 (2003) 979

14. N.H. Bings, J.M. Costa-Fernandez, J.P. Guzowski, A.M. Leach, G.M. Hieftje, Spectrochim. Acta Part B – At. Spectrosc., 55(7) (2000) 767

15. N.H. Bings, Nachrichten aus der Chemie, 49(9) (2001) 1069

16. C. Lüdke, J. Skole, K. Taubner, M. Kriews, Spectrochim. Acta Part B – At. Spectrosc., 60(11) (2005) 1412

17. E. Hoffmann, C. Lüdke, Spectrosc. Eur., 17(No.1) (2005) 20

18. E. Hoffmann, C. Lüdke, J. Skole, H. Stephanowitz, J. Wollbrandt, W. Becker, Spectrochim. Acta Part B, 57 (2002) 1535

19. EPICA Community Members, Nature, 444 (2006) 195

20. EPICA Community Members, Nature, 429 (2004) 623

21. U. Ruth, J.M. Barnola, J. Beer, M. Bigler, T. Blunier, E. Castellano, H. Fischer, F. Fundel, P. Huybrechts, P. Kaufmann, S. Kipfstuhl, A. Lambrecht, A. Morganti, H. Oerter, F. Parrenin, O. Rybak, M. Severi, R. Udisti, F. Wilhelms, E. Wolff, Climate of the Past, 3 (2007) 475

22. L. Augustin, J. Jouzel, PANGAEA, doi:10.1594/PANGAEA.198743, http://store.pangaea.de/Projects/EPICA/EDC_descr.pdf (2004)

23. H. Fischer, M.-L. Siggaard-Andersen, U. Ruth, R. Röthlisberger, and E. Wolff, Rev. Geophys., 45, (2007) RG1002, doi:10.1029/2005RG000192.

24. D. Yeghicheyan, J. Carignan, M. Valladon, M. B. Le Coz, F. Le Cornec, M. Castrec-Rouelle, M. Robert, L. Aquilina, E. Aubry, C. Churlaud, A. Dia, S. Deberdt, B. Dupré, R. Freydier, G. Gruau, O. Hénin, A.M. de Kersabiec, J. Macé, L. Marin, N. Morin, P. Petitjean, E. Serrat, Geostand Geoanal Res, 25(2-3) (2001) 465

25. Agilent ICP-MS Journal, 20 (2004) 1

26. CETAC, http://www.cetac.com/pdfs/Aspire-400_2.pdf (13.11.2007)
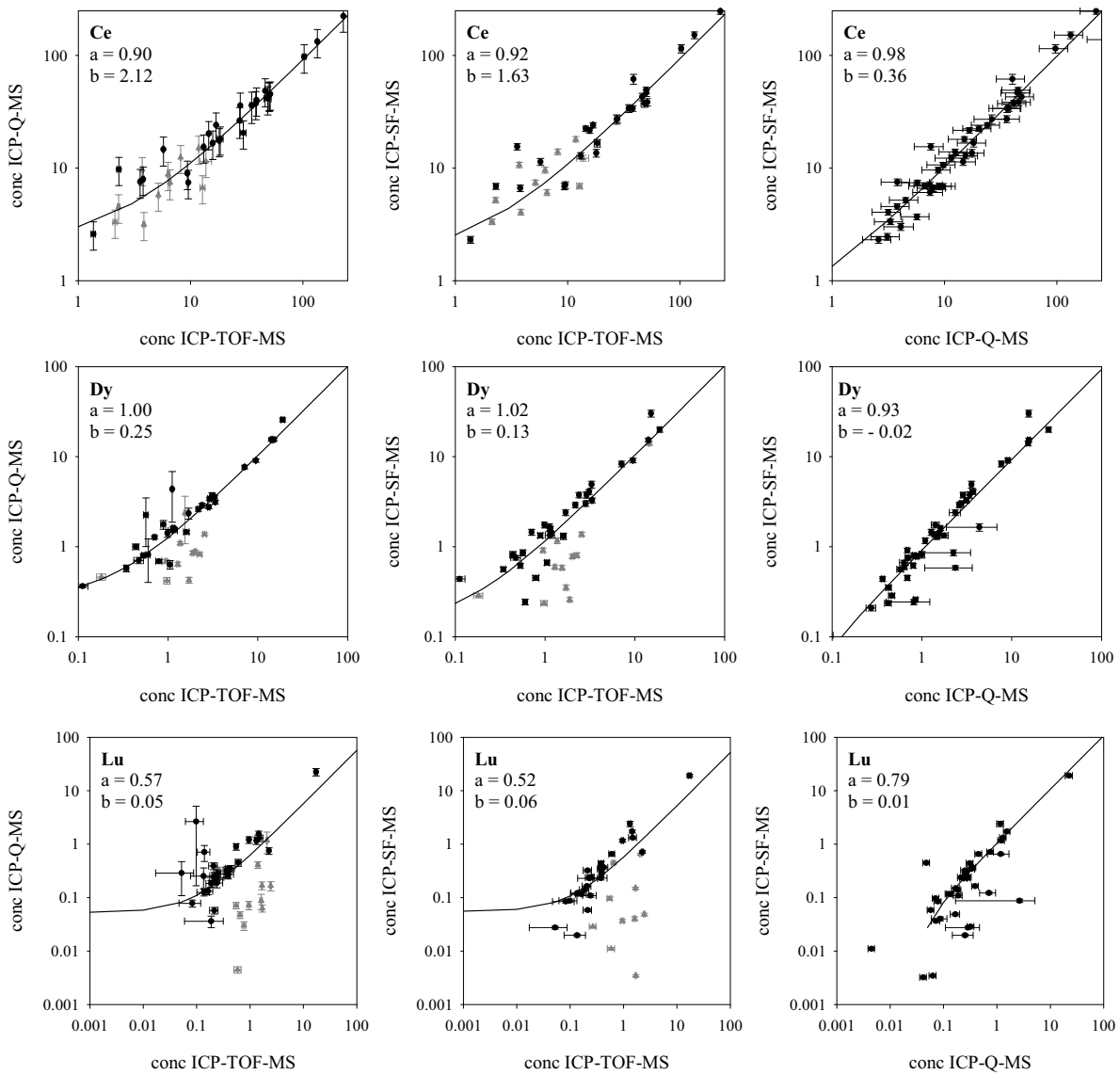
Figure 1: *Analysed Ce, Dy and Lu concentrations in Antarctic ice core samples diagrammed as ICP-Q-MS concentrations vs ICP-TOF-MS concentrations, ICP-SF-MS concentrations vs ICP-TOF-MS concentrations and ICP-SF-MS concentrations vs ICP-Q-MS concentrations with associated parameters of a linear fit (a = slope, b = intercept). Errors of each measurement were taken as weighing parameter. Samples presented as grey dots are expected to be analysed wrong by ICP-TOF-MS and are therefore not included in linear fit calculations.*

Table 1: *Instrumental conditions and measurement parameters for the ICP-TOF-MS, ICP-Q-MS and ICP-SF-MS and desolvation units.*

	ICP-TOF-MS (Analytik Jena)	ICP-Q-MS (Elan 6000, PE)	ICP-SF-MS (Element 2, Finnigan)
ICP-MS			
RF Power /W	1050	1350	1250
Plasma gas / L min^{-1}	14.5	15	15.5
Auxiliary gas / L min^{-1}	1.4	0.8	1.8
Nebulizer gas / L min^{-1}	0.98	0.62	0.8-1.1
resolution adopted (m Δm^{-1})	700	300	~400
Nebulizer (with desolvatisation)	Aridus II	MCN 6000	Aridus I
Sweep gas / L min^{-1}	4.6 - 5.0	2.35	3.40-4.15
Nitrogen / mL min^{-1}	21 - 22	12	1 - 18
T (spray chamber) / °C	110	110	95
T (desolvating unit) / °C	160	160	175
Sample uptake / µl min^{-1}	160	100	100
Data aquisition			
Isotopes analysed	All	~40	19
Replicates	6	3	40
Integration time / s	7	0.1 (each isotope)	
Sweeps	175000	20	30
Measuring time per sample / min	1.5	7	
Oxides / %	0.2 - 0.5	0.03	
Double charged ions / %	14 - 15	5 - 7	

Table 2: *ICP-TOF-MS calibration data for the investigations of reference materials and intercomparison samples. The slope with its SD, the intercept with its SD, standard errors for two different calibration standards, the correlation coefficient (r^2) and the instrumental detection limit (IDL) are given. Values were calculated on the basis of 5 different calibrations. Each standard was analysed 10 times per calibration.*

	No. Of data points	slope $\pm$ SD	intercept $(\times10^{-4})$ $\pm$ SD $(\times10^{-4})$	standard error y		r^2	IDL / ng L^{-1}	conc. digested acid blanks / ng L^{-1}
				Blank $(\times10^{-4})$	50 ng L^{-1} $(\times10^{-4})$			
La	6	2.04 $\pm$ 0.09	3.02 $\pm$ 7.43	1.38	6.43	0.9997	0.6	0.9 $\pm$ 0.03
Ce	7	1.80 $\pm$ 0.07	25.73 $\pm$ 3.59	1.62	6.51	0.9999	0.9	3.4 $\pm$ 0.06
Pr	6	2.31 $\pm$ 0.09	6.43 $\pm$ 9.06	1.29	7.03	0.9996	0.5	0.7 $\pm$ 0.01
Nd	5	2.10 $\pm$ 0.08	5.68 $\pm$ 8.31	1.58	7.29	0.9992	0.7	1.9 $\pm$ 0.06
Sm	6	1.28 $\pm$ 0.05	4.74 $\pm$ 3.78	1.34	4.64	0.9993	1.0	0.4 $\pm$ 0.04
Eu	5	2.31 $\pm$ 0.09	4.56 $\pm$ 6.37	1.43	7.13	0.9993	0.6	0.1 $\pm$ 0.01
Gd	5	1.64 $\pm$ 0.06	4.54 $\pm$ 5.45	1.57	5.84	0.9994	0.9	0.5 $\pm$ 0.03
Tb	6	2.34 $\pm$ 0.06	4.07 $\pm$ 5.90	0.81	7.68	0.9998	0.3	0.1 $\pm$ 0.01
Dy	5	1.64 $\pm$ 0.05	5.30 $\pm$ 3.84	1.40	5.11	0.9996	0.8	0.7 $\pm$ 0.01
Ho	5	2.21 $\pm$ 0.07	2.02 $\pm$ 4.12	0.90	6.42	0.9996	0.4	0.1 $\pm$ 0.01
Er	5	1.30 $\pm$ 0.06	2.78 $\pm$ 2.72	1.09	4.82	0.9997	0.8	0.3 $\pm$ 0.02
Tm	5	2.21 $\pm$ 0.08	3.47 $\pm$ 4.79	0.72	7.11	0.9995	0.3	0.1 $\pm$ 0.01
Yb	5	1.84 $\pm$ 0.06	6.11 $\pm$ 6.35	1.36	5.54	0.9992	0.7	0.6 $\pm$ 0.04
Lu	6	2.02 $\pm$ 0.08	7.15 $\pm$ 3.68	0.84	5.85	0.9998	0.4	0.2 $\pm$ 0.00

Table 3: REE Concentrations in ng L^{-1} with SD in reference materials SPS-SW1, SLRS-4 and NIST 1640 obtained by ICP-TOF-MS and ICP-Q-MS. Recovery rates for reference material SPS-SW1 are shown in brackets below the concentrations obtained by ICP-TOF-MS and ICP-Q-MS. Concentrations of reference materials SPS-SW1 were derived by analysing a 1:100 dilution. REE from La to Nd in SLRS-4 were analysed out of a 1:10 dilution, all other REE were analysed without any dilution. In NIST1640 all REE concentrations were analysed using a 1:10 dilution.

	SPS-SW1			**SLRS-4**			**NIST 1640**		
	certified	ICP-TOF-MS	ICP-Q-MS	ICP-TOF-MS	ICP-Q-MS	reference [24]	ICP-TOF-MS	ICP-Q-MS	reference [25]
La	500 ± 10	586 ± 10 (117.3)	495 ± 13 (84.4)	304 ± 4.3	279 ± 3.6	287 ± 7.2	706 ± 8.8	299 ± 7.0	420
Ce	500 ± 10	581 ± 22 (116.1)	516 ± 8 (88.9)	411 ± 12.3	361 ± 1.8	360 ± 10.9	553 ± 9.9	350 ± 5.7	520
Pr	500 ± 10	516 ± 17 (103.2)	510 ± 6 (98.7)	77 ± 0.7	67 ± 1.6	69 ± 1.7	200 ± 3.8	72 ± 3.9	76
Nd	500 ± 10	505 ± 37 (101.1)	510 ± 6 (100.9)	260 ± 9.9	264 ± 8.5	269 ± 12.8	499 ± 13.4	391 ± 39.6	350
Sm	500 ± 10	497 ± 17 (99.4)	497 ± 1 (100.0)	64 ± 1.5	57 ± 2.0	57 ± 2.5	182 ± 6.8	103 ± 7.1	72
Eu	500 ± 10	497 ± 14 (99.4)	510 ± 6 (102.7)	12 ± 0.3	11 ± 1.0	8 ± 0.5	40 ± 1.6	46 ± 3.7	10
Gd	500 ± 10	490 ± 10 (98.0)	513 ± 6 (104.7)	37 ± 1.3	41 ± 2.8	34 ± 1.8	65 ± 7.9	53 ± 2.8	65
Tb	500 ± 10	482 ± 13 (96.3)	506 ± 5 (105.0)	4 ± 0.2	5 ± 0.4	4 ± 0.3	11 ± 1.5	1 ± 0.6	2
Dy	500 ± 10	603 ± 5 (120.7)	852 ± 16 (141.2)	22 ± 1.9	24 ± 0.3	24 ± 1.4	49 ± 3.7	36 ± 4.2	21
Ho	500 ± 10	486 ± 17 (97.3)	519 ± 10 (106.7)	5 ± 0.2	4 ± 0.4	5 ± 0.3	13 ± 0.8		6
Er	500 ± 10	461 ± 36 (92.2)	498 ± 4 (108.1)	12 ± 0.4	15 ± 0.6	13 ± 0.5	31 ± 2.6	32 ± 2.5	16
Tm	500 ± 10	490 ± 20 (98.0)	510 ± 4 (104.1)	2 ± 0.1	2 ± 0.2	2 ± 0.1			0.4
Yb	500 ± 10	503 ± 28 (100.7)	503 ± 13 (99.9)	11 ± 0.7	11 ± 0.5	12 ± 0.3	23 ± 3.2	11 ± 2.1	8
Lu	500 ± 10	490 ± 22 (98.1)	517 ± 2 (105.4)	3 ± 0.1	2 ± 0.2	2 ± 0.1		2 ± 1.0	1

Table 4: *Summary of average concentrations of analysed REE via ICP-SF-MS during interglacial and glacial periods for DML ice core samples and EDC ice core samples. Additionally the proportion of glacial / interglacial concentrations is given.*

	DML ice core samples						glacial / interglacial	EDC ice core samples						glacial / interglacial
	interglacial			glacial				interglacial			glacial			
La	4.2	±	2.1	52.7	±	43.8	12.6	5.0	±	6.6	16.3	±	5.8	3.3
Ce	9.4	±	5.4	101.2	±	72.5	10.7	9.8	±	11.5	33.6	±	11.7	3.4
Pr	1.3	±	0.8	16.8	±	17.7	12.8	1.3	±	5.3	4.5	±	1.6	3.5
Nd	21.9	±	66.1	53.8	±	55.7	2.5	3.9	±	6.0	15.3	±	5.2	3.9
Sm	1.0	±	0.5	12.2	±	12.1	12.0	0.9	±	5.2	3.8	±	1.3	4.2
Eu	0.4	±	0.3	3.2	±	3.1	8.2	0.5	±	5.6	0.9	±	0.3	1.9
Gd	1.0	±	0.7	10.0	±	9.8	10.1	0.8	±	5.1	3.4	±	1.1	4.1
Tb	0.3	±	0.3	1.7	±	1.6	6.2	0.2	±	5.5	0.5	±	0.2	2.2
Dy	1.8	±	3.4	9.2	±	9.0	5.3	0.8	±	4.8	3.0	±	1.0	3.9
Ho	0.3	±	0.3	1.9	±	1.8	6.8	0.2	±	5.2	0.6	±	0.2	2.5
Er	0.5	±	0.4	5.3	±	5.0	10.0	0.5	±	4.8	1.8	±	0.6	3.7
Tm	0.2	±	0.3	0.9	±	0.8	4.0	0.2	±	5.3	0.3	±	0.1	1.7
Yb	0.5	±	0.4	5.2	±	4.9	9.9	0.5	±	4.7	1.7	±	0.6	3.5
Lu	0.2	±	0.3	0.9	±	0.8	4.1	0.2	±	5.5	0.3	±	0.1	1.6

8   Supplementary Material

Digestion of samples: Druckaufschluss-System DAS, Picotrace GmbH, Germany

Figure S 1: *left: Experimental setup for preconcentration of liquid samples before the addition of acids and after acid digestion. Right: Experimental setup for the acid digestion of Antarctic ice core samples.*

Concentration of samples before digestion

Programme	heating plate	time / hours	command	Temperature [°C]
concentration	bottom plate	2	heat up to	160
		1.12`	keep constant on	160
	upper plate	1.20`	heat up to	110
		1.30`	keep constant on	110
		1	keep constant on	90

Digestion

Programme	heating plate	time / hours	command	Temperature [°C]
digestion	bottom plate	1	heat up to	100
		5	keep constant on	100
		1	heat up to	120
		2	keep constant on	120
		1	heat up to	140
		2	keep constant on	140
		1	heat up to	160
		2	keep constant on	160
		1	heat up to	180
		4	keep constant on	180
		2	heat up to	210
		7	keep constant on	210
		2		170
		2		160
		1.30`		140

Concentration of samples after digestion

Programme	heating plate	time / hours	command	Temperature [°C]
concentration	bottom plate	2	heat up to	160
		0.32`	keep constant on	160
	oben	1.20`	heat up to	110
		1.30`	keep constant on	110
		1	keep constant on	90

Table S 1: Analysed isotopes with its natural abundance and potential interefence species, which are taken into account for evaluating ICP-TOF-MS data.

Analyte		Potential Interferences	
Isotope	Abundance	Species	Abundance[a]
^{139}La	99.91		
^{140}Ce	88.48		
^{141}Pr	100		
^{142}Nd	27.13	^{142}Ce	11.08
^{143}Nd	12.18		
^{144}Nd	23.8	^{144}Sm	3.1
^{145}Nd	8.3		
^{146}Nd	17.19		
^{147}Sm	15		
^{149}Sm	13.8		
^{152}Sm	26.7		
^{151}Eu	47.8		
^{153}Eu	52.2		
^{155}Gd	14.8	^{139}La^{16}O	99.67
^{156}Gd	20.47	^{140}Ce^{16}O	88.26
^{157}Gd	15.65	^{141}Pr^{16}O	99.76
^{158}Gd	24.84	^{142}Nd^{16}O	27.09
		^{142}Ce^{16}O	11.05
^{159}Tb	100	^{143}Nd^{16}O	12.15
^{161}Dy	18.9	^{145}Nd^{16}O	8.28
^{163}Dy	24.9	^{147}Sm^{16}O	14.96
^{164}Dy	28.2	^{148}Sm^{16}O	11.27
		^{148}Nd^{16}O	5.75
		^{164}Er	1.61
^{165}Ho	100	^{149}Sm^{16}O	13.77
^{166}Er	33.6	^{150}Nd^{16}O	5.63
^{167}Er	22.95	^{151}Eu^{16}O	47.69
^{168}Er	26.8	^{152}Sm^{16}O	26.64
^{169}Tm	100	^{153}Eu^{16}O	52.07
^{171}Yb	14.3	^{155}Gd^{16}O	14.76
^{172}Yb	21.9	^{156}Gd^{16}O	20.42
^{173}Yb	16.12	^{157}Gd^{16}O	15.61
^{174}Yb	31.8	^{158}Gd^{16}O	24.78
^{175}Lu	100	^{159}Tb^{16}O	99.76

[a]For polyatomic species calculated as the product of
the natural abundances of each isotope divided by
100
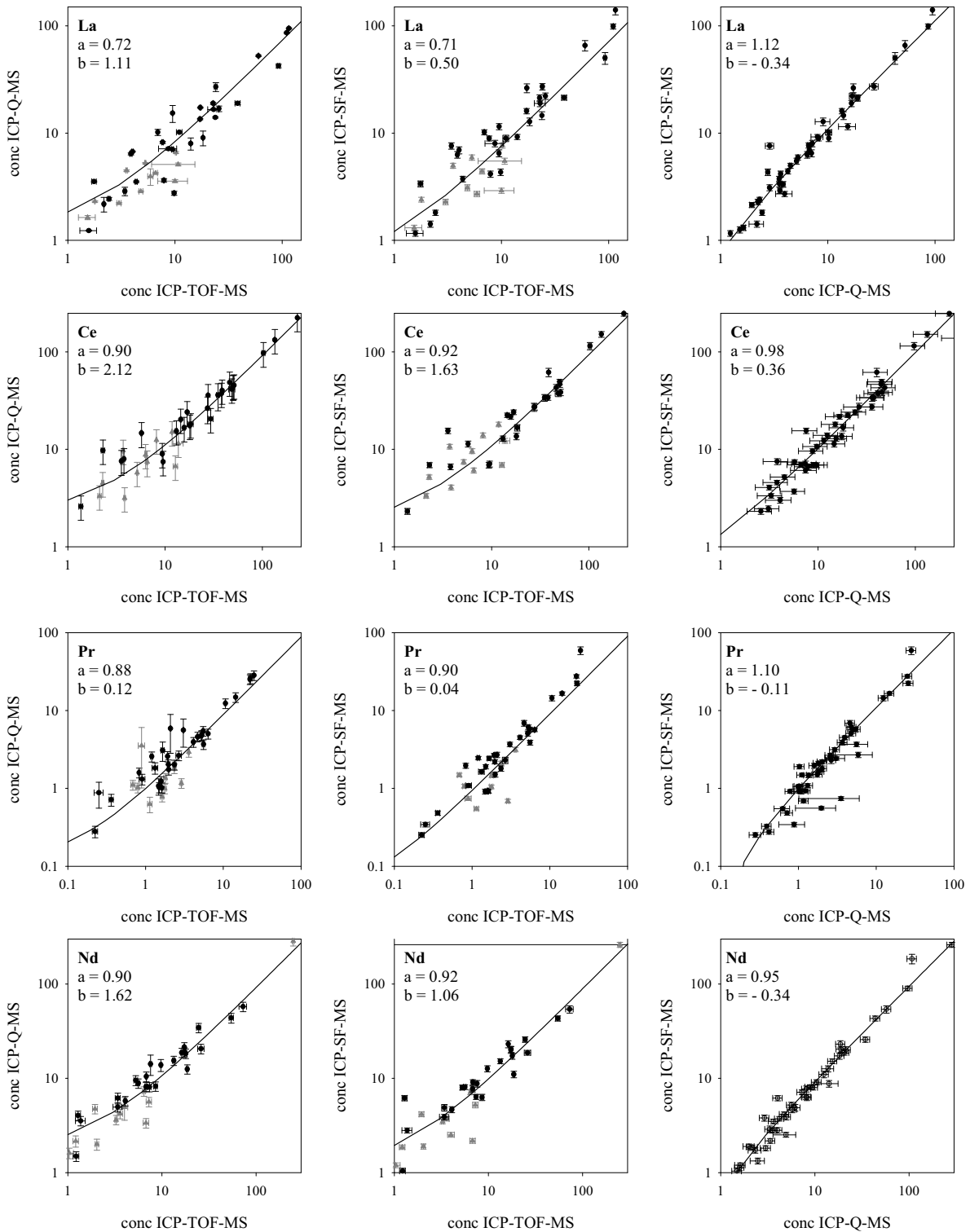
Figure S 2: *Analysed REE concentrations (ng L^{-1}) in Antarctic ice core samples diagrammed as ICP-Q-MS concentrations vs ICP-TOF-MS concentrations, ICP-SF-MS concentrations vs ICP-TOF-MS concentrations and ICP-SF-MS concentrations vs ICP-Q-MS concentrations with associated parameters of a linear fit (a = slope, b = intercept). Errors of each measurement were taken as weihjing parameters. Samples presented as grey dots are expected to be wrong analysed by ICP-TOF-MS and are therefore not included in linear fit calculations.*
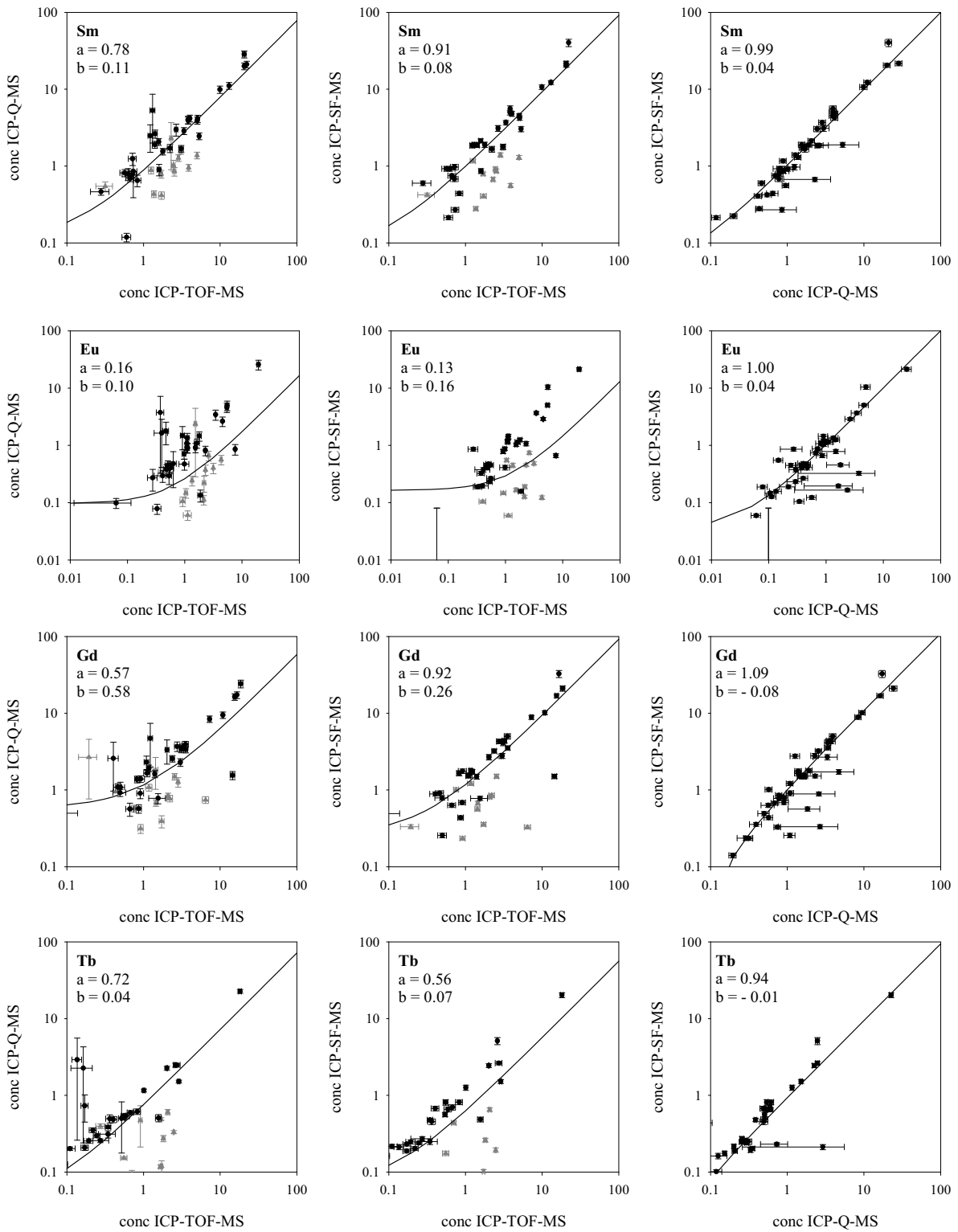
Figure S 2: Continuation
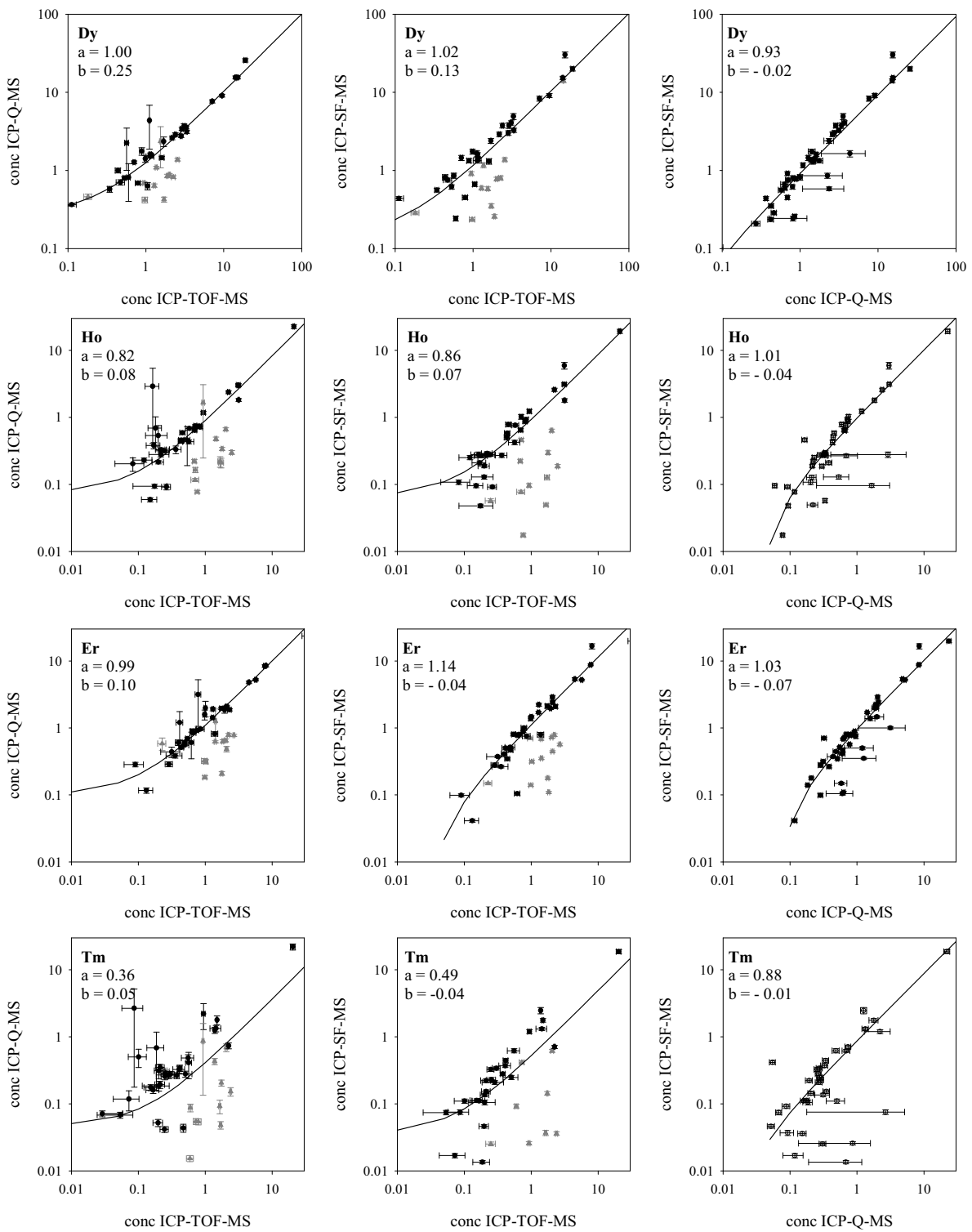
Figure S 2: Continuation
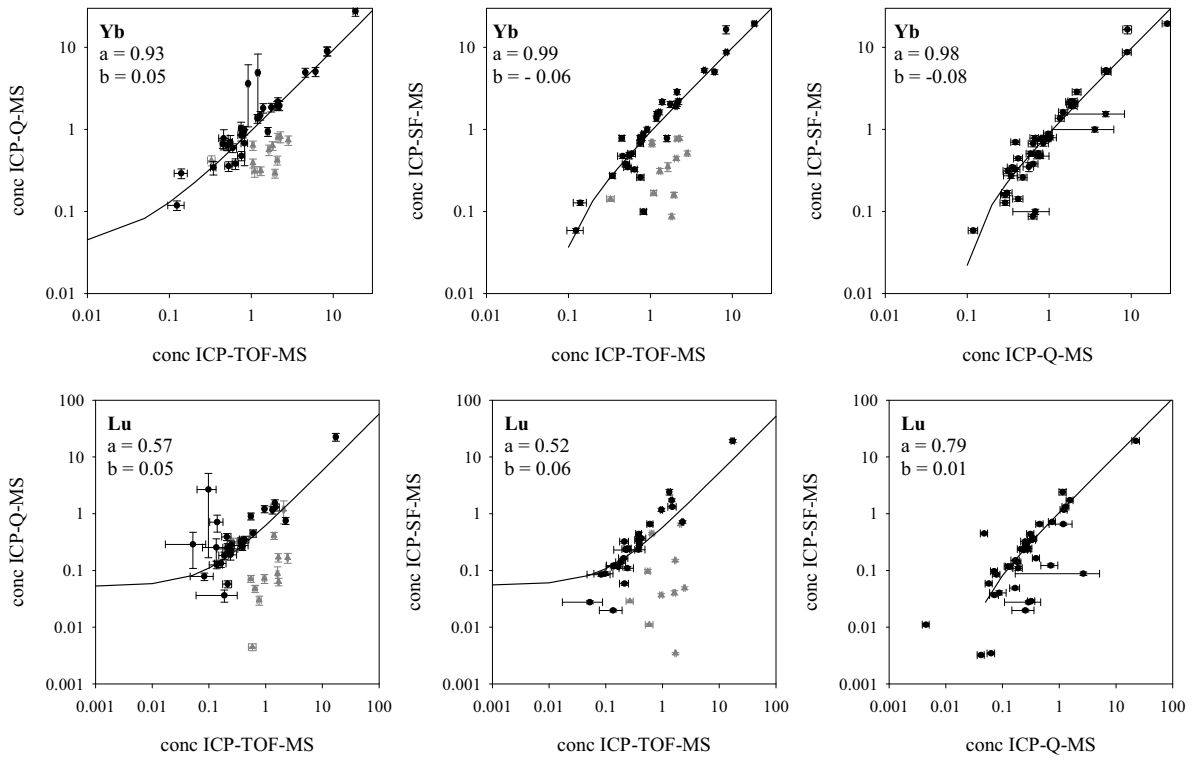
Table S 2: Continuation

Paper IV

Proxies and measurement techniques for mineral dust in Antarctic ice cores

Ruth, U., Barbante, C., Bigler, M., Delmonte, B., Fischer, H., Gabrielli, P., Gaspari, V., Kaufmann, P., Lambert, F., Maggi, V., Marino, F., Petit, J.-R., Steffensen, J.-P., Udisti, R., Wagenbach, D., Wegner, A., Wolff, E., resubmitted to Environmental Science & Technology.

Proxies and measurement techniques for mineral dust in Antarctic ice cores

Urs Ruth[1*], Carlo Barbante[2], Matthias Bigler[3,4], Barbara Delmonte[5], Hubertus Fischer[1], Paolo Gabrielli[2,6], Vania Gaspari[2], Patrik Kaufmann[3], Fabrice Lambert[3], Valter Maggi[5], Federica Marino[5,7], Jean-Robert Petit[8], Roberto Udisti[7], Dietmar Wagenbach[9], Anna Wegner[1], Eric W. Wolff[10]

[1] Alfred-Wegener-Institute for Polar and Marine Research, Bremerhaven, Germany

[2] Department of Environmental Sciences, University of Venice, Venice, Italy

[3] Climate and Environmental Physics, Physics Institute, University of Bern, Bern, Switzerland

[4] Centre for Ice and Climate, Niels Bohr Institute, University of Copenhagen, Denmark

[5] Department of Environmental Sciences, University of Milano Biccoca, Italy

[6] School of Earth Sciences and Byrd Polar Research Center, Ohio State University, Columbus, USA

[7] Department of Chemistry, University of Florence, Florence, Italy

[8] Laboratoire de Glaciologie et Géophysique de l'Environnement, CNRS, Grenoble, France

[9] Institut für Umweltphysik, University of Heidelberg, Heidelberg, Germany

[10] British Antarctic Survey, Cambridge, United Kingdom

* Urs.Ruth@awi.de

Abstract

To improve quantitative interpretation of ice core aeolian dust records, a systematic methodological comparison was made. This involved methods for water-insoluble particle counting (Coulter Counter and laser-sensing particle detector), soluble ion analysis (ion chromatography, and continuous flow analysis), elemental analysis (inductively coupled plasma mass spectroscopy at pH 1 and after full acid digestion), and water-insoluble elemental analysis (proton induced X-ray emission). Antarctic ice core samples covering the last deglaciation from the EPICA Dome C (EDC) and the EPICA Dronning Maud Land (EDML) cores were used. All methods correlate very well amongst each other, but the ratios of glacial age to Holocene concentrations, which are typically a factor ~100, differ between the methods by up to a factor of 2 with insoluble particles showing the largest variability. The recovery of ICP-MS measurements depends on the digestion method and is different for different elements and during different climatic periods. EDC and EDML samples have similar dust composition, which suggests a common dust source or a common mixture of sources for the two sites. The analysed samples further reveal a change of dust composition during the last deglaciation.

1. Introduction

Mineral dust aerosol is an important part of the climate system (*1-3*). Apart from sea salt it is the most abundant primary aerosol and influences the radiative energy budget of the atmosphere (*4*). Aeolian mineral dust can enhance primary marine bioproductivity (*5*) and can be important for pedogenesis in remote land areas (*6*). To understand the climate changes of the past it is therefore necessary to have an accurate quantitative reconstruction of the past atmospheric dust load and aeolian dust fluxes. Projects dedicated to this, such as DIRTMAP (*7*), rely on modelling studies and on dust accumulation data from environmental archives. Although most ice cores come from polar regions – which invokes complex transport processes from the mid-latitude sources to high-latitude sites – they have a central role as dust archives because the dust is stored in the simple matrix of ultrapure water and because they offer excellent time control and temporal resolution.

The most common proxies for dust in ice cores are insoluble particle concentration, e.g. (*8-13*), and Ca^{2+} ion concentration, e.g. (*14-18*). These have been complemented over recent years by a large suite of other proxies with multiple measurement techniques for the soluble and insoluble fraction of the mineral dust aerosol. However, the term "dust" is often used without exactly specifying the proxy considered, and it is largely unknown how the different proxies relate quantitatively to each other, particularly under changing climatic conditions.

The objective of this paper is to present a systematic comparison of different proxies and measurement techniques for mineral dust in ice cores. All techniques investigated use melted samples; thus techniques based on light scattering on solid ice (*19, 20*) are omitted. The use of certified dust samples proved inappropriate because their size distribution, shape, optical properties, mineralogy and elemental composition differ significantly from aeolian dust accumulated in polar ice cores. Instead, real ice core samples were used from the two deep drilling sites of the European Project for Ice Coring in Antarctica (EPICA): EPICA Dome C (EDC) (*21*) and EPICA Dronning Maud Land (EDML) (*22*). Each set of some 20 samples spans the last glacial termination (Fig. 1), which took place approximately 10-20 ka BP (thousand years before the present). Thus, the samples cover the full range from low dust concentrations in the Holocene to high dust concentrations during the Last Glacial Maximum (LGM) and can also capture possible changes of dust composition over this important climatic transition. Methodological results from this study are expected to apply also to other ice cores from Antarctica or Greenland.

2. Methods

Ice samples were decontaminated by three repeated washings in ultra-pure water (Millipore). The initial weight of each sample was about 200 g, and the mass loss during decontamination was ~50%. The decontaminated samples were melted at room temperature in pre-washed LDPE bottles. Once melted, the samples were gently agitated for homogenization and then partitioned into individual vials (polystyrene Coulter-Counter accuvettes, pre-cleaned using ultra-pure water) for the different analyses. Repeated checks show that the dust concentration difference between the first and the last aliquots is typically around the level of measurement-reproducibility, i.e. the aliquots provided for the different analyses should be comparable. Exceptionally larger differences (up to 50%) were observed, probably due to contamination of selected aliquots. The washing and partitioning was performed in a class 100 laminar flow bench situated inside a class 1000 clean laboratory. The samples dedicated to insoluble particle analyses were analysed promptly after melting; all other samples were refrozen within several hours, shipped frozen to the respective laboratories, and kept at -20°C. The samples were then prepared for the respective analyses (Table 1) as described hereafter.

2.1 Insoluble particles – Coulter Counter (CC)

For Coulter Counter (CC) analysis an electrolyte (NaCl) is added to the sample, which then is pumped through a small orifice. The electrical conductance is measured across the orifice. Particles flowing through the orifice reduce the conductance, from which the total volume of each microparticle is directly estimated. A Multisizer IIe (Beckmann-Coulter) set up in the clean room of LGGE was used with a 50 µm orifice, allowing measurement of particles with diameters between 0.7 and 20 µm (256 size channels). Procedures are described elsewhere (*11, 23*). Size calibration was achieved via a certified standard of spherical latex particles (Beckman-Coulter). Each sample was measured three times with 0.5 mL sample volume per measurement. For calculation of the microparticle mass an average mineral density of 2.5 g/cm^3 was assumed.

2.2 Insoluble particles – Laser-sensing Particle Detector (LPD)

A field-portable laser-based detection system LDS 23/25 (Klotz) was used, which was developed in cooperation with the University of Heidelberg (*24*). The liquid sample is

pumped through a detection cell, where the attenuation of transmitted light (680 nm) is measured for each particle (32 channels). Conversion of this signal to particle size is difficult because complex scattering processes occur. Size assignment was obtained by a posteriori alignment of the LPD size spectra to the CC size spectra (Ruth et al., in preparation). Using this procedure, a lower particle detection limit of 1.04 μm diameter was found. The particle mass below this limit was estimated from a log-normal fit to the data (*25*) assuming a single-mode distribution. Each sample was measured three times with 2 mL per measurement. A mean density of 2.5 g/cm^3 was used to convert particle volume to mass.

2.3 Soluble Calcium – Ion Chromatography (IC)

Ion chromatography (IC) is a commercially available method to quantify soluble major ion concentrations and is well-established for measurement of Ca^{2+} in ice cores (*17, 18, 26*). A sample loop of 1 mL was used with Dionex CG12A and CS12A guard and separation columns in an isocratic run using methanesulfonate eluent (20mM); low background conductivity and noise was accomplished using autosuppression (Dionex CSRS Ultra II). Standardization was achieved by use of cation solutions of certified concentrations. The error for Ca^{2+} concentration is strongly dependent on the blank contribution and variability (typically 1±1 ppb (1 ppb = 1 μg/kg)). With this blank variability, the reproducibility is better than 10 % for concentrations larger than 20 ppb (i.e. samples from LGM) but increases to ±100 % for concentrations of 1 ppb (i.e. samples from the Holocene). Each sample was measured once with 3 mL per sample.

2.4 Soluble Calcium – Continuous Flow Analysis (CFA) fluorimetry

CFA is an established technique for continuous measurement of selected ion concentrations at high spatial resolution in ice cores (*27*). The analytical method (*28*) to quantify soluble Ca^{2+} ion concentrations was adapted at the University of Bern for CFA use (*29*). In a continuous flow reactor Ca^{2+} was converted at pH 7 to a fluorescent complex. The concentration was deduced from the fluorescence intensity, which was measured by a custom-made spectrometer at 495 nm wavelength. Standardization was achieved by use of certified Ca^{2+}-solutions. The method has a detection limit of 0.1 ppb. Typically, the sample water is obtained continuously from an ice-core melting device, but for this study discrete samples were injected into the system. Each sample was measured once with ~5 mL per sample.

2.5 Elemental concentrations – Inductively Coupled Plasma Mass Spectrometry

The samples for Inductively Coupled Plasma Mass Spectrometry (ICP-MS) were subdivided at the University of Venice to compare two different sample preparation methods. For determination of the "acid-leachable" fractions the samples were melted and acidified to pH 1 with ultrapure nitric acid (Romil) 24 hours prior to the analysis. For determination of the total content the samples underwent an acid digestion for complete dissolution: to 1 mL of melted sample were added about 0.3 mL of HNO_3 and 0.3 mL of HF (both ultrapure, Romil) with subsequent microwave irradiation in a PTFE pressure bomb. Procedural blanks were prepared to check for contamination and values were subtracted from the measured sample concentrations. Sector field ICP-MS (Element2, Thermo Finnigan) (*30, 31*) analyses were performed for aluminum (^{27}Al), vanadium (^{51}V), iron (^{56}Fe) and other trace elements at medium resolution (m/Δm=4000) allowing for separation of major interferences for Fe such as ^{40}Ar^{16}O. Standardization was achieved using HNO_3-acidified and digested dilutions, respectively, of a multi-element standard (Merck) (*32*).

2.6 Insoluble element concentrations – Proton Induced X-ray Emission (PIXE)

PIXE is an X-ray spectrometry technique based on primary ionization of the inner shells of a target atom by an impinging proton beam. The production of characteristic X-rays allows for highly sensitive bulk dust analysis of elements with atomic numbers ranging from 11 (Na) to 92 (U) (*33*). For analysis of Antarctic ice dust at very low concentrations, PIXE is able to measure Na, Mg, Al, Si, K, Ca, Ti, Mn and Fe with analytical detection limits <1 ppb. PIXE targets were prepared directly by filtering each melted sample through a polycarbonate membrane (Nuclepore, pore size 0.45 µm) without pre-treatment such as acidification or precipitation (*34*). Sample preparation was performed inside a class 100 laminar-flow bench inside a clean laboratory at the University of Milano-Bicocca. Procedural blanks were prepared by filtration of ultrapure water following identical procedures. The PIXE analyses were carried out at the 2 MeV AN2000 accelerator at the National Laboratories of Legnaro (Padova) (*34-36*). One target was prepared from each sample with sample volumes from 7 to 50 mL.

3. Results: Methodological Comparison

In total, more than 50 different species related to mineral dust were measured, but only the most relevant ones are discussed here. In this section, an overview of the results is given first followed by selected comparisons. Most plots shown are logarithmic scatter plots. Linear regression lines calculated from the logarithms of the data are also shown: EDML and EDC data combined (black, continuous line), EDC data only (red, dashed line) and EDML data only (blue, dotted line). Additionally, in the scatter plots some statistical measures are given; they are evaluated for the combined sets of EDML and EDC data: R_{log} is the correlation coefficient R calculated from the logarithms of the data. c_{log} is the slope of the linear regression line calculated from the logarithms of the data; a slope $\neq 1$ means that the y/x-ratio changes with concentration; the values given correspond to the slopes of the black regression lines. *median-ratio* is the median of all ratios y_i /x_i, where y_i is the species of the y-axis and x_i is the species of the x-axis for every data point i; *median-ratio* gives the typical ratio of the y-parameter to the x-parameter. *rel-gain* is the relative concentration increase of the y-parameter for an increase of the x-parameter by a factor $f=100$; this is a measure of the sensitivity of the y-parameter to changes of the x-parameter in linear space. *rel-gain* = 0.5 means that for a 100-fold increase of the x-parameter the y-parameter increases by 50. Note that *rel-gain* $= f^{(c\_log-1)}$, i.e. *rel-gain* does not transform linearly for factors $f' \neq 100$.

3.1 Overview of most important proxies and methods

Figure 2 shows a comprehensive overview of scatter plots for different species. For purposes of comparability, they are all plotted against a common reference, for which insoluble particle concentrations (from CC) are chosen. The dust concentration in the EDML-samples is typically 2-3 times that of EDC-samples. Insoluble particles exhibit the largest concentration variance of all species shown; the ratio between highest glacial and lowest Holocene particle concentration is about 200 (119 for EDC and 337 for EDML for the particular sets of samples from this study). All chemical species exhibit a good correlation with insoluble particles, typically $R_{log} > 0.9$. However, c_{log} is > 0.8, and *rel-gain* > 0.5 for most species, which means that the y/x-ratio is up to a factor of 2 lower at high than at low concentrations. This indicates considerable changes in dust composition or detection between the climate regimes. Thus, a quantitative reconstruction of dust deposition fluxes will depend on the particular choice of the parameter.

3.2 Insoluble Particles

The comparison of LPD vs. CC data of insoluble particle mass concentrations is shown in Figure 2a. While the CC is an established technique for measurement of discrete samples (*10, 11*), the LPD is a novel ice core method that is capable of CFA operation (*25*). The data have a very high correlation (R_{log}=1.00); and the c_{log} of 0.96 is very close to 1. Good correspondence (R_{log}=1.00 and c_{log} = 0.92) is found also between the respective number concentrations (data not shown). The very low scatter of the data suggests that the LPD is a reliable method to quantify variations of insoluble particle concentrations in ice cores; this is not a consequence of using CC data for the size calibration of the LPD because changes of mass concentration are caused primarily by changes of particle numbers and not of particle size. The *median-ratio* of 0.90 and the *rel-gain* of 0.82 show, however that the LPD does not fully reproduce the large variance of the CC data; this may possibly result from coincidence-losses (a particle passing while the detector is still busy evaluating the previous particle), which are compensated for in the CC but not in the LPD. Altogether, the LPD vs. CC plots show the smallest amount of scatter, which presumably is the consequence of the two methods both counting particles and also of the high precision of both methods.

3.3 Soluble Calcium

Unfortunately, there is evidence for possible analytical shortcomings regarding the determination of Ca^{2+} in this particular study. Part of the early Holocene samples from this study showed unrealistically high Ca^{2+} concentrations when compared to the exhaustive profiles available from EDC (*17*) and EDML (*18*) and were therefore excluded from the data set. This applied to IC- as well as CFA data. In addition, the low *rel-gain* for Ca^{2+} reported here (see below) is not in agreement with previous data for EDC (*17, 21*) and EDML (*18, 22*), where similar factors were found for insoluble particles and Ca^{2+}. Thus, this section should be viewed with caution as there may be unidentified analytical problems for low concentrations.

Figures 2b and 2e show the total Ca^{2+} and the $nssCa^{2+}$ (non-sea-salt, see section 4.2) ion concentrations vs. insoluble particles. The correlation is high (R=0.96 for each); but the c_{log} of only 0.61 and 0.69 and the *rel-gain* of only 0.16 and 0.24, respectively, are unexpectedly low.

A methodological comparison for IC measurements and CFA measurements is shown in Figure 3. The methods show a good correspondence with R_{log} = 0.96, *median-ratio* = 1.13, c_{log} = 1.03 and *rel-gain* = 1.13. This confirms good results from earlier comparisons (*26*), possibly with a higher scatter for IC measurements due to a higher blank contribution.

3.4 ICP-MS: acidification to pH 1 vs. full digestion

Comparing elemental concentrations measured by ICP-MS to insoluble particle concentrations (Figure 2), R_{log} are all very high (0.93 – 0.96). c_{log} ranges from 0.83 (Al-HNO_3) to 0.93 (V-HNO_3). Vanadium (V) shows the best *rel-gain* (0.72). This confirms that V is a good proxy of Antarctic dust as there are no other sources even during interglacial periods (*37*).

The method of sample preparation has a large influence on the results obtained from ICP-MS measurements. A full acid digestion is expected to yield total element concentrations; but this method poses a significantly larger risk of contamination than an acidification to pH 1 using ultra-pure HNO_3. In Figure 4 results obtained with these two sample preparation methods are compared for the major crustal elements Fe and Al. The correlation is generally good; but there is considerably larger variability for the early Holocene samples. For the species shown this higher variability is not a problem of detection limit or blank, nor a statistical consequence of smaller concentrations; instead, it points to enhanced compositional variations possibly related to variations of mineral identity of the dust during the Holocene.

By assuming 100 % recovery for full acid digestion, the recovery of the pH 1 acidification can be quantified. This is found to vary between climatic periods. For the early Holocene samples the recovery is ~30% (Fe), and 45% (Al) with large scatter; for the late glacial samples the recovery is ~55% (Fe) and 40% (Al). This confirms earlier findings of a 30-65 % recovery for Fe (*32*). The recovery at pH 1 is least variable for Al, which should therefore be the preferred reference element when assessing variations of terrestrial enrichment factors from pH 1 digested samples. Unfortunately, blank problems in the full acid digested samples prevent a check on the robustness of the recovery rate for V at pH 1.

3.5 PIXE

Comparing elemental concentrations measured by PIXE to insoluble particle concentrations (Figure 2) R_{log} ranges from 0.92 (Al) to 0.97 (Si, Fe) with c_{log} from 0.8 (Ca) to 0.97 (Si). For Ca (Figure 2c) low concentration data give a different ratio between the two methods for EDC and EDML; however, concentrations are close to the detection limit.

PIXE measures the elemental composition of water-insoluble dust after filtration. By assuming 100 % filtration efficiency for PIXE and 100 % recovery for ICP-MS measurements (full acid digestion), the elements Fe and Al can be attributed to a water-insoluble fraction and a soluble residual. In Figure 5 results obtained with the two methods are compared.

For Fe a very good log-correlation is found (R_{log} =0.95) with c_{log} =1.0. The *median-ratio* is 0.76, suggesting that ~25% of the Fe is water-soluble. This ratio does not change between glacial times and early Holocene. The upper limit for the fraction of bio-available iron, which still depends on the oxidation state, would thus be ~25%, which is larger by a factor 5-10 than the values typically used in models for simulating the effect of iron-fertilization in the Southern Ocean (*38-40*).

For Al the insoluble fraction amounts to ~100 %. However, early Holocene samples show a large scatter (especially for EDC-samples) with PIXE concentrations exceeding the ICP-MS concentrations. This may be caused by analytical uncertainties with the ICP-MS full acid digestion method in this case.

A comparison between CFA-Ca (Figure 2b, mean concentration ~10 ppb) and PIXE-Ca (Figure 2c, mean concentration ~1 ppb) suggests that ~ 90 % Ca is present in soluble form while only 10 % are water-insoluble; this confirms and quantifies earlier findings (*3, 15, 35*).

4. Discussion of dust composition

The most noticeable observation from Figures 2-5 is that no obvious systematic differences occur between EDC and EDML samples. In all scatter plots shown the samples from EDC and EDML overlap strongly and do not fall into separate groups. An exception is PIXE-Ca data during early Holocene, however, values are close to the detection limit and thus

questionable. This suggests that the dust composition is geochemically very similar at the two sites and that they likely receive dust from a common dust source or the same mixture of sources as has been suggested also for other locations (41).

The mean composition of the insoluble dust can be characterized by referring elemental concentrations determined by PIXE to the total particle mass from CC. This yields mean ratios of approximately 0.26 (Si), 0.08 (Al), and 0.05 (Fe), which deviate only slightly from the mean composition of upper continental crust of 0.30 (Si), 0.08 (Al), and 0.03 (Fe) (42). Detailed compositional investigations should be made using material from potential dust sources and focussing on fractionation during uptake, atmospheric transport and dissolution.

Although the mean composition for Si, Al, Fe and Ca as referenced to CC insoluble particle mass give reasonable results similar to crustal averages, the *rel-gain* is always below 1. This could imply that either the dust is depleted in these elements at high or enriched at low concentrations, possibly resulting from fractionation during transport. Alternatively, there could be analytical issues, and further work is needed to clarify this issue.

4.1 Terrestrial vs. marine contributions to Ca^{2+} and Na^+

Ca^{2+} and Na^+ contain soluble terrestrial contributions from mineral dust and marine contributions from sea salt. To evaluate these contributions separately the respective mass ratios $(Na/Ca)_{sol,dust}$ of soluble Na^+ and Ca^{2+} from mineral dust and $(Na/Ca)_{ss}$ from sea salt aerosol must be known. $(Na/Ca)_{ss}$ ranges between 23 (brine rejected during sea ice formation (43)) and 26 (bulk sea water (44)). However, $(Na/Ca)_{sol,dust}$ is far more variable and less well known.

The apportionment of Ca^{2+} into a "non sea salt" fraction (nssCa) and a "sea salt" fraction (ssCa) often considers $(Na/Ca)_{sol,dust} = 0.56$ (e.g. (3, 45)), which corresponds to the total (not only soluble) elemental composition of mean continental crust (44). Alternatively, total element ratios for upper continental crust could be used (Na/Ca=0.87) (42) ; and from high-resolution ice core data $(Na/Ca)_{sol,dust} = 0.94\pm0.07$ is suggested (46). Here we take another complementary approach based on linking insoluble dust, Ca^{2+} and Na^+ concentrations. The following equations are considered: $[Ca^{2+}] = [Ca_{ss}] + [Ca_{sol,dust}] = \alpha^{-1} [Na_{ss}] + a [CC]$, where $\alpha = (Na/Ca)_{ss}$ is chosen to be 26 ($\alpha = 23$ gives the same results for b), $a = [Ca_{sol,dust}] / [CC]$, and $[CC]$ is the insoluble particle mass concentration. Further, $[Na^+] = [Na_{ss}] + [Na_{sol,dust}] = [Na_{ss}]$

+ ab [CC], where $b = (Na/Ca)_{sol,dust}$ is the parameter of interest. Parameter optimization yields $b = 0.91\pm0.2$ ($a = 0.085$) for all samples from this study [$b = 1.05$ ($a = 0.057$) for samples dated older than 16 ka BP to circumvent potential problems with Holocene Ca^{2+} data, and $b = 0.83$ ($a = 0.092$) for samples dated younger than 16 ka BP]. Thus, we suggest an average of $(Na/Ca)_{sol,dust} = 0.91\pm0.2$ by mass, which is in good agreement with (46).

4.2 Temporal changes of dust composition

Compositional changes of the ice core dust over time can be identified by calculating ratios between different dust-related parameters on identical ice-core samples. Figure 6 shows time series of selected ratios on the common *EDML1/EDC3* time scale (47, 48): the recovery of ICP-MS measurements for sample preparation at pH 1 for Fe and Al, the Fe/Al ratio at pH 1, and the element ratios Si/Al and K/Al from PIXE. It is clearly noticeable that a regime-shift happens during the deglaciation. The sample-to-sample variability of the ratios is much higher for the early Holocene samples than for the late glacial samples. Also, the average recovery of acidified samples (pH 1) measured by ICP-MS changes during the deglaciation, albeit less prominently. Further, the insoluble elemental composition of the dust (PIXE) shifts to relatively more Al, less Si and less K.

A change in dust mineralogy during the last deglaciation is consistent with other observations: A similar shift to less K and more Ca in the Taylor Dome ice core (49), and a difference of Nd and Sr isotope ratios at EDC (50) and a change of Li solubility at EDC (51). This regime shift dates between ~16.5 and ~15.0 ka BP from our data. It suggests that either the characteristics of the dust source changes (e.g. soil development), or there is a change in the relative contributions of different sources (e.g. transport changes). The overlap of EDC and EDML samples indicates that even at times of higher variability there are no distinct sources and transport paths to the two ice core sites. Thus, the controlling factors for dust concentrations on the East Antarctic plateau likely are the emission intensity in the dust sources as well as the ability of the dust to intrude the polar vortex. Once inside the polar vortex the dust transport to the two sites is either very homogeneous or effectively randomized.

Acknowledgements

References

1. Prospero, J. M.; Charlson, R. J.; Mohnen, V.; Jaenicke, R.; Delany, A. C.; Moyers, J.; Zoller, W.; Rahn, K., The atmospheric aerosol systen: an overview. *Reviews of Geophysics and Space Physics* **1983,** 21, (7), 1607-1629.

2. Rea, D. K., The paleoclimatic record provided by eolian deposition in the deep sea: the geologic history of wind. *Reviews of Geophysics* **1994,** 32, (2), 159-195.

3. Fischer, H.; Siggaard-Andersen, M. L.; Ruth, U.; Röthlisberger, R.; Wolff, E., Glacial/interglacial changes in mineral dust and sea-salt records in polar ice cores: Sources, transport, and deposition. *Reviews of Geophysics* **2007,** 45, (RG1002), doi:10.1029/2005RG000192.

4. Sokolik, I. N.; Winker, D. M.; Bergametti, G.; Gillette, D. A.; Carmichael, G.; Kaufman, Y. J.; Gomes, L.; Schuetz, L.; Penner, J. E., Introduction to special section: Outstanding problems in quantifying the radiative impacts of mineral dust. *Journal of Geophysical Research* **2001,** 106, (D16), 18015-18027.

5. Boyd, P. W.; Jickells, T.; Law, C. S.; Blain, S.; Boyle, E. A.; Buesseler, K. O.; Coale, K. H.; Cullen, J. J.; de Baar, H. J. W.; Follows, M.; Harvey, M.; Lancelot, C.; Levasseur, M.; Owens, N. P. J.; Pollard, R.; Rivkin, R. B.; Sarmiento, J.; Schoemann, V.; Smetacek, V.; Takeda, S.; Tsuda, A.; Turner, S.; Watson, A. J., Mesoscale Iron Enrichment Experiments 1993-2005: Synthesis and Future Directions. *Science* **2007,** 315, 612-617, DOI: 10.1126/science.1131669.

6. Wang, P.; Clemens, S. C.; Beaufort, L.; Branconnot, P.; Ganssen, G. M.; Jian, Z.; Kershaw, P.; Sarnthein, M., Evolution and variability of the Asian monsoon system: State of the art and outstanding issues. *Quaternary Science Reviews* **2005,** 24, 595-629.

7. Kohfeld, K. E.; Harrison, S. P., DIRTMAP: the geological record of dust. *Earh-Science Reviews* **2001,** 54, 81-114.

8. Cragin, J. H.; Herron, M. M.; Langway Jr., C. C.; Klouda, G., Interhemispheric comparison of changes in the composition of atmospheric precipitation during the late Cenozoic era. In *Polar Oceans*, Dunbar, M. J., Ed. Arctic Institute of North America: Calgary, AB, Canada, 1977; pp 617-631.

9. Hammer, C. U. In *Dust studies on Greenland ice cores*, Isotopes and impurities in snow and ice-symposium, Proceedings of the Grenoble Symposium, 1977; Proceedings of the Grenoble Symposium, 1977; pp 365-370.

10. Petit, J.-R.; Briat , M.; Royer, A., Ice age aerosol content from East Antarctic ice core samples and past wind strenght. *Nature* **1981,** 293, 391-394.

11. Steffensen, J. P., The size distribution of microparticles from selected segments of the Greenland Ice Core Project ice core representing different climatic periods. *Journal of Geophysical Research* **1997,** 102, (C12), 26755-26763.

12. Delmonte, B.; Basile-Doelsch, I.; Petit, J.-R.; Maggi, V.; Revel-Rolland, M.; Michard, A.; Jagoutz, E.; Grousset, F. E., Comparing the EPICA and Vostok dust records during the last 220,00 years: stratigraphical correlation and provenance in glacial periods. *Earh-Science Reviews* **2004,** 66, 63-87.

13.   Lambert, F.; Delmonte, B.; Petit, J.-R.; Bigler, M.; Kaufmann, P.; Hutterli, M. A.; Stocker, T.; Ruth, U.; Steffensen, J. P.; Maggi, V., Dust-climate couplings over the past 800,000 years from the EPICA Dome C ice core. *Nature* **2007**, in review.

14.   Legrand, M.; Delmas, R., Soluble impurities in four Antarctic ice cores over the last 30000 years. *Annals of Glaciology* **1988,** 10, 116-120.

15.   de Angelis, M.; Barkov, N. I.; Petrov, V. N., Sources of continental dust over Antarctica during the last glacial cycle. *Journal of Atmospheric Chemistry* **1992,** 14, 233-244.

16.   Mayewski, P. A.; Meeker, L. D.; Whitlow, S.; Twickler, M. S.; Morrison, M. C.; Bloomfield, P.; Bond, G. C.; Alley, R. B.; Gow, A. J.; Grootes, P. M.; Meese, D. A.; Ram, M.; Taylor, K. C.; Wumkes, W., Changes in atmospheric circulation and ocean ice cover over the North Atlantic during the last 41,000 years. *Science* **1994,** 263, 1747-1751.

17.   Wolff, E. W.; Fischer, H.; Fundel, F.; Ruth, U.; Twarloh, B.; Littot, G.; Mulvaney, R.; Röthlisberger, R.; de Angelis, M.; Boutron, C.; Hansson, M.; Jonsell, U.; Hutterli, M.; Bigler, M.; Lambert, F.; Kaufmann, P.; Stauffer, B.; Steffensen, J. P.; Siggaard-Andersen, M. L.; Udisti, R.; Becagli, S.; Castellano, E.; Severi, M.; Wagenbach, D.; Barbante, C.; Gabrielli, P.; Gaspari, V., Southern Ocean sea-ice extent, productivity and iron flux over the past eight glacial cycles. *Nature* **2006,** 440, 491-496, doi:10:1038/nature04614.

18.   Fischer, H.; Fundel, F.; Ruth, U.; Twarloh, B.; Wegner, A.; Udisti, R.; Becagli, S.; Castellano, E.; Morganti, A.; Severi, M.; Wolff, E.; Littot, G.; Röthlisberger, R.; Mulvaney, R.; Hutterli, A.; Kaufmann, P.; Federer, U.; Lambert, F.; Bigler, M.; Hansson, M.; Jonsell, U.; de Angelis, M.; Gabrielli, P.; Boutron, C.; Siggaard-Andersen, M. L.; Steffensen, J. P.; Barbante, C.; Gaspari, V.; Gabrielli, P.; Wagenbach, D., Reconstruction of millenial changes in dust emission, transport and regional sea ice coverage using the deep EPICA ice cores from the Atlantic and Indian Ocean sectors of Antarctica. *Earth and Planetary Science Letters* **2007,** 260, 340-354.

19.   Bay, R. C.; Price, B. P.; Clow, G. D.; Gow, A. J., Climate logging with a new rapid optical technique at Siple Dome. *Geophysical Research Letters* **2001,** 28, (24), 4635-4638.

20.   Ram, M.; Koenig, G., Continuous dust concentration profile of pre-Holocene ice from the Greenland Ice Sheet Projct 2 ice core: dust stadials, interstadials, and the Eemian. *Journal of Geophysical Research* **1997,** 102, (C12), 26641-26648.

21.   EPICA-community-members, Eight glacial cycles from an Antarctic ice core. *Nature* **2004,** 429, 623-628, doi:10.1038/nature02599.

22.   EPICA-community-members, One-to-one coupling of glacial climate variability in Greenland and Antarctica. *Nature* **2006,** 444, 195-198, doi:10.1038/nature05301.

23.   Delmonte, B.; Petit, J. R.; Maggi, V., Glacial to Holocene implications of the new 27,000-year dust record from the EPICA Dome C (East Antarctica) ice core. *Climate Dynamics* **2002,** 18, (8), 647-660.

24.   Ruth, U.; Wagenbach, D.; Bigler, M.; Steffensen, J. P.; Röthlisberger, R.; Miller, H., High resolution dust profiles at NGRIP: Case studies of the calcium-dust relationship. *Annals of Glaciology* **2002,** 35, 209–216.

25.   Ruth, U.; Wagenbach, D.; Steffensen, J. P.; Bigler, M., Continuous record of microparticle concentration and size distribution in the central Greenland NGRIP ice core during the lastglacial period. *Journal of Geophysical Research* **2003,** 108, (D3), doi:10.1029/2002JD002376.

26.   Littot, G.; Mulvaney, R.; Röthlisberger, R.; Udisti, R.; Wolff, E.; Castellano, E.; de Angelis, M.; Hansson, M. E.; Sommer, S.; Steffensen, J. P., Comparison of analytical methods used for measuring mahor ions in the EPICA Dome C (Antarctica) ice core. *Annals of Glaciology* **2002,** 35, 299-305.

27.   Röthlisberger, R.; Bigler, M.; Hutterli, A.; Sommer, S.; Stauffer, B.; Junghans, H. G.; Wagenbach, D., Technique for continuous high-resolution analysis of trace substances in firn and ice cores. *Environmental Science and Technology* **2000,** 34, 338-342.

28.   Tsien, R. Y.; Pozzan, T.; Rink, T. J., Calcium homeostasis in intact lymphocytes: cyroplasmic free calcium monitored with a new, intracellularly trapped fluorecent indicator. *The Journal of Cell Biology* **1982,** 94, 325-334.

29.   Sigg, A.; Fuhrer, K.; Anklin, M.; Staffelbach, T.; Zurmühle, D., A continuous analysis technique for trace species in ice cores. *Environmental Science and Technology* **1994,** 28, 204-210.

30.   Barbante, C.; Cozzi, G.; Capodaglio, G.; van de Velde, K.; Ferrari, C.; Boutron, C.; Cescon, P., Trace element determination in alpine snow and ice by double focussing inductively coupled plasma spectrometry. *J. Anal. At. Spectrom.* **1999,** 14, 1433.

31.   Planchon, F. A. M.; Boutron, C.; Barbante, C.; Wolff, E. W.; Cozzi, G.; Gaspari, V.; Ferrari, C.; Cescon, P., Ultrasensitive determination of heavy metals at the sub-picogram per gram level in ultraclean Antarctic snow samples by inductively coupled plasma sector field mass spectrometry. *Analytica Chimica Acta* **2001,** 450, (1), 193-205.

32.   Gaspari, V.; Barbante, C.; Cozzi, G.; Cescon, P.; Boutron, C.; Gabrielli, P.; Capodaglio, G.; Ferrari, C.; Petit, J. R.; Delmonte, B., Atmospheric iron fluxes over the last deglaciation: climatic implications. *Geophysical Research Letters* **2006,** 33, L03704, doi:10.1029/2005GL024352.

33.   Johansson, S. A. E.; Campbell, J. L.; Malmqvist, K. L., *Particle induced X-ray emission (PIXE)*. John Wiley and Sons, Inc.: New York, 1995.

34.   Marino, F.; Maggi, V.; Delmonte, B.; Ghermandi, G.; Petit, J.-R., Elemental composition (Si, Fe, Ti) of atmospheric dust over the last 220 kyr from the EPICA ice core (Dome-C, Antactica). *Annals of Glaciology* **2004,** 39, 110-118.

35.   Ghermandi, G.; Cecchi, R.; Capotosto, M.; Marino, F., Elemental composition determined by PIXE analysis of the insoluble aerosol particles in EPICA-Dome C ice core samples representing the last 27000 years. *Geophysical Research Letters* **2003,** 30, (22), doi:10.1029/2003GL018169.

36.   Marino, F. Geochemical chracterization of the EPICA Dome-C ice core dust by major elements PIXE analysis and its paleoclimatic implications. PhD thesis, University of Siena, Siena, 2006.

37.   Gabrielli, P.; Planchon, F.; Hong, S.; Lee, K.; Hur, S. D.; Barbante, C.; Ferrari, C.; Petit, J.-R.; Lipenkov, V. Y.; Cescon, P.; Boutron, C., Trace elements in Vostok Antarctic ice during the last four climatic cycles. *Earth and Planetary Science Letters* **2005,** 234, (1-2), 249-259.

38.   Moore, J. K.; Doney, S. C.; Lindsay, K., Upper ocean ecosystem dynamics and iron cycling in a global three-dimensional model. *Global Biogeochemical Cycles* **2004,** 18, (GB4028), doi:10.1029/2004GB002220.

39.   Fung, I. Y.; Meyn, S. K.; Tegen, I.; Doney, S. C.; John, J. G.; Bishop, K. B., Iron supply and demand in the upper ocean. *Global Biogeochemical Cycles* **2000,** 14, (1), 281-295.

40.   Cassar, N.; Bender, M. L.; Barnett, B. A.; Fan, S.; Moxim, W. J.; Il, H. L.; Tilbrook, B., The Southern Ocean Biological Response to Aeolian Iron Deposition. *Science* **2007,** 317, 1067-1070, DOI: 10.1126/science.1144602.

41.   Hinkley, T.; Pertsiger, F.; Zavjalova, L., The modern atmospheric background dust load: recognition in Central Asian snowpack, and compositional contraints. *Geophysical Research Letters* **1997,** 24, (13), 1607-1610.

42.   Wedepohl, K. H., The composition of the continental crust. *Geochim. Cosmochim. Acta* **1995,** 59, (7), 1217-1232.

43.   Wagenbach, D.; Ducroz, F.; Mulvaney, R.; Keck, L.; Minikin, A.; Legrand, M.; Hall, J. S.; Wolff, E. W., Sea-salt aerosol in coastal Antarctic regions. *Journal of Geophysical Research* **1998,** 103, (D9), 10961-10974.

44.   Bowen, H. J. M., *Environmental Chemistry of the Elements*. Academic Press: London, 1979.

45.   Röthlisberger, R.; Mulvaney, R.; Wolff, E.; Hutterli, M.; Bigler, M.; Sommer, S.; Jouzel, J., Dust and sea salt variability in central East Antarctica (Dome C) over the last 45 kyrs and its implications for southern high-latitude climate. *Geophysical Research Letters* **2002,** 29, (20), 1963, doi:10.1029/2002GL015186.

46.   Bigler, M.; Röthlisberger, R.; Lambert, F.; Stocker, T.; Wagenbach, D., Aerosol deposited in East Antarctica over hte last glacial cycle: Detailed apportionment of continental and sea-salt contributions. *Journal of Geophysical Research* **2006,** 111, (D08205), doi:10.1029/2005JD006469.

47.   Ruth, U.; Barnola, J.-M.; Beer, J.; Bigler, M.; Blunier, T.; Castellano, E.; Fischer, H.; Fundel, F.; Huybrechts, P.; Kaufmann, P.; Kipfstuhl, S.; Lambrecht, A.; Morganti, A.; Parrenin, F.; Rybak, O.; Severi, M.; Udisti, R.; Wilhelms, F.; Wolff, E., EDML1: A chronology for the EPICA deep ice core from Dronning Maud Land, Antarctica, over the last 150,000 years. *Climate of the Past* **2007,** 3, 475-484.

48.   Parrenin, F.; Barnola, J.-M.; Beer, J.; Blunier, T.; Castellano, E.; Chappellaz, J.; Dreyfus, G.; Fischer, H.; Fujita, S.; Jouzel, J.; Kawamura, K.; Lemieux, B.; Loulergue, L.; Masson-Delmotte, V.; Narcisi, B.; Petit, J.-R.; Raisbeck, G.; Raynaud, D.; Ruth, U.; Schwander, J.; Severi, M.; Spahni, R.; Steffensen, J. P.; Svensson, A.; Udisti, R.; Waelbroeck, C.; Wolff, E., The EDC3 chronology for the EPICA Dome C ice core. *Climate of the Past* **2007,** 3, 485-497.

49.   Hinkley, T.; Matsumoto, A., Atmospheric regime of dust and salt through 75,000 years of Taylor Dome ice core: Refinement by measurement of mahor, minor, and trace metal suites. *Journal of Geophysical Research* **2001,** 106, (D16), 18487-18493.

50.   Delmonte, B.; Petit, J.-R.; Basile-Doelsch, I.; Jagoutz, E.; Maggi, V., Late Quaternary Interglacials in East Antarctica from ice core dust records. In *The Climate of Past Interglacials*, Sirocko, F.; Litt, T.; Claussen, M., Eds. Elsevier: Amsterdam, 2006.

51.   Siggaard-Andersen, M. L.; Gabrielli, P.; Steffensen, J. P.; Stromfeldt, T.; Barbante, C.; Boutron, C.; Fischer, H.; Miller, H., Soluble and insoluble lithium dust in the EPICA DomeC ice core - Implications for changes of the East Antarctic dust provenance during the recent glacial-interglacial transition. *Earth and Planetary Science Letters* **2007,** 258, 32-43.

Tables and Figures with Captions

Table 1 – Parameter overview: List of species and measurement methods of mineral dust discussed in this paper; also given are the respective limits of detection (LOD, including procedural blanks) for typical applications.

Acronym	Species	Method	LOD [ppb]
CC-mass	total water-insoluble particle mass (from particle volume)	Coulter Counter	2
LPD-mass	total water-insoluble particle mass (from particle diameter)	Laser-sensing Particle Detector	1
IC-Ca	soluble Ca^{2+}	Ion Chromatography	2
CFA-Ca	soluble Ca^{2+}	Continuous Flow Analysis	0.1
nss-CFA-Ca*	soluble non-sea-salt Ca^{2+} [$(Na/Ca)_{sol,dust}$ = 0.91]	calculated	---
ICPMS-digest-Al	total Al (full acid digestion)	ICP-MS	0.5
ICPMS-digest-Fe	total Fe (full acid digestion)	ICP-MS	0.2
ICPMS- HNO_3-Al	leachable Al (HNO_3-digestion at pH 1)	ICP-MS	0.1
ICPMS- HNO_3-Fe	leachable Fe (HNO_3-digestion at pH 1)	ICP-MS	0.03
ICPMS- HNO_3-V	leachable V (HNO_3-digestion at pH 1)	ICP-MS	0.001
PIXE-Al	water-insoluble, particulate dust Al	PIXE	0.8
PIXE-Ca	water-insoluble, particulate dust Ca	PIXE	0.2
PIXE-Fe	water-insoluble, particulate dust Fe	PIXE	0.1
PIXE-Si	water-insoluble, particulate dust Si	PIXE	0.7

Table 1.

Figure 1:
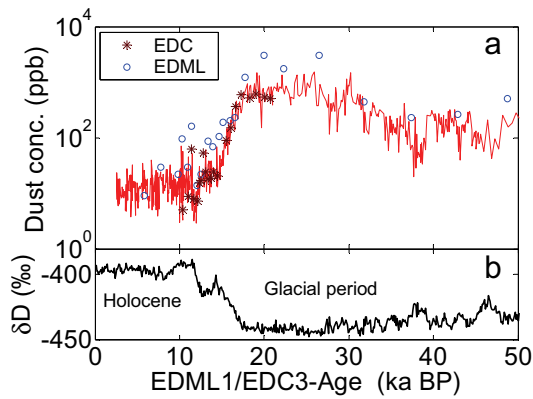
Figure 1:

Upper panel (a): Overview of samples used in this study shown on the *EDML1/EDC3* time scale (*47, 48*); EDC samples shown as dark red asterisks, EDML samples shown as blue circles. Insoluble particle mass concentrations (CC-mass) are plotted here as a representative of mineral dust concentrations. For orientation, the EDC dust profile is also shown as a red line (*12*). Note that samples range from low concentrations during Holocene to high concentrations during the LGM for EDC as well as for EDML. Lower panel (b): For orientation, EDC deuterium isotopic deviation as a proxy for atmospheric temperature (*21*).
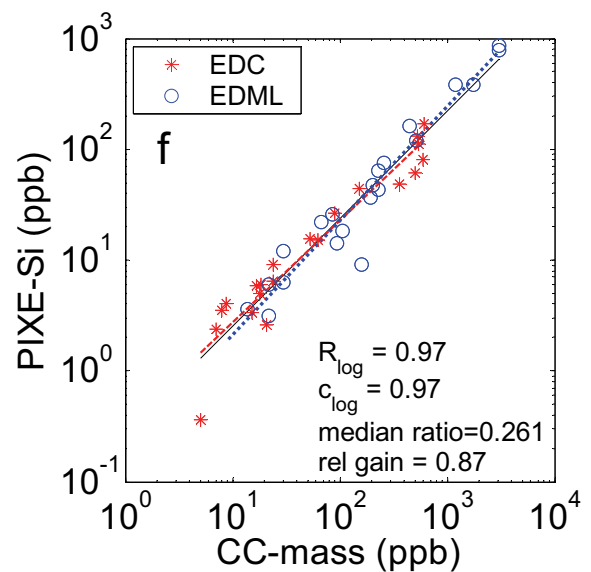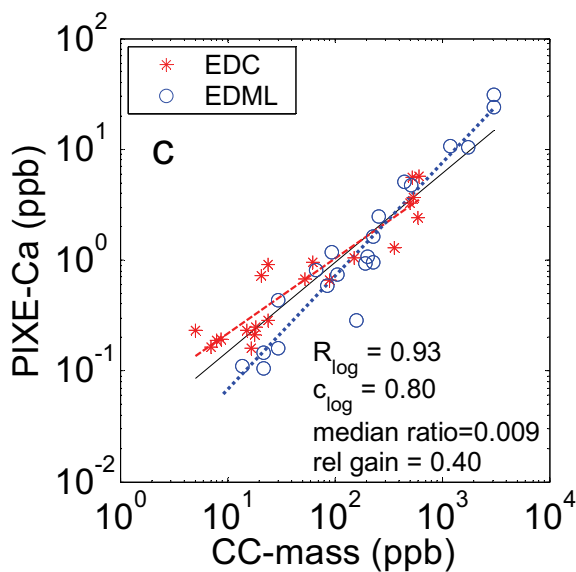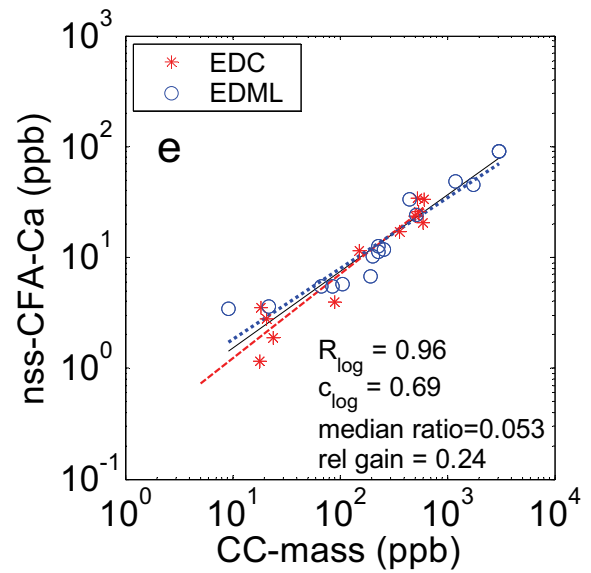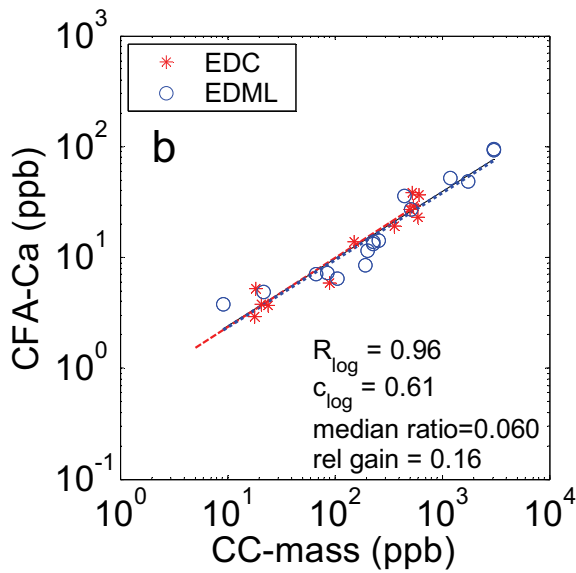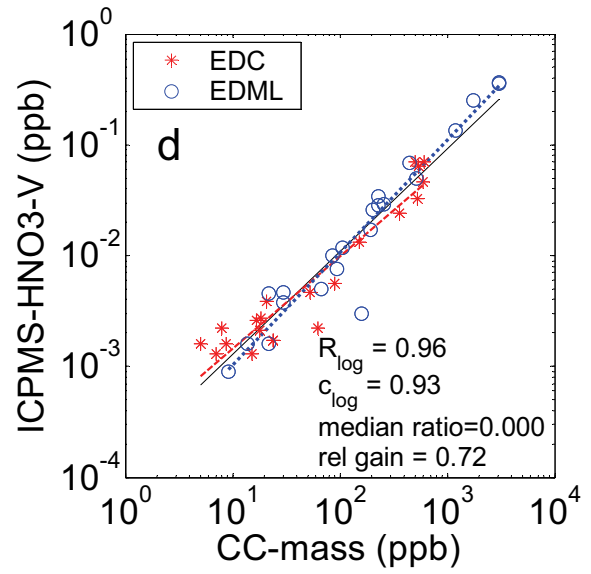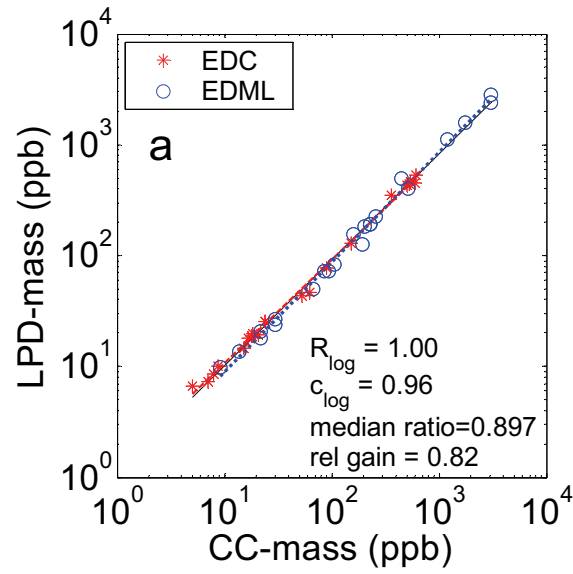
Figure 2 a-f:
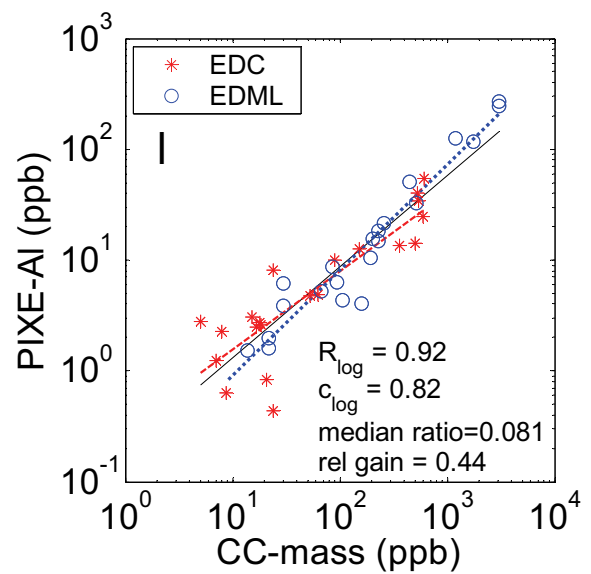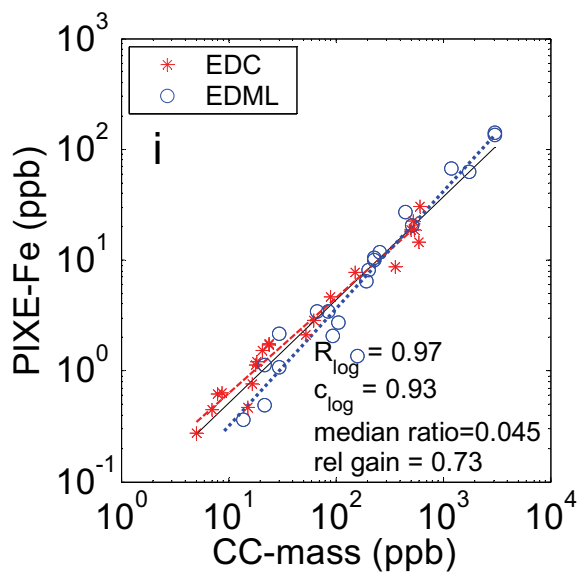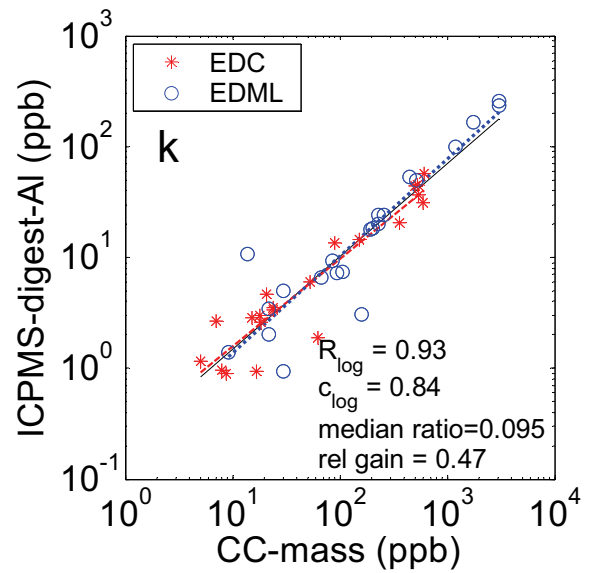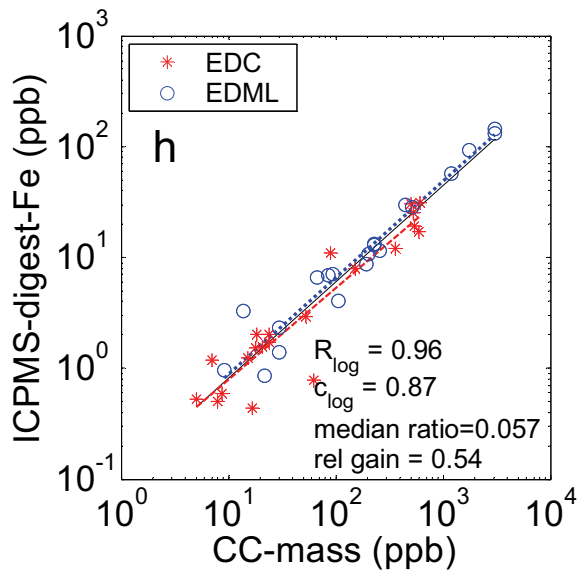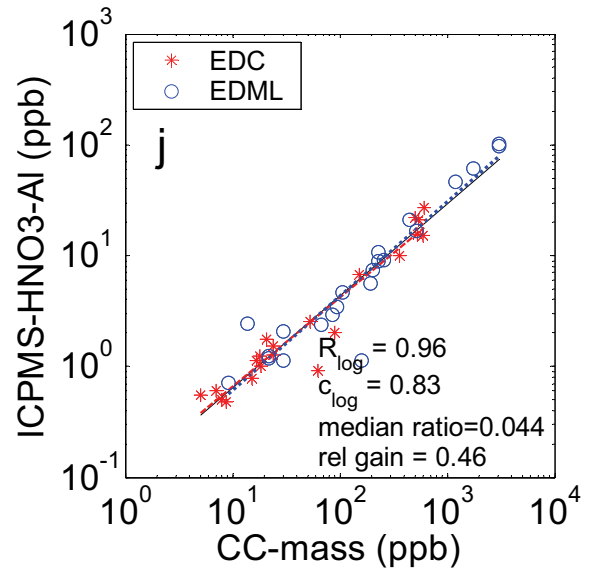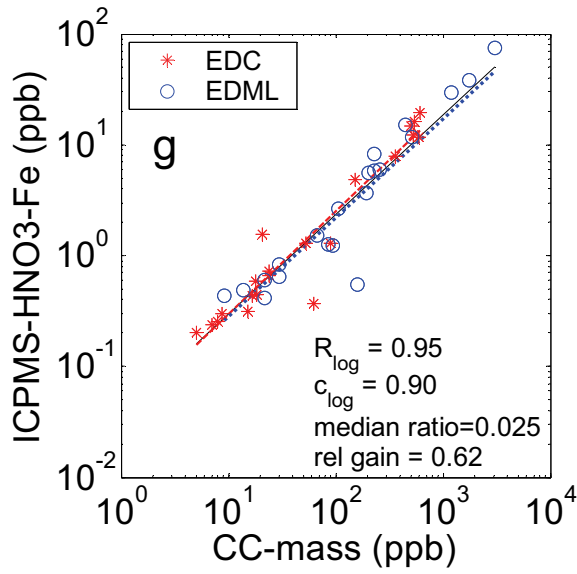
Figure 2 g-l:

Figure 2:

Scatter plots of different parameters all plotted vs. insoluble particle mass (from Coulter Counter) as a common reference for comparison. All values in ppb. Note logarithmic scales. Shown also are linear regression lines calculated from the logarithms of the data: EDML and EDC data (black continuous line), EDC data only (red, dashed line) and EDML data only (blue, dotted line). Selected statistical measures are given in each plot for all (EDC and EDML) data: R_{log} – correlation coefficient (in loglog-space); c_{log} – slope of linear regression line (in loglog-space); *median ratio* – median of ratios (y_i/x_i) of concentrations; *rel gain* – relative gain of y-parameter for a concentration increase of factor 100 for the x-parameter. For details see text; for abbreviations of parameters: see Table 1.

Figure 3:
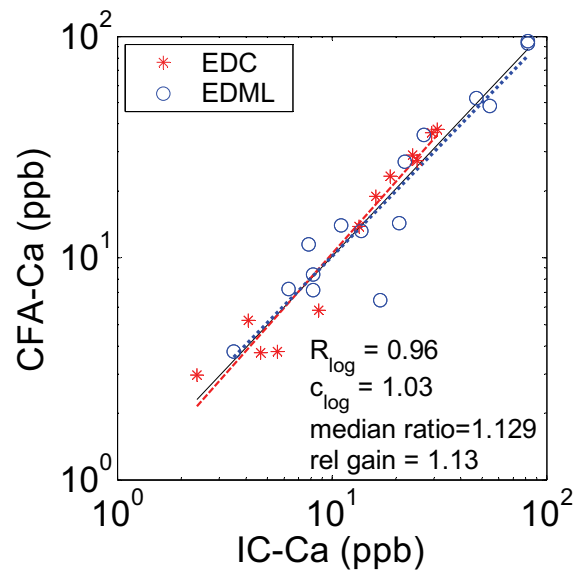
Figure 3:

Scatter plot of CFA-Ca^{2+} vs. IC-Ca^{2+}.

Figure 4:
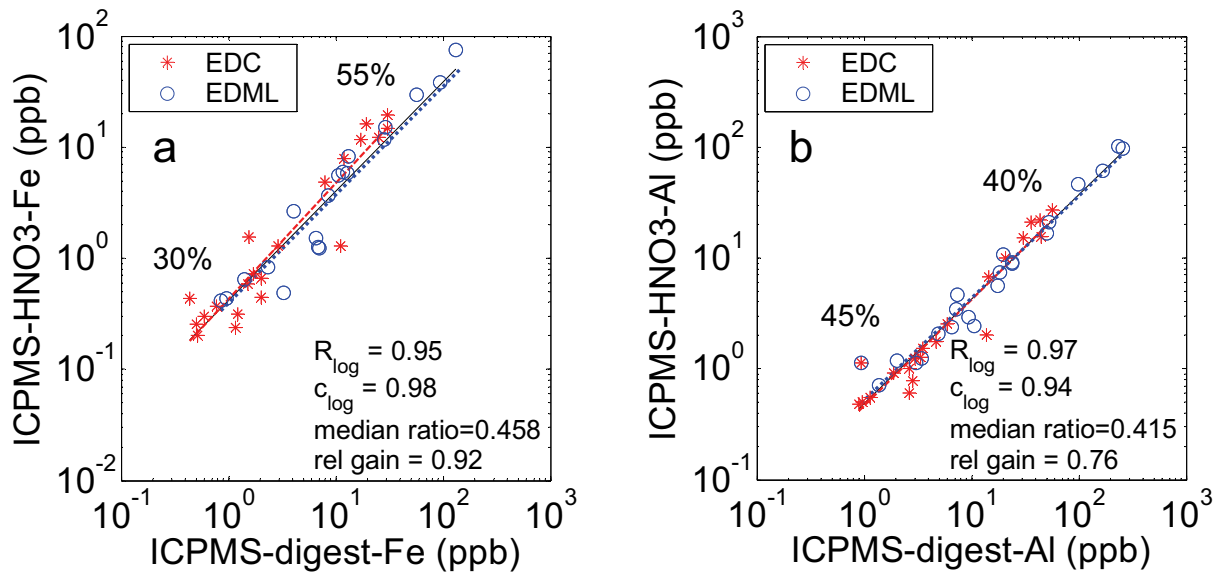
Figure 4:

Scatter plot of ICP-MS element concentrations of Fe (a) and Al (b) for two different sample preparation techniques: acidification to pH 1 (y-axis) vs. full acid digestion (x-axis). Typical recoveries of HNO_3-digestion (pH 1) are indicated for Holocene and LGM samples (see text for details).

Figure 5:
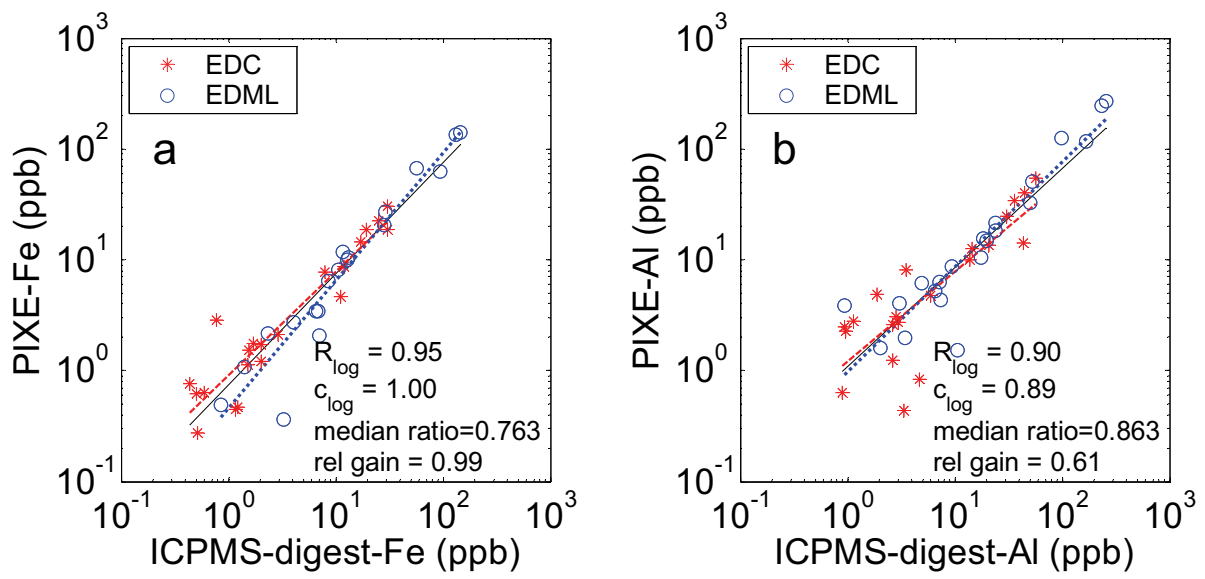
Figure 5:

Scatter plot of PIXE vs. ICP-MS (full digestion) for Fe (a) and Al (b).

Figure 6:
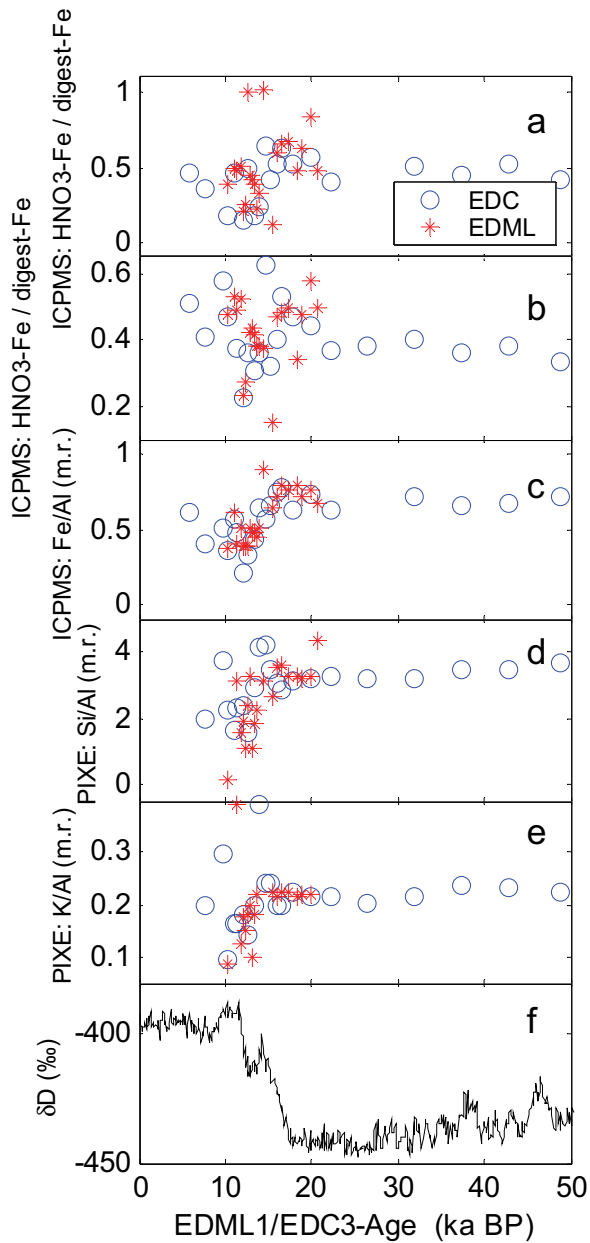
Figure 6:

Time series of different ratios of element concentrations shown on the common *EDML1/EDC3* time scale (*47, 48*): ICP-MS concentrations of HNO_3-digestion (pH 1) normalized to full acid digestion of Fe (a) and Al (b); Fe/Al mass ratio of ICP-MS concentrations (HNO_3-digestion) (c); PIXE concentrations of Si (d) and K (e) both normalized to PIXE-Al concentrations (expressed as mass ratios, m.r.). A regime shift at ~16 ka BP is noticeable from changing point-to-point variability and value of some ratios. For orientation, the EDC deuterium isotopic deviation as a proxy for atmospheric temperature is shown (*21*).

Acknowledgements

Abbreviations

ACR	Antarctic cold reversal
CFA	continuous flow analysis
CC	Coulter Counter
CI	chondrite
CPP	coarse particle percentage
CS_{PC}	coordinate system spanned by the principal components
CS_{REE}	coordinate system spanned by the rare earth elements
DML	Dronning Maud Land
EPICA-DML	EPICA Dronning Maud Land
EPICA	European project of ice coring in Antarctica
FPP	fine particle percentage
HREE	heavy rare earth element (Ho - Lu)
IC	ion chromatography
ICP-MS	inductively coupled plasma mass spectrometer
ICP-QP-MS	inductively coupled plasma quadrupole mass spectrometer
ICP-SF-MS	inductively coupled plasma sectorfield mass spectrometer
ICP-TOF-MS	inductively coupled plasma time of flight mass spectrometer
IPCC	Intergovernmental Panel on Climate Change
LREE	heavy rare earth element (La - Nd)
LS	laser sensor
MIS	marine isotope stage
MMD	mean mass diameter
MREE	medium rare earth element (Sm - Dy)
PAAS	post archean Australian shell
PC	principcal component
PCA	principcal component analysis
PS	polystyrene
PSA	potential source area
PTFE	polytetrafluoroethylen
REE	rare earth elements
TE	trace elements
UCC	upper continental crust

E r k l ä r u n g

Hiermit versichere ich, dass ich

1. die Arbeit ohne unerlaubte fremde Hilfe angefertigt habe,

2. keine anderen als die von mir angegebenen Quellen und Hilfsmittel benutzt habe und

3. die den benutzten Werken wörtlich oder inhaltlich entnommenen Stellen als solche kenntlich gemacht habe.

Bremerhaven, den 25.1.08

(Unterschrift)